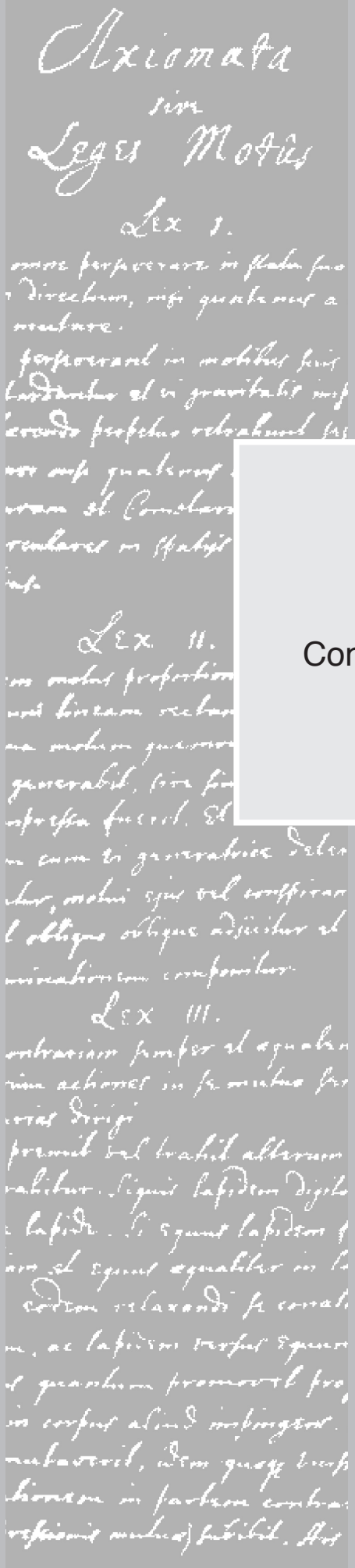

Technische Universität
Kaiserslautern

Rouven Mohr

Consistent Time-Integration of Finite Elasto-Plasto-Dynamics

UKL/LTM T 08-04 Juni 2008
Lehrstuhl für Technische Mechanik

Bibliografische Information Der Deutschen Bibliothek
Die Deutsche Bibliothek verzeichnet diese Publikation in der Deutschen Nationalbibliografie; detaillierte bibliografische Daten sind im Internet über **http://dnb.ddb.de** abrufbar.

Bibliographic information published by Die Deutsche Bibliothek
Die Deutsche Bibliothek lists this publication in the Deutsche Nationalbibliografie; detailed bibliographic data is available in the Internet at **http://dnb.ddb.de.**

Farbig erschienen auf http://kluedo.ub.uni-kl.de

Herausgeber: Fachbereich Maschinenbau und Verfahrenstechnik
Lehrstuhl für Technische Mechanik
Postfach 3049
Technische Universität Kaiserslautern
D-67653 Kaiserslautern

Verlag: Technische Universität Kaiserslautern

Druck: Technische Universität Kaiserslautern
ZBT – Abteilung Foto-Repro-Druck

D-386

Als Manuskript gedruckt. Printed in Germany.

ISSN 1610-4641
ISBN 978-3-939432-81-4

Consistent Time-Integration of Finite Elasto-Plasto-Dynamics

vom Fachbereich Maschinenbau und Verfahrenstechnik
der Technischen Universität Kaiserslautern
zur Verleihung des akademischen Grades

Doktor-Ingenieur (Dr.-Ing.)

genehmigte Dissertation
von

Dipl.-Ing. Rouven Mohr

aus
Saarbrücken

Hauptreferent:	Prof. Dr.-Ing. P. Steinmann
Korreferenten:	Prof. Dr.-Ing. A. Menzel
	Prof. Dr.-Ing. D. Kuhl
	JP Dr.-Ing. J. Mergheim
Vorsitzender:	Prof. Dr.-Ing. J. C. Aurich
Dekan:	Prof. Dr.-Ing. S. Ripperger

Tag der Einreichung:	09. April 2008
Tag der mündl. Prüfung:	23. Juni 2008

Kaiserslautern, Juni 2008

D 386

‘The whole problem with the world is that fools and fanatics are always so certain of themselves, but wiser people so full of doubts.’

Bertrand Russell (1872 – 1970)

Preface

The work presented in this thesis has been carried out during my time as a PhD student at the Chair of Applied Mechanics in the Department of Mechanical and Process Engineering at the University of Kaiserslautern from March 2005 to February 2008. During this time period, my PhD project was embedded within the International Research Training Group 1131 'Visualization of Large and Unstructured Data Sets: Applications in Geospatial Planning, Modeling, and Engineering', providing an interdisciplinary and very stimulating research environment. In this context, the funding by the German Research Foundation DFG is gratefully acknowledged.

First of all, I want to thank Professor Paul Steinmann for his supervision, the continuous support, and the many friendly conversations not only during the last three years but also during my entire time period at the Chair of Applied Mechanics, starting already as a student co-worker in the year 2001. Moreover, the helpful input and the encouraging discussions with Professor Andreas Menzel, who is indeed more than a scientific advisor for me, are sincerely appreciated. Furthermore, special acknowledgements are dedicated to Professor Detlef Kuhl and JP Julia Mergheim for their interest in my work, acting also as referees of this thesis, as well as to Professor Jan Aurich, representing the head of the committee.

Finally, I thank all my colleagues for the pleasant working atmosphere and especially my friends Michael 'H' Scherer, Johannes 'J' Utzinger, and Stefan 'Steven' Uhlar who has spent several hours proofreading the manuscript, improving the quality of the visualisations, and discussing with me a multitude of topics.

Most of all, however, I would like to thank my parents for enabling my education and studies, and in particular my 'Schatzi' for her love, infinite understanding, and never-ending tolerance.

Kaiserslautern, June 2008 Rouven Mohr

Abstract

In the present contribution, a general framework for the completely consistent integration of nonlinear dissipative dynamics is proposed, that essentially relies on Finite Element methods in space and time. In this context, fully flexible structures as well as hybrid systems which consist of rigid bodies and inelastic flexible parts are considered. Thereby, special emphasis is placed on the resulting algorithmic fulfilment of fundamental balance equations, and the excellent performance of the presented concepts is demonstrated by means of several representative numerical examples, involving in particular finite elasto-plastic deformations.

Keywords: computational dynamics, consistent integration, Galerkin methods, inelastic multibody systems, finite elasto-plasticity

Zusammenfassung

In der vorliegenden Arbeit wird ein universelles Konzept zur vollständig konsistenten Integration nichtlinearer dissipativer Dynamik entwickelt, welches im Wesentlichen auf Finite-Element-Ansätzen in Raum und Zeit beruht. In diesem Zusammenhang werden sowohl vollkommen flexible Strukturen als auch hybride Systeme bestehend aus Starrkörpern und inelastischen flexiblen Anteilen betrachtet. Unter besonderer Berücksichtigung der algorithmischen Erfüllung grundlegender Bilanzgleichungen wird die Leistungsfähigkeit der vorgeschlagenen Verfahren anhand diverser numerischer Beispiele demonstriert, wobei insbesondere finite elasto-plastische Deformationen näher untersucht werden.

Schlagwörter: numerische Dynamik, konsistente Integration, Galerkin Verfahren, inelastische Mehrkörpersysteme, finite Elasto-Plastizität

Contents

1. Introduction **1**

2. Prolog – Motivation **15**
2.1. Friction-Element Oscillator 15
2.1.1. Friction-element 15
2.1.2. Dynamics 17
2.2. Linear Spring Characteristic 18
2.2.1. Constitutive update 18
2.2.2. Time-stepping scheme 19
2.3. Nonlinear Spring Characteristic 23
2.3.1. Constitutive update 23
2.3.2. Time-stepping schemes 24

3. Fundamental Concepts **31**
3.1. Nonlinear Continuum Dynamics 31
3.1.1. Kinematics 31
3.1.2. Dissipative materials 32
3.1.3. Balance laws – Conservation properties 33
3.2. Semidiscrete Dynamics 34
3.2.1. Spatial discretisation 35
3.2.2. Semidiscrete Hamiltonian-type formulation 35
3.2.3. Conservation properties – Semidiscrete system 37
3.3. Time Discretisation 40
3.3.1. Finite Elements in time – A general framework 40
3.3.2. Approximation of time-integrals 41
3.3.3. Conservation properties – Completely discrete system 45

4. Finite Elasticity **49**
4.1. Constitutive Modelling – Principal Stretches 50
4.1.1. Formulation 50
4.1.2. Algorithmic treatment 52
4.2. Conserving Time-Stepping Schemes 54

4.2.1. Standard quadrature rule . . . 55
4.2.2. Non-standard quadrature rule . . . 56
4.3. Enhancement and Principal Stretches – Pitfalls . . . 57
4.3.1. Basic properties – Numerical limit transition . . . 57
4.3.2. Key properties – Principal stretches . . . 61
4.4. Enhancement and Principal Stretches – Remedy . . . 63
4.4.1. Overall concept – Mixed strategy . . . 63
4.4.2. Assessment – Constitutive models . . . 66
4.5. Enhancement and Principal Stretches – Consequences . . . 73
4.5.1. Numerical performance . . . 74
4.5.2. Mechanical performance . . . 77
4.5.3. Perturbation vs. performance . . . 79
4.6. Numerical Examples – Spinning Wheel . . . 81
4.6.1. Quasi rigid motion . . . 81
4.6.2. Mixed stiffness motion . . . 85

5. Finite Elasto-Plasticity 89
5.1. Constitutive Modelling – Multiplicative Plasticity . . . 89
5.1.1. Formulation . . . 89
5.1.2. Return mapping algorithm . . . 91
5.2. Consistent Time-Stepping Schemes . . . 95
5.2.1. Standard quadrature rule . . . 95
5.2.2. Non-standard quadrature rule . . . 97
5.3. Numerical Examples – Fundamental Results . . . 101
5.3.1. Flying Frame . . . 101
5.3.2. Oscillating Bar . . . 103
5.3.3. Spinning Wheel . . . 105
5.4. Influence of the Predictor Strategy . . . 109
5.5. Aspects of Convergence . . . 111
5.5.1. Basic scheme . . . 112
5.5.2. Modified schemes . . . 119
5.6. Assessment of Integrators . . . 124
5.6.1. Standard vs. non-standard quadrature rule . . . 124
5.6.2. Standard vs. non-standard integrator . . . 135

6. Finite Elasto-Plastic Multibody Dynamics 145
6.1. Constrained Dissipative Dynamics . . . 145
6.1.1. Internal constraints – Rigid body dynamics . . . 148
6.1.2. External constraints – Kinematic pairs . . . 152
6.1.3. Coupling constraints – Flexible parts . . . 154
6.2. Consistent Time-Stepping Scheme . . . 156
6.3. Numerical Examples . . . 160

6.3.1. Flying Frame 160
6.3.2. Flying Conrod 166
6.3.3. Shaking Frame 172
6.3.4. Slider-Crank Mechanism 181

7. Epilog – Discussion **191**

A. Energy-Consistency **197**
A.1. Global Condition 197
A.2. Global vs. Local Condition 199
A.3. Local Condition 201

B. Challenges in Visualisation **205**
B.1. Motivation 205
B.2. Comparative Tensor Visualisation 206

C. Standard Time Integrators **213**
C.1. Newmark Scheme 213
C.2. HHT Methods 214
C.3. Collocation Methods 215

1. Introduction

In all disciplines of engineering, the application of modern simulation tools has dramatically increased in the last years. Enabled by today's computer performance, this trend is directly related to the virtual prototype scenario, which is essentially driven by the permanent requirement to reduce the design and production costs. In this context, the computational modelling of real technical systems often demands the incorporation of dynamic effects, dealing for instance with ride and handling simulations in the automotive industry, virtual crash tests, or the numerical investigation of metal forming processes. In each case, the first step consists of the transfer of the real system to an appropriately simplified physical model which, in a second step, can be often described mathematically by means of differential equations. Considering dynamical problems, at least ordinary differential equations have to be handled, however, mostly partial differential equations come into play. Finally, the resulting equations must be solved adequately in the actual simulation step. During the foregoing modelling and simulation procedure, basically two crucial issues have to be tackled, namely:

- The physical model has to be as simple as possible, but also as accurate as needed to represent all essential features of the considered real system.
- Moreover, usually numerical methods are required to simulate the system behaviour, since in most of the cases the resulting governing equations of the mathematical model can not be solved analytically.

Thereby, the applied methods should be chosen carefully with regard to the offered numerical performance and also in view of the obtained quality of the results. In any case, an increasing model complexity additionally requires more sophisticated numerical techniques and, hence, an advancing knowledge in mechanical as well as mathematical concepts.

Dealing in particular with the numerics of nonlinear dynamics, it is well-known that especially the selection of proper time-integration algorithms represents a demanding task. In this context, several time-stepping schemes are available, whereby most of them have been originally designed for linear problems. Unfortunately, the majority of these integrators can lead to strong numerical instabilities when nonlinear dynamical systems are taken into account, so that an application in the nonlinear setting can not

be recommended. Interestingly, it has turned out in this regard that the algorithmic fulfilment of physically motivated conservation properties – like the balance of momentum maps or the laws of thermodynamics – is of cardinal importance not only from the theoretical but even from a practical point of view, being related to the robustness of the considered time-stepping schemes. Motivated by this aspect, specific algorithms have been specifically developed in the past for nonlinear applications, considering for instance multibody systems or large strain elastodynamics. Apparently, the modelling of dissipative systems poses further challenges compared to the conservative case due to the higher complexity of the underlying physical and mathematical models. Nevertheless, the incorporation of dissipation is of fundamental relevance in many technical applications, considering friction effects or inelastic material behaviour.

In the present contribution, an advanced concept concerning the *time-integration* of *nonlinear inelastic dynamics* is developed for structural dynamics as well as for flexible multibody systems, dealing in particular with *finite elasto-plasticity*. Hereby, the main feature of the proposed algorithms is constituted by a *completely consistent* integration which guarantees also in the discrete setting a numerically exact fulfilment of fundamental balance principles, relying essentially on the proper approximation of involved time-integrals. In fact, it will be shown that the advocated methods offer a superior numerical performance and perfectly reflect the underlying physics of the real system.

Literature Survey

Before considering an outline of this work, we present a short survey on relevant publications which are related to computational dynamics in general, the modelling of plastic material behaviour, the simulation of elasto-plasto-dynamics, and the numerical treatment of (elasto-plastic) multibody systems.

Computational dynamics: In the literature, there exist a multitude of different time-stepping schemes for various applications, whereby initially the focus has been placed on linear dynamical systems. One of the most famous and widespread algorithms for structural dynamics is the well-known Newmark scheme which has originally been proposed by Newmark [143] in the late fifties of the last century. Subsequently, various authors have presented modifications of the Newmark scheme, whereby one of the main issues was certainly the incorporation of optimised numerical dissipation. In this context, a popular representative has been proposed by Hilber *et al.* [74], referred to as 'HHT methods', or by Chung and Hulbert [48], referred to as 'generalized-α method'. However, the performance of the Newmark-type algorithms is still strongly limited when dealing with nonlinear dynamics. Consequently, several alternative methods have been discussed in the past to improve the algorithmic properties with regard to robustness of the schemes and veritableness of the results.

In this context, a typical concept is to design algorithms which inherit conservation properties of the considered mechanical system, sometimes referred to as 'mechanical integrators'. As already mentioned, the conservation of the momentum maps and in particular the algorithmic energy balance play a central role in the such investigations. In the latter case, it can be basically distinguished between *energy-conserving methods* and *energy-dissipative schemes* which additionally incorporate numerical high-frequency damping. Early contributions related to energy-conserving time integrators can be found in LaBudde and Greenspan [97, 98] or Hughes *et al.* [77]. Further notable work in this area has been done more recently by Kuhl [91], Crisfield and Shi [49], and Krenk [88, 89, 90]. In the last decade, substantial formulations have been proposed in particular by Simo *et al.* [165, 166, 167, 168, 170], Tarnow and Simo [173], and Gonzalez [62, 63, 64], who has introduced a so-called 'discrete gradient/derivative' to guarantee algorithmic energy conservation. The famous and often cited 'energy-momentum method' for elastodynamics dates back to Simo and Tarnow [165], investigating in particular a constitutive model which bases on a quadratic form. Approximately ten years later, this concept has been revised with regard to general hyperelastic models by Laursen and Meng [101], solving iteratively an additional equation to determine an adequate Piola-Kirchhoff stress tensor. Moreover, several authors compared energy-conserving with energy-decaying/numerically dissipative methods taking care of high frequency modes, see e.g. Armero and Romero [7, 8] or Kuhl and Crisfield [92] with application to the dynamics of truss elements. An overview and a comparison of different schemes can be found in Bottasso and Trainelli [40]. A further class of time-stepping algorithms addresses specifically the (conserving) integration of shell or beam dynamics, see e.g. Bottasso *et al.* [38], Ibrahimbegovic and Mamouri [83], Sansour [155], Sansour *et al.* [156, 157, 158], Betsch and Steinmann [30], and Leyendecker *et al.* [110] favouring a formulation based on director triads to avoid rotational degrees of freedom. Furthermore, we refer in this context to the 'constraint energy momentum algorithm' by Kuhl and Ramm [94] who enforced energy as well as momentum conservation by means of additional Lagrange multipliers on the global level, similarly to the concept by Hughes *et al.* [77]. Moreover, the same authors apply the 'generalized energy-momentum method', which has been originally proposed in Reference [92], to the nonlinear dynamics of shells and combine this time-stepping scheme with an adaptive control of the time-step size, see Reference [95].

All of the concepts listed above essentially rely on the philosophy that a control of the algorithmic energy results in an improvement of the obtained performance of the integrators. An alternative approach consists in the design of *symplectic time-stepping schemes* based on a discrete variational principle which is motivated by the Hamiltonian structure. Symplecticity is hereby directly related to (geometric) properties of the Hamiltonian flow, preserving in the conservative case a characteristic two-form on the phase-space. A comprehensible introduction to this topic can be found for instance in

the textbooks by Hairer *et al.* [70] or Leimkuhler and Reich [103], and detailed background informations are presented in Marsden *et al.* [116], Kane *et al.* [87], Marsden and West [117], Lew *et al.* [106, 107], or West [176].

Beside the foregoing classification of the time-integration schemes with regard to the offered conservation properties, a fundamental difference is represented by the underlying discretisation concept. In contrast to commonly used *Finite Differences*, which represent the standard approach concerning the (time) discretisation of ordinary differential equations, a very attractive alternative is given by *Finite Elements in time*, providing a general framework to develop integration schemes with pre-defined algorithmic properties. Even if such time-FE methods or Galerkin-based schemes are not the standard case in computational dynamics, however, they have been discussed in several publications. Concerning an introduction and the investigations of basic aspects, the textbook by Eriksson *et al.* [54] is highly recommended. Moreover, fundamental results can be found for instance in Argyris and Scharpf [4], Hulme [80, 81], Hughes and Hulbert [78], French and Schaeffer [57], Hulbert [79], or Estep and French [55] amongst others. Especially during the last ten years, the concepts of Galerkin-based integrators have been advanced significantly, dealing with various applications and highly nonlinear systems. To mention just a few, we refer to Bauchau and Joo [17], Hansbo [72], Runesson *et al.* [152], Larsson *et al.* [99], Bui [43, 45, 46], Kuhl and Meschke [93], and Betsch and Steinmann [24, 25, 26, 28]. Concerning geometrically nonlinear elastodynamics and the resulting conservation properties, Reference [26] is of particular interest. Momentum and energy conservation concepts proposed therein, have been extended and generalised to higher-order approximations by Gross [67] and Gross *et al.* [68].

Computational plasticity: Nowadays, the concepts of computational plasticity are established and well-documented in several publications, considering small as well as large deformation continuum theory. In this context, we refer in particular to Simo and Hughes [164] for an introduction, to Simo [162] for a detailed overview, and to Han and Reddy [71] for mathematical aspects. Furthermore, basic concepts for the mechanical description of plastic material behaviour have been proposed by Lubliner [113] and Lee [102], whereby the widespread approach for finite plasticity, which relies on a *multiplicative decomposition* of the deformation gradient, dates back to the contribution by Lee. Concerning large strain formulations and advanced material modelling, fundamental results can be found in Eterovic and Bathe [56], Miehe and Stein [132], Ibrahimbegovic [82], Miehe [130], Menzel [120], Menzel and Steinmann [124, 125], Menzel *et al.* [122], and Ekh and Menzel [53]. One particular challenge in the context of computational plasticity is the formulation of adequate algorithms to update the involved plastic variables. Significant results concerning the numerical treatment of plasticity are once more discussed by Simo and co-workers based on the so-called 'return mapping' concept, compare References [161, 162, 163, 164]. However, also other authors have successfully investigated the integration of the plastic governing equations during the last decades, see e.g. Runesson

et al. [153, 154], De Borst and Heeres [50], Büttner and Simeon [47], Miehe [128], Rosati and Valoroso [151], and Artioli *et al.* [10, 11, 12, 13] amongst others. In this context, it is quite obvious that the application of multiplicative kinematic assumptions in the finite strain regime causes further challenges for the design of the local update. In contrast to the classical 'Euler backward' scheme which is typically applied in the case of small defomations based on additive kinematics, an *'exponential update'* represents the mostly used concept when large deformations are taken into account. Interestingly, the obtained algorithm is on particular conditions – like e.g. isotropic material behaviour combined with a formulation of the elastic response in logarithmic strains – similar to the classical return mapping procedure of the small strain theory.

Elasto-plasto-dynamics: In the context of computational dynamics, there are only few approaches dealing with dissipative systems in general or elasto-plastic deformations in particular, which focus on algorithmic conservation properties. The pioneer work concerning the consistent time-integration of finite elasto-plasto-dynamics has been published by Meng and Laursen [118, 119], dealing with additive as well as multiplicative plasticity models. Furthermore, Noels *et al.* [144, 145, 146] have proposed an energy momentum conserving algorithm for plasticity based on a hypoelastic model, whereas Reference [147] deals with a corresponding scheme for visco-plasticity by applying an incremental potential for the stress evaluation. Lately, the same authors have modified in Reference [148] the variational formulation to included numerical dissipation with respect to high frequency modes, rendering a first-order energy-dissipative scheme. Following the concepts by Meng and Laursen [118, 119], Love and Sulsky [112] have discussed the consistent time-integration of dynamic finite deformation plasticity by incorporating a material-point method to solve the continuum equations. Recently, an energy-dissipative momentum-conserving algorithm for finite strain multiplicative plasticity has been presented by Armero [5, 9], whereby use of a non-standard local update procedure has been made which additionally requires local iterations. All of the afore mentioned approaches rely on one particular time discretisation based on Finite Differences with one certain order of accuracy. Typically, the formulations start with the second-order 'energy-momentum method' presented by Simo and Tarnow [165] and supplement the scheme with a particularly designed 'discrete gradient/derivative' originally proposed by Gonzalez [64] for hyperelasticity. To the contrary, the formulation by Mohr *et al.* [134, 135, 136, 137, 139, 140, 141] bases conceptually on the general framework of Finite Elements in time, and the actual time-stepping schemes are determined by selecting a specific polynomial degree for the time approximations and adequate quadrature rules.

Multibody dynamics: The investigation of computational multibody dynamics represents until today an active field of research. For an introduction to this topic, we refer to the textbooks by Schiehlen [159], Shabana [160], Angeles [3], Eich-Soellner and Führer [52], and Geradin and Cardona [58]. A comparison of the literature discloses

that multibody formulations are subdivided into a multitude of different approaches and concepts. In this context, fundamental differences occur especially with regard to the chosen formulation of the equations of motion and also concerning the applied discretisation procedure. It can be summarised that in particular the additional constraints, which are related to involved bearings or joints between rigid bodies, crucially complicate the integration of the governing equations. Obviously, the incorporation of flexible parts poses further challenges to the numerical concepts and demonstrates impressively the limitations of many classical multibody formulations which traditionally superimpose (small) deformations to large rigid body rotations. However, state of the art formulations and advanced time-stepping schemes can be found for instance in Bauchau *et al.* [14, 15, 16], Borri *et al.* [36, 39], Ibrahimbegovic *et al.* [84, 85], and Lens *et al.* [105, 104]. Furthermore, the outstanding references by Betsch [20] and Betsch and Steinmann [27, 28, 29] are mentionable, dealing with specific director formulations of the rigid bodies kinematics. Hereby, the authors favour a direct integration of the obtained set of differential algebraic equations, since this strategy is particularly well-suited to design algorithms which offer the claimed conservation properties. A further advantage of this formulations is the straightforward incorporation of rigid bodies, flexible parts, and several types of joints or bearings. Recently, the so-called 'null space method' has been developed based on the forgoing concepts to reduce basically the number of unknowns, see Betsch [21], Betsch and Leyendecker [23], Leyendecker *et al.* [111], and Betsch and Uhlar [31] for further details.

Elasto-plastic multibody dynamics: Of particular interest for the present work are furthermore the existing concepts to model elasto-plastic deformations within a multibody framework. However, there exist only few approaches in the literature concerning this topic. From a classical multibody perspective, a straightforward formulation is applied in Dias and Pereira [51], Ambrosio *et al.* [2], and Biakeu and Jezequel [33]. Therein, the authors circumvent the actual modelling of the constitutive behaviour by incorporating so-called plastic hinges, modelled as additional joints and force/torque elements between (linear elastic) flexible or rigid components. This approach is strongly motivated by the fact that often plastic deformations only take place in small regions of the structures. However, crucial tasks related to this concept are the identification of the final position of the hinge and also the choice of the adequate (nonlinear) reaction characteristic. Both have to be verified either in experiments or based on additional Finite Element simulations. Moreover, the results are hardly transferable to different structures or load cases, so that in our opinion the generality and also the physical quality of this approach is quite questionable. A less phenomenological and more physical possibility to incorporate plastic deformations within flexible multibody systems has been discussed in Ambrosio and Nikravesh [1]. Therein, the authors propose an updated Lagrangian formulation for the flexible parts and the elasto-plastic constitutive model relies on an additive decomposition of the differential strain increment. However, the authors do not address the essential integration of the resulting governing equations and, moreover,

they do not present any numerical example. Further work concerning this topic has been recently published by Gerstmayr [59, 60], Gerstmayr and Irschik [61], and Vetyukov *et al.* [175]. Therein, the authors apply Runge-Kutta schemes for the time-integration and the constitutive response bases on small strain assumptions combined with additive elasto-plastic kinematics. Finally, the papers by Sugiyama and Shabana [171, 172] have to be mentioned, using an 'absolute nodal coordinate formulation' in combination with a Lagrangian description of the plasticity model to circumvent a conceptual limitation to small strains. To the knowledge of the author, however, the consistent time-integration of inelastic multibody dynamics in general and finite elasto-plastic multibody dynamics in particular has not been addressed at all in the literature so far, aside from the contribution by Mohr *et al.* [141].

Outline of the Present Work

In the following, a short summary of each chapter is presented to give the reader a better overview of the underlying structure of the present work.

Chapter 2: In the second chapter, main aspects concerning the modelling and time-integration of dissipative dynamics are discussed by means of a one-dimensional mechanical system which consists of a mass, a spring, and a friction-element. In this context, most of the essential issues, that are also relevant in subsequent chapters, can already be investigated based on this fundamental example in a very comprehensible manner, requiring only basic knowledge in physics and mathematics. In particular, the crucial influence of nonlinearities on the numerical behaviour and the adequate approximation of involved time-integrals are significant results.

Chapter 3: Subsequently to the introductory example, the scope is extended in the third chapter to the nonlinear dynamics of inelastic structures. For this purpose, we apply concepts of geometrically nonlinear continuum mechanics and Finite Elements in space to receive a semidiscrete system of equations of motion. Concerning the focal approximation in time of the resulting semidiscrete system, again, a Finite Element method – more precisely: a *continuous Galerkin method* – is used, whereby the decisive role of required quadrature rules is investigated once more in detail. In this context, we introduce an adequate non-standard quadrature rule derived from a constrained optimisation problem, providing a general framework to design completely consistent time-stepping schemes for inelastic continuum dynamics.

Chapter 4: In the first instance, the general concepts of Chapter 3 are restricted to the non-dissipative hyperelastic case, and we consider in particular constitutive models formulated in principal stretches. In the isotropic case, such eigenvalue-based constitutive laws are very significant to model various types of elastic and even inelastic material

behaviour. However, it is shown that the efficient algorithmic treatment of principal stretches based on a well-established perturbation approach requires, especially within the context of specific conserving schemes, advanced techniques to circumvent numerical problems. Accordingly, we propose an adequate solution strategy to avoid potential pitfalls which are directly related to numerical artefacts of the applied non-standard quadrature rule. All relevant aspects are extensively demonstrated by means of several numerical examples, considering a specific representative of the general time-FE methods of Chapter 3 which bases on linear approximations in time.

Chapter 5: In this chapter, the general concepts are specified to finite elasto-plasto-dynamics, whereby the elastic response relies again on a formulation in principal stretches and the plasticity model refers to a multiplicative decomposition of the deformation gradient in elastic and plastic parts. Regarding the local time-integration of the plastic evolution equations, we exemplarily discuss an approved exponential return map to benefit from its several advantages: It is well-known that for specific models this update conserves the simple structure of the infinitesimal theory and, moreover, it performs very cost-efficiently. Using this benchmark update on the local level, special emphasis is placed on the global time-integration, investigating once more specific time-stepping schemes based on linear Finite Elements in time as a fundamental case. Since the applied format of the local exponential update is only first-order accurate, the resulting (global) order of accuracy will be reduced for this specific choice when plastic deformations are involved, whereby the final convergence performance also depends crucially on the applied integration strategy to fit the local into the global scheme. Nevertheless, keep in mind that also other local update algorithms could be incorporated instead, without too much of additional effort, in consequence of a modular structure of the resulting equations. Moreover, the time integrators for finite elasto-plasto-dynamics are analysed regarding their conservation properties by means of several representative numerical examples. Thereby, the excellent performance of the completely consistent algorithm is demonstrated for a wide range of material parameters, considering also a comparison to well-established standard time-stepping schemes that are widespread in the literature and implemented in several commercial software packages.

Chapter 6: Finally, we extend the foregoing concepts to constrained dissipative dynamics, dealing with inelastic multibody systems. In this context, the modelling of the (inelastic) flexible parts relies on the same fully nonlinear continuum approach, which has been extensively discussed in Chapter 3, and for the rigid body dynamics a rotationless formulation is preferred, resulting in a set of differential algebraic equations. Instead of applying a reformulation, the obtained equations are integrated directly, whereby the prior continuous Galerkin method of unconstrained systems is adequately generalised to a *mixed Galerkin method* for the constrained case. Provided again that the resulting time-integrals are appropriately approximated, a completely consistent time-integration is obtained analogously to the unconstrained case, including this time additionally the

fulfilment of the involved constraints. Once again, a particular scheme based on linear time shape functions is considered in more detail and its numerical performance is exhaustively analysed by means of multiple numerical examples, using the elasto-plastic constitutive model of Chapter 5.

Appendix A-C: The appendix consists of three independent parts. In Appendix A, one essential aspect of the general concepts discussed in Chapter 3, which is related to the claimed consistency properties of the integrators, is studied in more detail, focussing on the algorithmic fulfilment of a discrete energy balance. In Appendix B, some related aspects of visualisation are broached, whereby these aspects are directly motivated by the desire to get a deeper insight into the functioning of the consistent non-standard quadrature rule. For the sake of completeness, we have summarised in Appendix C all fundamental equations of those standard integrators which are used in Chapter 5 for a comparison to the proposed algorithms.

Einleitung

In nahezu allen Disziplinen des Ingenieurwesens hat die Verwendung von modernen Simulationstechniken stark zugenommen. Ermöglicht durch die enorme Rechenleistung heutiger Computersysteme, ist diese Entwicklung unmittelbar mit dem Wunsch einer möglichst virtuellen Produktentwicklung verbunden, um die entstehenden Kosten zu reduzieren. In diesem Zusammenhang erfordert die Modellierung realer technischer Systeme häufig die Berücksichtigung von dynamischen Effekten, wobei als typische Anwendungen zum Beispiel die Komfort- und Fahrdynamiksimulationen der Automobilindustrie, die virtuellen Crash-Tests oder auch die dynamische Modellierung von Metallumformprozessen zu erwähnen sind. In jedem Fall muss das betrachtete reale Systemverhalten in einem ersten Schritt durch ein entsprechendes physikalisches Modell idealisiert werden. Anschließend wird in einem zweiten Schritt das physikalische Ersatzmodell mathematisch beschrieben und so der eigentlichen Simulation zugänglich gemacht. Meist ist hierbei die Lösung von gewöhnlichen, oftmals sogar von partiellen Differentialgleichungen erforderlich. Im Laufe des zuvor beschriebenen Modellierungs- und Simulationsprozesses müssen insbesondere die folgenden beiden Aspekte beachtet werden:

- Das physikalische Modell soll so einfach wie möglich aber auch so genau wie nötig sein, um alle wesentlichen Charakteristika des realen Systems abbilden zu können.

- Darüber hinaus müssen in der Regel numerische Methoden verwendet werden um das Systemverhalten zu simulieren, da bereits bei vergleichsweise einfachen physikalischen Modellen keine analytische Lösung gefunden werden kann.

In diesem Zusammenhang ist es von entscheidender Bedeutung, die verwendeten Methoden sorgfältig im Hinblick auf die zu erzielende numerische Leistung, aber auch speziell hinsichtlich der erreichbaren Qualität der Ergebnisse auszuwählen. Generell kann man sagen, dass eine steigende Modellkomplexität stets auch anspruchvollere numerische Verfahren und somit ein tieferes Verständnis sowohl der mechanischen, als auch der mathematischen Grundlagen unbedingt erfordert.

Betrachtet man nun speziell die Numerik nichtlinearer Dynamik so ist es wohlbekannt, dass insbesondere die Auswahl eines geeigneten Zeitintegrationsalgorithmus eine entscheidende, aber auch nicht-triviale Aufgabe darstellt. So sind zwar diverse Zeitschrittverfahren verfügbar, jedoch wurden die meisten von ihnen ursprünglich für lineare Problemstellungen entwickelt und führen, angewendet auf nichtlineare Systeme, oftmals zu schwerwiegenden numerischen Instabilitäten. Aus diesem Grund kann die Anwendung von solchen Algorithmen in einem nichtlinearen Kontext nur bedingt empfohlen werden. Interessanterweise hat sich diesbezüglich herausgestellt, dass insbesondere die algorithmische Erfüllung physikalisch motivierter Erhaltungseigenschaften – wie zum Beispiel die Erhaltung der Impulsabbildungen oder die Berücksichtigung der Hauptsätze der Thermodynamik – von essentieller Bedeutung ist. In der Tat wurde in diversen Veröffentlichungen belegt, dass eine derartige Konsistenz der Algorithmen nicht nur von theoretischem Interesse ist, sondern auch entscheidend die Robustheit der Verfahren beeinflusst. Motiviert durch diese Ergebnisse wurden deshalb in der Vergangenheit spezielle Integrationsverfahren für diverse nichtlineare Anwendungen entwickelt, wobei verstärkt klassische Mehrkörpersysteme oder auch die nichtlineare Dynamik elastischer Strukturen untersucht wurde. Bedingt durch die in der Regel höhere Modellkomplexität stellt die Modellierung dissipativer Dynamik eine zusätzliche Schwierigkeit im Vergleich zur Dynamik konservativer Systeme dar. Nichtsdestotrotz ist eine Berücksichtigung dissipativer Effekte, wie zum Beispiel Reibung oder inelastisches Materialverhalten, von grundlegender Relevanz in vielen technischen Anwendungen.

In der vorliegenden Arbeit werden nun fortschrittliche Konzepte zur *Zeitintegration nichtlinearer inelastischer Dynamik* entwickelt. Hierbei werden sowohl Fragestellungen der Strukturdynamik als auch der flexiblen Mehrkörperdynamik untersucht, unter spezieller Betrachtung *finiter Elasto-Plastizität*. Ein besonderes Merkmal der vorgeschlagenen Algorithmen ist in diesem Zusammenhang die Ermöglichung einer *vollständig konsistenten* Integration. Bedingt durch die Wahl geeigneter Approximationen für bestimmte Zeitintegrale wird somit auch im diskreten Kontext eine numerisch exakte Erfüllung grundlegender Bilanzprinzipien garantiert. Dabei wird sich zeigen, dass die entsprechenden Verfahren nicht nur möglichst exakt die zu Grunde liegende Physik des betrachteten realen Systems abbilden, sondern zudem eine überlegene numerische Leistungsfähigkeit aufweisen. Nachfolgend wird eine kurze Zusammenfassung der einzelnen Kapitel präsentiert, um dem Leser einen besseren Überblick hinsichtlich des Aufbaus der vorliegenden Arbeit zu ermöglichen.

Kapitel 2: Im zweiten Kapitel werden grundlegende Aspekte der Modellierung und Zeitintegration dissipativer Dynamik anhand eines einfachen mechanischen Modells – bestehend aus einer Masse, einer Feder und einem Reibelement – erörtert. In diesem Zusammenhang zeigt sich, dass man bereits basierend auf Grundlagenwissen in Physik und Mathematik wesentliche Einflüsse, welche auch bei den nachfolgenden komplexeren Systemen von Bedeutung sein werden, studieren kann. Insbesondere wird der Einfluss von

Nichtlinearitäten auf das numerische Verhalten und eine angemessene Approximation auftretender Zeitintegrale diskutiert.

Kapitel 3: Im Anschluss an das Einführungsbeispiel wird im dritten Kapitel das Blickfeld erweitert und die nichtlineare Dynamik inelastischer Strukturen untersucht. Zu diesem Zweck werden allgemeine Konzepte der geometrisch nichtlinearen Kontinuumsmechanik verwendet, um mit Hilfe einer räumlichen Finite Element Diskretisierung die semidiskreten Bewegungsgleichungen zu erhalten. Im Gegensatz zu den üblichen Algorithmen basierend auf Finiten Differenzen wird in dieser Arbeit auch hinsichtlich der Zeitdiskretisierung eine Finite Element Methode – genauer gesagt: eine *kontinuierliche Galerkin Methode* – verwendet. In diesem Zusammenhang wird vor allem der entscheidende Einfluss verschiedener Quadraturregeln, welche zur numerischen Auswertung bestimmter Zeitintegrale benötigt werden, aufgezeigt. Insbesondere wird ausgehend von einem Optimierungsproblem mit Nebenbedingung eine geeignete Nichtstandard-Quadratur hergeleitet. Diese garantiert die Erfüllung geforderter algorithmischer Erhaltungseigenschaften und ermöglicht somit die Formulierung eines allgemeinen Konzeptes zur konsistenten Zeitintegration inelastischer Kontinuumsdynamik.

Kapitel 4: Zunächst wird das allgemeine Konzept aus Kapitel 3 auf den nicht-dissipativen Fall der Hyperelastizität beschränkt, wobei speziell in Hauptstreckungen formulierte Materialmodelle betrachtet werden. Im isotropen Fall sind solche Eigenwert-basierten Formulierungen weit verbreitet, sowohl im Hinblick auf die Modellierung von elastischem als auch von inelastischem Materialverhalten. Hinsichtlich einer effizienten numerischen Umsetzung ist es vorteilhaft, einen so genannten Störansatz im Falle gleicher Eigenwerte zu verwenden. Es wird sich allerdings zeigen, dass eine intuitive Verwendung dieser Technik im Rahmen der hier betrachteten konsistenten Zeitintegration zu erheblichen algorithmischen Problemen führen kann, welche unmittelbar mit numerischen Artefakten der verwendeten Nichtstandard-Quadratur in Beziehung stehen. Des Weiteren wird eine geeignete Lösungsstrategie zur Beseitigung dieser Probleme vorgeschlagen und deren Effektivität verifiziert. Alle relevanten Aspekte werden anhand diverser Beispiele demonstriert und diskutiert, wobei ausgehend von den allgemeinen Konzepten in Kapitel 3 ein spezielles Zeitschrittverfahren basierend auf linearen Zeitapproximationen betrachtet wird.

Kapitel 5: In diesem Kapitel wird die allgemeine Formulierung bezüglich der Modellierung finiter Elasto-Plasto-Dynamik spezifiziert. Hierbei basiert die elastische Materialantwort erneut auf einer Formulierung in Hauptstreckungen und die Kinematik des Plastizitätsmodells beruht auf einer multiplikativen Zerlegung des Deformationsgradienten in elastische und plastische Anteile. Hinsichtlich der lokalen Zeitintegration der internen Variablen wird ein bewährter exponentieller Projektionsalgorithmus verwendet. Für das hier betrachtete Materialmodell weist dieses Verfahren eine besonders einfache Struktur, ähnlich der infinitesimalen Theorie, auf und ermöglicht zudem eine effiziente

und robuste Berechnung. Unter Verwendung dieses Beispielalgorithmus auf der lokalen Ebene wird vor allem die globale Zeitintegration näher untersucht, wobei wiederum spezifische Verfahren basierend auf linearen Finiten Elementen in der Zeit verwendet werden. Aufgrund des speziellen Formats der verwendeten exponentiellen Projektion, welche lediglich eine Genauigkeit erster Ordnung aufweist, wird auch die Gesamtordnung des (globalen) Zeitschrittverfahrens im plastischen Fall reduziert. Es ist jedoch wichtig zu betonen, dass aufgrund der modularen Struktur der entsprechenden Gleichungen auch ein anderer Algorithmus zur lokalen Integration verwendet werden kann, ohne die vorgeschlagenen Grundkonzepte auf globaler Ebene ändern zu müssen. Ein besonderes Augenmerk liegt in diesem Kapitel auf der Analyse der vorgestellten Zeitintegrationsverfahren für finite Elasto-Plasto-Dynamik hinsichtlich der gebotenen Erhaltungseigenschaften anhand einer Vielzahl repräsentativer Beispielrechnungen. Hierbei zeigt sich speziell im Vergleich zu Standardverfahren der Literatur, welche auch in diversen kommerziellen Software-Paketen verwendet werden, die hervorragende Leistungsfähigkeit der vorgeschlagenen Algorithmen.

Kapitel 6: In einem letzten Schritt werden nun die vorgestellten Verfahren auf dissipative Systeme mit Zwangsbedingungen erweitert und inelastische Mehrkörpersysteme betrachtet. Dabei beruht die Modellierung der (inelastischen) flexiblen Komponenten auf den gleichen, vollkommen nichtlinearen Kontinuumskonzepten, welche bereits ausführlich in Kapitel 3 diskutiert wurden. Hinsichtlich der Starrkörperbeschreibung wird eine rotationsfreie Formulierung bevorzugt. Um das resultierende System differential-algebraischer Gleichungen direkt zu integrieren, wird eine *gemischte Galerkin Methode* verwendet, welche eine geeignete Verallgemeinerung der zuvor betrachteten kontinuierlichen Galerkin Methode im Hinblick auf Systeme mit Zwangsbedingungen darstellt. Wiederum unter der Voraussetzung, dass die auftretenden Zeitintegrale geeignet ausgewertet werden, ermöglicht dieses Konzept erneut eine vollständig konsistente Integration, wobei nun zusätzlich die numerisch exakte Erfüllung der beteiligten Zwangsbedingungen ermöglicht wird. Auch in diesem Kapitel wird ein spezielles Verfahren basierend auf linearen Zeitansätzen in Kombination mit dem elasto-plastischen Materialmodell aus Kapitel 5 näher untersucht und seine Leistungsfähigkeit mit Hilfe verschiedener numerischer Beispiele belegt.

Anhang A-C: Der Anhang gliedert sich in drei unabhängige Teile: In Anhang A wird ein ganz wesentlicher Aspekt der allgemeinen Konzepte aus Kapitel 3, nämlich die algorithmische Erfüllung der diskreten Energiebilanz, aufgegriffen und detailiert hergeleitet. In Anhang B werden auftretende Visualisierungsaspekte diskutiert, welche in unmittelbarem Zusammenhang mit der Wirkungsweise der konsistenten Nichtstandard-Quadratur stehen. Aus Gründen der Vollständigkeit sind abschließend in Anhang C alle wesentlichen Gleichungen der in Kapitel 5 zum Vergleich herangezogenen Standardintegrationsverfahren zusammengestellt.

2. Prolog – Motivation

Starting with a motivating example, we consider a one-dimensional model which consists of a mass, a spring and a friction-element, referred to as friction-element oscillator. Basically, the investigation of such a simple dynamical system makes sense for two fundamental reasons:

- On the one hand, essential issues concerning the time-integration of dissipative systems in general can already be studied based on this basic system.
- On the other hand, the combination of a spring and a friction-element represents indeed a perfect motivation for the underlying structure of elasto-plastic constitutive models.

In fact, it will be shown in subsequent chapters that key aspects of the following investigations can be transferred one-to-one to a more complicated context.

2.1. Friction-Element Oscillator

In this section, the fundamental equations to describe the dynamical behaviour of the friction-element oscillator will be summarised in a time-continuous format, starting with the governing equations for the friction-element followed by the dynamics of the system.

2.1.1. Friction-element

We begin with the underlying kinematics of the friction-element oscillator. A sketch of the mechanical model is pictured in Figure 2.1. Based on the considered serial arrangement, an additive decomposition of the resulting position q of the mass m can be motivated, rendering

$$q(t) = q_e(t) + q_p(t) \tag{2.1}$$

corresponding to a geometrically linear theory [1]. Herein, the position (plastic slip) of the friction-element is denoted by q_p, involving dissipation effects, and q_e measures the

[1] As discussed extensively in Simo and Hughes [164], the 'friction-element spring device' represents also an adequate approach to model elasto-plastic material behaviour in a small strain context, involving an analogous kinematic assumption for the strain measure.

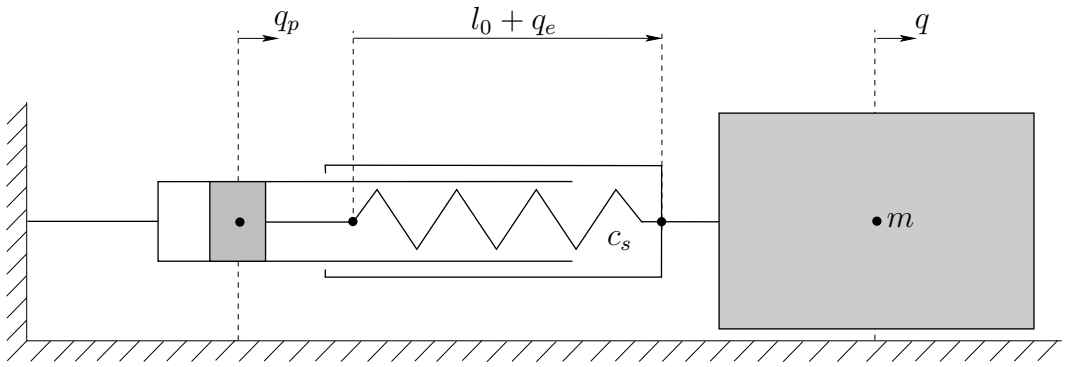

Figure 2.1.: friction-element oscillator in a geometrically linear setting

change in length of the elastic spring, corresponding to reversible deformations. In this context, the spring with the stiffness c_S is supposed to have initially unit length $l_0 = 1$, being relaxed for $q_e = 0$. Please note, that from a practical point of view only the position of the mass q can be measured directly in the considered model. In contrast, the actual position of the friction-element q_p as well as the resulting elongation of the spring q_e are hidden and can not be determined with a simple ruler by an outstanding observer, compare Figure 2.1. Basically, the friction-element limits the achievable magnitude of the effective force in the spring F, resulting in

$$|F| \leq F_{fric}^{max} \,. \tag{2.2}$$

In a next step, the so-called yield function

$$\Phi := |F| - F_{fric}^{max} \tag{2.3}$$

is introduced, and consequently the admissible range for the spring force can be defined as $\mathbb{E}_F = \{F \in \mathbb{R} \,\big|\, |F| - F_{fric}^{max} \leq 0\}$. To describe the movement of the friction-element, we specify the rate of q_p via

$$\dot{q}_p(t) := \dot{\gamma}(t)\, \mathrm{sign}(F)\,, \tag{2.4}$$

wherein the direction of the slip has been formulated based on the 'sign'-function with $\mathrm{sign}(F) := F/|F|$ for $F \neq 0$ and $\mathrm{sign}(0) = 0$ [2]. Hence, the multiplier $\dot{\gamma}$ is obviously related to the amount of the rate of the irreversible slip, since $|\dot{q}_p| = |\dot{\gamma}|\,|\mathrm{sign}(F)| = |\dot{\gamma}|$. Moreover, the proper (un)loading procedure is governed by the conditions

$$\dot{\gamma} \geq 0\,, \qquad \Phi \leq 0\,, \qquad \dot{\gamma}\,\Phi = 0\,, \quad \text{and} \quad \dot{\gamma}\,\dot{\Phi} = 0\,. \tag{2.5}$$

For further details concerning the behaviour of the 'friction-element spring device', we refer to Reference [164] and focus now on the formulation of the system dynamics.

[2] Representing a special case, the supposed evolution equation for the plastic slip can be reformulated based on the yield function, leading to $\dot{q}_p = \dot{\gamma}\,\partial_F \Phi$.

2.1.2. Dynamics

Analogously to the conservative (purely) elastic case, we introduce an energy function $\widehat{V}(q_e) = V(q; q_p)$ which measures the stored energy in the spring, being related to the resulting spring characteristic via $|F(q_e)| = |\partial_{q_e}\widehat{V}(q_e)|$. Furthermore, the sum of the kinetic energy K and the stored energy V renders the so-called total energy of the system $H(q, p; q_p) := K(p) + V(q; q_p)$, wherein the definition of the linear momentum $p(t) := m\, v(t)$ with the velocity $v(t) := \dot{q}(t)$ has been incorporated. Consequently, we obtain

$$H(q(t), p(t); q_p(t)) = \frac{1}{2m}\, p(t)^2 + V(q(t); q_p(t))\,. \tag{2.6}$$

In this context, the entirely different character of the measurable quantities q, p, on the one hand, and the hidden or internal variable q_p, on the other hand, should be recalled once more. Moreover, the involved dissipation $\mathcal{D} = F\,\dot{q}_p$ can be directly related to the frictional force F_{fric}^{max} by means of Equation (2.4), since $\dot{\gamma} > 0$ yields $\Phi = 0$ and thus

$$\mathcal{D}(t) = \dot{\gamma}(t)\, F_{fric}^{max} \geq 0\,. \tag{2.7}$$

Following standard arguments of thermodynamics, we obtain the energy balance

$$\dot{H}(t) = -\mathcal{D}(t)\,, \tag{2.8}$$

implying obviously a monotonic decrease of the total energy related to the second law of thermodynamics. Regarding the subsequent discretisation procedure, we write the resulting equation of motion of the mass as system of two first-order differential equations, namely

$$\begin{aligned} \dot{q}(t) &= \frac{1}{m}\, p(t) = \partial_p K(p(t)) \\ \dot{p}(t) &= -F(q_e(t)) = -\partial_{q_e}\widehat{V}(q_e(t)) = -\partial_q V(q(t); q_p(t))\,. \end{aligned} \tag{2.9}$$

Obviously, Equations (2.9) can also be derived from the function H by applying technically a Hamiltonian-type formalism with respect to the variables $[q(t), p(t)] =: z(t)$. In following chapters, a Hamiltonian-type formalism will be applied as well since it offers a very compact notation, implying inherently a description of the dynamics from an energy-based perspective. However, the classical Hamiltonian interpretation is of course no longer valid for the non-conservative case, when dealing with dissipative systems.

Remark 2.1: Please note, that the here considered friction-element oscillator, and consequently also elasto-plastic material behaviour, represents a particular kind of a dissipative system, since the dissipation effects might be switched on and off controlled by the conditions (2.5), involving the yield function (2.3). Thus, the behaviour possibly changes from conservative to non-conservative and vice versa, representing hence a partially or temporarily Hamiltonian system, in contrast to permanent dissipative systems.

2.2. Linear Spring Characteristic

Before considering the algorithmic treatment, the energy function V and the corresponding spring characteristic has to be specified, determining the actual elastic response of the spring. The simplest case represents in this context a linear force-elongation relation given by

$$F(q(t); q_p(t)) = c_S \left[q(t) - q_p(t)\right], \tag{2.10}$$

which is obviously related to the quadratic stored energy format

$$V(q(t); q_p(t)) = \frac{1}{2} c_S \left[q(t) - q_p(t)\right]^2. \tag{2.11}$$

Based on these basic elastic relations, the proper constitutive behaviour of the 'friction-element spring device' can be specified according to the fundamental relations that have been discussed in Section 2.1.1. Next, the discretisation in time of the constitutive equations is considered, followed by the time-integration of the equations of motion (2.9) in the subsequent paragraph. In this context, we refer from an algorithmic point of view to the equations of motion as global and to the constitutive equations as local level, interpretable as algorithmic black box which is called by the global superordinate time-stepping scheme.

2.2.1. Constitutive update

First, we use a subdivision of the time interval of interest, rendering

$$[0, T] = \bigcup_{n=0}^{N} [t_n, t_{n+1}]. \tag{2.12}$$

Concerning the local time-integration, it is accepted to apply a classical Euler-backward Finite Differences scheme. Consequently, the involved evolution equation for the plastic slip q_p (2.4) reads in a discrete format

$$q_p^{n+1} = q_p^n + \Delta\gamma \, \mathrm{sign}(F^{n+1}). \tag{2.13}$$

Moreover, the resulting discrete force F^{n+1} in the spring can be written based on the elastic response (2.10), namely

$$F^{n+1} = c_S \left[q^{n+1} - q_p^{n+1}\right]. \tag{2.14}$$

In this context, the internal force F^{n+1} has to fulfil the yield condition

$$\Phi^{n+1} = |F^{n+1}| - F_{fric}^{max} \leq 0 \tag{2.15}$$

and, additionally, it should also hold in the discrete setting

$$\Delta\gamma \geq 0 \qquad \text{and} \qquad \Delta\gamma\, \Phi^{n+1} \;=\; 0 \tag{2.16}$$

based on the (un)loading conditions (2.5). Concerning the computation of the increment $\Delta\gamma$, a two step approach is applied, representing a well-known predictor-corrector procedure. In a first step, the so-called trial state is introduced based on a frozen plastic slip, namely $q_p^{trial} := q_p^n$. Herewith, we can calculate the trial force in the spring

$$F^{trial} = c_S\,[q^{n+1} - q_p^{trial}] \tag{2.17}$$

to check the fulfilment of the yield condition

$$\Phi^{trial} = |F^{trial}| - F_{fric}^{max}\,. \tag{2.18}$$

At this stage, we have to distinguish between $\Phi^{trial} \leq 0$, corresponding to an elastic step with $\Delta\gamma = 0$, and $\Phi^{trial} > 0$, representing a plastic step with $\Delta\gamma > 0$. To compute in such a plastic step the resulting increment $\Delta\gamma$, the discrete yield function (2.15) can be rewritten based on Equations (2.13), (2.14), (2.17) by means of $\text{sign}(F^{n+1}) = \text{sign}(F^{trial})$, resulting in

$$\Phi^{n+1} = |F^{trial}| - \Delta\gamma\, c_S - F_{fric}^{max} \stackrel{!}{=} 0\,. \tag{2.19}$$

Consequently, a straightforward manipulation yields

$$\Delta\gamma = \frac{1}{c_S}\,\Phi^{trial}\,. \tag{2.20}$$

Obviously, the increment $\Delta\gamma$ can be calculated explicitly for the model at hand, when a linear spring characteristic is incorporated. However, it will be shown later on that in the nonlinear case such a simple relation can not be derived anymore, requiring in general an iterative solution procedure.

2.2.2. Time-stepping scheme

Now, the time-integration of the equations of motion (2.9) is investigated. For conceptual reasons, we transform in this case each physical sub-interval $\mathcal{T} := [t_n, t_{n+1}]$ to the reference interval $\mathcal{I} := [0, 1]$ by means of the mapping

$$\alpha(t) = \frac{t - t_n}{h_n}\,, \tag{2.21}$$

wherein $h_n := t_{n+1} - t_n$ denotes the applied time-step size. An illustration of this linear mapping can be regarded in Figure 2.2. Based on the applied transformation and the

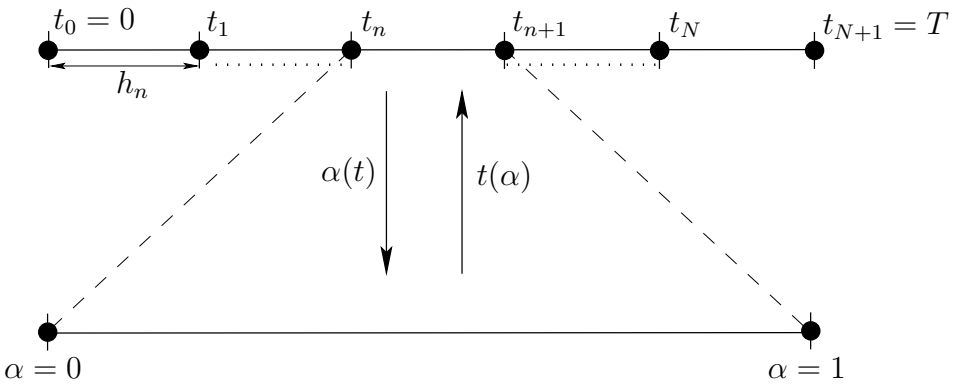

Figure 2.2.: mapping of the physical time interval $\mathcal{T}$ to the reference interval $\mathcal{I}$ via $\alpha(t)$

linear interpolation $z^h(\alpha) := [z_2 - z_1]\alpha + z_1$, we consider next a quite intuitive integration of the equations of motion over the interval $\mathcal{I}$, resulting in

$$\begin{aligned} q_2 - q_1 &= h_n \int_0^1 \frac{1}{m}\, p^h(\alpha)\, \mathrm{d}\alpha \\ p_2 - p_1 &= -h_n \int_0^1 F(\alpha)\, \mathrm{d}\alpha\,. \end{aligned} \tag{2.22}$$

Herein, we have introduced the notation $[\bullet]_1 := [\bullet](\alpha = 0)$ and $[\bullet]_2 := [\bullet](\alpha = 1)$ which corresponds on the physical time interval to t_n and t_{n+1} respectively. Moreover, the first integral in Equations (2.22) can be integrated analytically and, consequently, we obtain

$$\begin{aligned} q_2 - q_1 - \frac{h_n}{2}\frac{1}{m}\,[p_1 + p_2] &= 0 \\ p_2 - p_1 + h_n \int_0^1 F(\alpha)\, \mathrm{d}\alpha &= 0\,. \end{aligned} \tag{2.23}$$

To define the actual time-stepping scheme, the approximation of the remaining integral, which contains the internal force in the spring, has to be specified. A typical choice is the application of a midpoint approximation, related to a standard Gauss quadrature rule with only one integration point, rendering

$$\int_0^1 F(\alpha)\, \mathrm{d}\alpha \approx F_{1/2} \tag{2.24}$$

based on $F_{1/2} := F(q^h(1/2), q_{p_{1/2}})$ which is calculated by means of the constitutive update of the previous section. Consequently, the final global integration scheme reads

$$\begin{aligned} q_2 - q_1 - \frac{h_n}{2}\frac{1}{m}\,[p_1 + p_2] &= 0 \\ p_2 - p_1 + h_n\, F_{1/2} &= 0\,. \end{aligned} \tag{2.25}$$

Next, some numerical results are presented based on the parameters $m = 100$, $c_S = 10$, $F_{fric}^{max} = 50.5$, and $h_n \in \{0.01, 0.1, 0.3, 0.4\}$. Furthermore, an external force F^{ext} has been applied to start the motion, acting directly on the mass m in the positive direction of the coordinate q. Thereby, F^{ext} increases linearly in time up to the maximum value $f_{max} = 200$ and, subsequently, decreases again linearly to zero. After $T_{load} = 2.0$, the system oscillates without excitation. Fundamental aspects of the dynamical behaviour can be studied based on Figure 2.3 b) and Figure 2.4 a), showing the resulting position of the mass and the phase-space portrait respectively. The obtained response of the 'friction-element spring device' is illustrated in Figure 2.3 a) based on a plot of the internal force in the spring F, depending on the current position of the mass. In this context, it can be clearly seen that an increase of the position q renders initially an elastic elongation of the spring, characterised by a linear force-position relation. When the admissible limit for the force in the friction-element is achieved, a plastic slip occurs which results in a constant reaction force. The resulting plastic slip/displacement q_p of the friction element is pictured in Figure 2.4 b). Based on the fundamental relations (2.7), (2.12), a time-integration and summation over the sub-intervals yields for the discrete time $t = t_{n+1}$ the so-called accumulated dissipation

$$D_{n+1} := \sum_{k=0}^{n} \int_{t_k}^{t_{k+1}} \dot{\gamma}(t)\, F_{fric}^{max}\, \mathrm{d}t\,, \tag{2.26}$$

which is plotted in Figure 2.5 a). Particularly interesting in a discrete setting is furthermore the balance of the total energy H, since it is well-known in literature that especially the algorithmic energy behaviour can strongly affect as well the resulting performance of the integrator. Motivated by the time-continuous case, compare Equations (2.7), (2.8), the total energy has to be conserved for elastic steps, and it should be characterised by a monotonic decrease when the friction-element is active, corresponding to the second law of thermodynamics. As can be seen in Figure 2.5 b), both features are captured by the here considered time-stepping scheme, involving small as well as large time-step sizes.

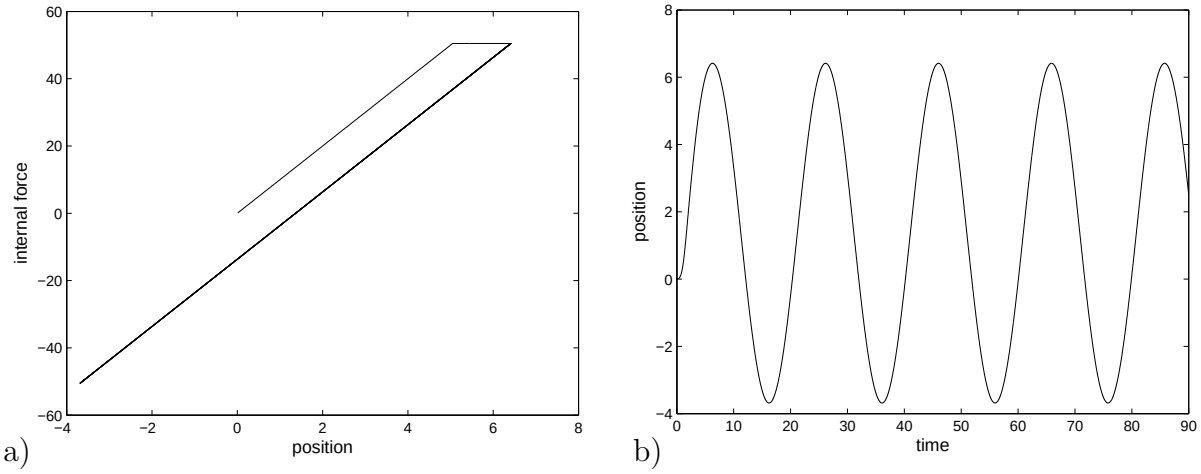

Figure 2.3.: a) internal force in the spring F, b) position of the mass q

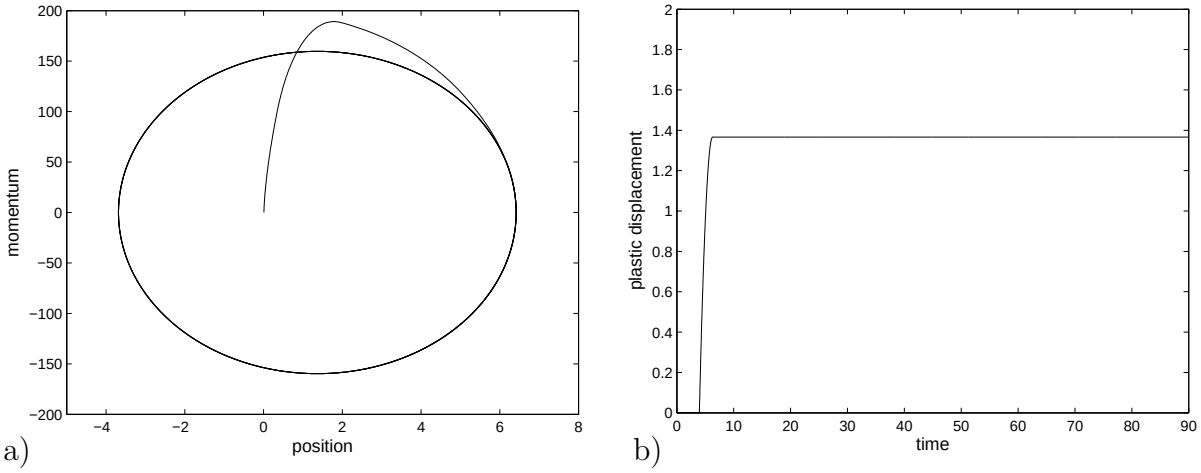

Figure 2.4.: a) phase-space portrait of the mass m, b) plastic slip q_p of the friction-element

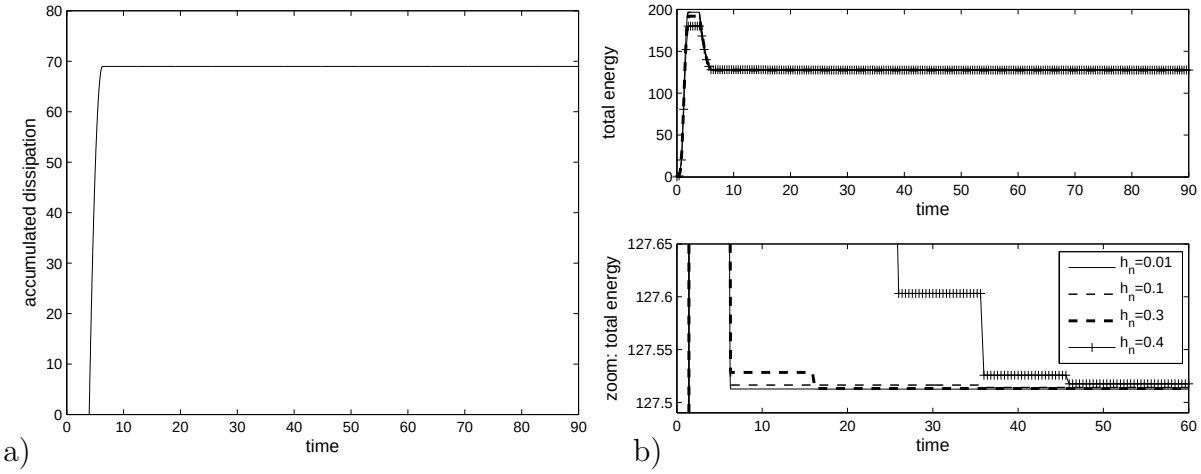

Figure 2.5.: a) accumulated dissipation D, b) total energy H

2.3. Nonlinear Spring Characteristic

As shown in the foregoing section, the basic midpoint evaluation of the time-integrated internal force is already able to capture fundamental thermodynamical properties, when a linear spring characteristic is applied. To study the potential influence of nonlinearities on the numerical behaviour of the time-stepping scheme, we exemplarily apply

$$F(q(t); q_p(t)) = c_S \left[q(t) - q_p(t)\right]^3 , \tag{2.27}$$

involving the underlying energy function

$$V(q(t); q_p(t)) = \frac{1}{4} c_S \left[q(t) - q_p(t)\right]^4 . \tag{2.28}$$

Hence, the governing equations for the constitutive behaviour of the system presented in Section 2.1.1 can be completed by Equation (2.27). Regarding a numerical implementation, we summarise next an adequate algorithmic treatment of the corresponding equations, analogously to the linear case discussed previously.

2.3.1. Constitutive update

Since the fundamental ideas of the constitutive update are unchanged, we focus in the present section basically on the modified aspects. For the discretisation of the evolution equation again an Euler-backward scheme is used, as given by Equation (2.13), and also the yield condition (2.15) and the discrete (un)loading conditions (2.16) are equivalent to the linear case. Furthermore, the already discussed predictor-corrector approach has been chosen once more as an appropriate algorithmic formulation. Consequently, we have to check in the first step

$$\Phi^{trial} = |F^{trial}| - F_{fric}^{max} \begin{cases} \leq 0 , \rightarrow \Delta\gamma = 0 \\ > 0 , \rightarrow \Delta\gamma > 0 \end{cases} \tag{2.29}$$

based on the modified spring characteristic (2.27), yielding

$$F^{trial} = c_S \left[q^{n+1} - q_p^n\right]^3 . \tag{2.30}$$

However, the main difference to the linear case is represented by the computation of the increment $\Delta\gamma$, since an explicit solution, as given by Equation (2.19) and Equation (2.19) respectively, is not feasible for the considered spring characteristic due to the nonlinearity of the resulting internal force. Therefore, an additional (local) iteration has to be applied to enforce the fulfilment of the yield condition, solving the coupled nonlinear system of equations

$$\begin{aligned} |F^{n+1}| - F_{fric}^{max} &= 0 \\ F^{n+1} - c_S \left[q^{n+1} - q_p^{n+1}\right]^3 &= 0 \\ q_p^{n+1} - q_p^n - \Delta\gamma \, \mathrm{sign}(F^{n+1}) &= 0 \end{aligned} \tag{2.31}$$

to compute the three unknowns $\{\Delta\gamma, q_p^{n+1}, F^{n+1}\}$. When additionally a directional equivalence of the trial and the final state is supposed, involving $\text{sign}(F^{n+1}) = \text{sign}(F^{trial})$, the set of Equations (2.31) can be reduced to the single requirement

$$\Phi^{n+1} = \left| c_S \left[q^{n+1} - q_p^n - \Delta\gamma \, \text{sign}(F^{trial}) \right]^3 \right| - F_{fric}^{max} \stackrel{!}{=} 0 \,, \tag{2.32}$$

which has to be solved for the unknown increment $\Delta\gamma > 0$. Consequently, the related unknowns $\{q_p^{n+1}, F^{n+1}\}$ can be updated based on Equations $(2.31)_{2,3}$.

2.3.2. Time-stepping schemes

For the time-integration on the global level, the same approach as introduced in Section 2.2.2 is applied, resulting basically in the equations of motion (2.23). However, it will be demonstrated in the following, that the adequate approximation of the time-integrated internal force represents a challenging task in the nonlinear case, particularly when fundamental physical principles shall be respected.

Standard quadrature rule

Motivated by the foregoing positive results, we start again with an approximation of the relevant integral by means of a standard Gauss quadrature rule with one integration point, compare Equation (2.24), resulting in Equations (2.25).
For the computation, we have incorporated the same parameters as for the linear case. The results are shown in Figure 2.6-2.8. In particular, the nonlinearity of the spring response as well as a distinct slip period can be seen in Figure 2.6 a). Moreover, the occurring plastic slip/displacement in the friction-element is plotted in Figure 2.7 b), causing evidently dissipation effects which are once more displayed in Figure 2.8 a) based on the accumulated dissipation D. Furthermore, the resulting offset in the oscillating position of the mass is pictured in Figure 2.6 b), involving as well a visible drift of the corresponding phase-space portrait due to the movement of the friction-element as shown in Figure 2.7 a). As already discussed, particularly interesting in the context of dissipative dynamical systems is the discrete energy balance, that should reproduce essential laws of thermodynamics. Concerning this aspect, crucial differences to the prior linear case become obvious when a plot of the total energy is considered, see Figure 2.8 b). Herein, it is shown that the requirement of a monotonic decrease of the total energy based on a strictly positive (local) dissipation, corresponding to Equations (2.7), (2.8), is not offered in general. Rather, the total energy is characterised by notable oscillations accompanied by unphysical increasing periods, especially for larger time-step sizes. In fact, the global energy behaviour of the algorithm differs quantitatively and even qualitatively when the step size is increased. Aside from a doubtful physical quality of the results, it is well-studied for the conservative case that a disregard of fundamental balance principles by the time-stepping scheme can degrade appreciably the robustness of the integrator, as also investigated in more detail in subsequent chapters.

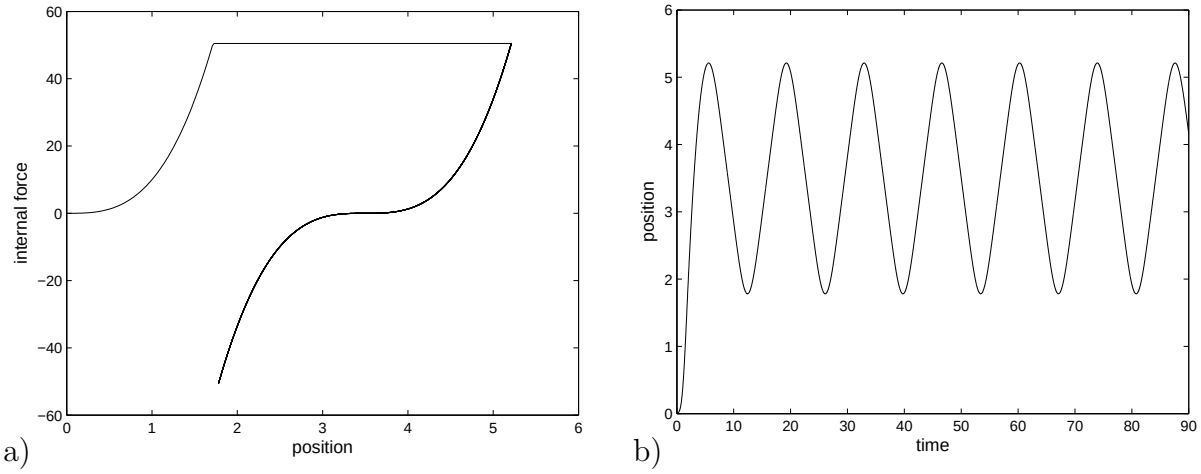

Figure 2.6.: a) internal force in the spring F, b) position of the mass q

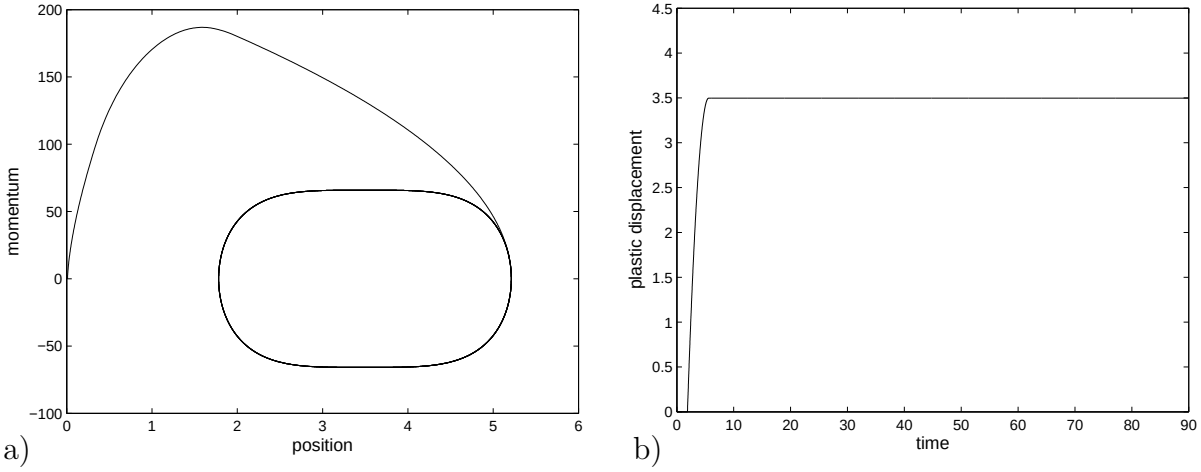

Figure 2.7.: a) phase-space portrait of the mass m, b) plastic slip q_p of the friction-element

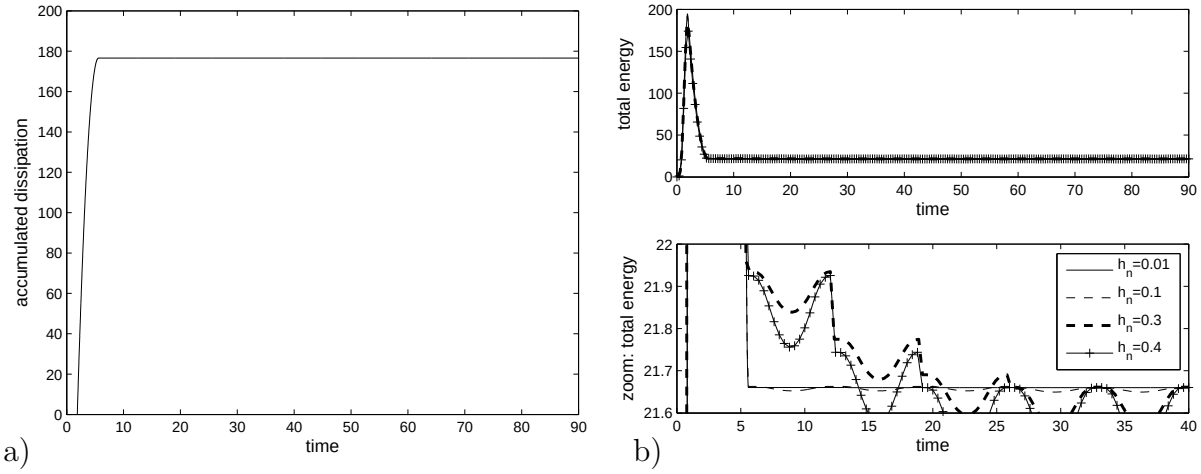

Figure 2.8.: a) accumulated dissipation D, b) total energy H

Non-standard quadrature rule I

As demonstrated above, the application of a midpoint approximation, related to a standard Gauss quadrature rule, does not render a satisfying algorithmic energy behaviour of the resulting time-stepping scheme, when a nonlinear constitutive response of the spring is taken into account. Consequently, the approximation of the time-integrated internal force has to be modified. In this context, a widespread modification for classical Hamiltonian dynamics dates back to Gonzalez [62, 64], involving explicitly the underlying potential of a considered conservative system. Due to the partially Hamiltonian character of the present 'friction-element spring device', as noted in Remark 2.1, an obvious 'ad hoc' approach could be the modification of the quadrature rule only when the friction-element is inactive and, hence, the system is indeed (temporarily) conservative. In this case, we introduce the non-standard quadrature rule

$$\int_0^1 F(\alpha)\,\mathrm{d}\alpha \approx {}^{el}F^{alg}(1/2) \tag{2.33}$$

based on the particularly designed algorithmic force for the elastic case ${}^{el}F^{alg}$. Thereby, the so-called elastic-enhanced algorithmic force is given by

$${}^{el}F^{alg}(1/2) = F_{1/2} + \frac{V_{\alpha=1} - V_{\alpha=0} - F_{1/2}\,[q_2 - q_1]}{|q_2 - q_1|^2}[q_2 - q_1]\,, \tag{2.34}$$

which can be accounted as an adequate algorithmic perturbation of the standard midpoint approximation in the form ${}^{el}F^{alg}(1/2) = F_{1/2} + {}^{el}\Omega\,[q_2 - q_1]$ with the scaling factor ${}^{el}\Omega$ [3]. However, the midpoint approximation (2.24) is still used for time steps in which the friction-element is active, caused by the involved dissipation effects which prohibit a classical Hamiltonian interpretation.
The resulting influence on the algorithmic energy balance can be studied based on Figure 2.9 and Figure 2.10. In this context, a direct comparison with the standard quadrature rule in Figure 2.9 illustrates obviously the notable upgrade in the quality of the algorithmic energy behaviour due to an application of the foregoing 'ad hoc' approach, dealing with small as well as large time-step sizes. Moreover, the present example clearly demonstrates that the unphysical increasing periods in the nonlinear case have been basically affected by the lack of the standard quadrature rule concerning the required conservation of the total energy during elastic periods. In fact, the shown monotonic decrease of the

[3] Please note, that Equation (2.34) could be simplified in the here considered one-dimensional case to

$${}^{el}F^{alg}(1/2) = \frac{V_{\alpha=1} - V_{\alpha=0}}{q_2 - q_1}\,, \tag{2.35}$$

representing a kind of secant modulus. Nevertheless, we favour the extended version (2.34) for the sake of generality, reflecting furthermore better the underlying structure of the enhanced algorithmic quantity.

total energy seems to recapture qualitatively even the energy behaviour that has been observed in the linear case, compare Figure 2.5 b) and Figure 2.10 a). Encouraged by these positive results, we investigate the discrete energy balance in more detail. For this purpose, a time-integration of Equation (2.8) over the physical interval $\mathcal{T}$ results in the requirement

$$R := H_{n+1} - H_n + \Delta D \stackrel{!}{=} 0\,, \tag{2.36}$$

wherein the dissipation increment

$$\Delta D := \int_{t_n}^{t_{n+1}} \dot{\gamma}(t)\, F_{fric}^{max}\, \mathrm{d}t = \Delta\gamma\, F_{fric}^{max} \tag{2.37}$$

has been introduced based on Equation (2.7) with the increment $\Delta\gamma$ provided by the (local) constitutive update. Conceptually, we aim at a fulfilment of Equation (2.36) within the calculation accuracy influenced by the applied iteration tolerance to solve the nonlinear equations of motion, compare Betsch and Steinmann [24]. A plot of the residual R given by Equation (2.36) is pictured in Figure 2.10 b). Herein, it can be seen that especially for large time-step sizes the residual is characterised by single peaks, which are in the order of magnitude $\mathcal{O}(10^{-4})$. Since for the present example the tolerance of the global iteration procedure has been set to 10^{-8}, a rigorous fulfilment of Equation (2.36) is obviously not guaranteed by means of the discussed concepts.

Non-standard quadrature rule II

In the previous paragraph, it has been shown that already the first non-standard quadrature, which is applied solely for elastic steps, is apparently able to feature a notable improvement of the algorithmic performance concerning the required monotonic decrease of the total energy in the dissipative case. Nevertheless, even this 'ad hoc' approach based on the well-studied conservative case is not able to capture correctly the underlying energy balance of the dissipative system related to a conservation of the sum of the total energy and the dissipation within the calculation accuracy, compare Equation (2.36). Evidently, the essential flaw is hereby the nonexistent modification of the standard quadrature rule during dissipative steps. Consequently, the question is how to adapt appropriately the foregoing non-standard quadrature rule, so that it is also valid when the friction-element is active. For this purpose, we calculate the difference between the kinetic energy at $\alpha = 1$ and $\alpha = 0$, yielding

$$K(p_2) - K(p_1) = \frac{1}{2m}\left[p_2^2 - p_1^2\right] = \frac{1}{m}\,\frac{p_1 + p_2}{2}\left[p_2 - p_1\right]. \tag{2.38}$$

By incorporating furthermore the equations of motion (2.25), Equation (2.38) can be rewritten, resulting in

$$K(p_2) - K(p_1) = \frac{1}{m}\left[\frac{m}{h_n}\left[q_2 - q_1\right]\right](-1)\, h_n\, F_{1/2} = -F_{1/2}\left[q_2 - q_1\right]. \tag{2.39}$$

Based on Equation (2.39), it follows directly that the approximation $F_{1/2}$ has to fulfil the condition

$$F_{1/2}\left[q_2 - q_1\right] \stackrel{!}{=} V_{\alpha=1} - V_{\alpha=0} + \Delta D \tag{2.40}$$

to capture the correct energy balance (2.36) within the here considered reference interval $\mathcal{I}$. Since in general a fulfilment of condition (2.40) can not be guaranteed by means of the standard approximation $F_{1/2}$, we introduce the enhanced algorithmic force

$$F^{alg}(1/2) = F_{1/2} + \Omega\left[q_2 - q_1\right], \tag{2.41}$$

motivated by the 'ad hoc' approach based on the format (2.34). By inserting Equation (2.41) into Equation (2.40), the involved scaling factor Ω of the perturbation can be calculated straightforwardly, rendering

$$F^{alg}(1/2) = F_{1/2} + \frac{V_{\alpha=1} - V_{\alpha=0} + \Delta D - F_{1/2}\left[q_2 - q_1\right]}{|q_2 - q_1|^2}[q_2 - q_1]\,. \tag{2.42}$$

Obviously, Equation (2.42) represents the adequate generalisation of Equation (2.34) to the dissipative case, leading to the second non-standard quadrature rule

$$\int_0^1 F(\alpha)\,\mathrm{d}\alpha \approx F^{alg}(1/2) \tag{2.43}$$

which is also used when the friction-element is active. Please note, that for elastic steps with $\Delta D = 0$ both non-standard quadrature rules are identical.
The results can be regarded in Figure 2.11. Once more, the plot of the total energy in Figure 2.11 a) shows the claimed monotonic decrease, being in analogy to the basic results of the linear case pictured in Figure 2.5 b). However, the main feature of the second non-standard quadrature rule becomes obvious when the residual R given by Equation (2.36) is investigated. Hereby, the corresponding plot in Figure 2.11 b) clearly confirms that the discrete energy balance is indeed fulfilled within the calculation accuracy, using small as well as large time-step sizes. For the present example, the resulting errors are in the order of magnitude $\mathcal{O}(10^{-11})$ and $\mathcal{O}(10^{-13})$ respectively, demonstrating particularly in comparison to Figure 2.10 b) the entire potential of the foregoing non-standard quadrature rule (2.43) based on the specific enhanced algorithmic force (2.42).

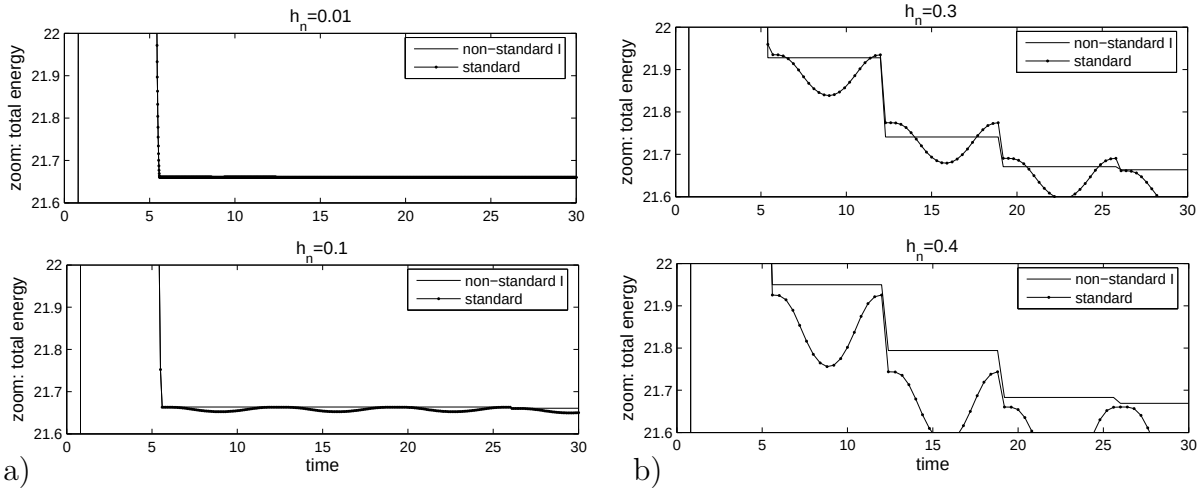

Figure 2.9.: total energy H (standard vs. non-standard quadrature rule I): a) $h_n = 0.01$ and $h_n = 0.1$, b) $h_n = 0.3$ and $h_n = 0.4$

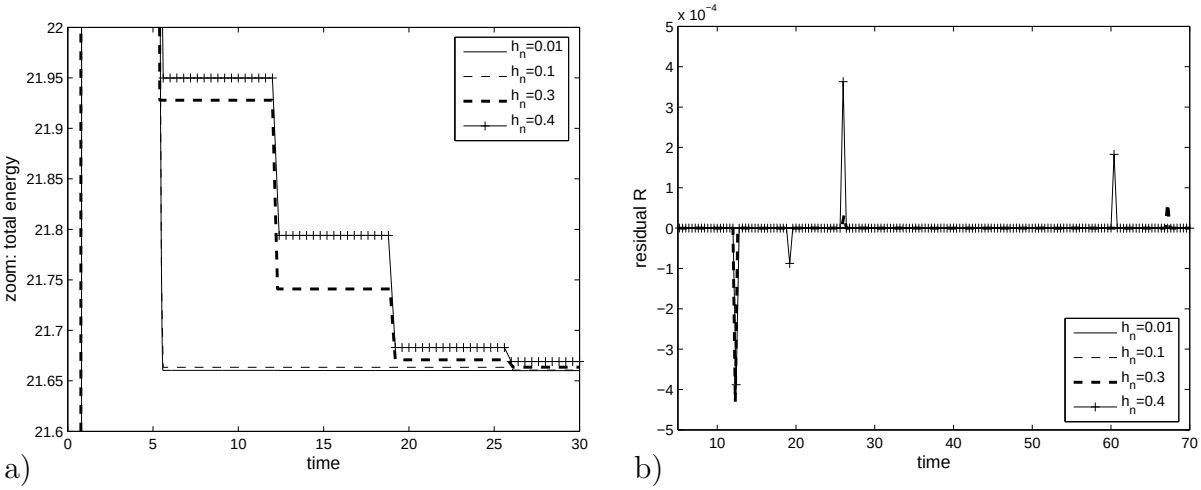

Figure 2.10.: non-standard quadrature rule I: a) total energy H, b) residual R

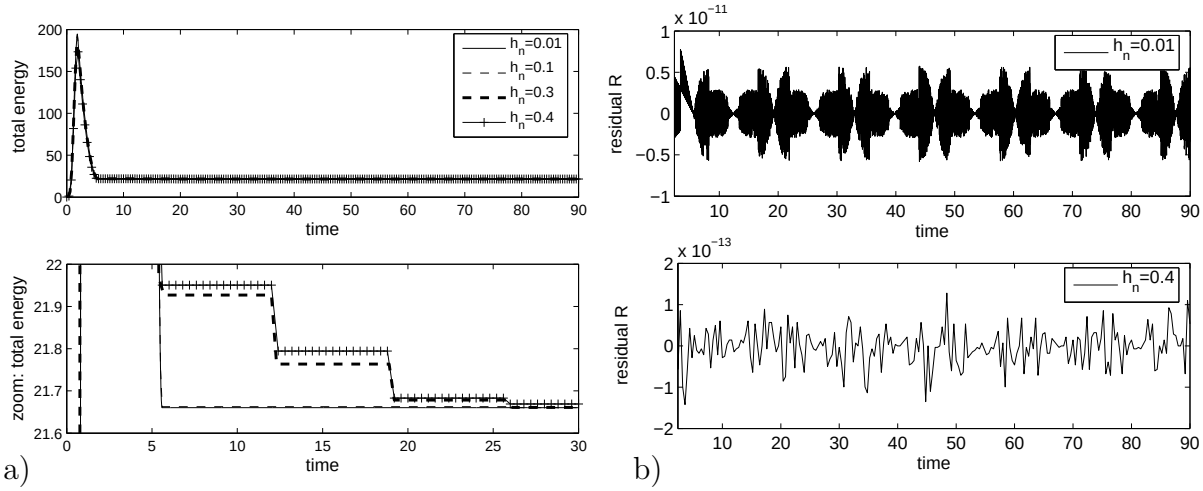

Figure 2.11.: non-standard quadrature rule II: a) total energy H, b) residual R

3. Fundamental Concepts

Previously, fundamental issues concerning the time-integration of nonlinear dissipative systems have been discussed by means of a simple one-dimensional friction-element oscillator. However, it will be shown in subsequent chapters that quite similar effects occur also in the context of nonlinear structural dynamics, involving large elastic and inelastic deformations. Thereby, the discrete format of the system dynamics is once more prone to suffer from crucial violations of physically motivated balance laws analogously to the introducing example, rendering potentially a degradation of the numerical performance. Obviously, the modelling of continuous structures including finite deformations requires a more advanced description based on geometrically nonlinear continuum mechanics. Therefore, we start in the following with the essential concepts of nonlinear continuum dynamics, followed by the spatial discretisation of the continuous system using the Finite Element method. Finally, a general framework for the time-integration of dissipative systems based on Finite Elements in time is proposed at the end of the present chapter. Hereby, special emphasis will be placed on a physically correct representation of related conservation properties.

3.1. Nonlinear Continuum Dynamics

To set the stage, basic concepts commonly used in geometrically nonlinear continuum mechanics are summarised in this section. For further details and background informations, we refer to standard literature, like for instance References [69, 75].

3.1.1. Kinematics

First, the underlying kinematic assumptions of the applied geometrically nonlinear continuum theory are recapitulated. To describe the motion of a continuous body $\mathcal{B}$ including finite deformations, the nonlinear deformation map

$$\boldsymbol{q} := \boldsymbol{\varphi}(\boldsymbol{X}, t) \tag{3.1}$$

is introduced as a mapping from the reference configuration $\mathcal{B}_0$ to a spatial configuration $\mathcal{B}_t$. Based on the definition (3.1), we obtain directly the physical velocity

$$\dot{\boldsymbol{q}} = \dot{\boldsymbol{\varphi}}(\boldsymbol{X}, t) =: \boldsymbol{v}(\boldsymbol{X}, t) \tag{3.2}$$

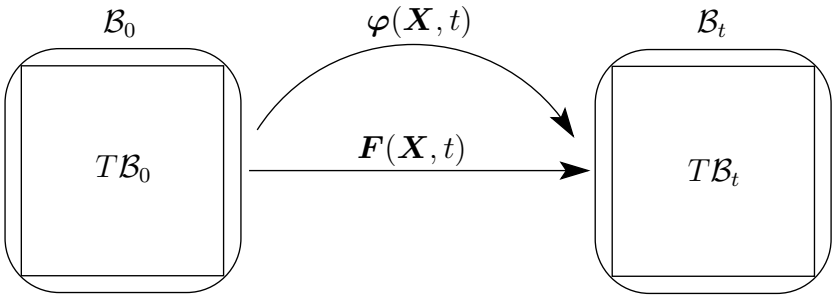

Figure 3.1.: resulting configurations of nonlinear continuum mechanics

and the linear tangent map

$$\boldsymbol{F} = \nabla_{\boldsymbol{X}} \boldsymbol{\varphi}(\boldsymbol{X}, t) \tag{3.3}$$

which is well-known as deformation gradient, mapping line elements from the reference tangent space $T\mathcal{B}_0$ to the spatial tangent space $T\mathcal{B}_t$. The foregoing kinematic relations are also sketched in Figure 3.1.

3.1.2. Dissipative materials

In a next step, the constitutive behaviour of the deformable body $\mathcal{B}$ has to be considered, whereby we deal in this chapter with a general class of dissipative materials. Specific types of material behaviour which are included within these concepts and their detailed formulation will be discussed in subsequent chapters. Analogously to the purely elastic case, the constitutive response is crucially influenced by the considered deformation state, represented by appropriate strain respectively deformation measures. In this context, the so-called right Cauchy-Green tensor

$$\boldsymbol{C} = \boldsymbol{F}^{\mathrm{t}} \cdot \boldsymbol{F} \tag{3.4}$$

is introduced based on the deformation gradient, representing a deformation measure which is defined in the reference configuration $\mathcal{B}_0$. Similarly to the (elastic) potential of a simple spring discussed in Chapter 2, a strain energy density ψ is introduced, referred to as Helmholtz energy density respectively free energy density. Since we intend to consider dissipative systems, additional internal variables enter into the Helmholtz energy density to cover also inelastic effects. In the following, we assume that all relevant internal variables are represented by the general quantity $\boldsymbol{\kappa}$ [1]. By incorporating requirements on

[1] At this point, it is important to notice that several types of inelastic effects can be formulated by means of the considered format based on internal variables, compare also Holzapfel [75] page 279: 'The concept of internal variables serves as a profound basis for the development of constitutive equations for dissipative materials studied in the following section.'

objectivity, we obtain the representation $\psi(\boldsymbol{C}, \boldsymbol{\kappa})$. Following standard arguments based on the Clausius-Planck inequality, the Piola-Kirchhoff stresses are given by

$$\boldsymbol{S} := 2\,\nabla_{\boldsymbol{C}}\,\psi\,. \tag{3.5}$$

Furthermore, it is accepted to introduce conjugated thermodynamical forces

$$\boldsymbol{\beta} := -\nabla_{\boldsymbol{\kappa}}\,\psi \tag{3.6}$$

which will become important for subsequently elaborated thermodynamical aspects, compare also Reference [75, 162]. Referring to the second law of thermodynamics, it is essentially assumed that the dissipation is strictly positive for the underlying constitutive formulation, resulting in

$$\mathcal{D} = \left\langle \boldsymbol{\beta}, \dot{\boldsymbol{\kappa}} \right\rangle \;\geq 0\,. \tag{3.7}$$

Therein, we have introduced the bracket product $\langle \bullet, \bullet \rangle$ which denotes a generalised scalar product. Moreover, the rate of the internal variables $\dot{\boldsymbol{\kappa}}$ has to be defined via a specific evolution equation, depending on the considered dissipative effect and on the particular model of interest. The fulfilment of inequality (3.7) is an absolutely essential modelling-feature which must also be guaranteed by the resulting time-stepping scheme later on.

Remark 3.1: Often, the Helmholtz energy density is assumed to be additively decomposed into micro- and macroscopic parts respectively, rendering

$$\psi(\boldsymbol{C}, \boldsymbol{\kappa}) = \psi^{mac}(\boldsymbol{C}, \boldsymbol{\kappa}^{mac}) + \psi^{mic}(\boldsymbol{\kappa}^{mic}) \tag{3.8}$$

based on the partition of the internal variables $\boldsymbol{\kappa} = [\boldsymbol{\kappa}^{mac}, \boldsymbol{\kappa}^{mic}]$. Furthermore, in several constitutive models the strain-dependent part is additionally decoupled concerning the volumetric and the isochoric response.

3.1.3. Balance laws – Conservation properties

In the following, the balance laws for a continuous system (cf. References [69, 73, 75, 149]) will be briefly considered, since we aim at a step-by-step inheritance of the resulting conservation properties from the continuous case to the completely discrete formulation. It will be shown that advanced numerical techniques are needed to satisfy these requirements within the discrete setting. Introducing the mass-density ρ and the definition of a linear momentum density $\boldsymbol{p} := \rho\,\dot{\boldsymbol{q}}$, the linear momentum of the continuous body reads $\boldsymbol{I} = \int_{\mathcal{B}_0} \boldsymbol{p}\;\mathrm{d}V$. The resulting global balance of linear momentum can then be written as

$$\dot{\boldsymbol{I}} = \int_{\partial\mathcal{B}_0} \boldsymbol{P}\cdot\mathrm{d}\boldsymbol{A} + \int_{\mathcal{B}_0} \boldsymbol{b}\;\mathrm{d}V\,. \tag{3.9}$$

In Equation (3.9), the volume force is denoted by $\boldsymbol{b}$, while $\boldsymbol{P} = \boldsymbol{F} \cdot \boldsymbol{S}$ characterises the Piola stress tensor. In analogy to the linear momentum, an angular momentum density $\boldsymbol{l} := \boldsymbol{q} \times \boldsymbol{p}$ and the resulting angular momentum $\boldsymbol{L} = \int_{\mathcal{B}_0} \boldsymbol{l} \, \mathrm{d}V$ are defined. Consequently, the global balance equation for a continuous body is given by

$$\dot{\boldsymbol{L}} = \int_{\partial \mathcal{B}_0} \boldsymbol{q} \times \boldsymbol{P} \cdot \mathrm{d}\boldsymbol{A} + \int_{\mathcal{B}_0} \boldsymbol{q} \times \boldsymbol{b} \, \mathrm{d}V \, . \tag{3.10}$$

To investigate the energy balance, the free energy Ψ and the kinetic energy K – introducing the corresponding density k – must be taken into account, namely

$$\Psi = \int_{\mathcal{B}_0} \psi \, \mathrm{d}V \qquad \text{and} \qquad K = \int_{\mathcal{B}_0} k \, \mathrm{d}V \, . \tag{3.11}$$

Dealing with dissipative systems, the global (accumulated) dissipation D – which is defined by means of the local (time-integrated) dissipation $d = \int_0^t \mathcal{D} \, \mathrm{d}t$ – must be included, involving

$$D := \int_{\mathcal{B}_0} d \, \mathrm{d}V \, . \tag{3.12}$$

Based on the classical Hamiltonian for the elastic case $H := K + \Psi$, which will also be referred to as total energy, an augmented Hamiltonian $\widetilde{H} := H + D$ is introduced, using the global dissipation representation (3.12). Consequently, the energy balance for the dissipative case can be written in the compact form

$$\dot{\widetilde{H}} = P^{ext} \, , \tag{3.13}$$

wherein P^{ext} denotes the power of external loads. In the case of vanishing external loading, we obtain from Equations (3.9), (3.10), and (3.13) the conservation properties

$$\dot{\boldsymbol{I}} = \boldsymbol{0} \qquad\qquad \dot{\boldsymbol{L}} = \boldsymbol{0} \qquad\qquad \dot{\widetilde{H}} = 0 \tag{3.14}$$

for the continuous case. Obviously, the mechanical and thermodynamical conservation properties claimed in Equations $(3.14)_{1,2,3}$ should also be reflected by the subsequently elaborated time-stepping schemes with regard to a physically correct integration.

3.2. Semidiscrete Dynamics

In contrast to the introductory example in Chapter 2 with only one degree of freedom, the modelling of continuum dynamics results in an infinite-dimensional dynamical system, requiring additionally a spatial discretisation procedure. Consequently, we perform next the first discretisation step which leads to a reduction of the continuous to a semidiscrete (finite-dimensional) system, whereby the maintenance of relevant conservation properties should be guaranteed for the semidiscrete case as well.

3.2.1. Spatial discretisation

We start with a standard Finite Element discretisation in space (cf. References [19, 177, 178]) of the reference configuration $\mathcal{B}_0 \subset \mathbb{R}^{n_{dim}}$. In this context, we introduce the dimension of the embedding Euclidian space n_{dim}, the number of Finite Elements in space n_{el} and thereby obtain a partition of the continuum

$$\mathcal{B}_0 = \bigcup_{el=1}^{n_{el}} \mathcal{B}_0^{el} \,. \tag{3.15}$$

Additionally, the global shape functions $N_I : \mathcal{B}_0 \to \mathbb{R}$ are introduced interpolating the values $\boldsymbol{q}_I : [0,T] \to \mathbb{R}^{n_{dim}}$ which are referred to the spatial nodes $I = 1, \ldots, n_{node}$. The interval $[0,T]$ denotes the time period of interest and n_{node} refers to the global number of nodes. Including these definitions, the spatial approximations of the nonlinear deformation map $\boldsymbol{\varphi}$ and the spatial velocity $\boldsymbol{v}$ result in

$$\boldsymbol{\varphi}(\boldsymbol{X},t) \approx \sum_{I=1}^{n_{node}} \boldsymbol{q}_I(t)\, N_I(\boldsymbol{X}) \qquad \text{and} \qquad \boldsymbol{v}(\boldsymbol{X},t) \approx \sum_{I=1}^{n_{node}} \dot{\boldsymbol{q}}_I(t)\, N_I(\boldsymbol{X}) \tag{3.16}$$

respectively. Accordingly, the approximation in space of the right Cauchy-Green tensor $\boldsymbol{C}$ can be formulated as

$$\boldsymbol{C}(\boldsymbol{X},t) \approx \sum_{I,J=1}^{n_{node}} \boldsymbol{q}_I(t) \cdot \boldsymbol{q}_J(t)\, \nabla_{\boldsymbol{X}} N_I(\boldsymbol{X}) \otimes \nabla_{\boldsymbol{X}} N_J(\boldsymbol{X}) \,. \tag{3.17}$$

To formulate the semidiscrete system of equations of motion in first-order format, a Hamiltonian-type notation is next applied that enables technically the same compact representation as in the purely elastic case, compare Reference [26].

3.2.2. Semidiscrete Hamiltonian-type formulation

As already mentioned, the general difference between the semidiscrete and the continuous case is manifested in the finite dimension of the resulting semidiscrete system. Using a spatial FE discretisation, the system of interest can be characterised by a vector of nodal coordinates $\bar{\boldsymbol{q}}(t) = [\boldsymbol{q}_1(t), ..., \boldsymbol{q}_{n_{node}}(t)]^{\mathrm{t}} \in \mathbb{R}^{n_{dof}}$ [2] and a vector of nodal velocities $\bar{\boldsymbol{v}}(t) = [\dot{\boldsymbol{q}}_1(t), ..., \dot{\boldsymbol{q}}_{n_{node}}(t)]^{\mathrm{t}} \in \mathbb{R}^{n_{dof}}$ with the number of degrees of freedom $n_{dof} = n_{dim}\, n_{node}$. According to Reference [26], the consistent mass matrix $\mathbb{M} \in \mathbb{R}^{n_{dof}} \times \mathbb{R}^{n_{dof}}$ of the semidiscrete system, which is constant in time, is introduced and consists of diagonal sub-matrices

$$\boldsymbol{M}_{IJ} := \int_{\mathcal{B}_0} \rho\, N_I N_J \,\mathrm{d}V\, \boldsymbol{I}_{n_{dim}} \tag{3.18}$$

[2] In the following, the notation $[\bar{\bullet}]$ denotes the vectorial collection of the values $[\bullet]_I$ at the spatial nodes $I = 1, ..., n_{node}$, namely $[\bar{\bullet}] := \left[[\bullet]_1, ..., [\bullet]_{n_{node}}\right]^{\mathrm{t}}$

for $I, J = 1, \ldots, n_{node}$ with the identity $\boldsymbol{I}_{n_{dim}} \in \mathbb{R}^{n_{dim}} \times \mathbb{R}^{n_{dim}}$. If we define additionally a vector consisting of nodal generalised momenta $\bar{\boldsymbol{p}} = [\boldsymbol{p}_1, ..., \boldsymbol{p}_{n_{node}}]^{\mathrm{t}} := \mathbb{M} \cdot \bar{\boldsymbol{v}} \in \mathbb{R}^{n_{dof}}$, the kinetic energy for the semidiscrete case reads

$$K(\bar{\boldsymbol{p}}) = \frac{1}{2}\, \bar{\boldsymbol{p}} \cdot \mathbb{M}^{-1} \cdot \bar{\boldsymbol{p}}\,. \tag{3.19}$$

Moreover, conservative external loads are assumed based on an external potential V^{ext}, so that a semidiscrete function

$$H(\bar{\boldsymbol{q}}, \bar{\boldsymbol{p}}; \boldsymbol{\kappa}) = \frac{1}{2}\, \bar{\boldsymbol{p}} \cdot \mathbb{M}^{-1} \cdot \bar{\boldsymbol{p}} + \Psi(\bar{\boldsymbol{q}}; \boldsymbol{\kappa}) + V^{ext}(\bar{\boldsymbol{q}}) \tag{3.20}$$

can be introduced analogously to the classical Hamiltonian for the hyperelastic case, wherein the free energy of the semidiscrete system $\Psi(\bar{\boldsymbol{q}}; \boldsymbol{\kappa})$ has been incorporated, compare Equations $(3.11)_1$, (3.17). As already discussed in Section 3.1.2, the quantity $\boldsymbol{\kappa}$ collects internal variables which are not directly 'visible' on the global (nodal) level of the equations of motion. Abbreviating the notation, a vector of nodal phase-space variables $\bar{\boldsymbol{z}}(t) = [\bar{\boldsymbol{q}}(t), \bar{\boldsymbol{p}}(t)]^{\mathrm{t}} \in \mathbb{R}^{2n_{dof}}$ and the skew-symmetric (symplectic) matrix

$$\mathbb{J} := \begin{bmatrix} \boldsymbol{0} & \boldsymbol{I} \\ -\boldsymbol{I} & \boldsymbol{0} \end{bmatrix} \tag{3.21}$$

are introduced based on $\boldsymbol{I} \in \mathbb{R}^{n_{dof}} \times \mathbb{R}^{n_{dof}}$ and $\boldsymbol{0} \in \mathbb{R}^{n_{dof}} \times \mathbb{R}^{n_{dof}}$. Pursuant to the purely elastic case, the semidiscrete system of equations of motion can still be formulated in the compact format

$$\dot{\bar{\boldsymbol{z}}}(t) = \mathbb{J} \cdot \nabla_{\bar{\boldsymbol{z}}}\, H(\bar{\boldsymbol{z}}(t); \boldsymbol{\kappa}(t))\,. \tag{3.22}$$

It is important to emphasise once more that the application of a Hamiltonian-type setting has been only used as a formalism of notation, being in analogy to the hyperelastic case. Naturally, the conservative character of the system and, consequently, the classical Hamiltonian interpretation gets lost when dissipation effects are involved. However, the structure of the equations of motion remains indeed unchanged [3]. If we use the definition of the free energy Ψ and introduce the global vector of external loads $\bar{\boldsymbol{F}}^{ext} := -\nabla_{\bar{\boldsymbol{q}}}\, V^{ext}$, the gradient $\nabla_{\bar{\boldsymbol{z}}}\, H$ can be specified via

$$\nabla_{\bar{\boldsymbol{z}}}\, H = \begin{bmatrix} \bar{\boldsymbol{F}}^{int} - \bar{\boldsymbol{F}}^{ext} \\ \mathbb{M}^{-1} \cdot \bar{\boldsymbol{p}} \end{bmatrix}, \tag{3.24}$$

[3] Obviously, the resulting first-order format can also be derived directly from the semidiscrete balance of momentum

$$\mathbb{M} \cdot \ddot{\bar{\boldsymbol{q}}} + \bar{\boldsymbol{F}}^{int} = \bar{\boldsymbol{F}}^{ext}\,, \tag{3.23}$$

which often represents the actual starting point for various standard time-stepping schemes based on Finite Differences, as also discussed in Appendix C. However, by introducing $\bar{\boldsymbol{p}} := \mathbb{M} \cdot \dot{\bar{\boldsymbol{q}}}$ it follows straightforwardly $\dot{\bar{\boldsymbol{p}}} = \bar{\boldsymbol{F}}^{ext} - \bar{\boldsymbol{F}}^{int}$, compare Equations (3.21), (3.22), (3.24).

wherein additionally the internal load vector [4] has formally been introduced as

$$\bar{\boldsymbol{F}}^{int}(\boldsymbol{S}) = \nabla_{\bar{\boldsymbol{q}}} \int_{\mathcal{B}_0} \psi \, \mathrm{d}V \,. \tag{3.25}$$

Thereby, the global vector $\bar{\boldsymbol{F}}^{int} := [\boldsymbol{F}_1^{int}, ..., \boldsymbol{F}_{n_{node}}^{int}]^{\mathrm{t}} \in \mathbb{R}^{n_{dof}}$ consists of nodal internal load vectors $\boldsymbol{F}_I^{int}$ which are defined as

$$\boldsymbol{F}_I^{int} := \sum_{J=1}^{n_{node}} \left[\int_{\mathcal{B}_0} [\nabla_{\boldsymbol{X}} N_I \otimes \nabla_{\boldsymbol{X}} N_J] : \boldsymbol{S} \, \mathrm{d}V \right] \boldsymbol{q}_J \tag{3.26}$$

for $I = 1, ..., n_{node}$ [5]. Based on Equation (3.26), once more the fundamental character of the applied internal variable formulation is reflected, since obviously the related quantities $\boldsymbol{\kappa}$ influence the semidiscrete equations of motion (3.22) only implicitly via the Piola-Kirchhoff stress tensor $\boldsymbol{S}(\boldsymbol{C}, \boldsymbol{\kappa})$, whereas the global format is identical to the hyperelastic case.

3.2.3. Conservation properties – Semidiscrete system

For the following investigations, absent external loads are assumed, implying $\bar{\boldsymbol{F}}^{ext} = \boldsymbol{0}$. Concerning conservation of total linear momentum $\boldsymbol{I} = \sum_{I=1}^{n_{node}} \boldsymbol{p}_I$, we deduce by means of the partition of unity property of the spatial shape functions N_I and definition (3.26) the expression

$$\dot{\boldsymbol{I}} = - \sum_{I=1}^{n_{node}} \boldsymbol{F}_I^{int} = \boldsymbol{0} \,. \tag{3.27}$$

Conservation of total angular momentum $\boldsymbol{L} = \sum_{I=1}^{n_{node}} \boldsymbol{q}_I \times \boldsymbol{p}_I$ for the semidiscrete system can be shown, if the symmetries of $\mathbb{M}^{-1}$ and $S_{IJ} := \nabla_{\boldsymbol{X}} N_I \cdot \boldsymbol{S} \cdot \nabla_{\boldsymbol{X}} N_J$ are taken into account in addition to the skew-symmetry of the vector product, rendering

$$\dot{\boldsymbol{L}} = \sum_{I=1}^{n_{node}} \left[\dot{\boldsymbol{q}}_I \times \boldsymbol{p}_I + \boldsymbol{F}_I^{int} \times \boldsymbol{q}_I \right] = \boldsymbol{0} \,. \tag{3.28}$$

As demonstrated above, conservation of the momentum maps in the semidiscrete case preserves the format of the well-studied hyperelastic case, discussed extensively in References [26, 67, 68]. This result is obtained as a direct consequence of the unchanged

[4] It is important to keep in mind, that the semidiscrete internal load vector could also be deduced from a spatially weak formulation of the balance of momentum following standard derivation steps, compare e.g. Reference [177].

[5] Please notice, that within an algorithmic implementation the involved spatial integrals are approximated by means of numerical quadrature rules, as discussed for instance in References [76, 178].

global structure of the semidiscrete system of equations of motion. Considering the total energy of the semidiscrete dissipative system $H = K(\bar{\boldsymbol{p}}(t)) + \Psi(\bar{\boldsymbol{q}}(t); \boldsymbol{\kappa}(t))$, we obtain by using the chain rule

$$\dot{H} = \nabla_{\bar{\boldsymbol{p}}} K \cdot \dot{\bar{\boldsymbol{p}}} + \nabla_{\bar{\boldsymbol{q}}} \Psi \cdot \dot{\bar{\boldsymbol{q}}} + \langle \nabla_{\boldsymbol{\kappa}} \Psi, \dot{\boldsymbol{\kappa}} \rangle \,. \tag{3.29}$$

Including next the definition of the internal load vector $\bar{\boldsymbol{F}}^{int}$ introduced in Equation (3.25), the conjugated thermodynamical forces $\boldsymbol{\beta}$ defined in Equation (3.6), and the free energy of the semidiscrete system Ψ, we conclude

$$\dot{H} = \dot{\bar{\boldsymbol{p}}} \cdot \mathbb{M}^{-1} \cdot \bar{\boldsymbol{p}} + \bar{\boldsymbol{F}}^{int} \cdot \dot{\bar{\boldsymbol{q}}} - \int_{\mathcal{B}_0} \left\langle \boldsymbol{\beta}, \dot{\boldsymbol{\kappa}} \right\rangle \mathrm{d}V \,. \tag{3.30}$$

Based on the (local) dissipation defined in Equation (3.7), Equation (3.30) can be obviously reformulated as

$$\dot{H} + \int_{\mathcal{B}_0} \mathcal{D} \, \mathrm{d}V = \dot{\bar{\boldsymbol{p}}} \cdot \mathbb{M}^{-1} \cdot \bar{\boldsymbol{p}} + \bar{\boldsymbol{F}}^{int} \cdot \dot{\bar{\boldsymbol{q}}} \,. \tag{3.31}$$

Using furthermore the semidiscrete equations (3.22) for the rate of the global (nodal) variables $\bar{\boldsymbol{q}}$ and $\bar{\boldsymbol{p}}$ respectively, it follows together with Equation (3.24)

$$\dot{\bar{\boldsymbol{p}}} \cdot \mathbb{M}^{-1} \cdot \bar{\boldsymbol{p}} + \bar{\boldsymbol{F}}^{int} \cdot \dot{\bar{\boldsymbol{q}}} = 0 \,, \tag{3.32}$$

accordingly to Reference [26]. Consequently, Equation (3.30) results in

$$\dot{H} + \int_{\mathcal{B}_0} \mathcal{D} \, \mathrm{d}V = 0 \,. \tag{3.33}$$

By incorporating moreover the previously introduced augmented Hamiltonian $\widetilde{H}$ and the definition of the global (accumulated) dissipation D, we obtain by means of the local rate $\dot{d} = \mathcal{D}$ the relation

$$\dot{\widetilde{H}} = 0 \,. \tag{3.34}$$

In case that one of the abovementioned conservation properties (3.27), (3.28), and (3.34) of the semidiscrete system is transferred to the completely discrete system, the resulting time-stepping scheme will be referred to as consistent. Inspired by the results of Chapter 2, we will distinguish in the following paragraphs between

- *mechanical consistency* which includes the conservation of both momentum maps,
- *thermodynamical consistency* including the conservation of the total energy for elastic deformations combined with a strictly positive (local) dissipation, and finally

- *energy-consistency* that actually contains a conservation of the augmented Hamiltonian $\widetilde{H}$ in general, representing a physically correct energy-dissipation balance related to a constant sum of total energy and (strictly positive) dissipation. Consequently, the demand of energy-consistency poses a stronger requirement on the resulting time-stepping scheme as the claim of thermodynamical consistency.

If mechanical consistency as well as energy-consistency are both guaranteed by the specific time integrator, it will be referred to as *completely consistent*, respecting all of the physically motivated balance principles that have been discussed in Section 3.1.3 for the continuous system.

Remarks 3.2:

1. Based on the foregoing definitions, both non-standard quadrature rules that have been used in Chapter 2 within the context of the friction-element oscillator can be classified. Obviously, the first 'ad hoc' formulation has guaranteed the conservation of the total energy for elastic periods, so that in combination with the strictly positive (local) dissipation of the friction-element an unphysical increase of the total energy has been apparently circumvented. However, it has been shown that a conservation of the sum consisting of the total energy and the dissipation can not be guaranteed. Thus, the resulting integrator might be referred to as thermodynamically consistent. To the contrary, the second non-standard quadrature rule has featured indeed a conservation of the corresponding sum, even within the calculation accuracy. Consequently, the resulting time-stepping scheme can be labelled as energy-consistent.

2. Interestingly, Equation (3.32) represents the balance of kinetic energy respectively the theorem of expended power in a semidiscrete format, see e.g. Holzapfel [75]. By using the (inverse) chain rule based on Equation (3.19), Equation (3.32) yields
$$\dot{K}(\bar{\boldsymbol{p}}) = \dot{\bar{\boldsymbol{p}}} \cdot \mathbb{M}^{-1} \cdot \bar{\boldsymbol{p}} = -P^{int} \,, \tag{3.35}$$
wherein $P^{int} := \bar{\boldsymbol{F}}^{int} \cdot \dot{\bar{\boldsymbol{q}}}$ denotes the rate of internal mechanical work of the semidiscrete system. Obviously, the theorem of expended power is directly related to the underlying equations of motion, whereby it could also be obtained by multiplying the semidiscrete balance of momentum (3.23) with the velocity vector $\dot{\bar{\boldsymbol{q}}}$ or, alternatively, by inserting the velocity as admissible test function into a corresponding weak form in space, as discussed for instance in References [9, 165].

3. Moreover, the step from Equation (3.29) to Equation (3.30) includes implicitly the balance of free energy related to the total rate
$$\dot{\Psi}(\bar{\boldsymbol{q}}; \boldsymbol{\kappa}) = \nabla_{\bar{\boldsymbol{q}}} \Psi \cdot \dot{\bar{\boldsymbol{q}}} + \langle \nabla_{\boldsymbol{\kappa}} \Psi, \dot{\boldsymbol{\kappa}} \rangle = P^{int} - \int_{\mathcal{B}_0} \mathcal{D} \, \mathrm{d}V \,, \tag{3.36}$$
using once more $P^{int} := \bar{\boldsymbol{F}}^{int} \cdot \dot{\bar{\boldsymbol{q}}}$ and the definition of the (local) dissipation (3.7).

3.3. Time Discretisation

So far, the formulation of dissipative continuum dynamics as well as the corresponding discretisation in space have been discussed, focussing on related conservation properties. However, the fundamental step from the continuous to the completely discrete system, that essentially determines the achievable consistency properties, is the application of adequate approximations in time, analogously to the introductory one-dimensional example.

3.3.1. Finite Elements in time – A general framework

In this section, the discretisation in time of the semidiscrete system of equations of motion, as represented by the canonical equations (3.22), will be performed. In accordance with Chapter 2, we start again with a decomposition of the time interval of interest

$$[0,T] = \bigcup_{n=0}^{N} [t_n, t_{n+1}] \tag{3.37}$$

and a mapping of each physical sub-interval $\mathcal{T} = [t_n, t_{n+1}]$ to the reference interval $\mathcal{I} := [0,1]$ by means of the function

$$\alpha(t) = \frac{t - t_n}{h_n}\,, \tag{3.38}$$

wherein $h_n = t_{n+1} - t_n$ still refers to the time-step size, compare particularly Figure 2.2. In contrast to the quite intuitive approach in the prolog, once more a general Finite Element method is taken into account for the approximations in time. More precisely, a continuous Galerkin method – or short a 'cG(k) method' – will be applied, since its underlying structure represents a perfect framework to design time-stepping schemes with pre-defined consistency properties. Fundamental aspects can also be found in References [20, 24, 25, 26, 54, 67, 68, 72]. In this context, the unknown (spatial) nodal vector $\bar{\boldsymbol{z}}$ and the vector of test functions $\delta\bar{\boldsymbol{z}}$ are approximated by

$$\bar{\boldsymbol{z}}^h = \sum_{i=1}^{k+1} M_i(\alpha)\,\bar{\boldsymbol{z}}_i \qquad \text{and} \qquad \delta\bar{\boldsymbol{z}}^h = \sum_{i=1}^{k} \widetilde{M}_i(\alpha)\,\delta\bar{\boldsymbol{z}}_i \tag{3.39}$$

respectively [6]. According to References [26, 68], the continuous Galerkin approximation in time is characterised by polynomials $M_i(\alpha) \in \mathcal{P}^k : \mathcal{I} \to \mathbb{R}$ of degree k and polynomials $\widetilde{M}_i(\alpha) \in \mathcal{P}^{k-1} : \mathcal{I} \to \mathbb{R}$ of degree $k-1$, whereby $\mathcal{P}^k$ and $\mathcal{P}^{k-1}$ denote the related function

[6] The notation $[\bullet]^h$ will also indicate subsequently the approximation in time of the quantity $[\bullet]$ which consists of a linear combination of (time-)nodal values $[\bullet]_i$ and time shape functions M_i, rendering $[\bullet]^h := \sum_{i=1}^{k+1} M_i(\alpha)\,[\bullet]_i$. Hereby, time-nodes will be denoted by small indices, whereas spatial nodes are still indicated by capital letters for the sake of clarity.

spaces. Moreover, it is important to underline that the nodal shape functions fulfil the condition $M_i(\alpha_j) = \delta_{ij}$. Consequently, the coefficients $\bar{\boldsymbol{z}}_i$ may be interpreted as the values of the spatial nodes $\bar{\boldsymbol{z}}$ at the time node i. To obtain a completely discrete system of equations of motion, a weak form in time of the canonical equations (3.22) renders

$$\int_0^1 \left[\mathbb{J} \cdot \delta\bar{\boldsymbol{z}}^h\right] \cdot \left[\mathrm{D}_\alpha \bar{\boldsymbol{z}}^h - h_n \, \mathbb{J} \cdot \nabla_{\bar{\boldsymbol{z}}} \, H(\bar{\boldsymbol{z}}^h; \boldsymbol{\kappa})\right] \mathrm{d}\alpha = 0 \qquad \forall \ \delta\bar{\boldsymbol{z}}^h \in \mathcal{P}^{k-1}\,, \tag{3.40}$$

wherein $\mathrm{D}_\alpha[\bullet]$ denotes the derivative in time of $[\bullet]$ with respect to the reference-time parameter α. Using the approximations (3.39), we directly obtain the discrete system of equations

$$\begin{aligned}
\sum_{j=1}^{k+1} \int_0^1 \widetilde{M}_i M_j' \, \mathrm{d}\alpha \, \bar{\boldsymbol{q}}_j - h_n \int_0^1 \widetilde{M}_i \, \nabla_{\bar{\boldsymbol{p}}} \, K(\bar{\boldsymbol{p}}^h) \, \mathrm{d}\alpha &= \boldsymbol{0} \\
\sum_{j=1}^{k+1} \int_0^1 \widetilde{M}_i M_j' \, \mathrm{d}\alpha \, \bar{\boldsymbol{p}}_j + h_n \int_0^1 \widetilde{M}_i \, \bar{\boldsymbol{F}}^{int\,h}(\boldsymbol{S}(\alpha)) \, \mathrm{d}\alpha &= \boldsymbol{0} \qquad \forall \ i = 1, ..., k\,.
\end{aligned} \tag{3.41}$$

Hereby, Equations (3.41) represent a system of $2k$ equations for the $2k$ unknown vectors $\bar{\boldsymbol{q}}_j, \bar{\boldsymbol{p}}_j \in \mathbb{R}^{n_{dof}}$ with $j = 2, ..., k{+}1$. The vectors at the time node $j = 1$ are already known as a result of the previous time step. According to the time-continuous case (3.26), the approximation in time of the global internal load vector $\bar{\boldsymbol{F}}^{int\,h} := [\boldsymbol{F}_1^{int\,h}, ..., \boldsymbol{F}_{n_{node}}^{int\,h}]^{\mathrm{t}}$ can be decomposed in time-approximated internal load vectors $\boldsymbol{F}_I^{int\,h}$ at the spatial nodes $I = 1, ..., n_{node}$, involving

$$\boldsymbol{F}_I^{int\,h}(\boldsymbol{S}(\alpha)) := \sum_{J=1}^{n_{node}} \left[\int_{\mathcal{B}_0} [\nabla_{\boldsymbol{X}} N_I \otimes \nabla_{\boldsymbol{X}} N_J] : \boldsymbol{S}(\alpha) \, \mathrm{d}V\right] \boldsymbol{q}_J^h(\alpha)\,. \tag{3.42}$$

Defining the actual time-stepping scheme, the final step to the completely discrete set of equations is discussed next, namely the calculation of the related time-integrals in Equations (3.41). In this context, most of the time-integrals can be calculated analytically, containing only polynomials formulated in the reference-time parameter α with the maximum degree $2\,k - 1$. However, in general the stress-dependent time-integral of Equation $(3.41)_2$ can not be integrated analytically and, consequently, an adequate approximation has to be taken into account.

3.3.2. Approximation of time-integrals

As motivated by the simple one-dimensional example in the prolog, it has been shown in Reference [26] for hyperelastic continuum dynamics that in fact the approximation of the highly nonlinear time-integral, which includes the internal load vector $\bar{\boldsymbol{F}}^{int\,h}$, plays a

crucial role in view of the obtained conservation properties of the resulting time-stepping schemes. Hence, the goal is to find an appropriate approximation $\bar{\boldsymbol{F}}_i$ with

$$\int_0^1 \widetilde{M}_i \bar{\boldsymbol{F}}^{int\,h}(\boldsymbol{S}(\alpha))\,\mathrm{d}\alpha \approx \bar{\boldsymbol{F}}_i\,. \tag{3.43}$$

Based on Equation (3.43), it is obvious that an evaluation in time of the Piola-Kirchhoff stress tensor $\boldsymbol{S}(\alpha)$ is sought. In this context, basically two options are possible concerning a time-approximation of the involved deformation measure. On the one hand, we could apply an approximation of the right Cauchy-Green tensor based on Equation (3.17) by approximating the nodal coordinates via Equation (3.39), rendering

$$\boldsymbol{C}(\alpha) = \sum_{I,J=1}^{n_{node}} \boldsymbol{q}_I^h(\alpha)\cdot\boldsymbol{q}_J^h(\alpha)\,\nabla_{\boldsymbol{X}} N_I \otimes \nabla_{\boldsymbol{X}} N_J\,. \tag{3.44}$$

On the other hand, the needed time approximation can also be introduced by means of an order-consistent Finite Element approximation of the deformation measure itself, yielding

$$\boldsymbol{C}^h(\alpha) = \sum_{i=1}^{k+1} M_i(\alpha)\,\boldsymbol{C}_i\,. \tag{3.45}$$

In this context, the approximation (3.45) will be referred to as assumed strain approximation in time, as suggested in References [26, 67, 68].

Standard quadrature rule

Based on the foregoing approximations in time of the right Cauchy-Green tensor, the proper approximation of the time-integral in Equation (3.43) is next investigated. Starting with the application of a standard Gauss quadrature rule and Equations (3.44),(3.45) at hand, we obtain straightforwardly

$$\bar{\boldsymbol{F}}_i := \sum_{l=1}^{n_{gp_t}} \widetilde{M}_i(\zeta_l)\,\bar{\boldsymbol{F}}^{int\,h}(\boldsymbol{S}(\boldsymbol{C}^{(h)}(\zeta_l),\boldsymbol{\kappa}_l))\,w_l\,, \tag{3.46}$$

wherein the number of integration points in time is denoted by n_{gp_t} and w_l characterise the weighting factors of the quadrature rule. Furthermore, $\boldsymbol{\kappa}_l$ represents the corresponding value of the internal variables $\boldsymbol{\kappa}$ at the time ζ_l which has to be calculated by means of an appropriate local integration procedure [7]. Inserting the approximation (3.46) into the

[7] At this stage, the local time-integration procedure is not specified purposely to avoid a loss of generality. In this context, an adequate choice crucially depends on the considered type of inelasticity and, moreover, the internal variable format actually motivates a decoupled investigation of the global framework. A specific example will be considered in Chapter 5 for the elasto-plastic model.

system of equations (3.41) renders the resulting set of equations of motion, representing a family of time-stepping schemes without imposing any conceptual order restriction. Initially, the achievable approximation order for the global set of equations of motion solely depends on the chosen polynomial degree k for the shape functions in time and on the number of time integration points n_{gp_t} respectively, even though it is of course influenced also by the specific local time-integration. Concerning the resulting conservation properties of the above family of higher-order time-stepping schemes, the chosen number of integration points n_{gp_t} (for given k) has also a crucial influence on the results, related to the fundamental collocation property which is associated with k Gaussian integration points in time for an approximation of the (global) time-integrals. For a detailed proof as well as for basic investigations of conservative dynamical systems, we refer to References [67, 68]. In this context, we intend to design time-stepping schemes for dissipative dynamical systems which allow a completely consistent time-integration, following the classification of Section 3.2.3. However, the combination of mechanical and energy-consistency can not be achieved in general by the abovementioned standard quadrature rule. Consequently, a non-standard formulation has to be incorporated once more, whereby this time a general design concept will be used in contrast to the quite intuitive approach of Chapter 2.

Non-standard quadrature rule

To guarantee the conservation of both momentum maps as well as energy-consistency in general, the non-standard approximation of the time-integral (3.43) reads

$$\bar{\boldsymbol{F}}_i := \sum_{l=1}^{k} \widetilde{M}_i(\zeta_l)\, \bar{\boldsymbol{F}}^{int\ h}(\boldsymbol{S}^{alg}(\zeta_l))\, w_l\,, \tag{3.47}$$

wherein a modified algorithmic stress tensor $\boldsymbol{S}^{alg}$ has been introduced to generally guarantee energy-consistency. Please note, that this stress tensor does not represent any additional physical stress measure in terms of the continuum formulation. In fact, it constitutes only an appropriate numerical option to remove the approximation-lack of the standard Gauss quadrature rule regarding the non-fulfilment of an energy-consistency condition. For lower-order approximation schemes, discussed in later sections, the modified quadrature rule is similar to the so-called 'discrete gradient' or 'discrete derivative' terminology which has originally been proposed by Gonzalez [62, 64]. Nowadays, this basic format is widespread in the context of time-stepping schemes based on Finite Differences, compare for instance References [5, 9, 118, 119]. However, in this contribution we deal with a generalisation of the 'discrete derivative/gradient' concept based on the 'enhanced assumed gradient' for hyperelasticity which leads to the so-called 'eG(k) method' and has originally been developed in Gross [67] and Gross *et al.* [68] respectively. This aspect is of cardinal importance, since any conceptual order-restriction of the global time-stepping scheme shall be circumvented, as opposed to the 'discrete gradient/derivative' methodology. Furthermore, within our approach the algorithmic stress

tensor $\boldsymbol{S}^{alg}$ is motivated and derived from a particular constrained optimisation problem in analogy to the elastic case. To be specific, we start with the optimisation

$$\mathcal{F}(\boldsymbol{S}^{alg}) = \frac{1}{2}\int_0^1 ||\boldsymbol{S}^{alg}(\alpha) - \boldsymbol{S}(\alpha)||^2 \,\mathrm{d}\alpha \quad \rightarrow \quad \mathrm{MIN}\,. \tag{3.48}$$

Obviously, the minimisation of the functional $\mathcal{F}$ correlates with a minimised norm of the difference between the original stress measure $\boldsymbol{S}$ of the continuum formulation and the algorithmic stress tensor $\boldsymbol{S}^{alg}$. Moreover, the solution is constrained by a local energy-consistency condition, represented by

$$\mathcal{E}(\boldsymbol{S}^{alg}) = \psi_{\alpha=1} - \psi_{\alpha=0} + \int_0^1 \mathcal{D}\,\mathrm{d}\alpha - \int_0^1 \boldsymbol{S}^{alg} : \frac{1}{2}\mathrm{D}_\alpha \boldsymbol{C}\,\mathrm{d}\alpha \stackrel{!}{=} 0\,. \tag{3.49}$$

Consequently, the corresponding Lagrange functional $\mathcal{L}$ reads

$$\mathcal{L} = \frac{1}{2}\int_0^1 ||\boldsymbol{S}^{alg} - \boldsymbol{S}||^2 \,\mathrm{d}\alpha + \mu\,\mathcal{E} \tag{3.50}$$

with μ denoting the underlying Lagrange multiplier. Based on $\boldsymbol{S}(\boldsymbol{C}^h, \boldsymbol{\kappa})$, the solution of the minimisation problem defined in Equation (3.48) is the so-called energy-consistent-enhanced algorithmic stress tensor

$$\boldsymbol{S}^{alg}(\alpha) = \boldsymbol{S} + 2\left[\frac{\psi_{\alpha=1} - \psi_{\alpha=0} + \int_0^1 \mathcal{D}\,\mathrm{d}\alpha - \int_0^1 \boldsymbol{S} : \frac{1}{2}\,\mathrm{D}_\alpha \boldsymbol{C}\;\mathrm{d}\alpha}{\int_0^1 \mathrm{D}_\alpha \boldsymbol{C}^h : \mathrm{D}_\alpha \boldsymbol{C}\;\mathrm{d}\alpha}\right]\mathrm{D}_\alpha \boldsymbol{C}^h\,. \tag{3.51}$$

Herein, the assumed strain approximation in time $\boldsymbol{C}^h$ corresponding to Equation (3.45) and its time derivative $\mathrm{D}_\alpha \boldsymbol{C}^h$ have been applied in view of superimposed rigid body motions, inspired by its positive influence in the purely elastic case discussed in References [67, 68]. Moreover, the mixed term in the denominator is a direct consequence of the required energy-consistency. Further details and a complete derivation are highlighted in Appendix A. Next, we demonstrate that the completely discrete system defined by Equations (3.41), Equation (3.47), and Equation (3.51) actually renders an energy-consistent and mechanically consistent (continuous) Galerkin-based time integrator, abbreviated by 'ECMC-cG(k) method'.

Remark 3.3: Please note, that the numerator of the enhancement $\mathcal{E}(\boldsymbol{S})$ in Equation (3.51) vanishes for the limit transition $h_n \rightarrow 0$, since both time-integrals in the constraint (3.49) can be rewritten due to the underlying format based on internal variables. By means of the (inverse) chain rule, the fundamental theorem of calculus, and the fact that in general the related integrals can not be integrated exactly, the application of a numerical integration with the accuracy $\mathcal{O}(h_n^p)$ renders

$$\int_0^1 \boldsymbol{S} : \frac{1}{2}\,\mathrm{D}_\alpha \boldsymbol{C}\;\mathrm{d}\alpha - \int_0^1 \mathcal{D}\,\mathrm{d}\alpha = \int_0^1 \mathrm{D}_\alpha \psi\;\mathrm{d}\alpha = \psi_{\alpha=1} - \psi_{\alpha=0} + \mathcal{O}(h_n^p)\,, \tag{3.52}$$

whereby the final order p is determined by the applied approximations of both integrals, including the stresses and the dissipation as well. By inserting relation (3.52) into Equation (3.51), it obviously follows for $p \geq 1$ that $\mathcal{E}(\boldsymbol{S}) \to 0$ and, consequently, $\boldsymbol{S}^{alg} \to \boldsymbol{S}$ for $h_n \to 0$. Thus, the proposed non-standard quadrature rule (3.47) converges to the standard quadrature rule (3.46) for decreasing time-step sizes. Furthermore, fundamental investigations concerning this matter will be discussed in Section 5.5 based on linear Finite Elements in time.

3.3.3. Conservation properties – Completely discrete system

In the following, we investigate the obtained conservation properties of the proposed Galerkin-based time-stepping schemes, depending on the applied quadrature rule. In this context, we basically focus on the fundamental aspects and summarise only the key equations [8]. The application of a standard Gauss quadrature rule is already sufficient to guarantee mechanical consistency, including the conservation of both momentum maps for vanishing external loading. For this purpose, it is important to use exactly k integration points in time corresponding to the required collocation property, when applying a cG(k) method. It is well-known that the application of $n_{gp_t} = k$ Gaussian integration points is already adequate to integrate polynomials of degree $2\,k-1$ exactly. The time-derivative of the linear momentum $\boldsymbol{I}$ is a polynomial of degree $k-1 < 2\,k-1$. Hence, the difference of the linear momentum for $\alpha = 1$ and $\alpha = 0$ can be rewritten based on the fundamental theorem of calculus as

$$\boldsymbol{I}_{\alpha=1} - \boldsymbol{I}_{\alpha=0} = \sum_{l=1}^{k} \mathrm{D}_{\alpha}\boldsymbol{I}(\zeta_l)\, w_l\,. \tag{3.53}$$

Since the total linear momentum is in the discrete case defined as the sum of the momenta $\boldsymbol{p}_I$ at the spatial nodes $I = 1, ..., n_{node}$ and the equations of motion (3.22) are fulfilled exactly at the integration points in time ζ_l due to the collocation property, it consequently follows

$$\boldsymbol{I}_{\alpha=1} - \boldsymbol{I}_{\alpha=0} = \sum_{l=1}^{k}\sum_{I=1}^{n_{node}} \mathrm{D}_{\alpha}\boldsymbol{p}_I^h(\zeta_l)\, w_l = -\sum_{l=1}^{k}\sum_{I=1}^{n_{node}} h_n\, \boldsymbol{F}_I^{int\,h}(\zeta_l)\, w_l\,. \tag{3.54}$$

Taking additionally the partition of unity property of the spatial shape functions into account, we obtain

$$\boldsymbol{I}_{\alpha=1} - \boldsymbol{I}_{\alpha=0} = \boldsymbol{0}\,, \tag{3.55}$$

[8] Once more, further details regarding the conservation of the momentum maps can be found in References [26, 68] due to the unchanged global structure of the equations of motion. Moreover, we refer to Appendix A for a more detailed investigation of the obtained algorithmic properties concerning the modified energy balance of dissipative systems.

similarly to the semidiscrete case (3.27). The time-derivative of the angular momentum $\boldsymbol{L}$ is of order $2\,k-1$. Consequently, the time-integral over the rate $\mathrm{D}_\alpha \boldsymbol{L}$ can also be integrated exactly with k Gauss points. By using the expression

$$\boldsymbol{L}(\alpha) = \sum_{I=1}^{n_{node}} \boldsymbol{q}_I^h(\alpha) \times \boldsymbol{p}_I^h(\alpha)\,, \tag{3.56}$$

the fundamental theorem of calculus and a Gauss quadrature rule render together with the collocation property at hand

$$\boldsymbol{L}_{\alpha=1} - \boldsymbol{L}_{\alpha=0} = \sum_{l=1}^{k} \sum_{I=1}^{n_{node}} \left[\mathrm{D}_\alpha \boldsymbol{q}_I^h(\zeta_l) \times \boldsymbol{p}_I^h(\zeta_l) + h_n\, \boldsymbol{F}_I^{int\,h}(\zeta_l) \times \boldsymbol{q}_I^h(\zeta_l)\right] w_l\,, \tag{3.57}$$

according to References [67, 68]. The skew-symmetry of the vector product in combination with the symmetry of the mass matrix $\mathbb{M}$ and $S_{IJ}(\alpha) := \nabla_{\boldsymbol{X}} N_I \cdot \boldsymbol{S}(\alpha) \cdot \nabla_{\boldsymbol{X}} N_J$ leads to a conservation of the angular momentum, namely

$$\boldsymbol{L}_{\alpha=1} - \boldsymbol{L}_{\alpha=0} = \boldsymbol{0}\,, \tag{3.58}$$

being in complete analogy to the semidiscrete case (3.28) [9]. To guarantee global energy-consistency, which includes a conservation of the augmented Hamiltonian $\widetilde{H}$ in general, we have introduced the non-standard quadrature rule (3.47) based on enhanced algorithmic stresses $\boldsymbol{S}^{alg}$ given by Equation (3.51). As shown in Section A.1, the characteristic format of the discrete equations of motion (3.41) involves straightforwardly the relation

$$\sum_{i=1}^{k+1} \int_0^1 M_i^{'}\, \bar{\boldsymbol{F}}^{int\,h}\, \mathrm{d}\alpha \cdot \bar{\boldsymbol{q}}_i + \int_0^1 M_i^{'}\, \mathbb{M}^{-1} \cdot \bar{\boldsymbol{p}}^h\, \mathrm{d}\alpha \cdot \bar{\boldsymbol{p}}_i = 0\,. \tag{3.59}$$

In analogy to the semidiscrete case discussed in Section 3.2.3, Equation (3.59) can be directly related to the balance of total energy. Hereby, it is demonstrated in Section A.1 that the enforcement of global energy-consistency for the completely discrete system can be reduced consequently to the requirement

$$\sum_{i=1}^{k+1} \int_0^1 M_i^{'}\, \bar{\boldsymbol{F}}^{int\,h}\, \mathrm{d}\alpha \cdot \bar{\boldsymbol{q}}_i \stackrel{!}{=} \Psi_{\alpha=1} - \Psi_{\alpha=0} + \Delta D\,, \tag{3.60}$$

representing an adequate criterion that has to be fulfilled by the involved quadrature rule. As discussed in detail in Section A.2, this global condition can be particularised

[9] It is important to emphasise, that the foregoing investigations basically rely on structural properties of the applied discretisations in space and time, like the inherent collocation or the fundamental partition of unity property. The only aspect regarding the involved constitutive modelling has been hereby the requirement of a symmetric stress tensor. Consequently, the corresponding conservation properties hold for the stresses $\boldsymbol{S}$ as well as for the algorithmic stress tensor $\boldsymbol{S}^{alg}$.

furthermore to a local energy-consistency statement for each spatial integration point, namely

$$\psi_{\alpha=1} - \psi_{\alpha=0} + \sum_{l=1}^{k} \mathcal{D}(\zeta_l)\, w_l \stackrel{!}{=} \sum_{l=1}^{k} \boldsymbol{S}(\zeta_l) : \frac{1}{2}\mathrm{D}_\alpha \boldsymbol{C}(\zeta_l)\, w_l \,, \tag{3.61}$$

representing obviously a fully discrete version of the constraint (3.49) for the algorithmic stress tensor (3.51). In this context, the investigations in Section A.3 clearly confirm the fulfilment of this local constraint by using the algorithmic stresses $\boldsymbol{S}^{alg}$. Consequently, the related non-standard quadrature rule (3.47) respects indeed the global condition (3.60) as well, and finally a combination of the foregoing results renders directly

$$\widetilde{H}_{\alpha=1} - \widetilde{H}_{\alpha=0} = 0 \,, \tag{3.62}$$

following the argumentation discussed in Section A.2. Apparently, this relation represents a completely discrete formulation of the semidiscrete equation (3.34). Thus, it has been conceptually demonstrated that the proposed framework enables indeed the design of (completely) consistent Galerkin-based time-stepping schemes of arbitrary order for nonlinear dissipative systems.

Remarks 3.4:

1. Please recall, that the applied integration of the dissipation integral also affects the resulting (global) order of accuracy of the time-stepping scheme. To be order-consistent, the accuracy of the (local) integration has to be characterised by $\mathcal{O}(h_n^{2k})$ related to k (Gaussian) integration points in time, corresponding to a cG(k)-method. However, the claimed energy-consistency is not strictly linked to an application of k integration points in time for the approximation of the dissipation integral, compare Appendix A.

2. Motivated by the semidiscrete case (3.32), Equation (3.59) can be regarded furthermore as time-integrated format of the balance of kinetic energy. As discussed in Section A.1, the second summand in Equation (3.59) can be reformulated based on the fundamental theorem of calculus, rendering

$$\int_0^1 \mathrm{D}_\alpha K \,\mathrm{d}\alpha = K_{\alpha=1} - K_{\alpha=0} = -\sum_{i=1}^{k+1} \int_0^1 M_i' \, \bar{\boldsymbol{F}}^{int\,h} \,\mathrm{d}\alpha \cdot \bar{\boldsymbol{q}}_i \,, \tag{3.63}$$

   compare Equation (3.35). Consequently, the integrated theorem of expended power (3.63) results inherently from the applied Galerkin-based time discretisation of the equations of motion. In this context, essential aspects are the underlying weak form in time as well as the fact that the time-derivatives $\mathrm{D}_\alpha \bar{\boldsymbol{z}}^h$ and the test functions $\delta\bar{\boldsymbol{z}}^h$ are included in the same function space $\mathcal{P}^{k-1}$. One could even interpret the

related continuous Galerkin scheme as the natural method of choice to respect a time-integrated (discrete) format of the theorem of expended power, which can also be recaptured directly from the weak form (in time) by incorporating $\mathrm{D}_\alpha \bar{\boldsymbol{z}}^h$ as an admissible test function. Interestingly, this fact is in entire analogy to the semidiscrete case when the point of departure for the discretisation is given by the balance of momentum, as pointed out in Remark 3.2.2.

3. Analogously, the resulting global condition (3.60) can also be interpreted as a requirement for the approximation of the time-integrated internal load vector to fulfil the balance of free energy, compare Remark 3.2.3. Based on the fundamental theorem of calculus including the total rate of the free energy $\mathrm{D}_\alpha \Psi$, a straightforward calculation yields

$$\int_0^1 \mathrm{D}_\alpha \Psi(\bar{\boldsymbol{q}}^h; \boldsymbol{\kappa}) \, \mathrm{d}\alpha = \Psi_{\alpha=1} - \Psi_{\alpha=0} = \sum_{i=1}^{k+1} \int_0^1 M_i' \, \bar{\boldsymbol{F}}^{int\, h} \, \mathrm{d}\alpha \cdot \bar{\boldsymbol{q}}_i - \Delta D \,, \quad (3.64)$$

representing furthermore the adequate global format of the local statement (3.52) that has been discussed in Remark 3.3. Moreover, please note that Equation (3.64) represents indeed a time-integrated version of the semidiscrete balance (3.36).

4. Basically, the previous investigations of the algorithmic energy balance have clearly exposed the fundamental significance of the theorem of expended power and of the balance of free energy. In fact, both relations have to be respected in the semi- as well as in the completely discrete setting to permit a corresponding energy-consistent time-integration. In this context, the (discrete) theorem of expended power has been shown to be closely linked to an adequate discretisation of the equations of motion, whereas the balance of free energy directly corresponds to the appropriate approximation of related time-integrals.

5. Even if the focus will be placed on finite elasto-plasticity in this contribution, it is important to emphasise once more that the general framework discussed in the present chapter also covers other types of dissipative systems which can be formulated based on an internal variable format, like for instance the modelling of visco-elastic material behaviour or the incorporation of damage effects.

4. Finite Elasticity

In the previous chapter, the basic ingredients to design completely consistent Galerkin-based time-stepping schemes have been presented, dealing with dissipative material behaviour that essentially relies on an internal variable formulation of the Helmholtz energy density. However, as a special case, this general framework will be temporarily reduced to the well-studied hyperelastic case without dissipation, whereby the next considered constitutive models will be formulated in principal stretches. Regarding the implementation of these constitutive laws, an efficient and general formulation in tensor bases combined with a well-established perturbation technique will be suggested. The investigation of such eigenvalue-based elastic formats is of particular interest for two reasons:

- On the one hand, the following concepts represent also an attractive basis for the formulation of finite elasto-plastic material behaviour, as discussed in Chapter 5.
- On the other hand, it will be shown that the special structure of the involved non-standard quadrature rule based on an enhanced algorithmic stress tensor of type (3.51) can prohibit an intuitive application of the eigenvalue-based format within a conserving time-integration scheme, especially if the conservation of the total energy is claimed within the calculation accuracy.

In this context, the potential pitfalls are strongly related to the numerical limit behaviour of a so-called 'stress enhancement', which is characterised by strong oscillations close to zero. Such oscillations are numerical artefacts caused by calculation errors and occur, for instance, if the considered limit transition is of the L'Hospital-type 0/0. A simple motivating example is pictured in Figure 4.1 using the function

$$f(x) = \frac{1 - \cos(x)}{x^2} \tag{4.1}$$

for the transition $x \to 0$, compare Reference [150]. Basically, such numerical artefacts are mentionable but non-crucial. However, it will be shown that the underlying oscillating limit behaviour of the 'stress enhancement' in combination with the recommended perturbation-based evaluation of the constitutive model is able to render extensive difficulties, also for the corresponding conserving time-stepping scheme. In the following, we focus on the potential numerical pitfalls and propose an appropriate solution strategy

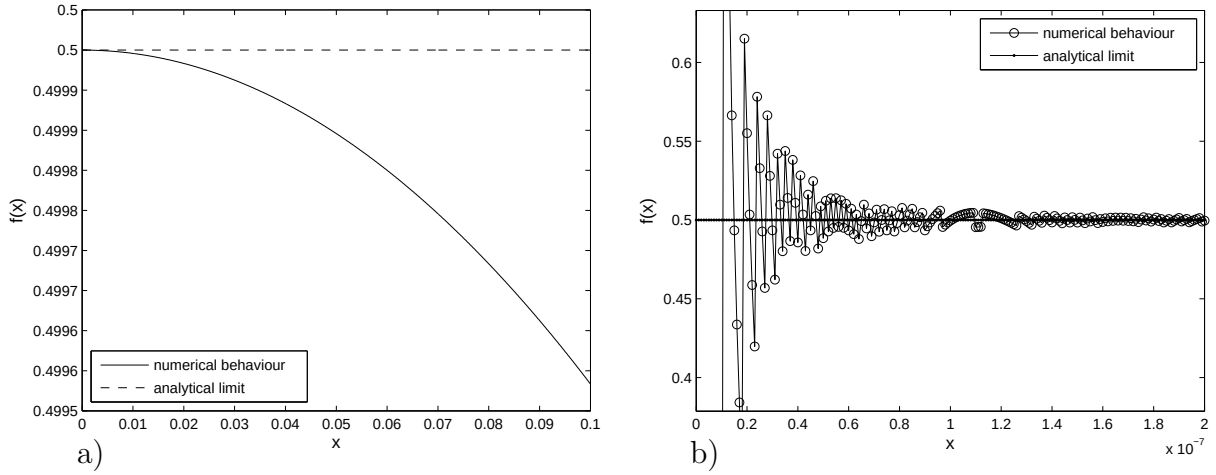

Figure 4.1.: numerical behaviour of $f(x)$ for the limit $x \rightarrow 0$: a) low & b) high resolution

which allows the efficient application of an eigenvalue-based constitutive model within the related non-standard quadrature rule based on Equation (3.51), compare Mohr *et al.* [138]. Thereby, we start our investigations on a local level, representing one spatial integration point, by means of a prescribed deformation to illustrate the essential aspects. Subsequently, the resulting consequences on the numerical and mechanical performance of the global time-integration scheme will be discussed in detail. Finally, the effectiveness of the resulting integrator will be confirmed based on two numerical examples with special emphasis on the required energy conservation.

4.1. Constitutive Modelling – Principal Stretches

One of the main aspects in this chapter is the adaption of conserving Galerkin-based integrators, which have been proposed in References [26, 68] for finite elastodynamics based on standard St.-Venant Kirchhoff or rather classical Neo-Hooke models, to a wide class on elastic formats. Further details concerning the continuum modelling of general elasticity have been extensively discussed in the literature, compare e.g. References [66, 73, 115, 124, 149]. In this context, we focus on eigenvalue-based models, representing one of the most significant formulations in the case of isotropic hyperelasticity.

4.1.1. Formulation

In the hyperelastic case, the stress response of the material is only a function of the current strain state, independent from the deformation history, and consequently no internal variables are involved. According to the representation theorem for isotropic tensor functions, cf. References [73, 149], the Helmholtz energy density $\psi(\boldsymbol{C}) = \Psi({}^{\boldsymbol{C}}J_1, {}^{\boldsymbol{C}}J_2, {}^{\boldsymbol{C}}J_3)$

can be formulated in the case of isotropy in terms of the principal invariants of the right Cauchy-Green deformation tensor defined by

$$\begin{aligned} {}^{C}J_1 &:= \operatorname{tr}(\boldsymbol{C}) \\ {}^{C}J_2 &:= \frac{1}{2}\left[{}^{C}J_1^2 - \operatorname{tr}(\boldsymbol{C}^2)\right] \\ {}^{C}J_3 &:= \det(\boldsymbol{C})\,, \end{aligned} \tag{4.2}$$

wherein $\operatorname{tr}([\bullet]) := \boldsymbol{I} : [\bullet]$ denotes the trace operation. To obtain an eigenvalue-based formulation of the Helmholtz energy density ψ, we consider the eigenvalue problem represented by

$$\boldsymbol{C} \cdot {}^{C}\boldsymbol{N}_i = {}^{C}\lambda_i \, {}^{C}\boldsymbol{N}_i \qquad \text{for} \qquad i = 1, 2, 3\,, \tag{4.3}$$

introducing the eigenvalues ${}^{C}\lambda_i$ and the principal directions ${}^{C}\boldsymbol{N}_i$ of the right Cauchy-Green tensor $\boldsymbol{C}$. To obtain non-trivial solutions the condition

$$\det\left(\boldsymbol{C} - {}^{C}\lambda_i \, \boldsymbol{I}\right) = 0 \tag{4.4}$$

renders the characteristic polynomial

$${}^{C}\lambda_i^3 - {}^{C}J_1 \, {}^{C}\lambda_i^2 + {}^{C}J_2 \, {}^{C}\lambda_i - {}^{C}J_3 = 0 \tag{4.5}$$

to compute the eigenvalues ${}^{C}\lambda_i$, whereby the eigenvalues of the right Cauchy-Green tensor $\boldsymbol{C}$ are related to the principal stretches λ_i via ${}^{C}\lambda_i = \lambda_i^2$. By means of the eigenvalues and principal directions the resulting spectral decomposition of the strains reads

$$\boldsymbol{C} = \sum_{i=1}^{3} {}^{C}\lambda_i \, {}^{C}\boldsymbol{N}_i \otimes {}^{C}\boldsymbol{N}_i \qquad \text{respectively} \qquad \boldsymbol{C} = \sum_{i=1}^{3} \lambda_i^2 \, \boldsymbol{M}_i\,, \tag{4.6}$$

wherein the definition of the tensor bases $\boldsymbol{M}_i := {}^{C}\boldsymbol{N}_i \otimes {}^{C}\boldsymbol{N}_i$ has been incorporated, as proposed e.g. in References [32, 126, 142, 169, 174]. Reformulating the principal invariants ${}^{C}J_i$ by means of the eigenvalues ${}^{C}\lambda_i$ or rather the principal stretches λ_i leads to the eigenvalue-based format of the Helmholtz energy density

$$\Psi({}^{C}J_1, {}^{C}J_2, {}^{C}J_3) = \psi({}^{C}\lambda_1, {}^{C}\lambda_2, {}^{C}\lambda_3) = \psi(\lambda_1^2, \lambda_2^2, \lambda_3^2)\,. \tag{4.7}$$

Accordingly, the spectral decomposition of the Piola-Kirchhoff stresses $\boldsymbol{S}$ yields for isotropic hyperelasticity

$$\boldsymbol{S} = \sum_{i=1}^{3} {}^{S}\lambda_i \, \boldsymbol{M}_i\,, \qquad \text{introducing} \qquad {}^{S}\lambda_i = \frac{1}{\lambda_i}\frac{\partial \psi}{\partial \lambda_i}\,. \tag{4.8}$$

It is important to emphasise that constitutive formats of the type given in Equation (4.7) are not only relevant for a few special cases. Constitutive laws based on principal stretches are well-established for a wide range of elastic materials, as discussed for instance in the textbooks [35, 73, 75]. Additionally, the modelling of inelastic material behaviour within an isotropic or even anisotropic setting often relies also on an eigenvalue-based approach; e.g. when generalised strain measures are applied, see Reference [121] and contributions cited therein. In this context, we refer for instance to commonly used formulations in finite plasticity (cf. e.g. References [82, 132, 162]) or to large strain visco-elasticity, compare Reference [34]. For the subsequent numerical investigations, first, a classical Neo-Hooke model given by the expression $\psi = \frac{1}{2}\mu\,[\boldsymbol{C}J_1 - 3] + U(J)$ with the material parameter μ and the volumetric part $U(J) = U(\det(\boldsymbol{F})) = U(\lambda_1\lambda_2\lambda_3)$ will be reformulated based on principal stretches

$$\psi = \frac{1}{2}\mu\,[\lambda_1^2 + \lambda_2^2 + \lambda_3^2 - 3] + U(J) \tag{4.9}$$

to demonstrate possible effects of an eigenvalue-based approach within the context of a non-standard quadrature rule, involving a particular case of Equation (3.51). However, the formulation of a standard Neo-Hooke model in principal stretches is solely of theoretical interest to illustrate the influences and potential consequences of a related numerical treatment. From a practical point of view, an Ogden model based on the Valanis-Landel hypothesis $\psi = \sum_{i=1}^{3} \psi_i(\lambda_i) + U(J)$ using

$$\psi_i(\lambda_i) = \sum_{j=1}^{N} \frac{\mu_j}{\alpha_j}[\lambda_i^{\alpha_j} - 1] \tag{4.10}$$

is, for instance, a more significant representative of eigenvalue-based constitutive models which is especially well-established for (compressible) rubberlike materials [1]. In Equation (4.10), the material parameters are denoted by α_j, μ_j, compare Ogden [149]. A further popular eigenvalue-based constitutive law is represented by the logarithmic Hencky model

$$\psi = \frac{1}{4}\mu\,[\ln^2(\lambda_1^2) + \ln^2(\lambda_2^2) + \ln^2(\lambda_3^2)] + U(J)\,, \tag{4.11}$$

studied e.g. in Reference [42]. Additionally, the Hencky model is particularly widespread in the context of isotropic multiplicative plasticity, as discussed for example in References [35, 131, 161]. Moreover, we refer to Chapter 5 for further details, where the logarithmic format (4.11) has also been incorporated for a specific plasticity model.

4.1.2. Algorithmic treatment

According to the general formulation of eigenvalue-based hyperelastic formats in Section 4.1.1, a particularly efficient implementation will be reviewed in this section. Referring

[1] Please note, that Equation (4.9) represents a special case of Equation (4.10).

to Equation (4.5), the eigenvalues ${}^{C}\lambda_i$ represent the solutions of a polynomial of degree 3 which can by solved by means of Cardano's formula in closed form, compare References [41, 114, 126]. Introducing the abbreviation

$$3\,\Gamma = \cos^{-1}\left(\frac{2\,{}^{C}J_1^3 - 9\,{}^{C}J_1\,{}^{C}J_2 + 27\,{}^{C}J_3}{2\,[{}^{C}J_1^2 - 3\,{}^{C}J_2]^{\frac{3}{2}}}\right) + 2\pi i \qquad \text{with} \qquad i = 1, 2, 3\,, \tag{4.12}$$

the relation to calculate the eigenvalue ${}^{C}\lambda_i$ results in

$${}^{C}\lambda_i = \frac{1}{3}\left[{}^{C}J_1 + 2[{}^{C}J_1^2 - 3{}^{C}J_2]^{\frac{1}{2}}\,\cos(\Gamma)\right]. \tag{4.13}$$

Concerning the bases-representation, we conceptually follow a formulation in terms of the second order tensors $\boldsymbol{M}_i$, compare Equation $(4.6)_2$. This approach has also been advocated by Miehe [126, 129] regarding isotropic tensor functions to avoid the costly numerical computation of the eigenvectors ${}^{C}\boldsymbol{N}_i$, compare e.g. References [35, 149, 162]. Supposing three distinct eigenvalues ${}^{C}\lambda_i \neq {}^{C}\lambda_j \neq {}^{C}\lambda_k$, the tensor bases can be computed by

$$\boldsymbol{M}_i = \frac{1}{D_i}\left[\boldsymbol{C}^2 - [{}^{C}J_1 - {}^{C}\lambda_i]\,\boldsymbol{C} + {}^{C}\lambda_j\,{}^{C}\lambda_k\,\boldsymbol{I}\right], \tag{4.14}$$

using the abbreviation

$$D_i := 2\,{}^{C}\lambda_i^2 - {}^{C}\lambda_i\,{}^{C}J_1 + {}^{C}\lambda_i^{-1}\,{}^{C}J_3\,. \tag{4.15}$$

Furthermore, a (consistent) linearisation of the constitutive model formulated in principal stretches is advantageous concerning the iterative solution procedure which is involved regarding the resulting nonlinear system of equations $(3.41)_{1,2}$. Based on the derivative of the tensor bases [2]

$$\nabla_{\boldsymbol{C}}\boldsymbol{M}_i = \frac{\lambda_i^2}{D_i}\left[\mathbb{I} - \frac{{}^{C}J_3}{\lambda_i^2}\,\mathbb{I}_{\boldsymbol{C}^{-1}}\right] + \frac{\lambda_i^2}{D_i}\sum_{j=1}^{3}\left[\frac{{}^{C}J_3}{\lambda_i^2} - \lambda_j^4\right]\lambda_j^{-4}\,\boldsymbol{M}_j \otimes \boldsymbol{M}_j \tag{4.16}$$

the compact representation of the tangent modulus $\mathbb{E}$ for general eigenvalue-based constitutive models yields

$$\mathbb{E} = x_1\mathbb{I} + x_2\,\mathbb{I}_{\boldsymbol{C}^{-1}} + \sum_{i,j=1}^{3} x_{ij}\,\lambda_i^{-2}\,\lambda_j^{-2}\,\boldsymbol{M}_i \otimes \boldsymbol{M}_j\,. \tag{4.17}$$

Therein, we have introduced the scalar-valued coefficients

$$x_1 := 2\sum_{k=1}^{3}\frac{\beta_k}{D_k} \qquad \text{respectively} \qquad x_2 := 2\sum_{k=1}^{3}\frac{\beta_k}{D_k\,\lambda_k^2}\,{}^{C}J_3 \tag{4.18}$$

[2] Herein, $\mathbb{I}$ and $\mathbb{I}_{\boldsymbol{C}^{-1}}$ denote the fourth order tensors $[\mathbb{I}]_{ijkl} := \frac{1}{2}[\delta_{ik}\delta_{jl} + \delta_{il}\delta_{jk}]$ and $[\mathbb{I}_{\boldsymbol{C}^{-1}}]_{ijkl} := \frac{1}{2}[C_{ik}^{-1}C_{jl}^{-1} + C_{il}^{-1}C_{jk}^{-1}]$ respectively.

with the scaled principal stresses $\beta_k := {}^{S}\lambda_k \, \lambda_k^2$ (cf. Equation (4.8)) and the coefficient matrix

$$x_{ij} := 2 \, \frac{\partial \beta_i}{\partial \lambda_j^2} \, \lambda_j^2 - [2\beta_i + x_1 \lambda_i^4 - x_2] \, \delta_{ij} \tag{4.19}$$

which must be specified for the applied constitutive model. Apparently, distinct eigenvalues have been assumed for the derivations highlighted above. However, in the case of two (${}^{C}\lambda_i = {}^{C}\lambda_j \neq {}^{C}\lambda_k$) or three (${}^{C}\lambda_i = {}^{C}\lambda_j = {}^{C}\lambda_k$) coincident eigenvalues, a well-established perturbation technique will be applied, as introduced by Simo [161] and Miehe [126, 127]. Further aspects and applications of the numerical perturbation approach can also be found, for instance, in References [86, 151]. Controlled by the condition

$$|{}^{C}\lambda_i - {}^{C}\lambda_j| \; < \; \Delta^{\delta} \max\{|{}^{C}\lambda_i|, |{}^{C}\lambda_j|, |{}^{C}\lambda_k|\} \tag{4.20}$$

with the machine-dependent tolerance Δ^{δ}, a numerical perturbation of the eigenvalues

$$\bar{\lambda}_i := [1 + \delta \,] \, {}^{C}\lambda_i \, , \qquad \bar{\lambda}_j := [1 - \delta \,] \, {}^{C}\lambda_j \, , \quad \text{and} \quad \bar{\lambda}_k := \frac{{}^{C}\lambda_k}{[1 + \delta \,][1 - \delta \,]} \tag{4.21}$$

shall be applied, incorporating the pre-defined perturbation size δ. Thus, the expressions for the tensor bases (4.14) and the tangent modulus (4.17) remain basically unchanged also in the case of two or three coincident eigenvalues. Accordingly, the outlined concept avoids further distinctions within the implementation, in contrast to the analytical consideration of equal eigenvalues which requires an explicit definition of different cases, as depicted e.g. in References [149, 169]. Consequently, the favoured formulation based on the tensor bases combined with the perturbation technique represents a general framework which basically allows an efficient numerical treatment.

Remark 4.1: From a numerical point of view, an analytical distinction of coincident eigenvalues also demands additional switching procedures between the different formulations controlled again by a numerical tolerance. In this regard, it will be demonstrated that especially within the context of the non-standard quadrature rule, involving different evaluation points in time (cf. Equation (4.27)), any numerical tolerance and switching procedure can cause severe convergence problems as well as a loss of the required energy conservation within the calculation accuracy, compare Section 4.5.

4.2. Conserving Time-Stepping Schemes

Based on the time-FE methods proposed in Section 3.3, we specify in this section the particular time-stepping schemes that will be used for the following numerical investigations. Since we have restricted ourselves in the present chapter on elastic constitutive models formulated in principal stretches, the general framework, that also includes the

incorporation of dissipation effects, results in the well-known conservative formulation, involving the local dissipation $\mathcal{D} = 0$. Consequently, the related time-integrated and volume-integrated expressions, which have been introduced in Section 3.1.3, vanish also, rendering $d = 0$ and $D = 0$ respectively. For a standard St.-Venant Kirchhoff and a classical Neo-Hooke model, the resulting class of Galerkin-based integrators has already been discussed extensively in the context of finite elastodynamics by Betsch and Steinmann [26] and by Gross *et al.* [68]. Nevertheless, it will be shown in the next sections that an extension to eigenvalue-based hyperelastic models, using the efficient perturbation technique, can lead to serious numerical problems that require a particular evaluation strategy for the involved algorithmic stress tensor based on Equation (3.51). Furthermore, the general case of arbitrary k will be specified in the following to the linear case $k = 1$, capturing well-known integrators based on Finite Differences. In the case of $k = 1$, the shape functions $M_i \in \mathcal{P}^1$ with $i = 1, 2$ are linear while the reduced shape function $\widetilde{M}_1 \in \mathcal{P}^0$ is constant, so that

$$M_1 = 1 - \alpha, \qquad M_2 = \alpha, \qquad \text{and} \qquad \widetilde{M}_1 = 1 \tag{4.22}$$

are obtained. Based on the general approximations (3.39), a linear approximation in time results in

$$\bar{\boldsymbol{z}}^h = [1 - \alpha]\bar{\boldsymbol{z}}_1 + \alpha\bar{\boldsymbol{z}}_2 \qquad \text{and} \qquad \delta\bar{\boldsymbol{z}}^h = \delta\bar{\boldsymbol{z}}_1 \tag{4.23}$$

respectively, wherein the nodal values $\bar{\boldsymbol{z}}_1$ are already known from the previous time step. Consequently, solely one unknown vector $\bar{\boldsymbol{z}}_2 = [\bar{\boldsymbol{q}}_2, \bar{\boldsymbol{p}}_2]^{\mathrm{t}} \in \mathbb{R}^{2n_{dof}}$ remains when applying linear shape functions in time. Inserting the shape functions (4.23) into Equations $(3.41)_{1,2}$, the discrete equations of motion read

$$\begin{aligned} \bar{\boldsymbol{q}}_2 - \bar{\boldsymbol{q}}_1 - \frac{h_n}{2}\,\mathbb{M}^{-1} \cdot [\bar{\boldsymbol{p}}_1 + \bar{\boldsymbol{p}}_2] &= \boldsymbol{0} \\ \bar{\boldsymbol{p}}_2 - \bar{\boldsymbol{p}}_1 + h_n \int_0^1 \bar{\boldsymbol{F}}^{int\,h}(\boldsymbol{S}(\alpha))\,\mathrm{d}\alpha &= \boldsymbol{0}\,, \end{aligned} \tag{4.24}$$

whereby in the here considered hyperelastic case the stresses are only a function of the strain measure, as already mentioned. Consequently, the time-dependency of the stresses is given by $\boldsymbol{S}(\boldsymbol{C}(\alpha))$. In analogy to the general case, the crux of the matter concerning resulting conservation properties consists in the approximation of the time-integrated internal load vector.

4.2.1. Standard quadrature rule

Motivated by Equation (3.46), one option for the approximation of the time-integral in Equation $(4.24)_2$ is the application of a standard Gauss quadrature rule. Accounting the desired collocation property, we apply only one integration point in time $n_{gp_t} = 1 = k$,

compare Reference [68]. The incorporation of Equation (3.42) renders the standard approximation

$$\int_0^1 \boldsymbol{F}_I^{int\,h}\,\mathrm{d}\alpha \approx \sum_{J=1}^{n_{node}} \left[\int_{\mathcal{B}_0} [\nabla_{\boldsymbol{X}} N_I \otimes \nabla_{\boldsymbol{X}} N_J] : \boldsymbol{S}(\boldsymbol{C}^h(1/2))\,\mathrm{d}V\right] \boldsymbol{q}_J^h(1/2)\,. \tag{4.25}$$

Taking additionally the discrete equations of motion $(4.24)_{1,2}$ into account, the resulting time integrator is equivalent to the well-known midpoint (difference) scheme, including the linear assumed strain approximation in time $\boldsymbol{C}^h = [\boldsymbol{C}_2 - \boldsymbol{C}_1]\alpha + \boldsymbol{C}_1$ as an additional feature, see Reference [26]. As discussed in Chapter 3, the resulting time-stepping scheme based on the approximation (4.25) enables the conservation of both momentum maps, featuring a mechanically consistent integration. However, it is well-known that the foregoing integrator is not able to guarantee the conservation of the total energy, aside from the trivial case when the constitutive relation relies on a St.-Venant Kirchhoff model, as pointed out in Reference [165].

4.2.2. Non-standard quadrature rule

Since we deal with highly-nonlinear stress-strain relations based on spectral representations, a non-standard quadrature rule is required to guarantee the conservation of the total energy in general. Therefore, the general format (3.47) is specified next for linear Finite Elements in time. Analogously to Equation (4.25), the application of one integration point in time leads to the approximation

$$\int_0^1 \boldsymbol{F}_I^{int\,h}\,\mathrm{d}\alpha \approx \sum_{J=1}^{n_{node}} \left[\int_{\mathcal{B}_0} [\nabla_{\boldsymbol{X}} N_I \otimes \nabla_{\boldsymbol{X}} N_J] : \boldsymbol{S}^{alg}(1/2)\,\mathrm{d}V\right] \boldsymbol{q}_J^h(1/2)\,. \tag{4.26}$$

Setting $\mathcal{D} = 0$, the (purely elastic) enhanced algorithmic stress tensor $\boldsymbol{S}^{alg}$ (3.51) can be written in the hyperelastic case as

$$\boldsymbol{S}^{alg}(1/2) := \boldsymbol{S}_{1/2} + \frac{2\,[\psi_{\alpha=1} - \psi_{\alpha=0}] - \boldsymbol{S}_{1/2} : [\boldsymbol{C}_2 - \boldsymbol{C}_1]}{||\boldsymbol{C}_2 - \boldsymbol{C}_1||^2} [\boldsymbol{C}_2 - \boldsymbol{C}_1]\,, \tag{4.27}$$

using the abbreviation $\boldsymbol{S}_{1/2} := \boldsymbol{S}(\boldsymbol{C}^h(1/2))$. Obviously, the non-standard quadrature rule introduced in Equations (3.47),(3.51) is for the hyperelastic case, using linear approximations in time, identical to the so-called 'discrete gradient/derivative' proposed by Gonzalez [64]. Consequently, the general Galerkin-based approach favoured in this contribution naturally recaptures well-established concepts for Finite Difference methods as special cases. Furthermore, it will be shown in Chapter 5 that such analogies can also be established for the elasto-plastic case.

Remark 4.2: At this point, it is important to emphasise once more that in addition to the widespread modification (4.27) several alternative concepts have been discussed in the literature to design energy conserving time-stepping schemes for elastodynamic problems, compare for instance References [57, 101, 165]. Particularly interesting in the context of Finite Elements in time is moreover the recent contribution by Bui [46] in which various conserving integrators for elastodynamics are discussed based on the midpoint and the trapezoidal scheme respectively, using scalar as well as vectorial enforcements to guarantee the required conservation properties.

4.3. Enhancement and Principal Stretches – Pitfalls

On the one hand, essential steps required to design consistent Galerkin-based integrators have been investigated in preceding sections. On the other hand, the efficient numerical treatment for constitutive models formulated in principal stretches based on a well-established perturbation technique has been reviewed, providing an excellent performance in the context of the standard quadrature rule (4.25). However, we will demonstrate in the following sections that a combination of the eigenvalue-based formulation and the non-standard quadrature rule (4.26) can lead to serious numerical problems concerning the numerical and, in particular, the mechanical performance of the resulting time-stepping schemes. It will be shown that the numerical problems are directly related to the numerical limit behaviour of the enhanced algorithmic stress tensor (4.27), which is strongly influenced by the eigenvalue formulation.

4.3.1. Basic properties – Numerical limit transition

In the case of linear Finite Elements in time, the enhanced algorithmic stress tensor (4.27) can be written in the compact form $\boldsymbol{S}^{alg}(1/2) = \boldsymbol{S}_{1/2} + \boldsymbol{S}^{enh}$. Therein, the 'stress enhancement' $\boldsymbol{S}^{enh} := \Omega\,[\boldsymbol{C}_2 - \boldsymbol{C}_1]$ can be formulated by introducing a so-called 'enhancement scaling factor'

$$\Omega := \frac{2\,[\psi_{\alpha=1} - \psi_{\alpha=0}] - \boldsymbol{S}_{1/2} : [\boldsymbol{C}_2 - \boldsymbol{C}_1]}{||\boldsymbol{C}_2 - \boldsymbol{C}_1||^2}\,. \tag{4.28}$$

One essential property of the stress enhancement with regard to the conceptual consistency is the following: it vanishs for the limit transition $h_n \to 0$, compare also Remark 3.3. For a decreasing time-step size the difference between the right Cauchy-Green deformation tensors, evaluated at $\alpha = 1$ respectively $\alpha = 0$, vanishes as well. By using the abbreviation $\Delta\boldsymbol{C} := \boldsymbol{C}_2 - \boldsymbol{C}_1$, it should consequently hold for the limit transition

$$\lim_{||\Delta\boldsymbol{C}||\to 0}\big(\Omega\big) = 0 \qquad \text{and} \qquad \lim_{||\Delta\boldsymbol{C}||\to 0}\big(||\boldsymbol{S}^{enh}||\big) = 0\,, \tag{4.29}$$

whereby especially the limit transition of the 'enhancement scaling factor' Ω is of the classical L'Hospital-type 0/0. In the following steps, we focus on the numerical consequences of this limit transition. We start with the investigation of the numerical limit behaviour of the scaling factor Ω and the stress enhancement $\boldsymbol{S}^{enh}$ on a local level, representing a single Gaussian integration point in space. In this context, consider a fixed initial deformation gradient $\boldsymbol{F}_1$ and update this deformation gradient via

$$\boldsymbol{F}_2 := \boldsymbol{F}_1 + \xi \boldsymbol{D} \tag{4.30}$$

based on a pre-defined deformation type represented by $\boldsymbol{D}$ and different values ξ within the interval $\xi \in [0, \xi^{max}]$. The difference between ξ_k and $\xi_{k+1} := \xi_k + \Delta\xi$ is prescribed by the given step size $\Delta\xi$, defining the resolution of the limit transition. A high resolution is related to slight differences between the initial and the current strain state, corresponding to small time-step sizes or mechanically stiff problems. First, the numerical limit behaviour is analysed incorporating a classical Neo-Hooke model with the exemplary choice

$$U(J) = \frac{\lambda}{2} \ln^2(J) - \mu \ln(J) \,. \tag{4.31}$$

For the computations (2d, plane strain conditions)

$$\boldsymbol{F}_1 \equiv \begin{bmatrix} 1 & 0 \\ 0 & 1 \end{bmatrix} , \qquad \boldsymbol{D} \equiv \begin{bmatrix} 1 & 0 \\ 0 & 0 \end{bmatrix} \tag{4.32}$$

and the material parameters $\lambda = 10000, \mu = 5000$ have been applied. First results are

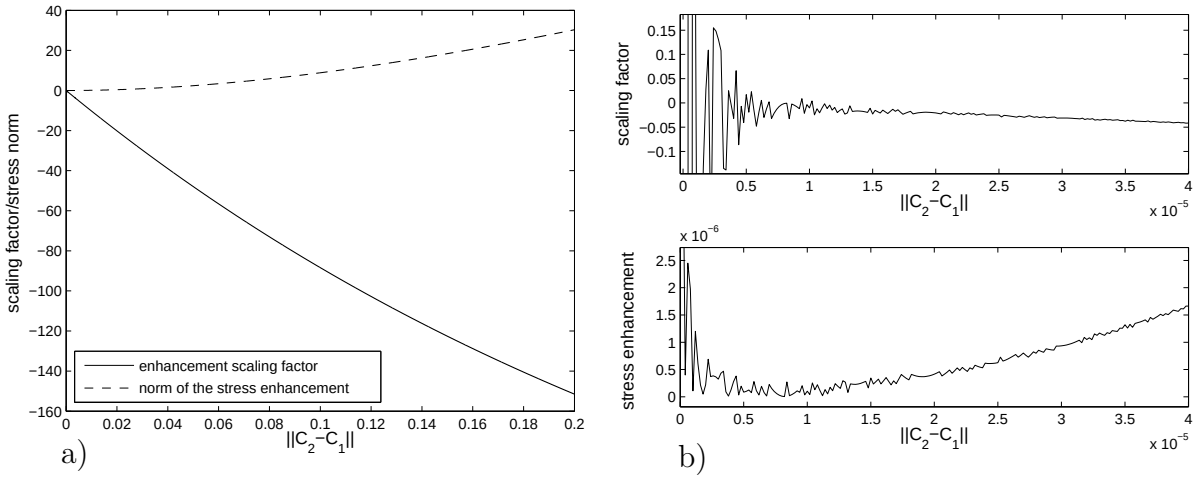

Figure 4.2.: numerical limit behaviour of the 'enhancement scaling factor' Ω and the norm of the 'stress enhancement' $||\boldsymbol{S}^{enh}||$ for the limit transition $||\Delta\boldsymbol{C}|| \to 0$: a) low & b) high resolution

shown in Figure 4.2. Using a low resolution, the numerical limit behaviour of the norm of the 'stress enhancement' as well as the behaviour of the 'enhancement scaling factor' offers the required asymptotic transition to zero, see Figure 4.2 a). However, the application of a high resolution shows strong oscillations of the 'enhancement scaling factor' in the order of magnitude $\mathcal{O}(10^{-1})$, compare Figure 4.2 b). Analogously to the first motivating example in the present chapter (cf. Figure 4.1), this effect is well-known in the literature and a direct consequence of problems related to numerical limit transitions that are influenced by the limited calculation accuracy in a computer code, particularly when dealing with very small or huge numbers. Usually, these difficulties can be circumvented by switching from the numerical to an analytical limit within a pre-defined tolerance. However, such a switching procedure does not represent an adequate option in the case of the 'stress enhancement', since this approach would yield a loss of the required energy conservation within the calculation accuracy. Fortunately, the oscillations in the norm of the 'stress enhancement' are only in the order of magnitude $\mathcal{O}(10^{-6})$, see Figure 4.2 b). Consequently, a robust application of the 'stress enhancement' is in our experience possible without any switching procedure, at least in the case of a classical Neo-Hooke constitutive law. Thereby, the numerical oscillations are nearly independent of the considered deformation type $\boldsymbol{D}$, as shown in Figure 4.3. For these computations we have used the initial deformation state

$$\boldsymbol{F}_1 \equiv \begin{bmatrix} 1.5 & 0 \\ 0.1 & 0.8 \end{bmatrix} \tag{4.33}$$

combined with the basic deformation types: compression, simple shear and a mixed deformation, whereby these deformation types are represented by the three tensors

$$\boldsymbol{D}^{comp} \equiv \begin{bmatrix} 0 & 0 \\ 0 & -1 \end{bmatrix}, \qquad \boldsymbol{D}^{shear} \equiv \begin{bmatrix} 0 & 1 \\ 0 & 0 \end{bmatrix}, \quad \text{and} \quad \boldsymbol{D}^{mix} \equiv \begin{bmatrix} 0 & 1 \\ 0 & -1 \end{bmatrix}. \tag{4.34}$$

Once more, the classical Neo-Hooke model of the previous calculation has been taken into account, applying the material parameters $\lambda = 10000, \mu = 5000$. Using a low resolution, the numerical limit transition shows the claimed behaviour. Nevertheless, oscillations occur for each type of deformation when the difference between two strain states is sufficiently small, compare Figure 4.3 b). However, independent of the deformation type the oscillations in the norm of the 'stress enhancement' are in the order of magnitude $\mathcal{O}(10^{-6})$ and, in general, do not lead to further numerical difficulties. In contrast to the deformation type, the stiffness plays an important role for the resulting numerical behaviour. For these computations the foregoing classical Neo-Hooke model has been incorporated once more, using three sets of material parameters $[\lambda,\, \mu] = [10000,\, 5000], [1000,\, 500]$, and $[100,\, 50]$ related to 'stiffness 1-3'. The initial deformation state and the deformation type can be specified by

$$\boldsymbol{F}_1 \equiv \begin{bmatrix} 1 & 0 \\ 0 & 1 \end{bmatrix} \qquad \text{and} \qquad \boldsymbol{D} \equiv \begin{bmatrix} 0 & 0 \\ 0 & 1 \end{bmatrix}. \tag{4.35}$$

The influences on the numerical limit behaviour of the norm of the 'stress enhancement' are pictured in Figure 4.4. Obviously, an increase of the stiffness leads to clearly stronger oscillations which are, nevertheless, generally not crucial concerning a robust implementation.

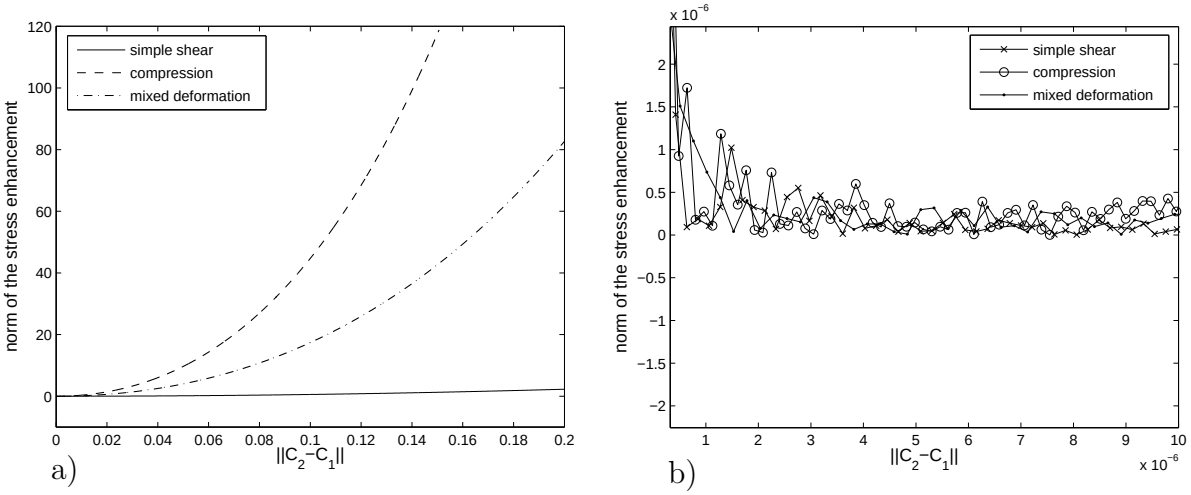

Figure 4.3.: numerical limit behaviour of the norm of the 'stress enhancement' $||\boldsymbol{S}^{enh}||$ for different deformation types: a) low & b) high resolution

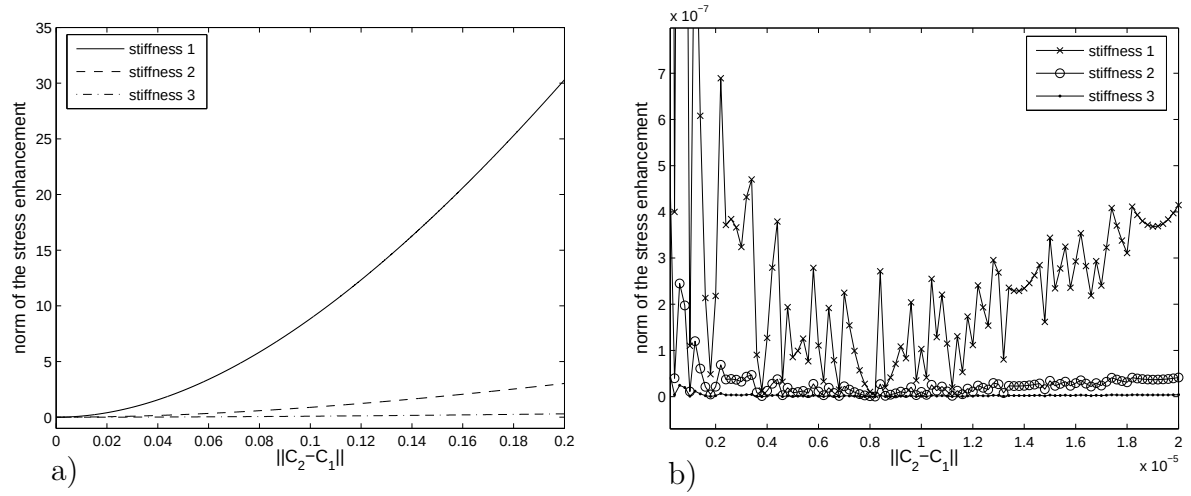

Figure 4.4.: numerical limit behaviour of the norm of the 'stress enhancement' $||\boldsymbol{S}^{enh}||$ for different material parameters: a) low & b) high resolution

So far, the described numerical artefacts are present but seem to be controllable, since in general they have no influence on the performance of the resulting algorithm. However, it will be shown in the following sections that the abovementioned numerical limit behaviour combined with a constitutive law formulated in principal stretches based on the well-established perturbation technique can induce serious consequences for the numerical and the mechanical performance. Furthermore, it will be demonstrated that the sensitivity of the enhancement with respect to the stiffness is of cardinal importance, when dealing with eigenvalue-based constitutive models in the context of energy-conserving Galerkin-based integrators.

4.3.2. Key properties – Principal stretches

We start once more with the consideration of a single Gaussian integration point in space and prescribe

$$\boldsymbol{F}_1 \equiv \begin{bmatrix} 1.1 & 0 \\ 0 & 1 \end{bmatrix} \qquad \text{and} \qquad \boldsymbol{D} \equiv \begin{bmatrix} -1 & 0 \\ 0 & 1 \end{bmatrix} . \tag{4.36}$$

To demonstrate possible influences of an eigenvalue-based constitutive model on the numerical limit behaviour of the 'stress enhancement', we rewrite the classical Neo-Hooke model of the previous section by means of principal stretches, analogously to Equation (4.9). In the case of coincident eigenvalues, the efficient well-established perturbation technique has been applied, compare Section 4.1.2. Regarding the material parameters, $\lambda = 10000, \mu = 5000$ have been chosen. A comparison between the classical formulation of the Neo-Hooke model and the reformulation based on principal stretches is pictured

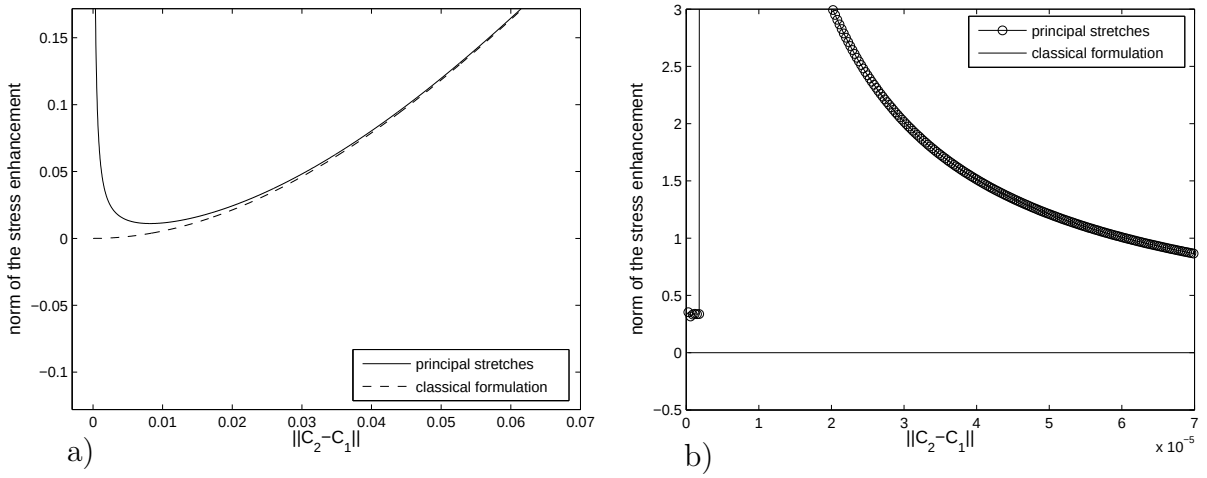

Figure 4.5.: numerical limit behaviour of the norm of the 'stress enhancement' $||\boldsymbol{S}^{enh}||$ using a classical/reformulated Neo-Hooke model: a) low & b) high resolution

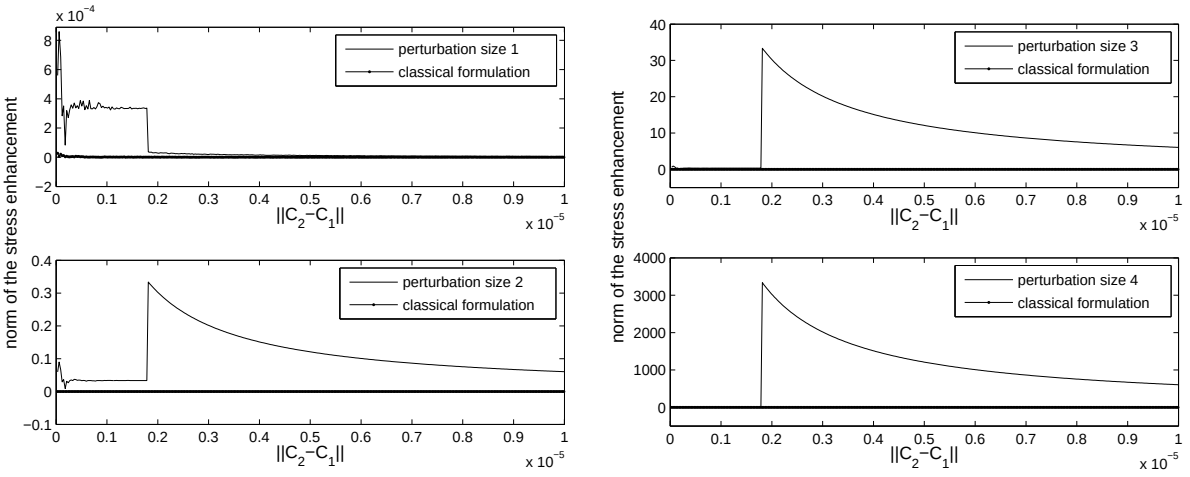

Figure 4.6.: numerical limit behaviour of the norm of the 'stress enhancement' $||\boldsymbol{S}^{enh}||$: influence of the perturbation size

in Figure 4.5 and it demonstrates impressively the potential pitfalls if the 'stress enhancement' is combined with an eigenvalue-based constitutive model. In contrast to the classical formulation, the eigenvalue-based formulation yields crucial numerical problems for the limit transition, even when we consider a low resolution, compare Figure 4.5 a). Thereby, the unphysical 'singularity-like' behaviour is strongly influenced by the applied perturbation technique and leads already for $||\Delta \boldsymbol{C}|| = \mathcal{O}(10^{-2})$ to significant errors which can no longer be neglected. On the one hand, such a numerical limit behaviour is absolutely unacceptable concerning an application in the framework of a robust time-stepping scheme. On the other hand, a switch-off of the 'stress enhancement' within a range of $||\Delta \boldsymbol{C}|| \leq \mathcal{O}(10^{-2})$ would completely destroy the required energy conservation properties. A further crucial aspect is the significant sensitivity with respect to the perturbation size, compare Figure 4.6. The errors range from the order of magnitude $\mathcal{O}(10^{-4})$ to $\mathcal{O}(10^{3})$ and increase drastically for stiffer material parameters. For these computations, the 'perturbation sizes 1-4' $\delta = 10^{-7}$, 10^{-5}, 10^{-4}, 10^{-3}, the material parameters $\lambda = 10000, \mu = 5000$, and the deformation parameters (4.36) have been applied. Once more, the 'singularity-like' behaviour can be clearly seen for each perturbation size, whereby in particular the application of larger sizes leads to immense errors. Additionally, the numerical behaviour close to zero is dominated by an unphysical 'offset' which also depends strongly on the applied perturbation size in the case of coincident eigenvalues, compare Figure 4.6.
All these numerical artefacts result, together with the abovementioned oscillations, in an interim disqualification of the perturbation-based evaluation of the eigenbases in the context of the non-standard quadrature rule (4.26), since it will be shown that the numerical limit behaviour has a direct influence on the obtained numerical and mechanical performance of the resulting time-stepping scheme, especially in the case of mechanically

stiff systems.

Remark 4.3: Please note, that the foregoing numerical artefacts are of entirely different nature compared to the 'basic properties' discussed in the previous section. In fact, the numerical oscillations investigated in Section 4.3.1 are the direct consequence of 'round-off' errors which are always present when dealing with numerical manipulations, independently whether the constitutive model is formulated in invariants or principal stretches. However, these 'spurious' oscillations are in general uncritical regarding the performance of corresponding time-stepping algorithms, as already mentioned. To the contrary, the 'key properties' of this section, which represent the focal issue of the present chapter, are directly caused by an inappropriate evaluation of the 'stress enhancement' when using the perturbation technique for the algorithmic treatment of eigenvalue-based constitutive laws. Actually, the resulting numerical errors are several orders of magnitude higher and add to the basic round-off errors.

4.4. Enhancement and Principal Stretches – Remedy

In Section 4.1.2, we have outlined the advantages of the well-established perturbation technique for a constitutive law which is formulated in principal stretches. Unfortunately, this approach has been disqualified in Section 4.3.2 concerning an application within the concept of the 'stress enhancement', due to severe numerical difficulties. These are strongly influenced, in general, by the applied stiffness and, in the case of coincident eigenvalues, by the chosen perturbation size. In this section, an adequate solution of the numerical problems – the remedy – will be presented that enables a robust and efficient evaluation of the 'stress enhancement' based on the perturbation technique, independently of the stiffness or the chosen perturbation size.

4.4.1. Overall concept – Mixed strategy

To achieve a robust evaluation of the 'stress enhancement', its numerical limit behaviour must be decoupled from the perturbation in the case of coincident eigenvalues. To accomplish such a decoupling, a 'mixed strategy' is proposed for the evaluation of the 'stress enhancement' [3]. This strategy implies a computation of some variables based on perturbed and other variables based on the unperturbed eigenvalues. Specifically, the stresses will be evaluated by means of perturbed eigenvalues, in contrast to the Helmholtz energy density which should be calculated based on unperturbed principal

[3] Moreover, it will be demonstrated in Section 4.5 that the proposed 'mixed strategy' represents, especially within a conserving time-stepping scheme, the only adequate evaluation concept regarding the obtained numerical and mechanical performance respectively.

stretches. Consequently, the enhanced algorithmic stress tensor is given by

$$\boldsymbol{S}^{alg}(1/2) := \boldsymbol{S}^{\delta}_{1/2} + \frac{2\left[\psi_{\alpha=1} - \psi_{\alpha=0}\right] - \boldsymbol{S}^{\delta}_{1/2} : [\boldsymbol{C}_2 - \boldsymbol{C}_1]}{||\boldsymbol{C}_2 - \boldsymbol{C}_1||^2}[\boldsymbol{C}_2 - \boldsymbol{C}_1]\,, \tag{4.37}$$

wherein the perturbation-based variables are denoted by $[\bullet]^{\delta}$. Hereby, this strategy is strongly motivated by the results of Section 4.3.2 which have clearly indicated that the 'stress enhancement' is very sensitive regarding the numerical evaluation of the scalar-valued energy density ψ. In this context, the application of numerically perturbed principal stretches within the Helmholtz energy density leads apparently to an artificial value that does not match sufficiently with the actual stress state, being amplified in the 'stress enhancement' during the limit transition $||\Delta\boldsymbol{C}|| \to 0$. To study the functioning of the foregoing mixed evaluation concept for Equation (4.37) in more detail, the difference between the results of a classical formulation in invariants and the reformulation based on principal stretches is investigated next, isolating the decisive influence of the perturbation on the numerical limit behaviour of the 'stress enhancement' [4]. The results are shown in Figure 4.7 and Figure 4.8, using a Neo-Hooke model with the same deformation and material parameters as introduced in Section 4.3.2. Therein, it can be clearly seen that indeed the evaluation of the Helmholtz energy densities with perturbed eigenvalues results in an offset caused by the involved perturbation size, see Figure 4.8 a). Hereby, not the magnitude of the offset itself, but the resulting influence on the numerical limit behaviour of the 'stress enhancement' represents the actual issue. Considering the components of $\boldsymbol{S}^{enh}$ pictured in Figure 4.8 b), in fact, it renders strong deviations from the classical formulation, being in the range of 10^1 for the present example. Please note, that the corresponding numerical artefacts are obviously several orders of magnitude higher than the uncritical differences within the continuum stresses or the related scalar product, plotted in Figure 4.7 a) and Figure 4.7 b) respectively. However, this crucial numerical behaviour can be completely removed, simply by evaluating the Helmholtz energy density with unperturbed eigenvalues. In this case, the causing offset within the energy densities vanishes and, consequently, the resulting aberrations in the components of the 'stress enhancement' are resolved as well, as can be seen in Figure 4.8.
To demonstrate furthermore the effectiveness of the advocated concept concerning the claimed decoupling of the numerical limit performance from the specific size of the applied perturbation, we consider once more the norm of the 'stress enhancement' and recalculate the results of Section 4.3.2, shown in Figure 4.6, by using this time the proposed 'mixed strategy'. Analogously to this previous section, the perturbation sizes

[4] More precisely, we calculate for each quantity of interest $\left[\,\bullet\,\right]$ the difference

$$\Delta[\bullet] := [\bullet]^{principal} - [\bullet]^{classical} \tag{4.38}$$

as a function of $||\boldsymbol{C}_2 - \boldsymbol{C}_1||$, considering separately the Piola-Kirchhoff stresses $\boldsymbol{S}^{\delta}_{1/2}$, the entire 'stress enhancement' $\boldsymbol{S}^{enh}$, the difference of the Helmholtz energy densities $\psi_{\alpha=1} - \psi_{\alpha=0}$, and the scalar product $\boldsymbol{S}^{\delta}_{1/2} : [\boldsymbol{C}_2 - \boldsymbol{C}_1]$ concerning the transition $\boldsymbol{C}_2 \to \boldsymbol{C}_1$.

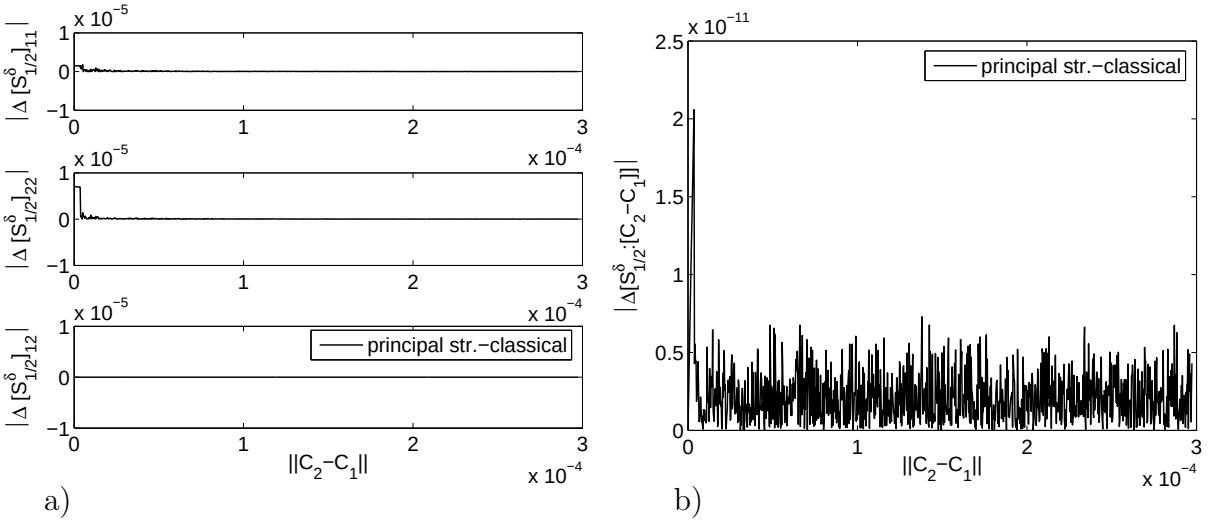

Figure 4.7.: classical formulation vs. reformulation in principal stretches (Neo-Hooke model): absolute value of the difference $|\Delta[\,\bullet\,]|$ considering a) components of the continuum stresses $[\bullet] := [\boldsymbol{S}^{\delta}_{1/2}]_{ij}$, b) $[\bullet] := [\boldsymbol{S}^{\delta}_{1/2} : [\boldsymbol{C}_2 - \boldsymbol{C}_1]]$

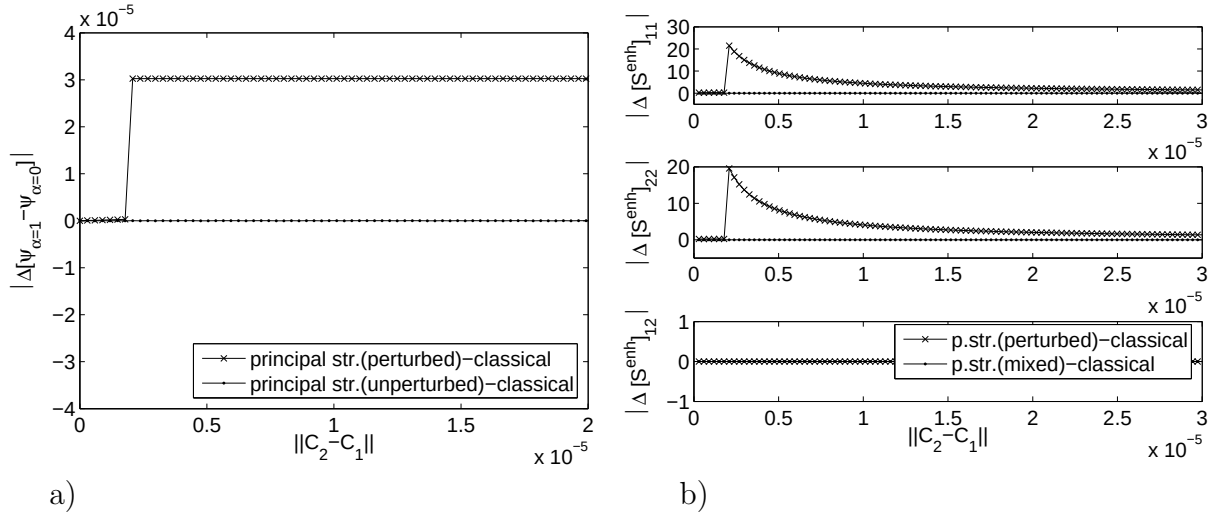

Figure 4.8.: classical formulation vs. reformulation in principal stretches (Neo-Hooke model): absolute value of the difference $|\Delta[\,\bullet\,]|$ considering a) $[\bullet] := [\psi_{\alpha=1} - \psi_{\alpha=0}]$, b) components of the 'stress enhancement' $[\bullet] := [\boldsymbol{S}^{enh}]_{ij}$

$\delta = 10^{-7}$, 10^{-5}, 10^{-4}, 10^{-3} have been incorporated for these computations, relying on Equation (4.36) and unchanged material parameters. The results for 'perturbation size 1-4' are shown in Figure 4.9. Primarily, it can be clearly seen that the sensitivity of the numerical limit performance of the norm of the 'stress enhancement' is nearly remedied. Furthermore, the numerical errors are conspicuously reduced and do not exceed the order of magnitude $\mathcal{O}(10^{-4})$ in the worst case. For comparison, this limit is equivalent to

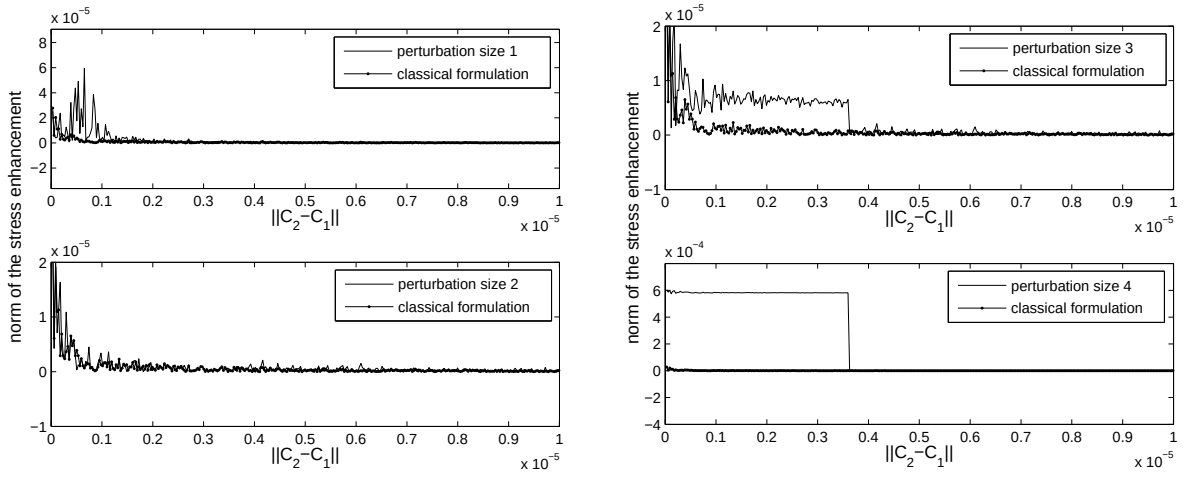

Figure 4.9.: numerical limit behaviour of the norm of the 'stress enhancement' $||\boldsymbol{S}^{enh}||$ calculated by means of the 'mixed strategy': influence of the perturbation size

the best result using exclusively the perturbed eigenvalues, see Figure 4.6. Moreover, it is remarkable that for 'perturbation size 2' with $\delta = 10^{-5}$ the numerical performance of the eigenvalue-based reformulation is absolutely competitive to the classical formulation of the Neo-Hooke constitutive model and nearly no differences are visible. Additionally, it is obvious that the 'singularity-like' behaviour has been basically caused by the evaluation of the Helmholtz energy density based on perturbed eigenvalues. Nevertheless, some numerical artefacts, like the 'offset' close to zero, persist if the perturbation size is too large. However, it will be subsequently shown that this remaining influence of the perturbation size is insignificant for the application within the framework of a time-stepping scheme. In fact, this influence does not pose further problems and, consequently, the required decoupling is achieved.

Remark 4.4: When compressible material behaviour is considered, the function $U(J)$ is involved, compare Equations (4.9)-(4.11). Thereby, the evaluation of the determinant J by means of perturbed eigenvalues is not crucial, since in the triple product of the eigenvalues the perturbations erase themselves, compare Equations $(4.21)_{1,2,3}$.

4.4.2. Assessment – Constitutive models

So far, a reformulated Neo-Hooke model served for our investigations to demonstrate the potential pitfalls based on numerical artefacts and to propose an appropriate solution strategy, illustrating directly the influence of the eigenvalue-based format in comparison to the classical formulation. In this section, we extend these elaborations with respect to other constitutive laws which are usually formulated in principal stretches, like the

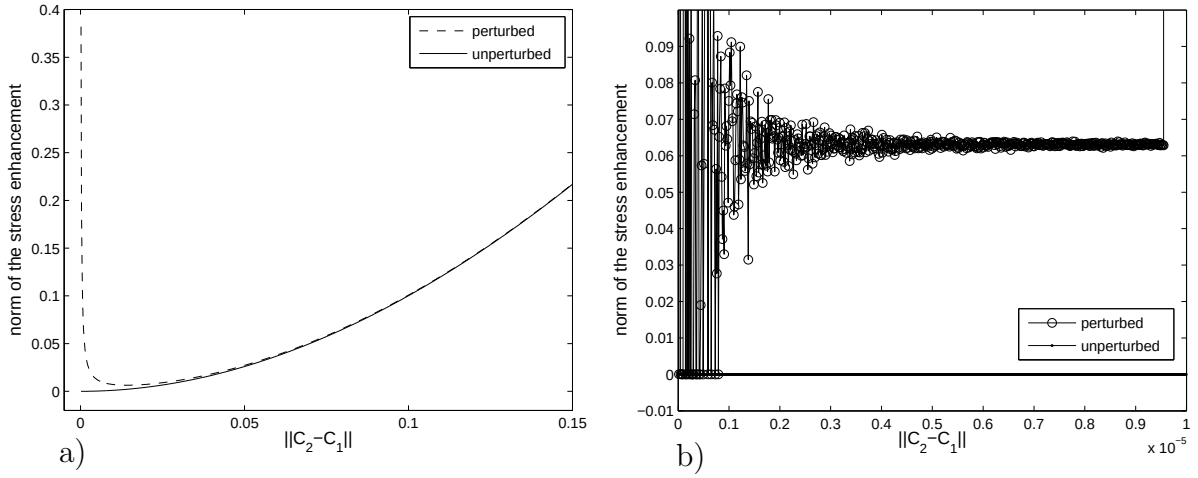

Figure 4.10.: numerical limit behaviour of the norm of the 'stress enhancement' $||\boldsymbol{S}^{enh}||$ using a Neo-Hooke model (perturbed/unperturbed evaluation of ψ): a) low & b) high resolution

Ogden or the Hencky model, compare Equation (4.10) and Equation (4.11) respectively. Thereby, the 'mixed strategy' will be applied for the abovementioned constitutive models and directly assessed in comparison to a perturbed evaluation of the Helmholtz energy density. We start once more with the reformulated Neo-Hooke model, incorporating the material parameters $\lambda = 10000$ and $\mu = 5000$. In this case, the local deformation process can be specified by

$$\boldsymbol{F}_1 \equiv \begin{bmatrix} 1.1 & 0 \\ 0 & 1 \end{bmatrix} \qquad \text{and} \qquad \boldsymbol{D} \equiv \begin{bmatrix} -10 & 100 \\ 0 & 10 \end{bmatrix} . \tag{4.39}$$

The differences between the 'mixed strategy' and the (completely) perturbed evaluation of the 'stress enhancement' are impressively displayed by the results shown in Figure 4.10. The naive evaluation of the Helmholtz energy density by means of perturbed eigenvalues results again in a crucial 'singularity-like' behaviour for coincident eigenvalues, whereby it is important to emphasise that the deviations are already visible for $||\Delta \boldsymbol{C}|| = \mathcal{O}(10^{-2})$, compare Figure 4.10 a). Consequently, a switch-off of the 'stress enhancement' to circumvent the numerical difficulties is absolutely out of the question with regard to the required conservation properties. Furthermore, the 'offset' accompanied by strong oscillations occurs close to zero, see Figure 4.10 b). Contrariwise, the application of the proposed 'mixed strategy', related to an unperturbed evaluation of ψ, renders the claimed numerical limit performance of the 'stress enhancement', unaffected by possibly coinciding eigenvalues. For the next eigenvalue-based constitutive law, a model of Ogden-type with the specific function

$$U(J) = -[\mu_1 + \mu_2 + \mu_3] \ln(J) \tag{4.40}$$

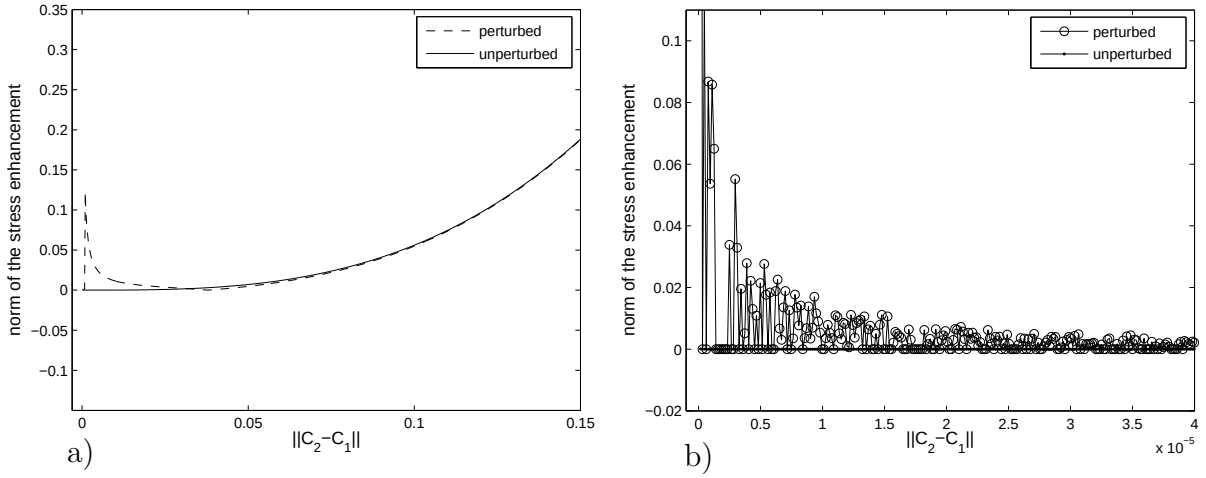

Figure 4.11.: numerical limit behaviour of the norm of the 'stress enhancement' $||\boldsymbol{S}^{enh}||$ using an Ogden model (perturbed/unperturbed evaluation of ψ): a) low & b) high resolution

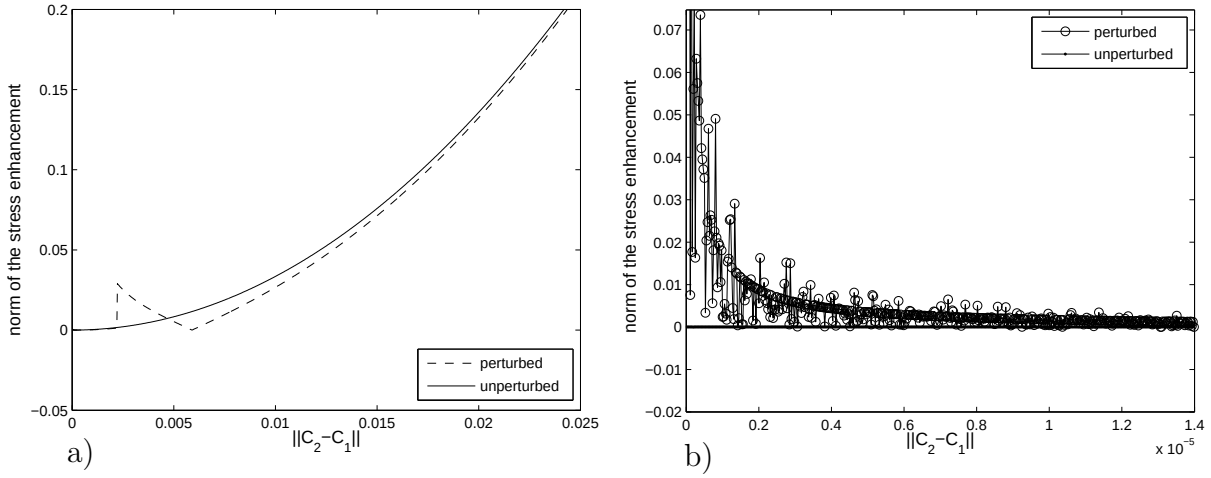

Figure 4.12.: numerical limit behaviour of the norm of the 'stress enhancement' $||\boldsymbol{S}^{enh}||$ using a Hencky model (perturbed/unperturbed evaluation of ψ): a) low & b) high resolution

has been chosen, using the parameters $\mu_1 = 10000$, $\mu_2 = 1000$, $\mu_3 = -1000$ and $\alpha_1 = 1.3$, $\alpha_2 = 4.0$, $\alpha_3 = -2.0$. The initial deformation gradient and the deformation type for the following calculations are given by

$$\boldsymbol{F}_1 \equiv \begin{bmatrix} 1.1 & 0 \\ 0 & 1 \end{bmatrix} \qquad \text{and} \qquad \boldsymbol{D} \equiv \begin{bmatrix} 0 & 10 \\ 0 & 0 \end{bmatrix}. \tag{4.41}$$

Analogously to the reformulated Neo-Hooke model, the transition $||\Delta \boldsymbol{C}|| \to 0$ is characterised by an unphysical peak in the order of magnitude $\mathcal{O}(10^{-1})$ if a perturbed evalua-

tion of the Helmholtz energy density is applied, compare Figure 4.11. Additionally, the norm of the 'stress enhancement' is superimposed by strong oscillations close to zero, but in this case without a distinct numerical 'offset', see Figure 4.11 b). Again, the 'mixed strategy' removes all these numerical artefacts and enables an excellent limit behaviour. For the last constitutive model formulated in principal stretches, a Hencky model with

$$U(J) = \frac{\lambda}{2} \ln^2(J) \tag{4.42}$$

shall be considered. Concerning the deformation process, we have used

$$\boldsymbol{F}_1 \equiv \begin{bmatrix} 1 & 0 \\ 0 & 1.2 \end{bmatrix} \qquad \text{and} \qquad \boldsymbol{D} \equiv \begin{bmatrix} 0 & 1 \\ 0 & -1 \end{bmatrix}, \tag{4.43}$$

whereby the applied material parameters are given by $\lambda = 10000$, $\mu = 5000$. Considering Figure 4.12, the norm of the 'stress enhancement' calculated exclusively based on perturbed eigenvalues shows once more severe numerical errors for the limit transition, especially if $||\Delta \boldsymbol{C}|| \in [10^{-3}, 10^{-2}]$. Similarly to the Ogden model, the behaviour of the norm of the 'stress enhancement' is dominated by substantial oscillations close to zero if the perturbed eigenvalues are inserted in the Helmholtz energy density, see Figure 4.12 b). However, the 'mixed strategy' enables, even in the case of coincident eigenvalues, an absolutely non-critical limit transition $||\Delta \boldsymbol{C}|| \to 0$.
In this section, we have demonstrated that the potential numerical problems concerning the limit behaviour of the enhancement, which basically rely on the combination of the 'stress enhancement' and a perturbation-based evaluation of an eigenvalue-based constitutive model, can be completely solved by using the 'mixed strategy', introduced in Equation (4.37). This evaluation strategy enables the efficient application of the general perturbation technique also in the context of the 'stress enhancement' without additional numerical effort. Thereby, the effectiveness of the 'mixed strategy' has been verified for different eigenvalue-based constitutive laws on a local level. Apart from these investigations referring to the so-called local level, or rather homogeneous deformations, we next address resulting consequences on the global time-integration when embedding the proposed concept into a (conserving) Galerkin-based time-stepping scheme, compare Equations (4.24)-(4.27).

Remark 4.5: Initially, the suggested 'mixed strategy' has been developed for the favoured format (4.27). However, as already mentioned, there exist several other concepts or divers modifications in literature to guarantee the fulfilment of required conservation properties by the resulting time-stepping schemes. In this context, we suppose that also alternative stress enhancements of type

$$\boldsymbol{S}^{alg} = \boldsymbol{S}_{1/2} + \frac{2\left[\psi_{\alpha=1} - \psi_{\alpha=0}\right] - \boldsymbol{S}_{1/2} : [\boldsymbol{C}_2 - \boldsymbol{C}_1]}{\boldsymbol{A} : [\boldsymbol{C}_2 - \boldsymbol{C}_1]} \boldsymbol{A} \tag{4.44}$$

would benefit in general from the advocated strategy. Obviously, Equation (4.44) recaptures also the preferred format (4.27) by setting $\boldsymbol{A} := [\boldsymbol{C}_2 - \boldsymbol{C}_1]$. In this context, a particularly interesting formulation has been recently discussed in Bui [46] for the specific case $\boldsymbol{A} := \boldsymbol{S}_{1/2}$, rendering

$$\boldsymbol{S}^{alg} = \boldsymbol{S}_{1/2} + \frac{2\,[\psi_{\alpha=1} - \psi_{\alpha=0}] - \boldsymbol{S}_{1/2} : [\boldsymbol{C}_2 - \boldsymbol{C}_1]}{\boldsymbol{S}_{1/2} : [\boldsymbol{C}_2 - \boldsymbol{C}_1]}\, \boldsymbol{S}_{1/2}\,. \tag{4.45}$$

Interestingly, the particular enhancement used in Equation (4.45) preserves the principal directions of $\boldsymbol{S}_{1/2}$ and can be interpreted as a modification of the integration weights of the involved quadrature rule, as proposed by French and Schaeffer [57]. In the following, we present exemplarily some basic investigations concerning the potential influence of eigenvalue-based constitutive laws on the foregoing formulation (4.45). Regarding the resulting numerical limit behaviour of the corresponding enhancement, the influence of the applied evaluation strategy will be demonstrated analogously to Section 4.3.2, using the same local deformation state and material parameters. Some results are shown in Figure 4.13-4.16 [5]. Using a classical Neo-Hooke model formulated directly in $\boldsymbol{C}$, the basic oscillations within the 'enhancement scaling factor', which is introduced analogously to Equation (4.28), are significantly reduced in the 'scaled stress' case. Nevertheless, the oscillations within the norm of the 'stress enhancement', which are more meaningful regarding the overall behaviour of the enhancement, are in the same order of magnitude for both formulations, see Figure 4.13. As already discussed, the key issue is the fundamental degradation of the numerical limit behaviour when perturbed eigenvalues are, in addition to the stress computation, also used to calculate the Helmholtz energy density. This effect is also present in the 'scaled stress' case, as demonstrated in Figure 4.14 based on a reformulation of the classical Neo-Hooke model by using principal stretches. However, the proposed mixed evaluation strategy works effectively also for the formulation (4.45) and avoids efficiently additional numerical artefacts, see Figure 4.15 regarding the 'enhancement scaling factor' and Figure 4.16 regarding the norm of the 'stress enhancement'. The foregoing investigations confirm our initial guess, at least for the here considered local example. Nevertheless, the actual numerical performance and, particularly, the interaction with a global conserving time-stepping scheme would require further investigations. However, we suggest an application of the proposed 'mixed strategy' in any case, since it requires only a simple modification without any additional costs. In fact, the numerical behaviour of general 'stress enhancements' of type (4.44) can only benefit from this remedy.

[5] In this context, the results of the calculations based on Equation (4.45) will be referred to as 'scaled stresses', in contrast to the results of computations relying on the preferential formulation (4.27) which are denoted as 'scaled strains'.

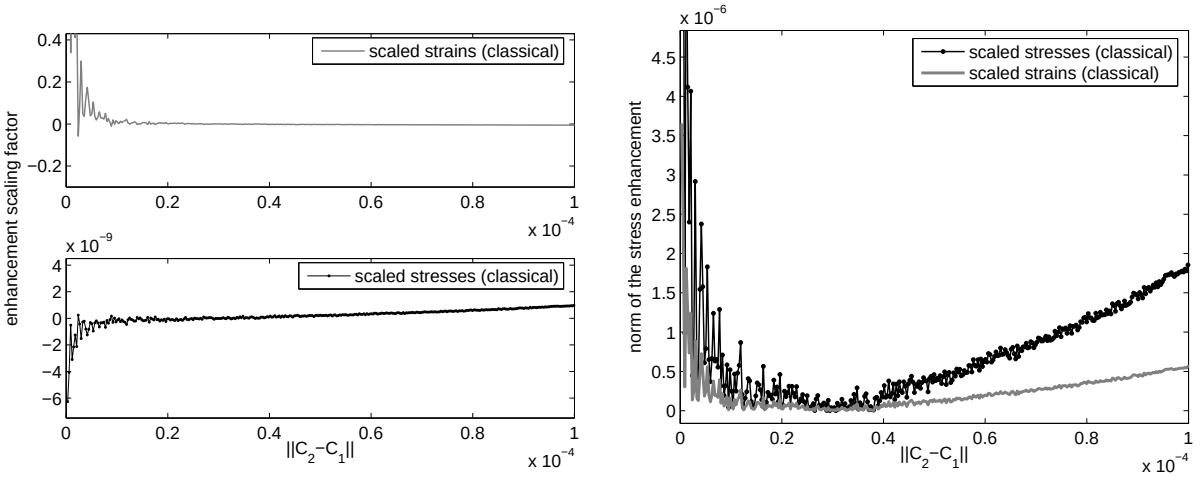

Figure 4.13.: numerical limit behaviour (high resolution, classical Neo-Hooke model) of: a) 'enhancement scaling factor' Ω, b) norm of the 'stress enhancement' $||\boldsymbol{S}^{enh}||$

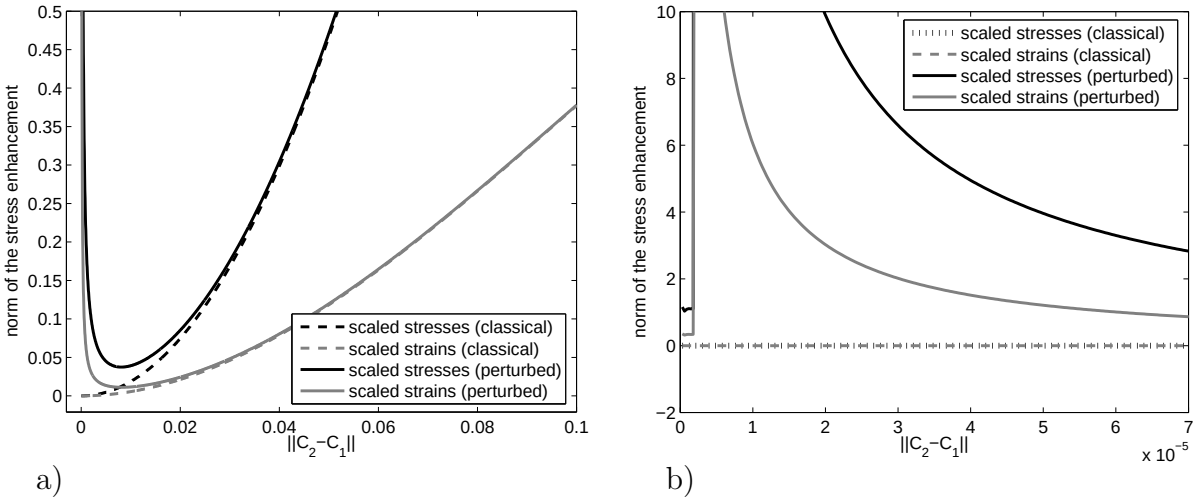

Figure 4.14.: numerical limit behaviour of the norm of the 'stress enhancement' $||\boldsymbol{S}^{enh}||$: a) low & b) high resolution

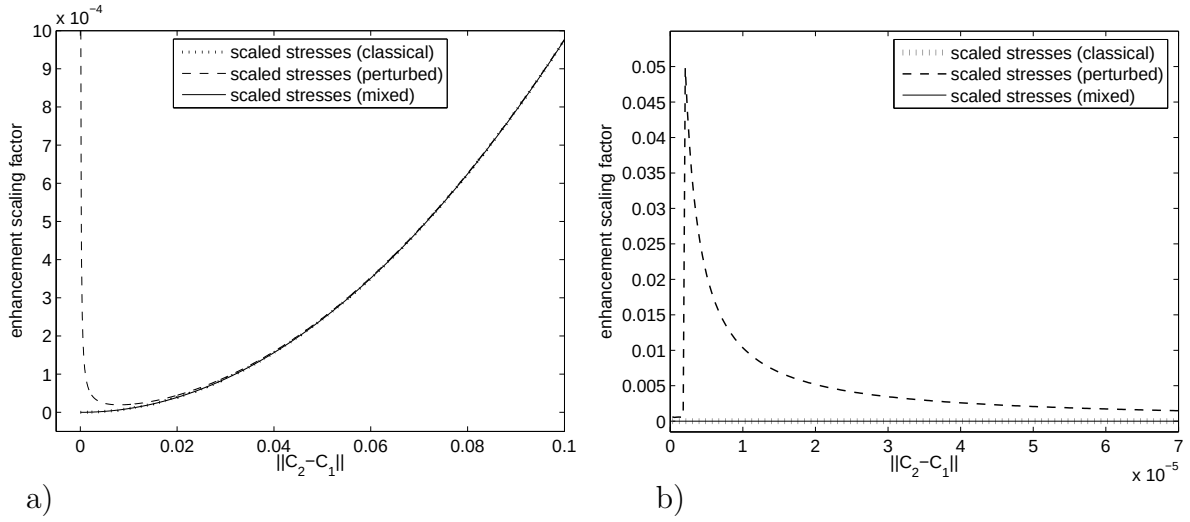

Figure 4.15.: numerical limit behaviour of the 'enhancement scaling factor' Ω (classical vs. eigenvalue-based Neo-Hooke model (perturbed/mixed strategy)): a) low & b) high resolution

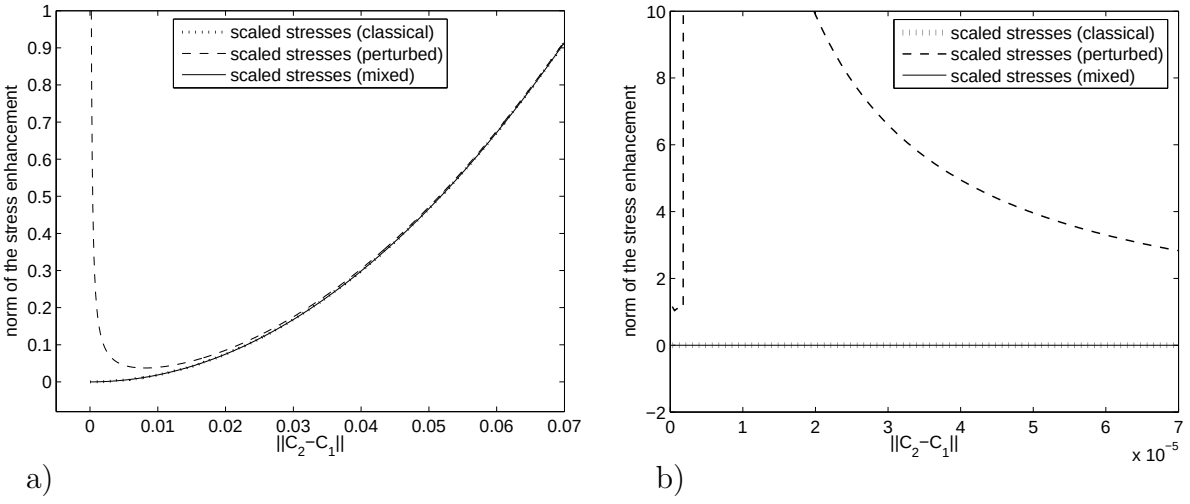

Figure 4.16.: numerical limit behaviour of the norm of the 'stress enhancement' $||\boldsymbol{S}^{enh}||$ (classical vs. eigenvalue-based Neo-Hooke model (perturbed/mixed strategy)): a) low & b) high resolution

4.5. Enhancement and Principal Stretches – Consequences

In the previous sections, the investigations have been restricted to a local level, representing one single integration point in space, based on particular prescribed deformation states and different deformation types, see Equation (4.30). Thus, the described pitfalls seem, at first glance, not to pose an actual problem concerning the implementation within a mechanical integrator. To prove the contrary, the non-negligible influence of the pitfalls and the effectiveness of the solution strategy, regarding the numerical as well as the mechanical performance of the time-stepping scheme, will be presented in this section. Moreover, it will be shown that the cruxes of the local considerations, like stiffness or independency of the perturbation size, are also relevant on the global time-integration level.

To demonstrate the resulting consequences, we consider the motion of a 'Flying Frame' calculated by a consistent Galerkin-based integrator (with $k = 1$), involving the non-standard quadrature rule (4.26). The frame with the mass density $\rho = 1.0$ is discretised in space (2d, plane strain conditions) using 48 isoparametric 4−node elements and exhibits an initial velocity $\bar{\boldsymbol{v}}_0$ in the horizontal direction with $||\bar{\boldsymbol{v}}_0|| = 85$. Furthermore, some external shear loads $\bar{\boldsymbol{F}}^{ext} := [\boldsymbol{F}^{ext}_1, ..., \boldsymbol{F}^{ext}_{n_{node}}]^{\mathrm{t}}$ have been applied, whereby the norm of the external load $||\boldsymbol{F}^{ext}_I|| = f(t)$ at the spatial node I increases linearly in time up to the maximum value f_{max} and, subsequently, decreases again linearly to zero within the loading period $t \in [0, T_{load}]$, compare Figure 4.17 a). In the following examples, the constitutive relation relies on a Helmholtz energy density ψ of the Hencky-type (compare Equation (4.11)), using once more $U(J) = \frac{\lambda}{2}\ln^2(J)$. A characteristic sequence of

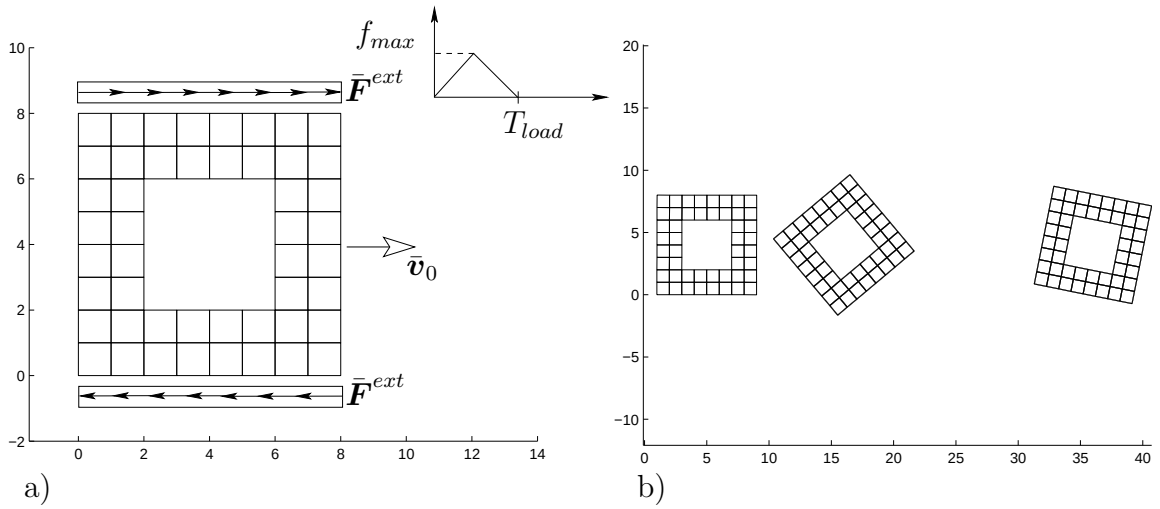

Figure 4.17.: a) initial configuration $\mathcal{B}_0$ of the 'Flying Frame' with external loads and loading history, b) characteristic sequence of the motion

the motion of the 'Flying Frame', represented by three deformed configurations $\mathcal{B}_t$, is pictured in Figure 4.17 b).

4.5.1. Numerical performance

First, we focus on the consequences for the numerical performance of the resulting time integrator. In this context, the number of iterations, which are required per time step, seems to be a candid measure for the provided convergence properties. To investigate the resulting numerical problems, which are directly related to the aforementioned pitfalls on the local level, the proposed 'mixed strategy' will be compared with the 'completely perturbed' and a 'completely unperturbed' evaluation of the 'stress enhancement'. For the first example, we have applied the parameters $f_{max} = 10.0$, $T_{load} = 1.0$, $\lambda = 10000$, and $\mu = 5000$. To confirm the correlation between the global numerical performance and the local problems, the influence of the applied time-step size will be examined. A reduction of the time-step size results (for given material parameters and loading conditions) in a decreasing difference of two sequent deformation states and, consequently, in a decrease of $||\Delta \boldsymbol{C}||$. As demonstrated on the local level, such a decrease can be accompanied by several numerical artefacts, especially, if an inappropriate strategy for the evaluation of the 'stress enhancement' has been chosen. For the present computations, the time-step sizes $h_n \in \{0.2, 0.005, 0.0001\}$ have been applied. The deformed configuration at $t = 20$ calculated with $h_n = 0.2$ can be seen in Figure 4.18 a). Figure 4.18 b) shows for each time-step size h_n the required iterations per time step for the case that the stresses as well as the Helmholtz energy density are both computed based on unperturbed eigenvalues ('completely unperturbed strategy'). As expected, the performance strongly depends on the applied time-step size and small time-step sizes obviously lead to significant convergence problems of the global iteration scheme. An evaluation of the stresses and the Helmholtz energy density with perturbed eigenvalues ('completely perturbed strategy') is not able to remove the difficulties. Moreover, this approach even degrades the resulting numerical performance, especially for $h_n = 0.0001$, and a calculation with small time-step sizes is in this case almost impossible, compare Figure 4.19 a). Contrariwise, the application of the proposed 'mixed strategy', characterised by a perturbed evaluation of the stresses combined with an unperturbed evaluation of the Helmholtz energy density, remedies the convergence problems and enables an efficient calculation that is (nearly) independent of the applied time-step size, as pictured in Figure 4.19 b).

As illustrated on the local level, the mechanical stiffness of the considered problem is a further relevant parameter regarding the numerical limit behaviour of the 'stress enhancement'. Additionally, an increasing stiffness naturally implies smaller differences $\Delta \boldsymbol{C}$ for given loading conditions. Consequently, the numerical performance of the global time-integration might also be affected by the stiffness. To investigate the relevance of the evaluation strategy, the 'mixed strategy' will be compared once more with the 'completely (un)perturbed strategy', incorporating the parameters $f_{max} = 10.0$, $T_{load} = 1.0$, and $h_n = 0.1$. Furthermore, 'stiffness 1-3' is related to $[\lambda, \mu] = [1000, 500], [10000, 5000]$,

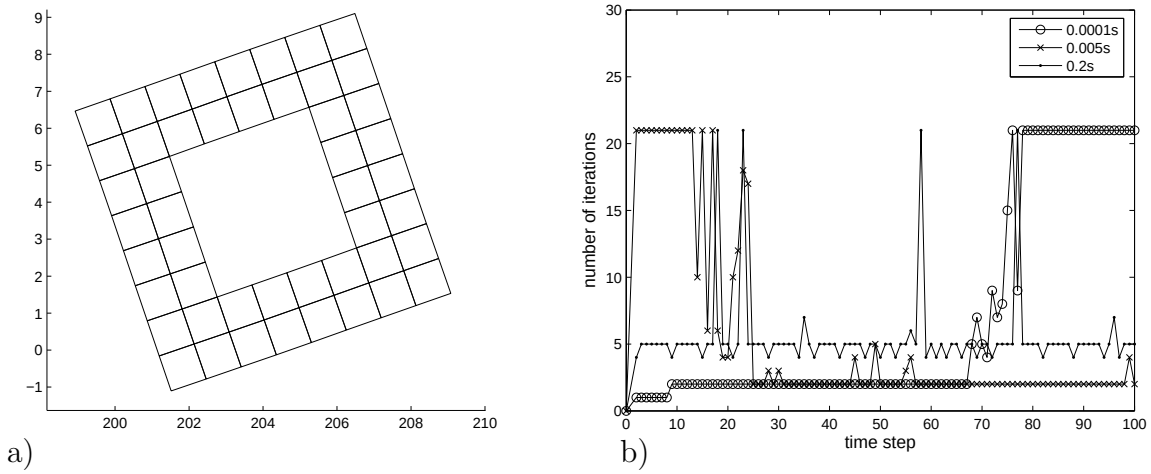

Figure 4.18.: a) deformed configuration $\mathcal{B}_t$ at $t = 20$ using $h_n = 0.2$, b) number of iterations per time step (influence of the time-step size): 'completely unperturbed strategy'

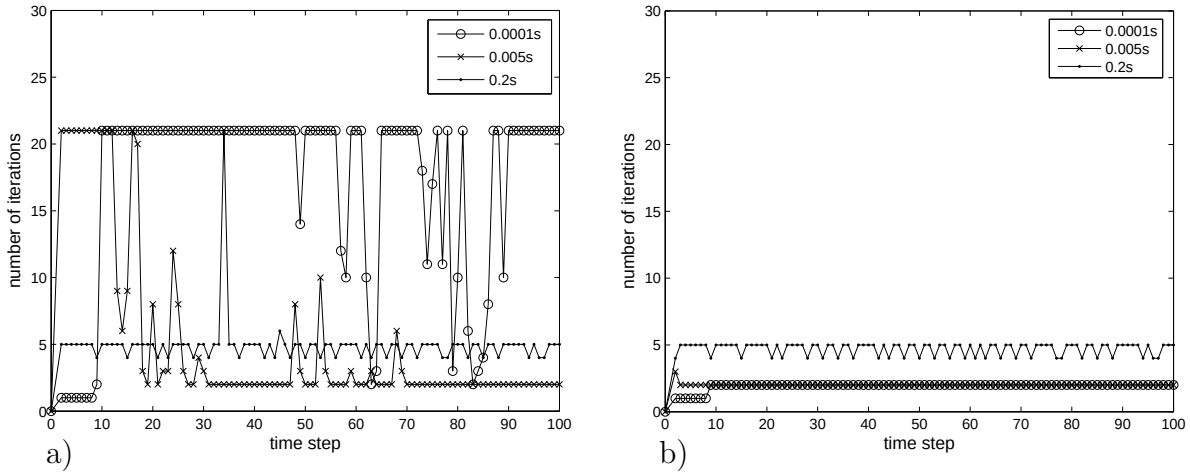

Figure 4.19.: number of iterations per time step (influence of the time-step size): a) 'completely perturbed strategy', b) 'mixed strategy'

and [100000, 50000] respectively. The corresponding deformed configurations at the time $t = 10$ are shown in Figure 4.20 a). An application of the 'completely unperturbed strategy' results in a substantial lack of convergence for mechanically stiff problems, compare Figure 4.20 b). If the 'completely perturbed strategy' is used, even a program abort [6] due to divergence of the global iteration scheme occurs for 'stiffness 3', as can be seen in Figure 4.21 a). However, the 'mixed strategy' represents once more an adequate

[6] A program abort within the calculations related to numerical problems is pictured by means of a vertical dashed line in the plots.

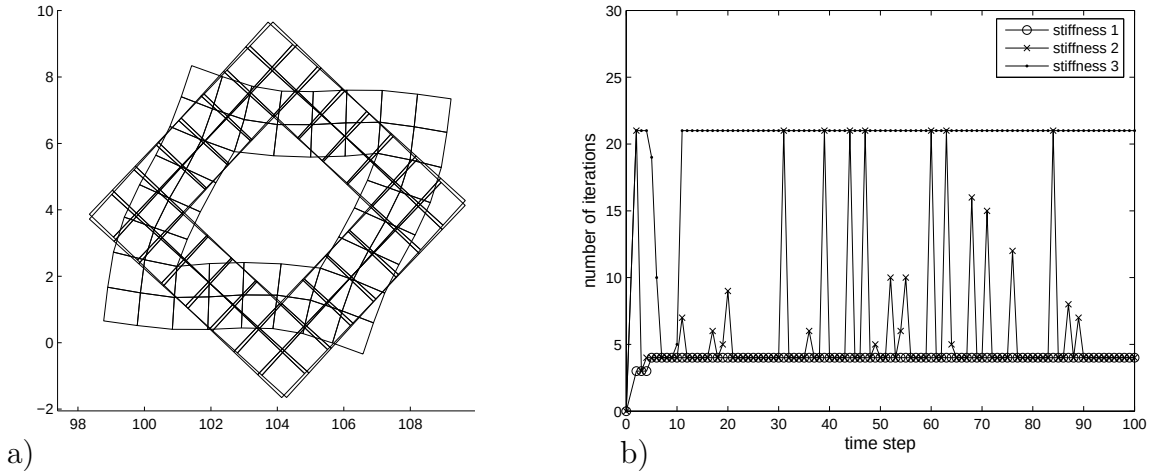

Figure 4.20.: a) deformed configurations $\mathcal{B}_t$ at $t = 10$ for 'stiffness 1-3', b) number of iterations per time step (influence of the stiffness): 'completely unperturbed strategy'

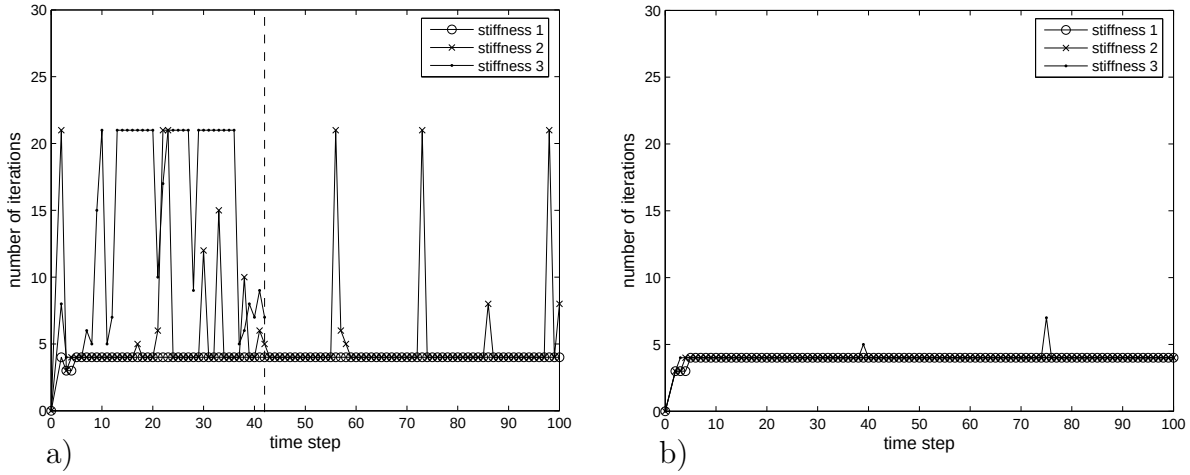

Figure 4.21.: number of iterations per time step (influence of the stiffness): a) 'completely perturbed strategy', b) 'mixed strategy'

remedy to circumvent numerical problems which are induced by the resulting sensitivity of the time-stepping scheme with respect to mechanical stiffness. In Figure 4.21 b), it is clearly shown that the proposed evaluation strategy enables, independently of the applied stiffness, an efficient calculation. The presented results clearly confirm the fact that an increasing stiffness amplifies the potential numerical artefacts of the 'stress enhancement'. This effect is already known from the investigations on the local level (compare Figure 4.4) and can be completely tackled by the application of the 'mixed strategy'.

Remark 4.6: The results presented in this section have clearly demonstrated that an inadequate evaluation strategy can cause crucial numerical problems for the global time-integration, especially, if small time-step sizes and mechanically stiff problems are taken into account. Vice versa, non-stiff problems cover possible convergence problems. Consequently, the motion of nearly rigid bodies poses the real challenge for conserving time-stepping schemes which rely on the enhanced algorithmic stress tensor combined with an eigenvalue-based constitutive law.

4.5.2. Mechanical performance

In this section, it will be shown that the numerical pitfalls can also considerably affect the obtained mechanical performance of the resulting time integrator. Originally, the introduction of a non-standard quadrature rule based on the 'stress enhancement' has been motivated by desired energy conservation properties. Hereby, energy conservation shall be assured within the calculation accuracy which is basically dominated by the chosen tolerance of the global iteration scheme. Once more, the results of the recommended 'mixed strategy' will be compared with the results of the 'completely (un)perturbed strategy', whereby a switching procedure [7] has been used in the following calculations, incorporating the parameters $f_{max} = 10.0$, $T_{load} = 1.0$, $h_n = 0.1$, $\lambda = 10000$, and $\mu = 5000$. The resulting deformed configuration $\mathcal{B}_t$ at $t = 10$ and the total energy H are pictured in Figure 4.22. At first glance, the conservation of the total energy seems to be unaffected by possible convergence problems induced by numerical artefacts of the 'stress enhancement'. However, visible differences between the three evaluation strategies become obvious when zooming-in. For the present examples, the application of the 'completely perturbed strategy' leads to a critical increase of the total energy and the 'completely unperturbed strategy' combined with the necessary switching procedure results in an oscillating behaviour. Contrariwise, the total energy is conserved if the 'mixed strategy' is applied, as shown in Figure 4.22 b). Inspired by the one-dimensional example in Chapter 2, compare Equation (2.36), we introduce for the purely elastic case with $D_n = D_{n+1} = 0$ the residual

$$R^{el} := H_{n+1} - H_n \stackrel{!}{=} 0\,, \tag{4.46}$$

which is of course covered inherently by the general balance (3.62) as a special case. Solely based on Equation (4.46), the mechanical performance of the time-stepping scheme, using the different evaluation strategies, can be fairly judged. The results are displayed in Figure 4.23. The 'completely unperturbed' as well as the 'completely perturbed strategy' do not allow a fulfilment of Equation (4.46) within the required tolerance. In fact, these strategies severely suffer from the numerical artefacts and degrade the potential of

[7] The switching procedure includes a switch-off of the 'stress enhancement' if the global iteration scheme does not converge within a pre-defined number of iterations.

the non-standard quadrature rule concerning the desired energy conservation, compare Figure 4.23 a). The real potential of the 'stress enhancement' can be exclusively achieved if the 'mixed strategy' is used and, consequently, the numerical problems are circumvented. For the discussed example, the application of the 'mixed strategy' enables the fulfilment of Equation (4.46) within the order of magnitude $\mathcal{O}(10^{-11})$, as displayed in Figure 4.23 b). Thus, the conservation of the total energy is guaranteed within the calculation accuracy and the actual purpose of the enhanced algorithmic stress tensor (4.27) is fulfilled.

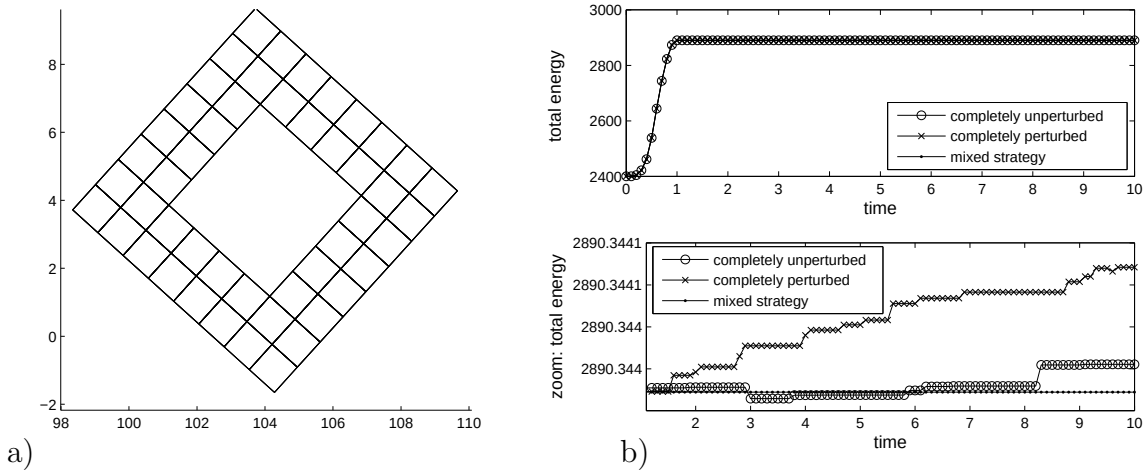

Figure 4.22.: a) deformed configuration $\mathcal{B}_t$ at $t = 10$, b) total energy H (zoom)

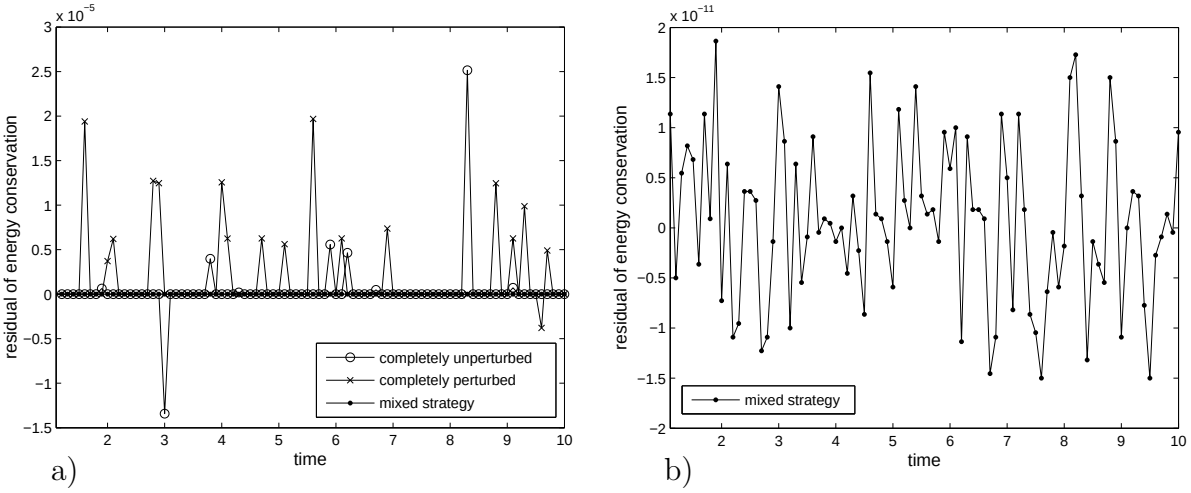

Figure 4.23.: residual of energy conservation R^{el}: a) 'completely (un)perturbed evaluation' & 'mixed strategy', b) 'mixed strategy'

4.5.3. Perturbation vs. performance

In the following, the influence of the perturbation size on the global performance of the time-stepping scheme will be investigated. In this context, the sensitivity of the numerical behaviour of the 'stress enhancement' concerning the applied perturbation size has been emphasised on the local level, compare Figure 4.6. Furthermore, the positive effect of the proposed 'mixed strategy' has been highlighted in Section 4.4.1, whereby the influence on the local numerical behaviour and the resulting decoupling from the perturbation size have been illustrated in Figure 4.9. Moreover, this positive influence is not locally restricted to a special prescribed deformation process, but it is also directly noticeable on the global level. To demonstrate the beneficial effects, the motion of the 'Flying Frame' is considered once more, using the parameters $f_{max} = 10.0$, $T_{load} = 1.0$, $h_n = 0.1$, $\lambda = 100000$, and $\mu = 50000$. The deformed configuration at $t = 5$ is pictured in Figure 4.24 a) and the successful decoupling of the perturbation size and the numerical performance of the (global) time integrator can be regarded in Figure 4.25. The required total number of iterations is completely independent of the perturbation size if the 'mixed strategy' is involved. An application of the 'completely perturbed strategy' yields a drastically increasing number of iterations which additionally depends on the perturbation size, compare Figure 4.25 a). Furthermore, it can be directly seen that the 'completely perturbed strategy' is not able at all to reach the performance of the 'mixed strategy', independently of the chosen perturbation size. Due to convergence problems in the case of the 'completely perturbed strategy', the 'stress enhancement' has been switched off after a certain number of iterations within one time step. The resulting number of steps without the 'stress enhancement' is displayed in Figure 4.25 b). Consequently, the simulation of such a mechanically stiff problem is nearly impossible applying the 'stress enhancement' combined with a completely perturbed evaluation. However, the 'mixed strategy' enables, independently of the perturbation size, an excellent numerical performance without any switch-off of the enhancement. Please recall, that the involvement of switching procedures ruins the desired energy conservation of the time integrator, as outlined in Section 4.5.2. Since the 'stress enhancement' is always active in the case of the 'mixed strategy', it can be concluded from Figure 4.24 b) that the residual of energy conservation R^{el} given by Equation (4.46) is equal to zero within the calculation accuracy, again, absolutely unaffected by the applied perturbation size. Thus, the consequences of the numerical pitfalls concerning the global time-integration have been demonstrated in this section and, moreover, the effectiveness of the proposed evaluation strategy, regarding the numerical as well as the mechanical performance of the conserving time-stepping scheme, has been confirmed.

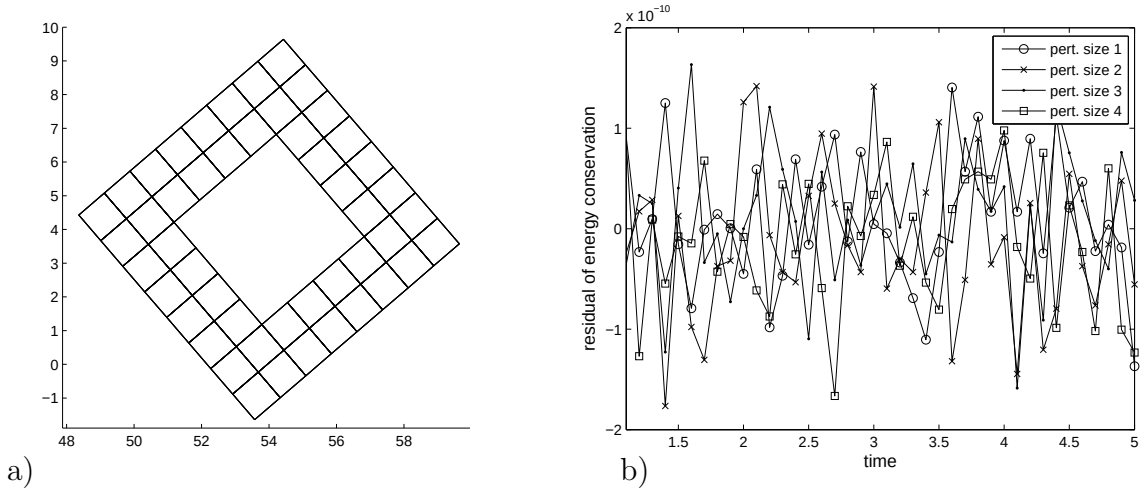

Figure 4.24.: a) deformed configuration $\mathcal{B}_t$ at $t = 5$, b) residual R^{el} for 'perturbation size 1-4' (related to $\delta = 10^{-3}$, 10^{-4}, 10^{-5}, 10^{-6}) using the 'mixed strategy'

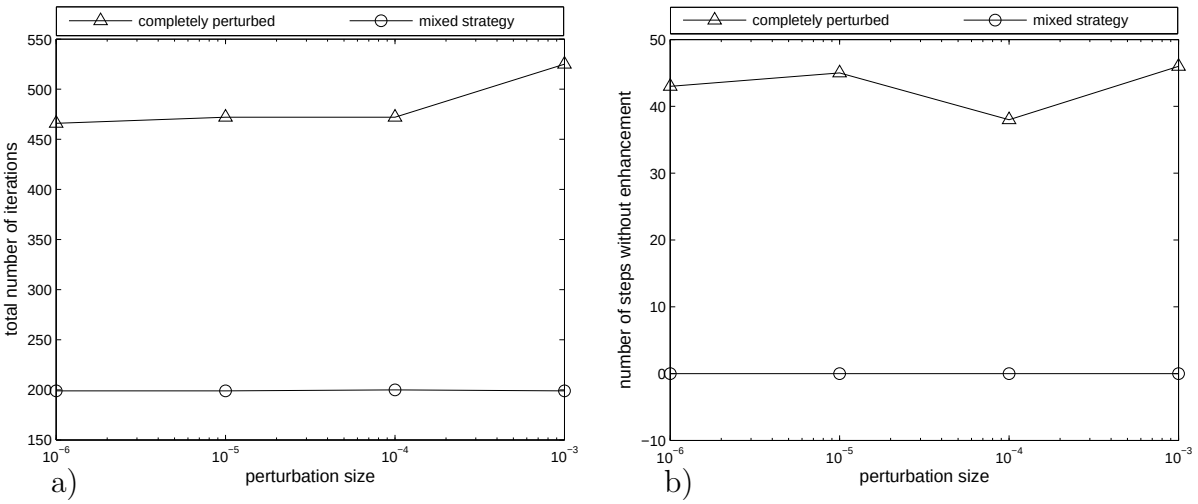

Figure 4.25.: a) total number of iterations for different perturbation sizes, b) number of time steps without the 'stress enhancement' for different perturbation sizes

4.6. Numerical Examples – Spinning Wheel

At the end of this chapter, we demonstrate extensively the excellent performance of the resulting Galerkin-based time-stepping schemes by means of two numerical examples, whereby a comparison between the standard and the non-standard quadrature rule will be discussed in this section. Special emphasis is placed on the influence of the evaluation strategy on the numerical and mechanical performance. The first example deals with a 'quasi rigid motion' of a 'Spinning Wheel' and the second example investigates a 'mixed stiffness motion', incorporating (highly) stiff and non-stiff regions. In our point of view, this is absolutely necessary to confirm the qualification of the developed integrators for a wide range of problems without restrictions. The initial configuration $\mathcal{B}_0$ of the wheel with the mass density $\rho = 1.0$ is discretised in space (2d, plane strain conditions) with 212 isoparametric $4-$node elements. To start the motion, the wheel is equipped with some external loads $\bar{\boldsymbol{F}}^{ext}$ on the circlet and an initial velocity $\bar{\boldsymbol{v}}_0$, using $||\bar{\boldsymbol{v}}_0|| = 415$. The norm of each external nodal-load $\boldsymbol{F}_I^{ext}$ follows the same piecewise linear function in time $f(t)$ as for the 'Flying Frame', compare Figure 4.26 a). Following the formulations in Section 4.2, the standard (4.25) respectively the non-standard quadrature rule (4.26) based on the (purely elastic) enhanced algorithmic stress tensor (4.27) have been applied. Hereby, the 'stress enhancement' has been evaluated by means of the proposed 'mixed strategy' introduced in Equation (4.37) and the constitutive relation relies once more on the Hencky model given by Equations (4.11), (4.42).

4.6.1. Quasi rigid motion

As highlighted in the previous sections, especially the motion of mechanically stiff systems constitutes an advanced challenge for time integrators that involve the 'stress enhancement' combined with an eigenvalue-based constitutive model, since the applied evaluation strategy of the 'stress enhancement' becomes really essential for stiff problems. Consequently, for the first numerical example we have chosen a nearly rigid motion of the 'Spinning Wheel', applying the parameters $f_{max} = 20.0$, $T_{load} = 1.0$, $\lambda = 10000$, and $\mu = 5000$. To expose the robustness of the time integrator with respect to variations of the time-step size, we change the step sizes during the calculation several times, compare Figure 4.26 b), involving $h_n \in \{0.001, 0.01, 0.1, 0.2, 0.4\}$. The resulting deformed configuration $\mathcal{B}_t$ at $t = 30$ and a sequence of the motion can be regarded in Figure 4.27 a). According to the applied material parameters, the rigid-body motion clearly dominates the deformation. The non-standard as well as the standard quadrature rule imply both a conservation of corresponding components of the linear and the angular momentum, as shown in Figure 4.27 b) respectively Figure 4.28 a). Considering Figure 4.28 b), both integrators seem to be energy-conserving at first glance. Nevertheless, a detailed consideration discloses an energy blow-up behaviour if a standard quadrature is applied. For the purpose of further investigations concerning the energy conservation, we refer to the residual R^{el} (4.46) which is pictured in Figure 4.29 for the relevant time

period without external loads. Therein, the differences between the standard and the non-standard quadrature rule become even more obvious, characterised by distinct oscillations of the residual in the case of the standard quadrature rule. By contrast, the non-standard quadrature rule based on the 'stress enhancement' guarantees indeed the conservation of the total energy within the calculation accuracy.

Remark 4.7: However, the excellent results of the non-standard quadrature rule are strictly linked to an appropriate evaluation strategy for the 'stress enhancement' to exploit its full potential. Regarding the numerical performance, we compare here the number of iterations required per time step for the standard and the non-standard quadrature rule evaluated based on the 'mixed' and the 'completely perturbed strategy'. As discussed in Section 4.5, the 'stress enhancement' is switched off if the global iteration scheme does not converge within a pre-defined number of iterations [8]. The results confirm impressively the significance and effectiveness of the proposed 'mixed strategy', enabling a numerical performance which is absolutely competitive to the time-stepping scheme based on the standard quadrature rule. Thereby, the maximum number of iterations per time step is equal to 5 for both quadrature rules. Contrariwise, the 'completely perturbed strategy' involves crucial convergence problems, demanding the switching procedure which induces for the present example 109 time steps without 'stress enhancement', compare Figure 4.30 a). Consequently, the conservation of energy is only guaranteed at first glance. In Figure 4.30 b), it can be clearly seen by zooming-in that the total energy increases not only for the standard quadrature rule, but also for the non-standard quadrature rule if the 'completely perturbed evaluation' is chosen. Thus, the 'mixed strategy' represents exclusively the proper method of choice.

[8] The allowed number of iterations per time step is pictured by means of a horizontal (dotted and dashed) line in the plots.

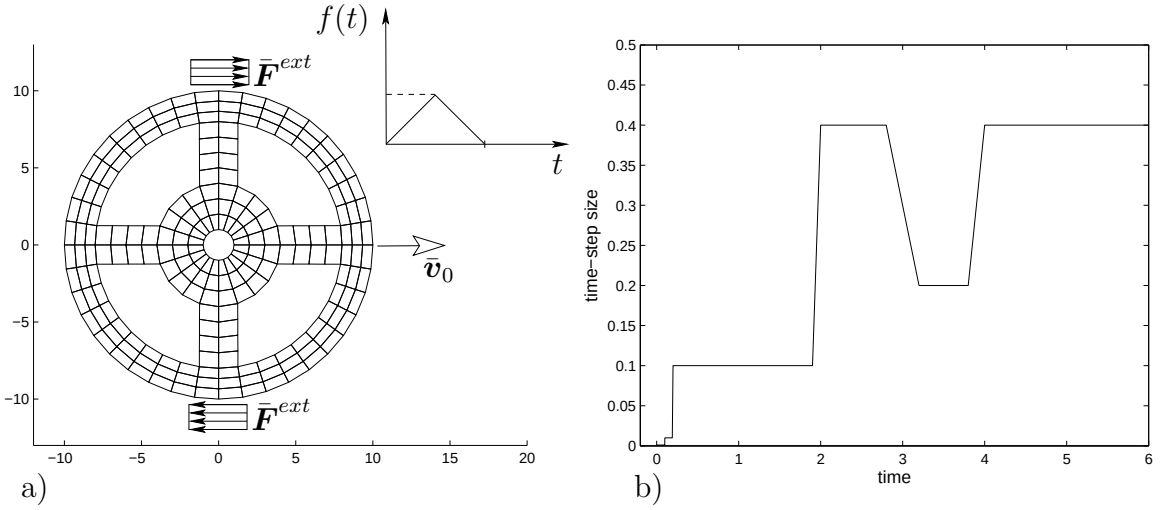

Figure 4.26.: a) initial configuration $\mathcal{B}_0$ with external loads and loading history, b) change of the time-step size

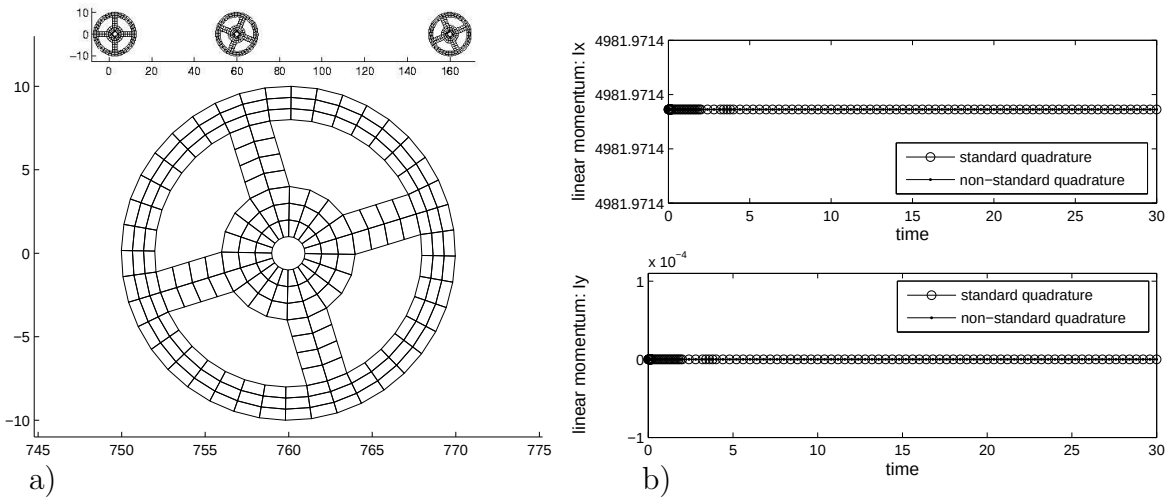

Figure 4.27.: a) sequence of the motion and deformed configuration $\mathcal{B}_t$ at $t = 30$, b) components of the linear momentum

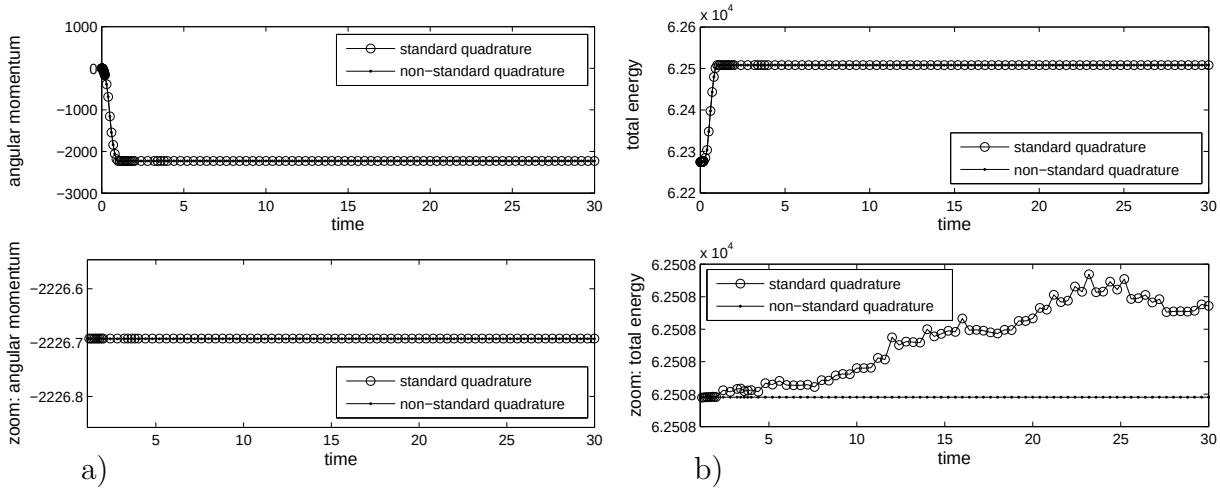

Figure 4.28.: a) component of the angular momentum (zoom), b) total energy H (zoom)

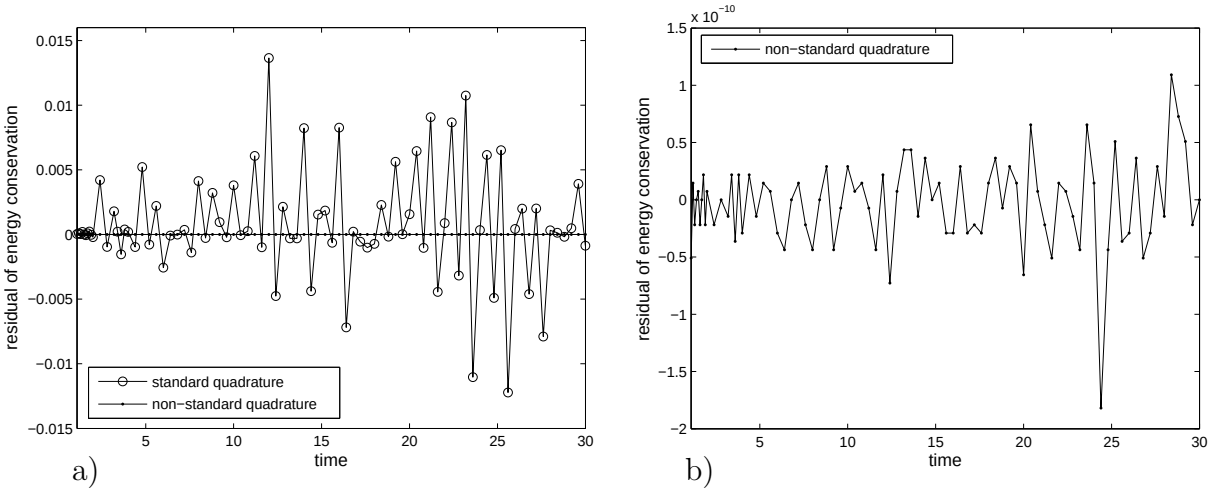

Figure 4.29.: residual of energy conservation R^{el} (zoom): a) standard & non-standard quadrature rule, b) non-standard quadrature rule

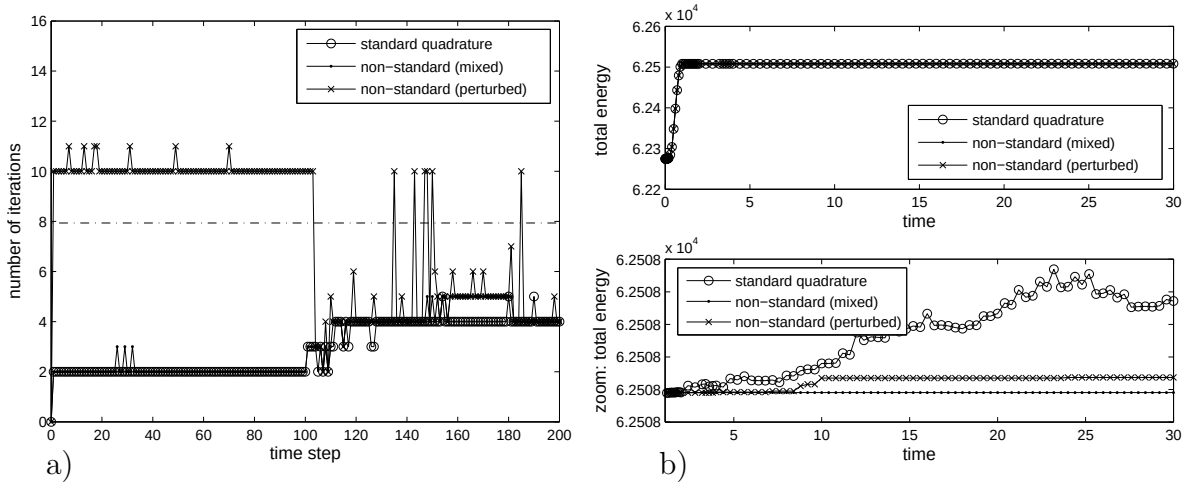

Figure 4.30.: standard & non-standard quadrature rule ('completely perturbed/mixed strategy'): a) number of iterations per time step, b) total energy H (zoom)

4.6.2. Mixed stiffness motion

The last example of the present chapter represents an exceedingly demanding challenge for time integrators, involving 'large strain' as well as 'nearly rigid parts'. Incorporating the loading parameters $f_{max} = 20.0$ and $T_{load} = 2.0$, the wheel is composed of stiff and non-stiff regions to fortify the qualification and effectiveness of the recommended concepts. For the spokes and the circlet, the material parameters $\lambda_1 = 200$, $\mu_1 = 100$ have been applied. In contrast, stiff material properties have been used for the nave, namely $\lambda_2 = 60000$ and $\mu_2 = 30000$. Additionally, we have once more included changes of the time-step size, involving $h_n \in \{0.02, 0.1, 0.2, 0.3\}$, to demonstrate the capability to handle small as well as large time steps, and to confirm the robustness of the proposed Galerkin-based time integrator, compare Figure 4.31 b). The deformed configuration subsequent to the loading period at $t = 2$ and some snapshots of the motion, calculated with the non-standard quadrature rule, are pictured in Figure 4.31 a). We observe comparatively large strains, especially within the circlet, and a quasi rigid nave. The non-standard as well as the standard quadrature rule provide both a mechanically consistent time-integration, as shown in Figure 4.32. However, the integrator based on the standard quadrature rule features a critical energy blow-up behaviour which leads to a break-off of the calculations (cf. dashed lines), whereas the proposed time-stepping scheme based on the non-standard quadrature rule, involving the 'mixed strategy', offers the required conservation of the total energy, as displayed in Figure 4.33 a). Moreover, it is shown in Figure 4.34 b) that the application of a non-standard quadrature rule guarantees energy conservation within the order of magnitude $\mathcal{O}(10^{-10})$. Contrariwise, the residual of energy conservation R^{el} (4.46) computed by means of a standard quadrature rule exposes strong deviations from zero, as can be seen in Figure 4.33 b) and Figure 4.34 a) respectively.

Remark 4.8: Once more, the results of the non-standard quadrature rule are strongly influenced by the applied evaluation strategy for the 'stress enhancement'. Analogously to the previous example, the application of the 'completely perturbed strategy' renders unacceptable convergence problems, requiring the switch-off of the 'stress enhancement' for 52 time steps. Thereby, the numerical problems are not only restricted to small time-step sizes, compare Figure 4.35 a). Naturally, this switching procedure entirely destroys the energy conservation property of the time-stepping scheme, as illustrated in Figure 4.35 b). Hereby, the corresponding plot shows an energy blow-up behaviour similar to the standard quadrature rule, resulting in a program abort due to divergence at $t = 18.92$. Moreover, it is pictured in Figure 4.36 that the residual of energy conservation R^{el} clearly deviates from zero not only for the standard but also for the non-standard quadrature rule combined with the 'completely perturbed strategy'. Hence, exclusively the combination of the non-standard quadrature rule and the 'mixed strategy' enables a robust integration related to the claimed guarantee of energy conservation within the calculation accuracy.

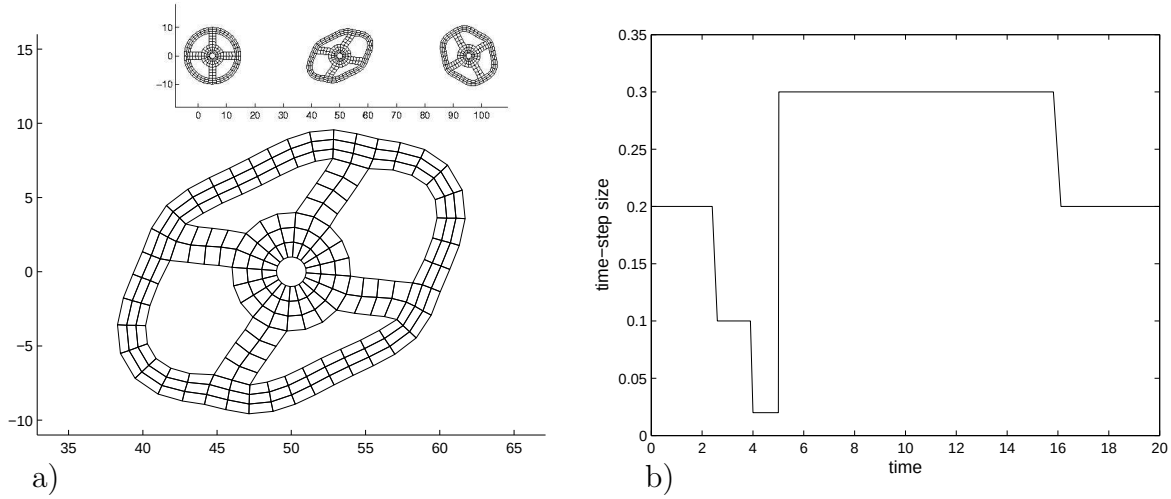

Figure 4.31.: a) sequence of the motion and deformed configuration $\mathcal{B}_t$ at $t = 2$, b) change of the time-step size

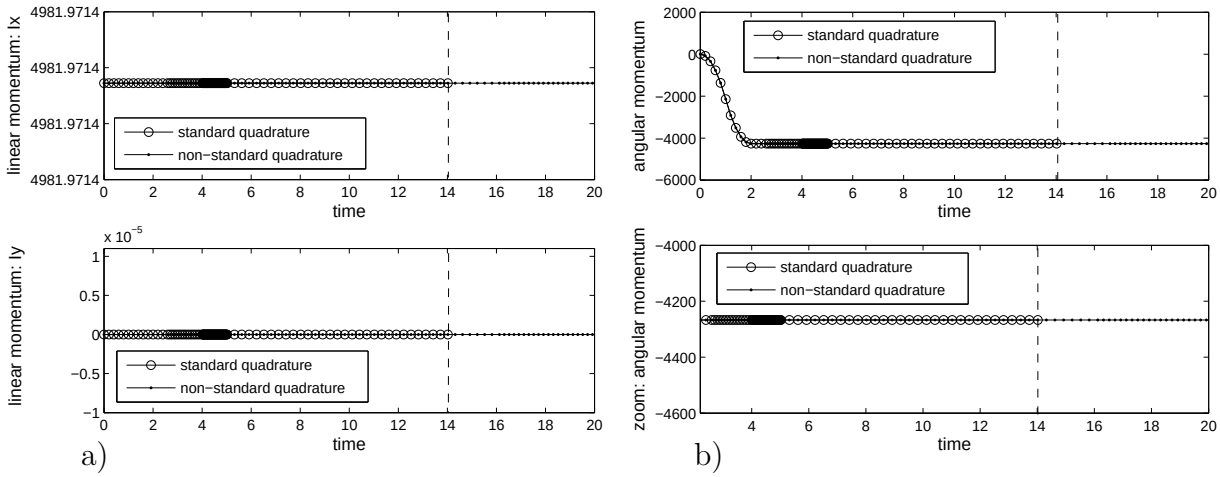

Figure 4.32.: components of: a) linear momentum, b) angular momentum (zoom)

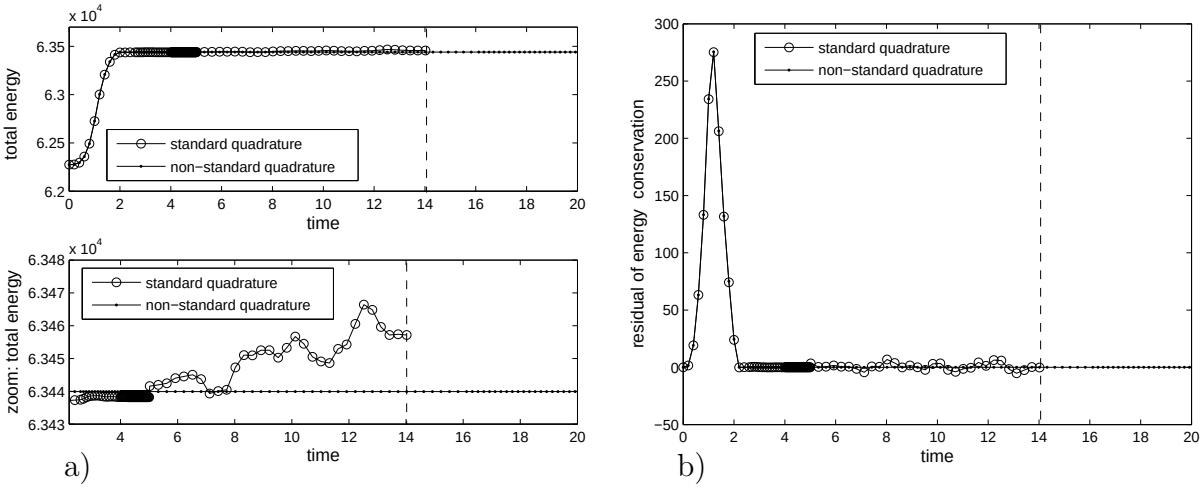

Figure 4.33.: a) total energy H (zoom), b) residual of energy conservation R^{el}

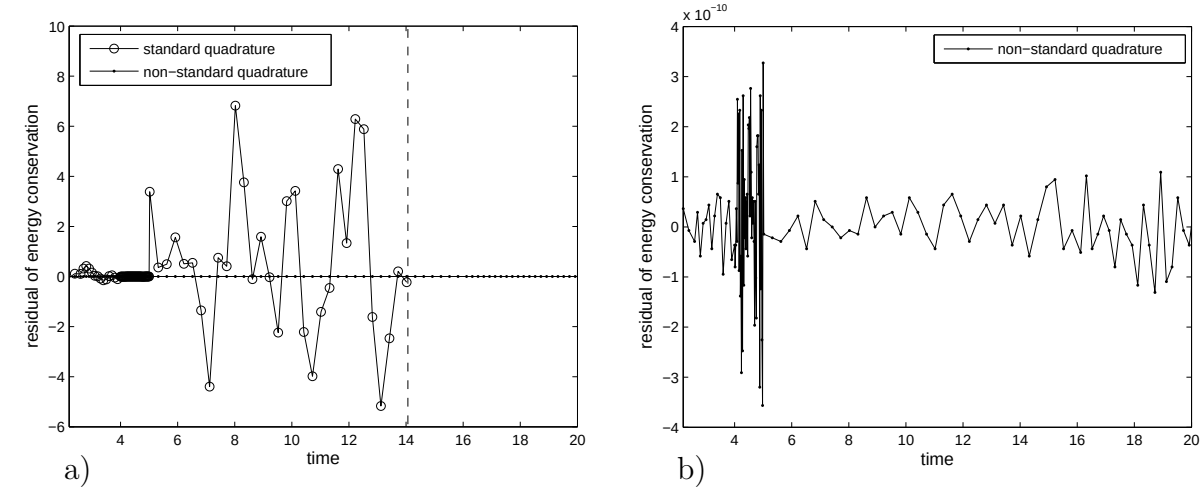

Figure 4.34.: residual of energy conservation R^{el} (zoom): a) standard & non-standard quadrature rule, b) non-standard quadrature rule

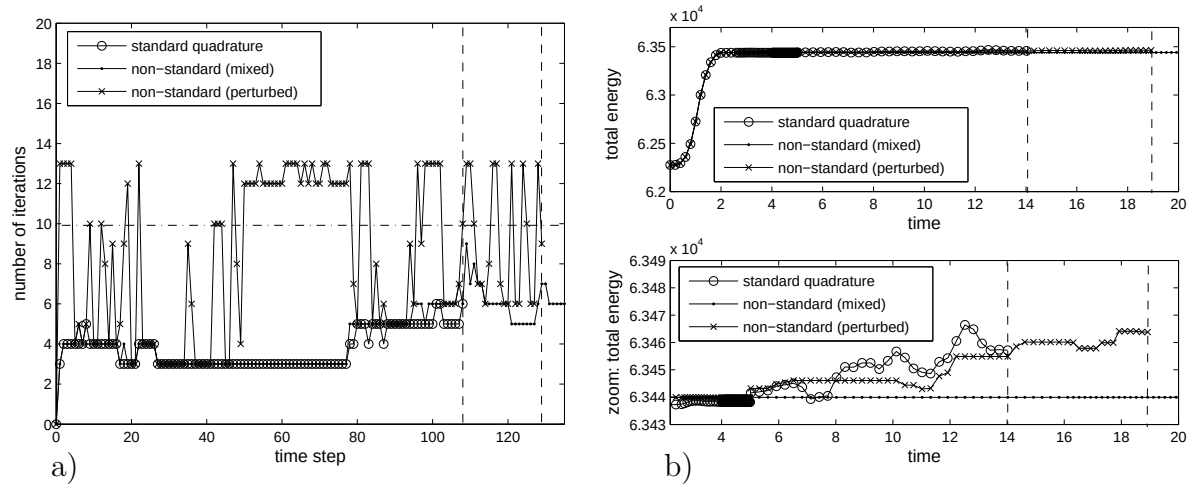

Figure 4.35.: standard & non-standard quadrature rule ('completely perturbed/mixed strategy'): a) number of iterations per time step, b) total energy H (zoom)

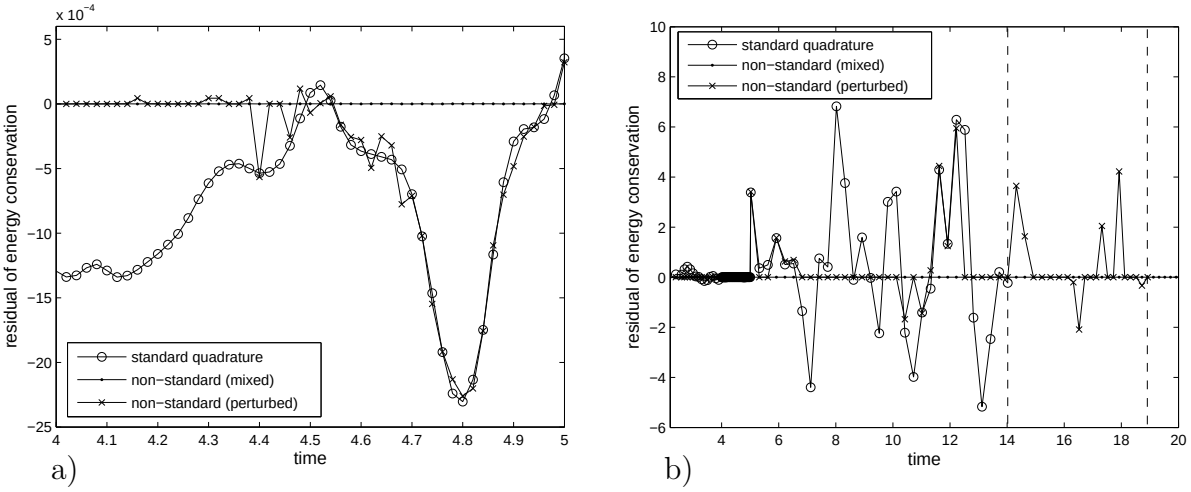

Figure 4.36.: residual of energy conservation R^{el} for the standard & non-standard quadrature rule ('completely perturbed/mixed strategy'): a) time period $t \in [4, 5]$, b) time period $t \in [2, 20]$

5. Finite Elasto-Plasticity

For the previous investigations, the general framework introduced in Chapter 3 has been restricted to the well-established conservative case, developing an efficient strategy that basically allows the incorporation of hyperelastic constitutive laws based on principal stretches within the context of energy-conserving time-stepping schemes. Furthermore, such eigenvalue-based formulations are also significant to describe finite inelasticity in general, particularly to model elasto-plastic material behaviour in a geometrically nonlinear setting. The main issue of the present chapter is now the application of the general concepts, that have been initially developed in Chapter 3 for arbitrary dissipative constitutive laws based on an internal variable formulation, to the specific case of large strain plasticity.

5.1. Constitutive Modelling – Multiplicative Plasticity

In contrast to small strain plasticity, an additive decomposition of the strain measure into elastic and plastic parts is controversial within the context of finite deformations, even if such additive formulations date back to Green and Naghdi [65] and have also been discussed in recent publications by several authors, compare e.g. References [118, 131]. Nevertheless, in the following, we favour a well-established multiplicative decomposition of the deformation gradient that perfectly fits into a configurational-based formulation and interpretation of nonlinear continuum mechanics, referring for instance to Lee [102], Simo [162], Miehe [130], or Menzel [121].

5.1.1. Formulation

Based on the fundamental kinematic relations of Section 3.1, the deformation gradient is assumed to be multiplicatively decomposed into an elastic and a plastic part, as indicated above. This assumption leads to the kinematic description

$$\boldsymbol{F} \doteq \boldsymbol{F}_e \cdot \boldsymbol{F}_p \,, \tag{5.1}$$

that naturally implies a stressfree (incompatible) configuration – the so-called intermediate configuration – represented by its tangent space $T\widehat{\mathcal{B}}$, as sketched in Figure 5.1. In

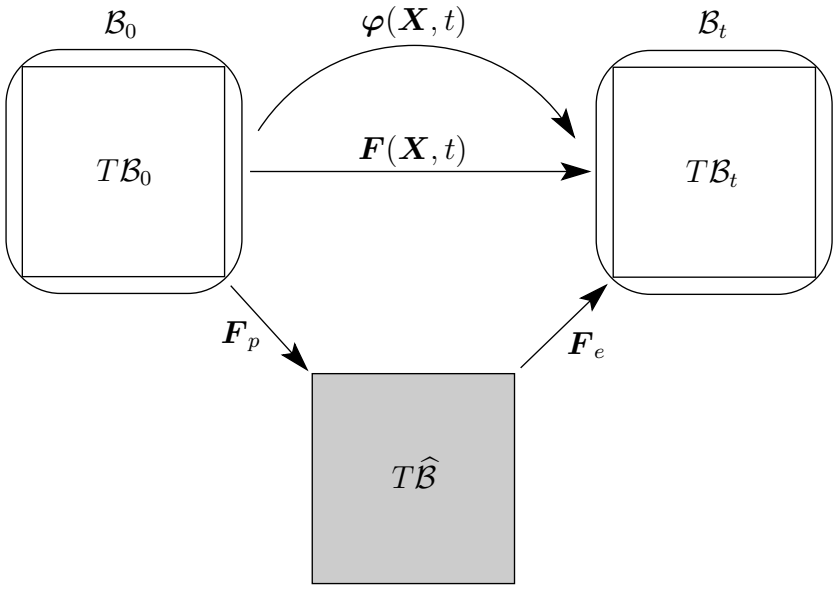

Figure 5.1.: resulting configurations within the framework of finite multiplicative plasticity

analogy to the right Cauchy-Green deformation tensor of the reference configuration $\mathcal{B}_0$, introduced in Equation (3.4), an elastic right Cauchy-Green tensor

$$\widehat{\boldsymbol{C}}_e := \boldsymbol{F}_e^{\mathrm{t}} \cdot \boldsymbol{F}_e \tag{5.2}$$

can be defined in the intermediate configuration, compare e.g. Reference [162]. As motivated in Section 3.1.2, internal variables $\boldsymbol{\kappa}$ are included in the Helmholtz energy density $\psi = \psi(\boldsymbol{F}, \boldsymbol{\kappa})$. Restricting to isotropy and incorporating invariance under superposed rigid body motions, the Helmholtz energy density can be formulated in terms of the eigenvalues of the elastic right Cauchy-Green strains based on the spectral decomposition

$$\widehat{\boldsymbol{C}}_e = \sum_{A=1}^{n_{dim}} {}^{A}\lambda_{\widehat{\boldsymbol{C}}_e}\, \widehat{\boldsymbol{N}}_A \otimes \widehat{\boldsymbol{N}}_A \,, \tag{5.3}$$

as discussed in detail in Section 4.1. According to the definition of the Piola-Kirchhoff stress tensor in the reference configuration $\mathcal{B}_0$, one obtains its intermediate counterpart $\widehat{\boldsymbol{S}} := 2\,\nabla_{\widehat{\boldsymbol{C}}_e}\,\psi$ and the (transposed) Mandel stress tensor

$$\widehat{\boldsymbol{M}}^{\mathrm{t}} = \widehat{\boldsymbol{C}}_e \cdot \widehat{\boldsymbol{S}} \,. \tag{5.4}$$

To distinguish between elastic and plastic deformation states, the yield function $\Phi \leq 0$ is introduced, defining the elastic range

$$\mathbb{E}_{\boldsymbol{\beta}} := \{\boldsymbol{\beta} \,\big|\, \Phi(\boldsymbol{\beta}; \boldsymbol{\kappa}) < 0\} \tag{5.5}$$

based on the conjugated quantities $\boldsymbol{\beta}$ given by Equation (3.6). To specify the evolution of the internal variables $\boldsymbol{\kappa}$, we apply the well-accepted postulate of maximum dissipation based on a minimisation of the functional $\mathcal{M} = -\mathcal{D} + \dot{\gamma}\,\Phi$, and obtain the local associated evolution

$$\dot{\boldsymbol{\kappa}} = \dot{\gamma}\,\nabla_{\boldsymbol{\beta}}\Phi\,. \tag{5.6}$$

Analogously to Chapter 2, the actual loading/unloading process can be characterised by the so-called Kuhn-Tucker conditions

$$\dot{\gamma} \geq 0 \qquad\qquad \Phi \leq 0 \qquad\qquad \dot{\gamma}\,\Phi = 0 \tag{5.7}$$

and the consistency condition respectively, that is given by $\dot{\gamma}\,\dot{\Phi} = 0$ for $\Phi = 0$. Further details are discussed in standard textbooks, like for instance in References [162, 164], dealing with the mechanical modelling of plasticity from a computational point of view.

Remarks 5.1:

1. Interestingly, also the multiplicatively decomposed deformation gradient implies an additive structure, namely an additive decomposition of the spatial velocity gradient $\nabla_{\boldsymbol{q}}\boldsymbol{v} := \dot{\boldsymbol{F}} \cdot \boldsymbol{F}^{-1}$ into elastic and plastic parts. By means of a pullback-operation with respect to the intermediate configuration, we obtain furthermore the format

$$\widehat{\boldsymbol{L}} := \boldsymbol{F}_e^{-1} \cdot \nabla_{\boldsymbol{q}}\boldsymbol{v} \cdot \boldsymbol{F}_e = \widehat{\boldsymbol{L}}_e + \widehat{\boldsymbol{L}}_p\,, \tag{5.8}$$

   wherein the elastic part $\widehat{\boldsymbol{L}}_e := \boldsymbol{F}_e^{-1} \cdot \dot{\boldsymbol{F}}_e$ and the plastic part $\widehat{\boldsymbol{L}}_p := \dot{\boldsymbol{F}}_p \cdot \boldsymbol{F}_p^{-1}$ have been introduced.

2. Using a plasticity model with isotropic hardening, the internal variables $\boldsymbol{\kappa}$ can be specified as $\boldsymbol{\kappa} := [\boldsymbol{F}_p, \kappa]$. Consequently, associated evolution equations can be written in the form

$$\dot{\boldsymbol{F}}_p = \dot{\gamma}\,\nabla_{\widehat{\boldsymbol{M}}^{\mathrm{t}}}\Phi \cdot \boldsymbol{F}_p \qquad\qquad \text{and} \qquad\qquad \dot{\kappa} = \dot{\gamma}\,\nabla_{\beta}\Phi\,, \tag{5.9}$$

   wherein the abovementioned definition of $\widehat{\boldsymbol{L}}_p$ has been incorporated to formulate the evolution of $\boldsymbol{F}_p$, compare e.g. Reference [132]. The integration in time of the local evolution equations (5.9) will be discussed in the following based on an exemplary return mapping scheme.

5.1.2. Return mapping algorithm

Since in the present contribution the focus has been placed on the Galerkin-based time-discretisation on the global level, we exemplarily apply for the local integration a standard approach: the commonly adopted exponential update scheme, see e.g. References

[118, 128, 161]. However, any other appropriate local update algorithm could be incorporated instead, whereby the exponential procedure has further significant advantages in addition to its elementary structure:

- Firstly, the exponential update scheme is well-established for finite multiplicative plasticity and it is able to preserve in combination with a logarithmic strain measure exactly the structure of the small strain theory.
- Furthermore, plastic incompressibility can be guaranteed for the following model without any additional costs and the application of a 'von Mises'-type yield function with a linear isotropic hardening part allows the computation of the incremental plastic multiplier without local iterations.

Taking all these aspects into account, the classical exponential update scheme for finite multiplicative plasticity performs well and cost-efficiently. Based on the continuous form (5.9), the associated evolution equations at hand are integrated via

$$\boldsymbol{F}_p^{n+1} = \exp(\Delta\gamma\,[\nabla_{\widehat{\boldsymbol{M}}^{\mathrm{t}}}\,\Phi]^{n+1}) \cdot \boldsymbol{F}_p^{n} \tag{5.10}$$

and

$$\kappa^{n+1} = \kappa^{n} + \Delta\gamma\,[\nabla_{\beta}\Phi]^{n+1} \tag{5.11}$$

respectively, whereby a classical Euler-backward scheme has been applied for the scalar-valued hardening variable κ. The actual return mapping algorithm can be performed in two steps: a trial step and a projection step, compare References [162, 164]. Regarding the chosen dynamical framework introduced in Chapter 3, the local update scheme should be formulated in terms of $\boldsymbol{C}$ and $\boldsymbol{F}_p$ as driving variables, extending the hyperelastic case discussed in Chapter 4. Consequently, we introduce an intermediate trial state $[\bullet]^{trial}$ by means of given $\boldsymbol{C}^{n+1}$ and frozen plastic deformations represented by $\boldsymbol{F}_p^n$ and κ^n, resulting in

$$\widehat{\boldsymbol{C}}_e^{trial} = \boldsymbol{F}_p^{n-\mathrm{t}} \cdot \boldsymbol{C}^{n+1} \cdot \boldsymbol{F}_p^{n-1} \qquad \text{and} \qquad \kappa^{trial} = \kappa^{n}\,. \tag{5.12}$$

Assuming isotropy, the stresses $\widehat{\boldsymbol{S}}$ commute with the elastic right Cauchy-Green tensor $\widehat{\boldsymbol{C}}_e$ and, hence, the Mandel stresses $\widehat{\boldsymbol{M}}$ are symmetric. Based on Equation (5.10), it follows consequently that the principal directions of the elastic right Cauchy-Green tensor and the trial state are coaxial and we obtain the update

$$\widehat{\boldsymbol{C}}_e^{n+1} = \exp(-2\Delta\gamma\,[\nabla_{\widehat{\boldsymbol{M}}^{\mathrm{t}}}\,\Phi]^{n+1}) \cdot \widehat{\boldsymbol{C}}_e^{trial} \tag{5.13}$$

for the projection step. Based on a spectral decomposition of the trial state

$$\widehat{\boldsymbol{C}}_e^{trial} = \sum_{A=1}^{n_{dim}} [{}^{A}\lambda_e^{trial}]^2\; \widehat{\boldsymbol{N}}_A^{trial} \otimes \widehat{\boldsymbol{N}}_A^{trial}\,, \tag{5.14}$$

the resulting updated elastic deformation tensor can be composed, rendering

$$\widehat{\boldsymbol{C}}_e^{n+1} = \sum_{A=1}^{n_{dim}} [{}^A\lambda_e^{n+1}]^2 \, \widehat{\boldsymbol{N}}_A^{trial} \otimes \widehat{\boldsymbol{N}}_A^{trial} \,. \tag{5.15}$$

Making use of the coaxiality relations, we obtain furthermore the Mandel stresses

$$\widehat{\boldsymbol{M}}^{\mathrm{t}\,n+1} = \sum_{A=1}^{n_{dim}} \widehat{M}_A^{\mathrm{t}\,n+1} \, \widehat{\boldsymbol{N}}_A^{trial} \otimes \widehat{\boldsymbol{N}}_A^{trial} \,. \tag{5.16}$$

Bearing Equations (5.13)–(5.15) in mind and introducing logarithmic strains, we obtain the update for the principal elastic stretches

$$\ln({}^A\lambda_e^{n+1}) = \ln({}^A\lambda_e^{trial}) - \Delta\gamma \, [\nabla_{\widehat{M}_A^{\mathrm{t}}} \Phi]^{n+1} \,. \tag{5.17}$$

Please note, that the principal directions satisfy $\widehat{\boldsymbol{N}}_A = \widehat{\boldsymbol{N}}_A^{trial}$, assuming fixed principal axes for the return mapping procedure as discussed e.g. in Reference [162]. For convenience of the reader, the complete structure of the local update algorithm is summarised in Table 5.1. Therein, we have incorporated a specific Helmholtz energy density ψ based on the macroscopic part

$$\psi^{mac} = \mu \, [\ln^2({}^1\lambda_e) + \ln^2({}^2\lambda_e) + \ln^2({}^3\lambda_e)] + \frac{\lambda}{2} \ln^2(J_e) \quad \text{with} \quad J_e = \sqrt{\det(\widehat{\boldsymbol{C}}_e)} \tag{5.18}$$

and a microscopic part related to linear isotropic hardening effects, namely

$$\psi^{mic} = \frac{1}{2} H^{rd} \kappa^2 \qquad \text{which renders} \qquad \beta = -H^{rd} \, \kappa \,, \tag{5.19}$$

compare Equation (3.8). Moreover, a yield function Φ of the 'v. Mises'-type has been chosen as a fundamental example.

Remarks 5.2:

1. The outlined local update relies substantially on a formulation of the constitutive behaviour based on principal stretches, involving spectral decompositions of the deformation measure and the related stresses. Once more, the algorithmic treatment rests upon the concepts that have been already discussed in Section 4.1.2 for the hyperelastic case, featuring an efficient numerical implementation.

2. Please keep in mind, that the particular format of the applied exponential-based local update discussed in this section is only first-order accurate in time. The influence on the (global) order of accuracy of the resulting time-stepping scheme will be investigated in Section 5.5.

Table 5.1.: exponential update (& Euler-backward) algorithm for isotropic finite multiplicative plasticity with isotropic hardening formulated with respect to the intermediate configuration

- elastic predictor step: **trial state**

$$\begin{aligned}
\widehat{\boldsymbol{C}}_e^{trial} &= \boldsymbol{F}_p^{n-\mathrm{t}} \cdot \boldsymbol{C}^{n+1} \cdot \boldsymbol{F}_p^{n-1} \qquad \text{and} \qquad \kappa^{trial} = \kappa^n \\
\widehat{\boldsymbol{C}}_e^{trial} &= \sum_{A=1}^{3} [{}^A\lambda_e^{trial}]^2 \, \widehat{\boldsymbol{N}}_A^{trial} \otimes \widehat{\boldsymbol{N}}_A^{trial} \\
{}^{dev}\widehat{M}_A^{\mathrm{t}\,trial} &= 2\,\mu\,[\ln({}^A\lambda_e^{trial}) - \frac{1}{3}\ln({}^1\lambda_e^{trial}\,{}^2\lambda_e^{trial}\,{}^3\lambda_e^{trial})]
\end{aligned}$$

- check yield condition: 'v. Mises'-type with linear isotropic hardening

$$\Phi^{trial} = ||{}^{dev}\widehat{\boldsymbol{M}}^{\mathrm{t}\,trial}|| - \sqrt{\frac{2}{3}}[Y_0 + H^{rd}\kappa^{trial}]$$

  IF $\Phi^{trial} > 0$: **radial return**

$$\Delta\gamma = \frac{\Phi^{trial}}{2\mu + \frac{2}{3}H^{rd}} > 0$$

  ELSE: $[\bullet]^{n+1} = [\bullet]^{trial} \qquad \Delta\gamma = 0$

- update:

$$\begin{aligned}
\kappa^{n+1} &= \kappa^{trial} + \Delta\gamma\,[\nabla_\beta\,\Phi]^{n+1} \\
\boldsymbol{F}_p^{n+1} &= \left[\sum_{A=1}^{3} \exp\big(\Delta\gamma\,[\nabla_{{}^{dev}\widehat{M}_A^{\mathrm{t}}}\,\Phi]^{trial}\big)\,\widehat{\boldsymbol{N}}_A^{trial} \otimes \widehat{\boldsymbol{N}}_A^{trial}\right] \cdot \boldsymbol{F}_p^n
\end{aligned}$$

$$\begin{aligned}
\ln({}^A\lambda_e^{n+1}) &= \ln({}^A\lambda_e^{trial}) - \Delta\gamma\,[\nabla_{{}^{dev}\widehat{M}_A^{\mathrm{t}}}\,\Phi]^{trial} \\
{}^{dev}\widehat{M}_A^{\mathrm{t}\,n+1} &= {}^{dev}\widehat{M}_A^{\mathrm{t}\,trial} - 2\,\mu\,\Delta\gamma\,[\nabla_{{}^{dev}\widehat{M}_A^{\mathrm{t}}}\,\Phi]^{trial}
\end{aligned}$$

- compute stresses in $\mathcal{B}_0$:

$$\begin{aligned}
\boldsymbol{M}^{\mathrm{t}\,n+1} &= \boldsymbol{F}_p^{n+1\mathrm{t}} \cdot \widehat{\boldsymbol{M}}^{\mathrm{t}\,n+1} \cdot \boldsymbol{F}_p^{n+1-\mathrm{t}} \\
\boldsymbol{S}^{n+1} &= \boldsymbol{C}^{n+1\,-1} \cdot \boldsymbol{M}^{\mathrm{t}\,n+1}
\end{aligned}$$

5.2. Consistent Time-Stepping Schemes

Analogously to the hyperelastic case discussed in Section 4.2, next, specific time-stepping schemes will be outlined with regard to following numerical investigations. For this purpose, the general format of consistent time-FE methods for dissipative material behaviour, developed in Section 3.3, will be specified in this section to finite elasto-plasticity, whereby the particular plasticity model and the exemplarily applied local update have been summarised in Table 5.1. In the following, the local scheme will be treated as a constitutive 'black box', emphasising that also other plasticity models or local update schemes could be incorporated without changing the main concepts on the global level [1]. Once more, linear Finite Elements in time with $k = 1$ are chosen for the following steps, rendering on the global level basically the same equations that have been already discussed in Section 4.2 for the hyperelastic case, compare Equations (4.24). Nevertheless, in the here considered plastic case, the approximation of the crucial time-integrated internal load vector has to be modified properly in comparison to the purely elastic formulation, involving the time-dependence $\boldsymbol{S}(\boldsymbol{C}(\alpha), \boldsymbol{\kappa}(\alpha))$.

5.2.1. Standard quadrature rule

Once more, we start with the application of standard Gauss quadrature rule. Thereby, the number of integration points in time n_{gp_t} is initially arbitrary to study in Section 5.3.1 its influence on the resulting consistency of the integrators, since in the context finite elasto-plasto-dynamics Galerkin-based integrators have not been investigated concerning this matter in literature. Referring to Equation (3.46), we introduce the approximation

$$\int_0^1 \boldsymbol{F}_I^{int\,h}\,\mathrm{d}\alpha \approx \sum_{l=1}^{n_{gp_t}} \left[\sum_{J=1}^{n_{node}} \int_{\mathcal{B}_0} [\nabla_{\boldsymbol{X}} N_I \otimes \nabla_{\boldsymbol{X}} N_J] : \boldsymbol{S}(\boldsymbol{C}(\zeta_l), \boldsymbol{\kappa}_{\zeta_l})\,\mathrm{d}V\, \boldsymbol{q}_J^h(\zeta_l) \right] w_l \quad (5.20)$$

for $I = 1, ..., n_{node}$. Please note, that in Equation (5.20) the time approximation of the right Cauchy-Green tensor relies indeed on a standard cG-approximation of the positions. As stated afore, we have exemplarily chosen one of the simplest and most established update procedures for the local evolution equations. To fit the return mapping procedure into the standard quadrature rule (5.20), the exponential update is applied for $n_{gp_t} + 1$ integration steps, related to n_{gp_t} intermediate stages represented by

$$\{\boldsymbol{F}_p^n, \kappa^n\} \longrightarrow \{\boldsymbol{S}^{n+\zeta_l}, \boldsymbol{F}_p^{n+\zeta_l}, \kappa^{n+\zeta_l}\}\,, \quad (5.21)$$

[1] In this context, the most important difference between plasticity and the modelling of other dissipative material behaviour based on an internal variable formulation, like for instance visco-elasticity, is basically the required fulfilment of the yield condition. Thereby, the efficient numerical treatment of the related inequality constraint is usually based on a predictor/corrector formulation of the local update, as outlined in Section 5.1.2. However, from a computational point of view, this additional constraint poses further challenges concerning the embedding into the global scheme, particularly within a dynamical framework. One crucial issue in this context is for instance the question, at which time the resulting stress state should be enforced to fulfil the yield condition.

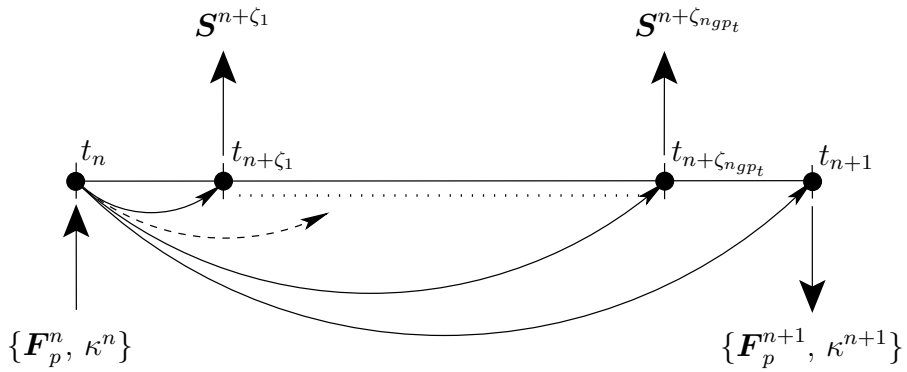

Figure 5.2.: local level: integration strategy (standard quadrature rule)

which are followed by the final projection

$$\{\boldsymbol{F}_p^n, \kappa^n\} \longrightarrow \{\boldsymbol{S}^{n+1}, \boldsymbol{F}_p^{n+1}, \kappa^{n+1}\} \tag{5.22}$$

driven by $\boldsymbol{C}^{n+\zeta_l}$ and $\boldsymbol{C}^{n+1}$ respectively, as illustrated in Figure 5.2 [2]. On the one hand, the foregoing update procedure allows the embedding of the exponential-based local integration into the standard quadrature rule in a quite intuitive way and, moreover, it guarantees on the other hand the fulfilment of the yield condition not only at the final state, but also for the involved intermediate stages. The influence of this basic projection strategy on the resulting (global) order of accuracy of the time-stepping scheme as well as an alternative approach will be discussed in Section 5.5. For the particular choice of one Gaussian integration point in time, the standard cG(1) method is equivalent to the classical midpoint (difference) scheme, involving

$$\int_0^1 \boldsymbol{F}_I^{int\,h}\, \mathrm{d}\alpha \approx \sum_{J=1}^{n_{node}} \left[\int_{\mathcal{B}_0} [\nabla_{\boldsymbol{X}} N_I \otimes \nabla_{\boldsymbol{X}} N_J] : \boldsymbol{S}(\boldsymbol{C}(1/2), \boldsymbol{\kappa}_{1/2})\, \mathrm{d}V \right] \boldsymbol{q}_J^h(1/2)\,. \tag{5.23}$$

Since in the hyperelastic case the positive influence of an assumed strain approximation is well-known, we apply also in the plastic case the linear approximation $\boldsymbol{C}^h(\alpha) = [\boldsymbol{C}_2 - \boldsymbol{C}_1]\alpha + \boldsymbol{C}_1$ based on Equation (3.45) and obtain the alternative representation

$$\int_0^1 \boldsymbol{F}_I^{int\,h}\, \mathrm{d}\alpha \approx \sum_{J=1}^{n_{node}} \left[\int_{\mathcal{B}_0} [\nabla_{\boldsymbol{X}} N_I \otimes \nabla_{\boldsymbol{X}} N_J] : \boldsymbol{S}(\boldsymbol{C}^h(1/2), \boldsymbol{\kappa}_{1/2})\, \mathrm{d}V \right] \boldsymbol{q}_J^h(1/2)\,. \tag{5.24}$$

Equation (5.24) represents the extension of Equation (4.25) to the elasto-plastic case and defines in combination with Equations (4.24) a modified midpoint scheme, incorporating an approximation of the right Cauchy-Green tensor as an additional feature.

[2] Hereby, the local integration is pictured based on the physical time interval $\mathcal{T} = [t_n, t_{n+1}]$ for the sake of conceptual clarity. However, keep in mind that the global integration is actually performed based on a mapping to the reference time interval $\mathcal{I} = [0, 1]$, as discussed in Section 2.2.2 and Section 3.3.1.

As discussed in Chapter 3 for the general case of arbitrary k, both integrators – the classical as well as the modified scheme defined by the approximations (5.23) and (5.24) respectively – feature the conservation of the momentum maps and can be consequently referred to as mechanically consistent, as classified in Section 3.2.3.

5.2.2. Non-standard quadrature rule

In general, the involvement of dissipation effects represents in the context of nonlinear dynamics a further challenge regarding the claimed fulfilment of a discrete energy balance. Particularly the modelling of finite elasto-plasto-dynamics leads to an increasing nonlinearity of the internal load vector in comparison to elasto-dynamics. Consequently, the application of a non-standard quadrature rule is once more required, since in general the related time-integrals can not be integrated exactly by a standard approximation. To guarantee energy-consistency in general, a non-standard quadrature rule for the time-integrated internal load vector is introduced based on Equation (3.47). Using once more one integration point in time, Equation (3.42) yields

$$\int_0^1 \boldsymbol{F}_I^{int\,h}\,\mathrm{d}\alpha \approx \sum_{J=1}^{n_{node}} \left[\int_{\mathcal{B}_0} [\nabla_{\boldsymbol{X}} N_I \otimes \nabla_{\boldsymbol{X}} N_J] : \boldsymbol{S}^{alg}(1/2)\,\mathrm{d}V\right] \boldsymbol{q}_J^h(1/2)\,. \tag{5.25}$$

By defining $\boldsymbol{S}_{1/2} := \boldsymbol{S}(\boldsymbol{C}^h(1/2), \boldsymbol{\kappa}_{1/2})$, the elasto-plastic enhanced algorithmic stress tensor $\boldsymbol{S}^{alg}$ follows directly from Equation (3.51), resulting in

$$\boldsymbol{S}^{alg}(1/2) := \boldsymbol{S}_{1/2} + \frac{2\,[\psi_{\alpha=1} - \psi_{\alpha=0} + \Delta d\,] - \boldsymbol{S}_{1/2} : [\boldsymbol{C}_2 - \boldsymbol{C}_1]}{||\boldsymbol{C}_2 - \boldsymbol{C}_1||^2}[\boldsymbol{C}_2 - \boldsymbol{C}_1]\,. \tag{5.26}$$

Therein, the local dissipation increment Δd must be provided by the local update algorithm.

Remark 5.3: Based on Equation (5.26), it can be clearly seen that the general algorithmic stresses $\boldsymbol{S}^{alg}$ (3.51) result for linear Finite Elements in time in the same formulation that has been proposed by Meng and Laursen [118, 119]. However, the applicability of the 'discrete' concept is strictly bounded to a specific (second-order accurate) integration of the global equations of motion based on Finite Differences. To the contrary, the general format (3.51) represents the appropriate generalisation against the background of Finite Elements in time, whereby especially the non-standard quadrature rule (3.47), including related collocation properties, turns out to be essential concerning the step from a commonly used 'discrete' concept to a time FE framework.

To fit the return mapping procedure into the non-standard quadrature rule (5.25), we apply basically the same procedure as for the standard quadrature rule, given by Equation (5.21) and Equation (5.22). In the particular case, the exponential update is applied

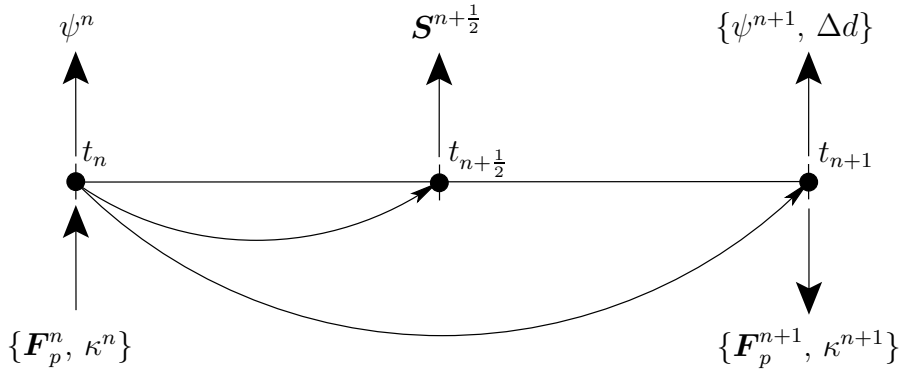

Figure 5.3.: local level: integration strategy (non-standard quadrature rule)

for two integration steps, namely for $t_n \rightarrow t_{n+\frac{1}{2}}$ and $t_n \rightarrow t_{n+1}$, which can be represented by

$$\{\boldsymbol{F}_p^n, \kappa^n\} \longrightarrow \{\boldsymbol{S}^{n+\frac{1}{2}}, \boldsymbol{F}_p^{n+\frac{1}{2}}, \kappa^{n+\frac{1}{2}}\} \tag{5.27}$$

and

$$\{\boldsymbol{F}_p^n, \kappa^n\} \longrightarrow \{\boldsymbol{S}^{n+1}, \boldsymbol{F}_p^{n+1}, \kappa^{n+1}; \psi^{n+1}, \Delta d\}\,, \tag{5.28}$$

as pictured in Figure 5.3. In contrast to the standard quadrature rule, the additional computation of the Helmholtz energy density ψ^{n+1} and the (local) dissipation increment Δd is required within each iteration step. For the applied plasticity model discussed in Section 5.1.2, the dissipation increment is given by

$$\Delta d = \Delta\gamma \sqrt{\frac{2}{3}}\, Y_0\,, \tag{5.29}$$

wherein Y_0 denotes the initial yield stress, compare Table 5.1. At this point, we emphasise once more that due to the specific formulation of the local update both integration steps (5.27), (5.28) are driven by $\boldsymbol{C}^{n+\frac{1}{2}}$ and $\boldsymbol{C}^{n+1}$ respectively. Furthermore, the fulfilment of the yield condition by the physical stress measure of the continuum formulation is consequently guaranteed at the quadrature point in time, related to the midpoint configuration at $t = t_{n+\frac{1}{2}}$, as well as at the current time $t = t_{n+1}$. In view of the resulting consistency properties of the particular integrator, it can be straightforwardly verified based on the general investigations in Chapter 3 that the chosen approximation in combination with Equation (5.26) fulfils the approximated local energy-consistency condition (3.49) which reads for linear Finite Elements in time

$$\psi_{\alpha=1} - \psi_{\alpha=0} + \Delta d - \frac{1}{2}\boldsymbol{S}^{alg}(1/2) : [\boldsymbol{C}_2 - \boldsymbol{C}_1] = 0\,, \tag{5.30}$$

as demonstrated more detailed in Section A.3. Moreover, the fundamental global condition for energy-consistency (3.60) yields

$$\bar{\boldsymbol{F}}^{int\ h}(1/2) \cdot [\bar{\boldsymbol{q}}_2 - \bar{\boldsymbol{q}}_1] \stackrel{!}{=} \Psi_{\alpha=1} - \Psi_{\alpha=0} + \Delta D \tag{5.31}$$

for the particular case $k = 1$. Following the same arguments as discussed in Section 3.3.3 respectively Appendix A, Equation (5.31) is fulfilled by the here considered time-stepping scheme, rendering a 'mechanically' as well as 'energy-consistent' time-integration [3]. Interestingly, the condition (5.31) is equivalent to a relation advocated by Noels *et al.* [144] for hypoelastic constitutive formats, which should be verified for the applied internal load vector. Furthermore, a similar approach has been proposed in Reference [147] by the same authors in the context of an energy momentum conserving algorithm for visco-plasticity based on a variational formulation. Consequently, the Galerkin-based approach proposed in this contribution recaptures once more well-established concepts for Finite Difference methods as special cases.

Remarks 5.4:

1. Please note, that in contrast to Armero [5, 9] a fulfilment of the yield condition by the algorithmic stress tensor is not enforced in this contribution (analogously to Meng and Laursen [118, 119]) since, in our opinion, its physical meaning is not obvious and, hence, the interpretation is quite problematic. Instead, we account for $\boldsymbol{S}^{alg}$ solely as a numerical modification of the quadrature rule based on the physically motivated stresses of the continuum model which are enforced to fulfil the yield condition not only at the current time but also at the intermediate stages related to the quadrature points.

2. In Meng and Laursen [118, 119], the global time-stepping scheme rests upon the energy-momentum algorithm proposed by Simo and Tarnow [165] combined with the concept of a 'discrete gradient/derivative', including an additional dissipation part. Concerning local time-integration, Meng and Laursen suggest also an exponential update, being second-order accurate. As shown above, the special case of linear time elements combined with one integration point in time results – by using the general non-standard quadrature rule (3.47) – basically in the same equations, even if the conceptual approach of Finite Differences and Finite Elements in time is fundamentally different. However, both formulations are similar but not identical, even not for $k = 1$. In fact, we have formulated purposely the local update with respect to the intermediate configuration instead of the classical spatial representation that has been used by Meng and Laursen. Consequently, in our approach the interpolation of the (relative) deformation gradient is not required and the

[3] Using an abbreviatory notation, the final scheme will be denoted as 'ECMC-cG(1) method', in accordance with Section 3.3.2.

update can be formulated solely based on the assumed strain approximation in time $\boldsymbol{C}^h$, inspired by the hyperelastic case discussed in Chapter 4. This concept avoids a potential coupling of strains and rotations affected by superimposed rigid body motions and renders a very robust integration including mechanically stiff problems, see also References [67, 68]. Moreover, in this contribution the physical stresses of the continuum model are projected to the yield surface at the quadrature point and at the current time as well, compare Equations (5.27), (5.28).

3. Recently, an energy-dissipative momentum-conserving time-stepping algorithm for finite plastodynamics has been proposed by Armero [5], inspired by earlier publications of Armero and Romero [7, 8]. Once more, the so-called 'EDMC-scheme' bases on the 'discrete gradient/derivative' concept by Gonzalez [62, 64], incorporating an additional numerical dissipation part. Thereby, the gradient has been completely formulated in terms of $\widehat{\boldsymbol{C}}_e$ in the intermediate configuration, requiring pull-back operations via $\boldsymbol{F}_p$. Moreover, a main difference to the here proposed concept consists in the limitation on elastic parts in the 'discrete gradient/derivative' which has been supplemented in Armero and Zambrana-Rojas [9] with a special metric, enforcing volumetric properties of the plastic flow. Furthermore, in sharp contrast to our formulation which actually allows the application of the local update in a modular way, the formulation of Armero [5, 9] rests upon a monolithic treatment of the global and local time-integration, involving necessarily a particularly designed non-standard update procedure for the plastic variables. Even if this specific update is second-order accurate, it additionally requires (staggered) local iterations in any case, accompanied by a crucially increasing implementation effort.

4. As investigated extensively in Chapter 4 for the non-dissipative case, an enhanced algorithmic stress tensor of type (5.26) can suffer from serious numerical pitfalls, when eigenvalue-based constitutive models in combination with the well-established perturbation technique are involved. In this context, a mixed evaluation strategy has been proposed in Section 4.4 as an appropriate remedy. Furthermore, also the specific formulation of isotropic plasticity, that has been chosen as a fundamental example, relies essentially on spectral representations, as shown in Section 5.1.2. In particular, the underlying Helmholtz energy density of the exemplary elasto-plastic model considered in this contribution is of the Hencky-type (4.11), compare Equation (5.18). Consequently, a mixed evaluation strategy has also been chosen for the dissipative case, rendering

$$\boldsymbol{S}^{alg}(1/2) := \boldsymbol{S}^{\delta}_{1/2} + \frac{2\,[\psi_{\alpha=1} - \psi_{\alpha=0} + \Delta d\,] - \boldsymbol{S}^{\delta}_{1/2} : [\boldsymbol{C}_2 - \boldsymbol{C}_1]}{||\boldsymbol{C}_2 - \boldsymbol{C}_1||^2}[\boldsymbol{C}_2 - \boldsymbol{C}_1]\,, \quad (5.32)$$

wherein a perturbed evaluation of the stresses is combined once more with an unperturbed evaluation of the Helmholtz energy density, compare Equation (4.37).

5.3. Numerical Examples – Fundamental Results

To demonstrate the excellent numerical performance and to investigate fundamental properties of the proposed time-stepping schemes, three representative examples (2d, plane strain conditions) are presented next, based on the specific algorithms outlined in Section 5.2. Already in this basic case the crucial properties of the time integrators can be shown. Nevertheless, please recall that the general Galerkin-based framework proposed in Section 3.3 conceptually allows the application of arbitrary polynomial degrees k. In the following, special emphasis will be placed on the claimed consistency properties. Analogously to Equation (4.46) for non-dissipative dynamics, we introduce in the dissipative case the residual

$$R := \widetilde{H}_{n+1} - \widetilde{H}_n \stackrel{!}{=} 0 \tag{5.33}$$

to investigate the fulfilment of the balance of the augmented Hamiltonian (3.62) in detail, representing a true measure for global energy-consistency. In the following numerical examples, the constitutive behaviour relies on a Helmholtz energy density of Hencky-type in combination with a 'v. Mises'-type yield function including linear isotropic hardening effects, as introduced in Section 5.1.2.

5.3.1. Flying Frame

The first example in this context deals with the free motion of the 'Flying Frame' introduced in Section 4.5, whereby the initial setup of the frame is pictured in Figure 4.17 a) [4]. The following computations have been performed with the constant time-step size $h_n = 0.1$, using the parameters $\rho = 3.0$, $||\bar{\boldsymbol{v}}_0|| = 85$, $f_{max} = 30$, $T_{load} = 0.5$, $\lambda = 1000$, $\mu = 500$, $Y_0 = 50$, and $H^{rd} = 100$. The main issue of the present example is the investigation of the influence of the applied number of integration points in time n_{gp_t} regarding the obtained conservation properties. Therefore, the standard approximation (5.20) has been chosen regarding the evaluation of the related time-integrated internal load vector, whereby the standard case of one integration point in time $n_{gp_t} = 1$ (indicated by '1 GP'), rendering the classical midpoint scheme, is exemplarily compared with the choice $n_{gp_t} = 2$ (referred to as '2 GP'). The results are shown in Figure 5.4 and Figure 5.5 respectively. Thereby, Figure 5.5 confirms once more the well-known fact that the resulting (midpoint) scheme based on a standard Gauss quadrature rule with $n_{gp_t} = 1$ features a

[4] In this and also in all following examples, a standard displacement-based formulation is still used for the FE discretisation in space, focussing on the actual time-integration. However, also a mixed formulation could by adapted appropriately to avoid volumetric locking effects related to (plastic) incompressibility, as discussed in Gonzalez [64] for the conserving integration of incompressible elastodynamics. Furthermore, an overview of different FE strategies to prevent locking in the context of conserving/decaying schemes can be found in Kuhl and Ramm [96] with special emphasis on shell dynamics. Moreover, adequate assumed strain formulations based on the so-called 'B-bar operator' have been recently investigated by Armero [6] in the context of dynamics.

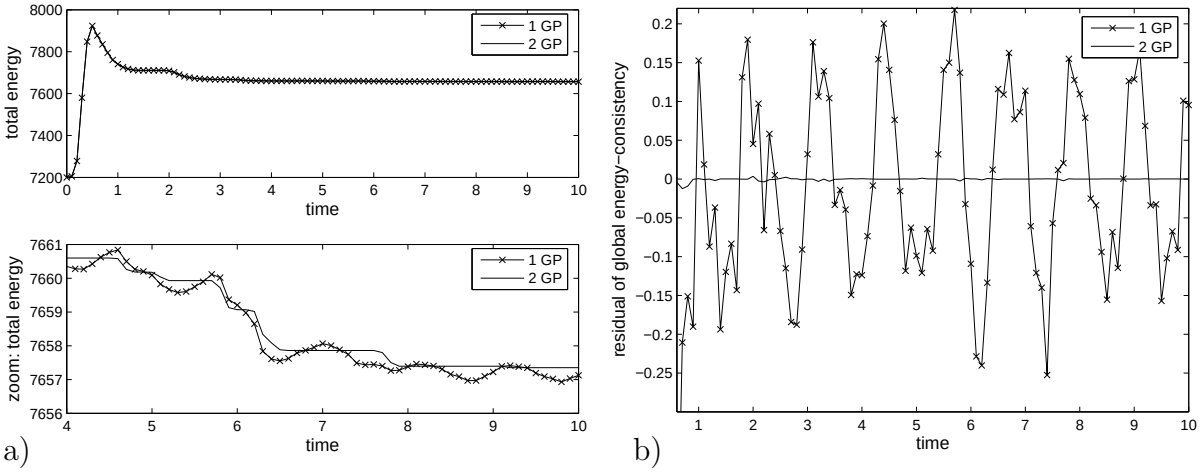

Figure 5.4.: influence of n_{gp_t}: a) total energy H, b) global energy-consistency based on R

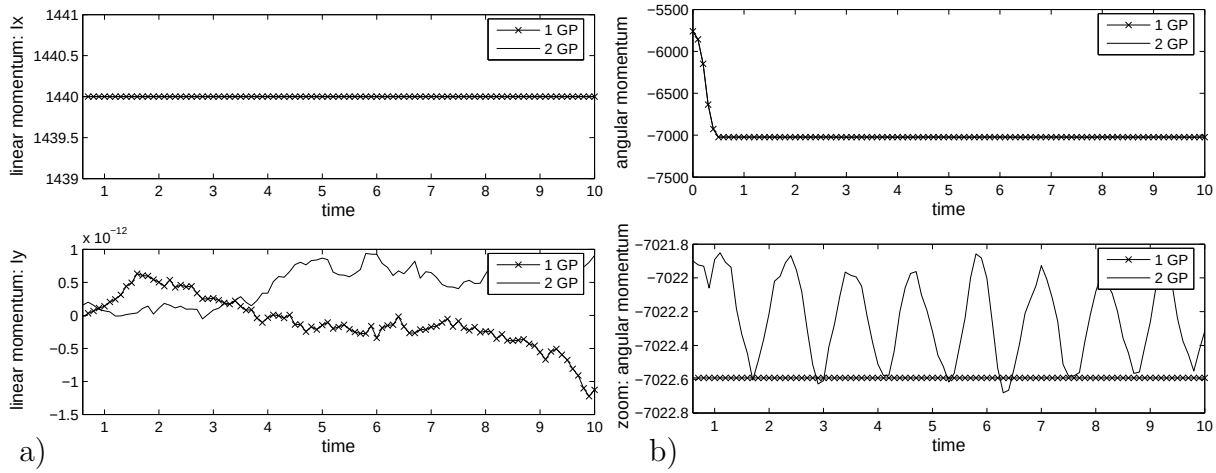

Figure 5.5.: influence of n_{gp_t}: a) components of the linear momentum, b) component of the angular momentum (zoom)

mechanically consistent integration also in the plastic case, including the conservation of the linear as well as the angular momentum. Nevertheless, such a standard quadrature rule combined with one Gaussian integration point in time suffers crucially from oscillations of the total energy, as shown in Figure 5.4 a), and violates clearly the claimed monotonic decrease of the total energy due to a (strictly) positive plastic dissipation. Consequently, the scheme is neither thermodynamically nor energy-consistent, compare also Figure 5.4 b). Please recall, that this inconsistency is caused by approximation errors of the used quadrature rule, since the highly nonlinear time integral including the internal load vector can not be integrated exactly. At first glance, one appropriate remedy could be an intuitive increase of the applied number of time-integration points.

As shown in Figure 5.4 a), the required monotonic decrease of the total energy seems to be featured for the resulting scheme based on $n_{gp_t} = 2$ and also the error within the residual R is visibly reduced, even if energy-consistency is still not guaranteed within the calculation accuracy. However, an increasing number of time-integration points does not represent an adequate solution, since in this case the better performance regarding the energy balance is gained at the expense of the conservation of the angular momentum, as shown in Figure 5.5 b). Therefore, mechanical consistency is not guaranteed anymore influenced by the violated collocation property. Moreover, it is well-known in literature that the conservation of the angular momentum might have a crucial influence on the quality of the results. Consequently, the standard quadrature rule (5.20) seems to be an improper choice in view of a completely consistent time-integration of finite elasto-plasto-dynamics, analogously to the well-studied hyperelastic case.

5.3.2. Oscillating Bar

The second example deals with an oscillating bar consisting of 27 isoparametric 4-node elements in space. The bar is fixed at its left side and excited due to some external loads $\bar{\boldsymbol{F}}^{ext}(t) := [\boldsymbol{F}_1^{ext}(t), ..., \boldsymbol{F}_{n_{node}}^{ext}(t)]^{\mathrm{t}}$ at the right end. In this regard, the norm of the external nodal-load $||\boldsymbol{F}_I^{ext}||$ at the loaded (spatial) node I increases once more linearly in time up to a maximum value $f_{max} = 600$. Subsequently, it decreases again linearly to zero, compare Figure 5.6 a). After a loading period of $T_{load} = 1.0$, the bar oscillates without excitation. For these computations a large time step $h_n = 0.1$ has been used in combination with the mass density $\rho = 3.0$. Exceedingly stiff material properties have been applied for the oscillating bar, namely $\lambda = 300\,000$, $\mu = 100\,000$, $Y_0 = 2000$, and $H^{rd} = 1$. Such a high stiffness has been chosen for two reasons: On the one hand, it is well-known that computations with stiff material properties can cause in general significant numerical problems in the context of computational dynamics due to involved high-frequency modes. On the other hand, it has been demonstrated in Chapter 4 that potential pitfalls, which are related to the specific type of the involved stress enhancement, might be exposed by an increase of the stiffness. To compare the resulting performance, three different Galerkin-based time-stepping schemes have been applied for the present example:

- A mechanically consistent cG(1) method based on the approximation (5.23) that renders the classical midpoint scheme.
- A mechanically consistent cG(1) scheme based on the approximation (5.24), including an assumed strain approximation in time as an additional feature. The resulting scheme represents a modified midpoint scheme and will be denoted in this and the following example as 'midpoint+' scheme.
- An 'ECMC-cG(1) method' based on the elasto-plastic enhanced algorithmic stress tensor (5.26).

In Figure 5.6, a large deflection of the bar can be seen as well as a huge plastic dissipation, which is in the range of 90% of the total energy. At first glance, the results of the three integrators regarding the total energy H are quite similar. However, the differences can be clearly seen in Figure 5.6 b), when zooming-in. In this context, the midpoint scheme renders once more an increase of the total energy, for instance at $t = 2.2$, that is obviously related to a strong violation of the energy-consistency. Considering the residual of global energy-consistency given by Equation (5.33), the differences between the three Galerkin-based schemes are serious. As displayed in Figure 5.7, global energy-

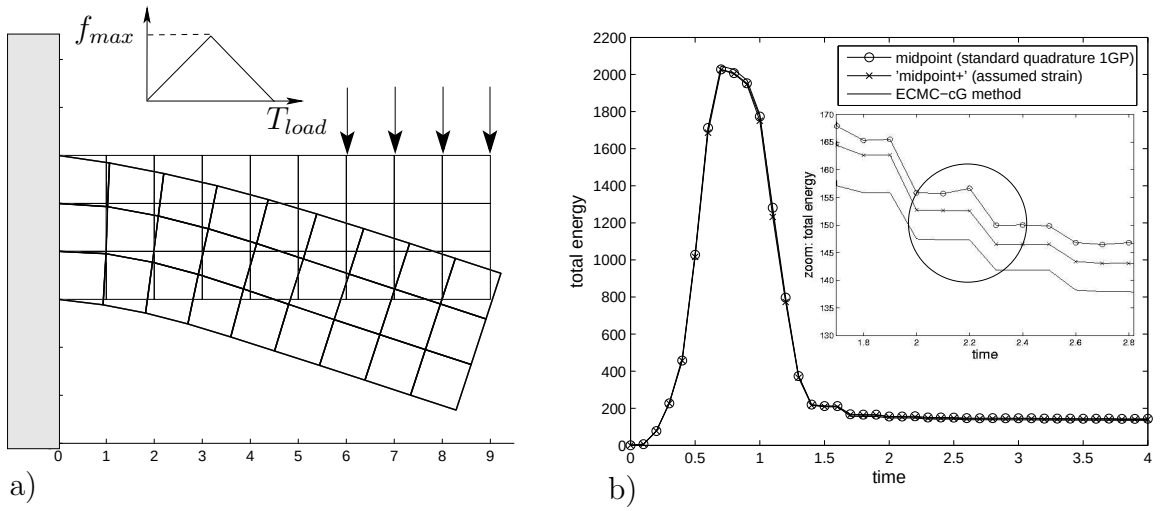

Figure 5.6.: a) undeformed/deformed configuration $\mathcal{B}_0/\mathcal{B}_t$ with external loads including loading history, b) total energy H (zoom) computed with different quadrature rules

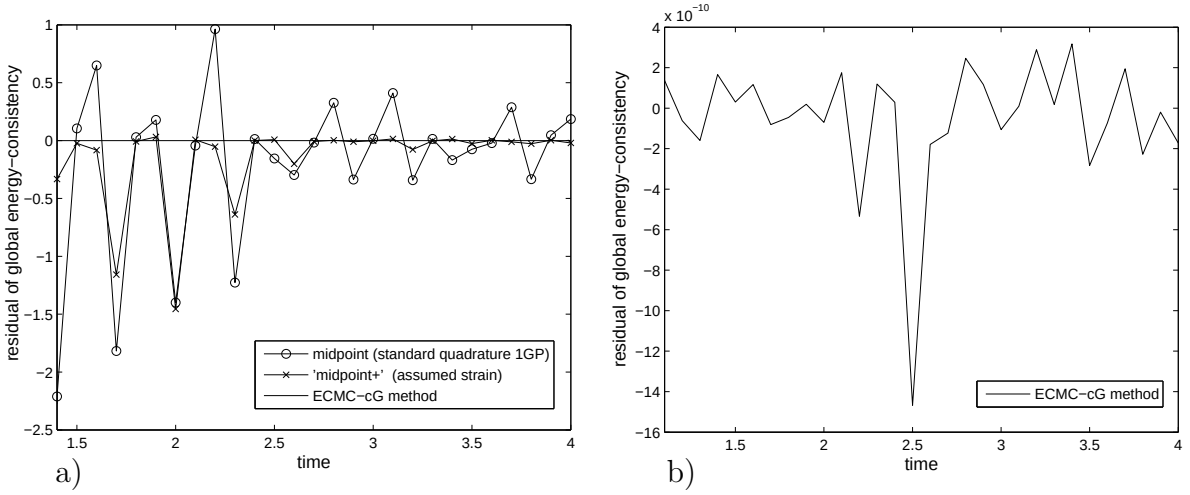

Figure 5.7.: a) global energy-consistency based on the residual R for different quadrature rules, b) zoom: global energy-consistency based on R for the 'ECMC-cG(1) method'

consistency can be guaranteed solely by using the 'ECMC-cG(1) method'. Moreover, the performance of the 'midpoint+' scheme concerning this matter is superior compared to the performance of the standard midpoint scheme. Consequently, the 'midpoint+' scheme will be preferred for the following benchmark computations. Hereby, it is important to emphasise once more that by incorporating the 'ECMC-cG(1) method' global energy-consistency is indeed guaranteed in a 'numerically exact manner', although the dissipation is immense. In fact, it can be seen in Figure 5.7 b) that the fulfilment of Equation (5.33) is guaranteed within the order of magnitude $\mathcal{O}(10^{-10})$.

5.3.3. Spinning Wheel

The third representative numerical example shows the motion of the 'Spinning Wheel', involving plastic deformations. In this context, the initial configuration of the wheel is equivalent to the hyperelastic case discussed in Section 4.6, using $\rho = 3.0$ and $||\bar{\boldsymbol{v}}_0|| = 83$. Again, external loads $\bar{\boldsymbol{F}}^{ext}$ act on the circlet, whereby in contrast to the hyperelastic case the norm of each external nodal-load $||\boldsymbol{F}_I^{ext}||$ is prescribed by a sinusoidal load function in time incorporating the amplitude $f_{max} = 10$ and the loading period $T_{load} = 2.5$, as shown in Figure 5.8 a). Analogously to the 'mixed stiffness motion' of the hyperelastic case considered in Section 4.6.2, the wheel is composed of stiff and non-stiff regions to fortify the capability of the proposed Galerkin-based time-stepping schemes also in the elasto-plastic context. For the spokes the parameters $\lambda_1 = 1000$, $\mu_1 = 500$, $Y_{0,1} = 50$, and $H_1^{rd} = 50$ have been incorporated. In contrast, stiff material properties have been used for the nave and the circlet, namely $\lambda_2 = 90\,000$, $\mu_2 = 30\,000$, and $Y_{0,2} = \infty$. Consequently, the plastic deformations will take place solely within the spokes, as can be regarded in Figure 5.10 based on a contour plot of the hardening variable κ. In the present case, two Galerkin-based schemes have been used for the computation of the motion, namely

- the 'midpoint+' scheme involving the approximation (5.24) and
- the 'ECMC-cG(1) method' based on the non-standard quadrature rule defined in Equation (5.25).

A further challenge for the applied time integrators is the change of the time-step size from $h_n = 0.1$ to $h_n = 0.2$ subsequent to a simulation time of $t = 3.5$, as illustrated in Figure 5.8 b). The deformed configuration at $t = 80$ and a sequence of the motion, including four particular configurations corresponding to $t = 0.1,\ 3.5,\ 30.5,\ 80$, are displayed in Figure 5.9. As expected, we observe comparatively large strains within the spokes and a nearly rigid nave. In Figure 5.11, it is confirmed that mechanical consistency, implying the conservation of related components of linear and angular momentum, is enabled by the 'midpoint+' scheme as well as by the 'ECMC-cG(1) method'. Nevertheless, this example demonstrates impressively the advantages of the 'ECMC-cG(1) method' and the positive influence of algorithmic energy-consistency concerning the robustness of the

resulting time-stepping scheme. Exclusively, the completely consistent scheme enables a simulation until $t = 80$ for the chosen time-step size. In sharp contrast, a calculation by means of the 'midpoint+' scheme stops at $t = 30.5$ due to an energy blow-up, compare Figure 5.12 a). However, the 'ECMC-cG(1) method' guarantees a conservation of the augmented Hamiltonian (see Figure 5.12 b)) in spite of an accumulated dissipation (compare Figure 5.13), which contains nearly 20% of the total energy. Furthermore, the differences between both integrators become obvious by comparing the obtained global energy-consistency based on Equation (5.33), see Figure 5.14. The application of the 'midpoint+' scheme yields strong oscillations in the order of magnitude $\mathcal{O}(10^0)$, whereas the 'ECMC-cG(1) method' guarantees (global) energy-consistency unaffected by a doubling of the time-step size.

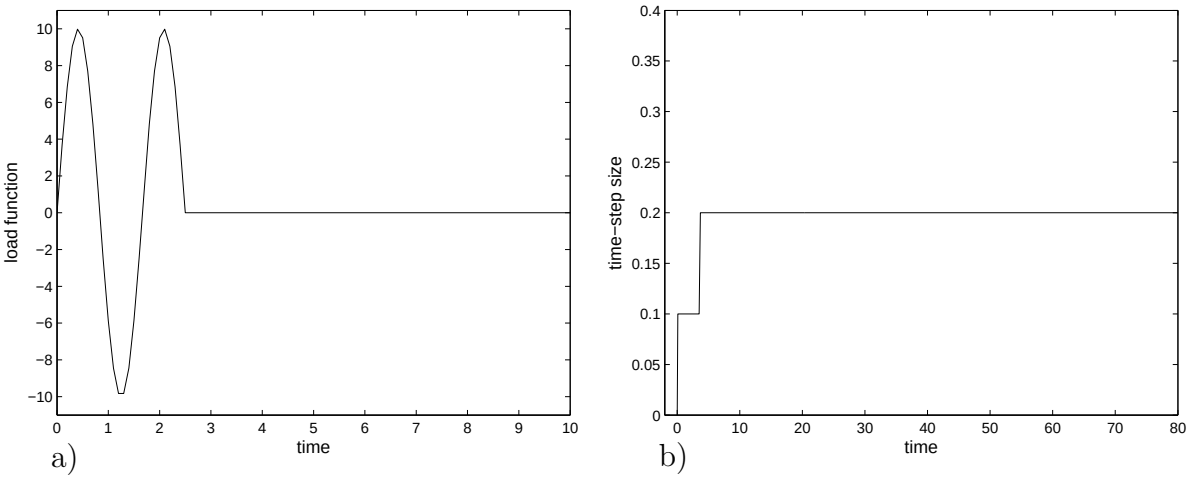

Figure 5.8.: a) sinusoidal loading history, b) change of the time-step size for $t > 3.5$

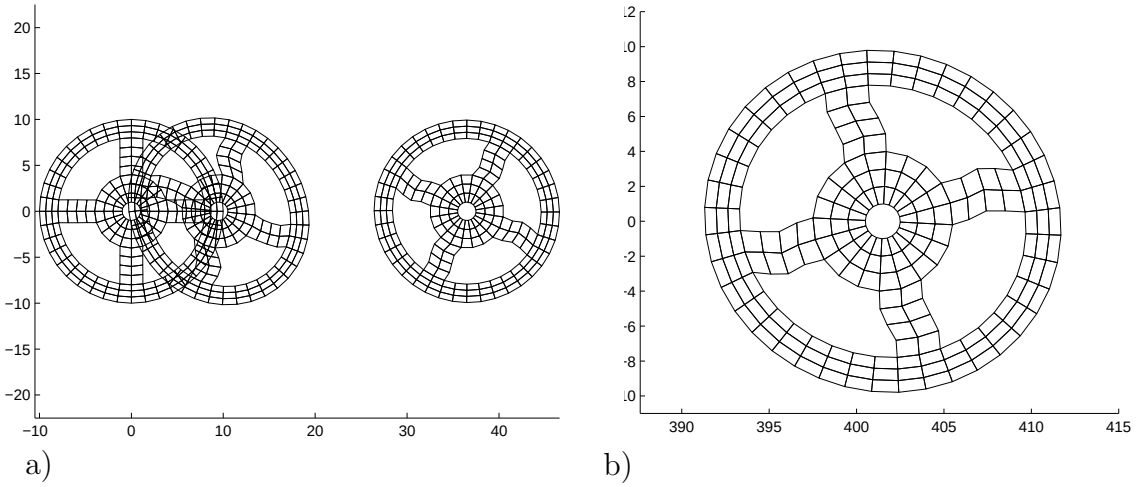

Figure 5.9.: a) sequence of the motion, b) deformed configuration $\mathcal{B}_t$ at $t = 80$

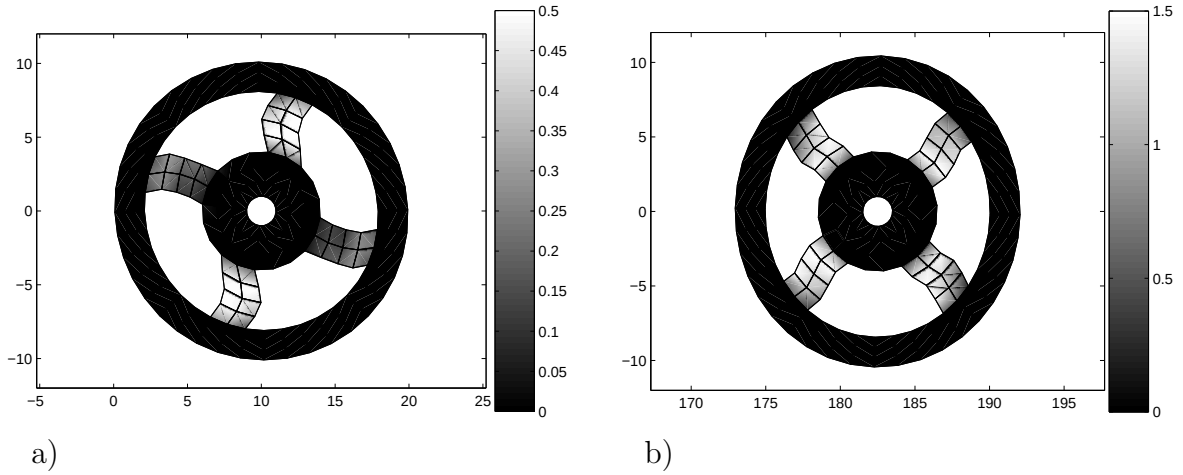

Figure 5.10.: contour plot of the hardening variable κ: a) $t = 2$, b) $t = 36.3$

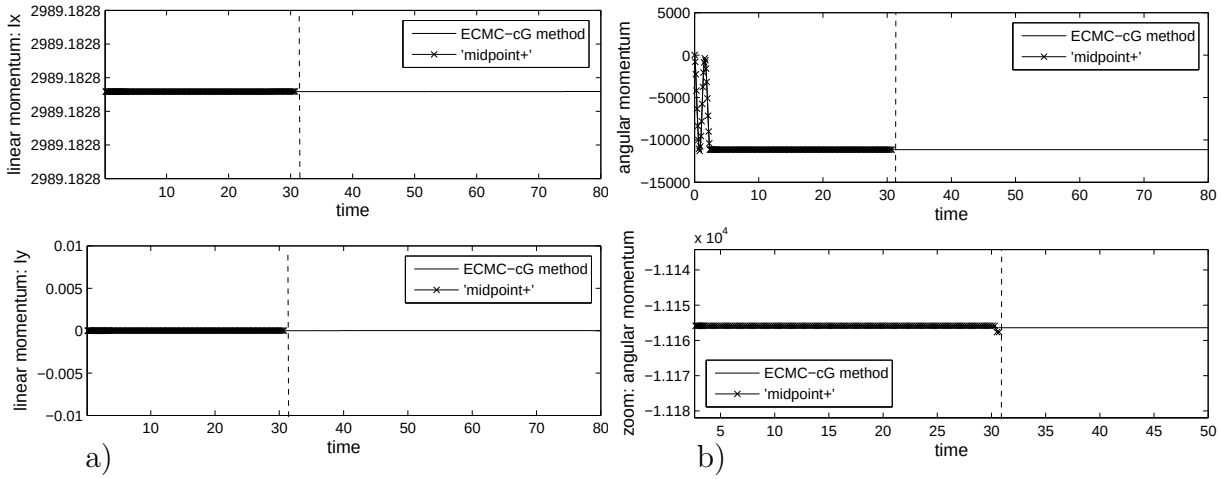

Figure 5.11.: a) components of the linear momentum, b) component of the angular momentum (zoom)

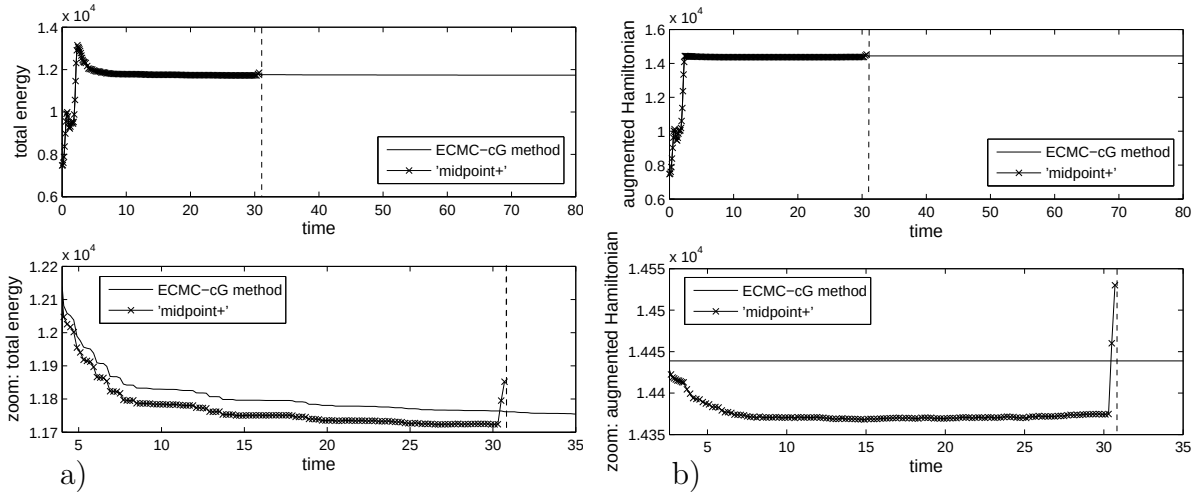

Figure 5.12.: a) total energy H (zoom), b) augmented Hamiltonian $\widetilde{H}$ (zoom)

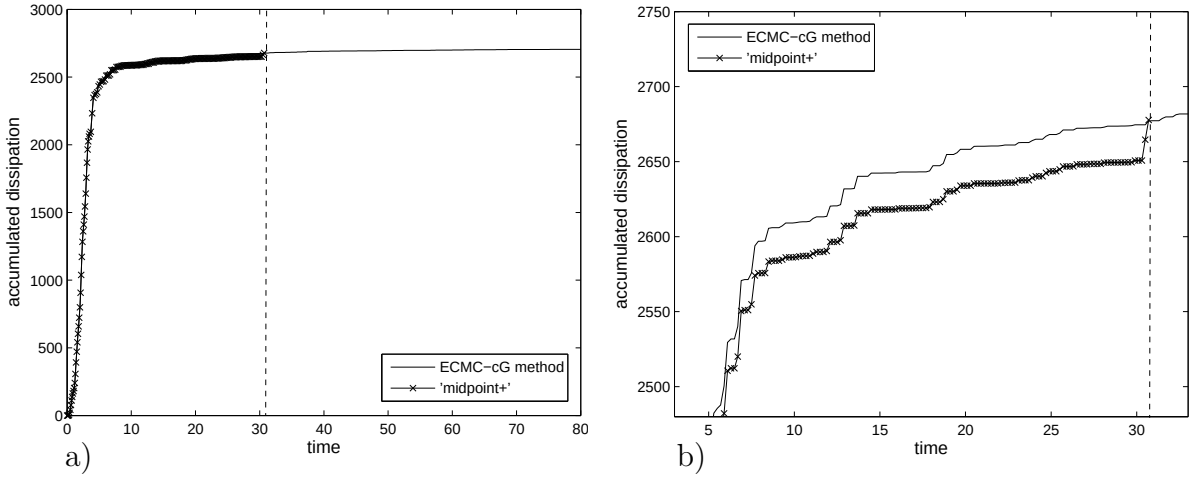

Figure 5.13.: a) accumulated dissipation D, b) zoom: accumulated dissipation D

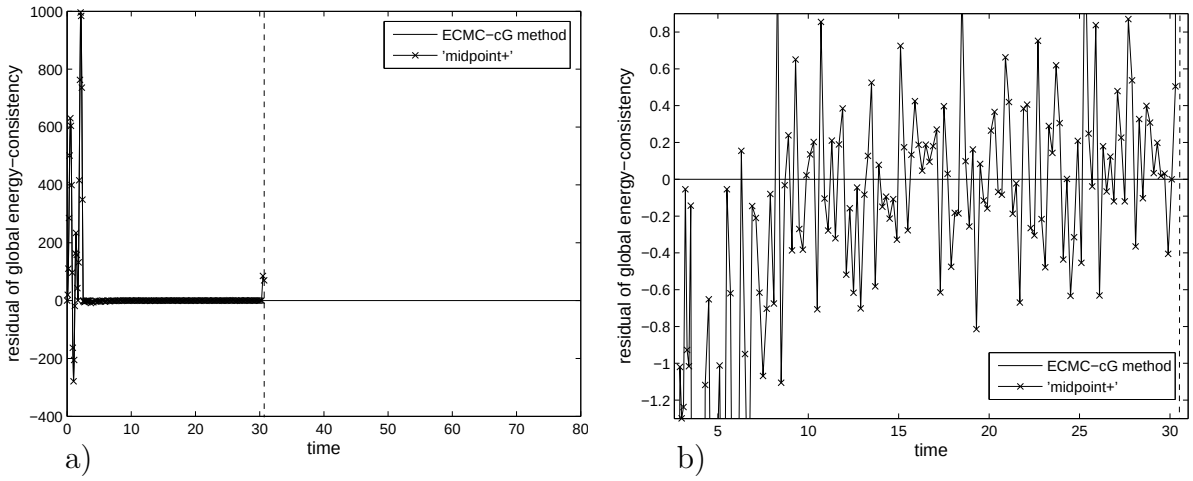

Figure 5.14.: a) global energy-consistency based on the residual R, b) zoom: global energy-consistency

5.4. Influence of the Predictor Strategy

In the previous section, several representative numerical examples have been presented, that have clearly demonstrated the excellent numerical performance of the Galerkin-based integrators, particularly of the 'ECMC-cG(1) method'. In this context, it has been shown that global energy-consistency can be guaranteed within the calculation accuracy even if huge plastic deformations are involved, rendering a robust integration. However, one aspect that has not been addressed so far is the application of an adequate predictor strategy to achieve the optimal performance of the integrator. In fact, it is quite obvious that, especially in the elasto-plastic case, an appropriate predictor step might be helpful concerning the convergence of the involved iteration scheme, which is needed to solve the global set of nonlinear equations of motion (4.24). In particular, it is demonstrated in this section that the realisable plastic deformations crucially depend on the chosen predictor strategy, since otherwise the limited radius of convergence of the underlying (standard) Newton-Raphson scheme prohibits a numerical calculation, especially if energy-consistency is additionally enforced. For this purpose, we consider once more the 'Oscillating Bar' introduced in Section 5.3.2 and reduce successively the initial yield stress Y_0 as long as a subsequent calculation is still possible for the time period $t \in [0, 4]$. By repeating this procedure for different time-step sizes h_n, we obtain the resulting map of the minimal achievable yield stress that is pictured in Figure 5.15 a). On the one hand, the 'ECMC-cG(1) method' combined with the standard predictor strategy [5]

$$\bar{\boldsymbol{q}}_2^{pre} = \bar{\boldsymbol{q}}_1 + h_n \, \mathbb{M}^{-1} \cdot \bar{\boldsymbol{p}}_1 \tag{5.35}$$

has been compared with a computation without any specific predictor step, meaning

$$\bar{\boldsymbol{q}}_2^{pre} = \bar{\boldsymbol{q}}_1 \, . \tag{5.36}$$

On the other hand, we propose a very powerful 'cG predictor strategy', that contains a pre-solution of the equations of motion based on the standard approximation (5.24), followed by the actual solution procedure relying on the non-standard quadrature rule (5.25). Formally, this predictor step can also be included directly in the 'ECMC-cG(1) method' by introducing a parameter χ into the elasto-plastic enhanced algorithmic stress tensor, resulting in

$$\boldsymbol{S}^{alg}(1/2) := \boldsymbol{S}_{1/2} + \chi \, \frac{2\,[\psi_{\alpha=1} - \psi_{\alpha=0} + \Delta d\,] - \boldsymbol{S}_{1/2} : [\boldsymbol{C}_2 - \boldsymbol{C}_1]}{||\boldsymbol{C}_2 - \boldsymbol{C}_1||^2} [\boldsymbol{C}_2 - \boldsymbol{C}_1] \, . \tag{5.37}$$

[5] Taking additionally the external load vector into account, an alternative formulation is represented by

$$\bar{\boldsymbol{q}}_2^{pre} = \bar{\boldsymbol{q}}_1 + h_n \, \mathbb{M}^{-1} \cdot \bar{\boldsymbol{p}}_1 + \frac{1}{2} \, h_n^2 \, \mathbb{M}^{-1} \cdot \bar{\boldsymbol{F}}^{ext} \, , \tag{5.34}$$

whereby, in our experience, the foregoing predictor step works particularly effective for free motion problems. However, for the here considered example Equation (5.34) has not performed sufficiently well and consequently Equation (5.35) has been preferred for this study.

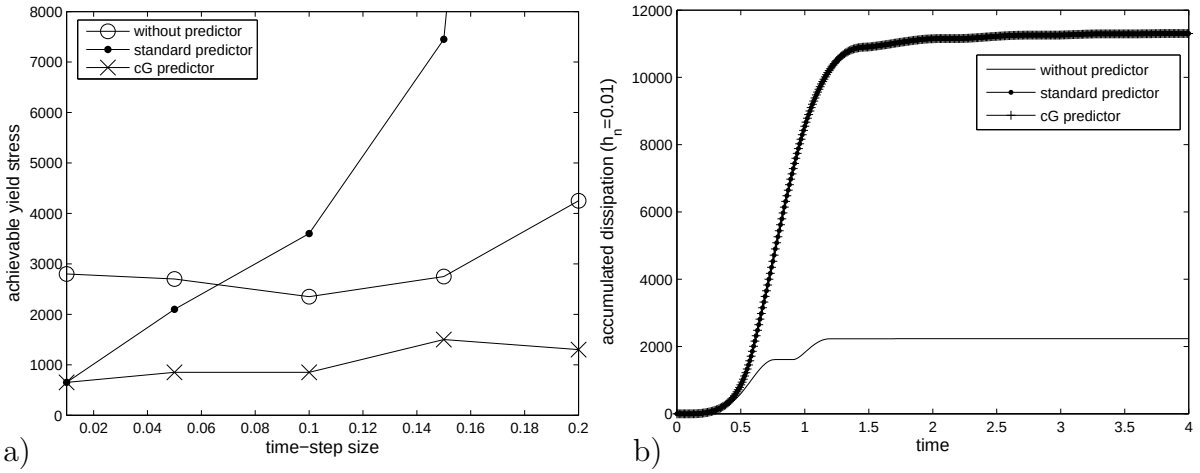

Figure 5.15.: a) minimal achievable yield limit Y_0 for different predictor strategies, b) accumulated dissipation D for $h_n = 0.01$

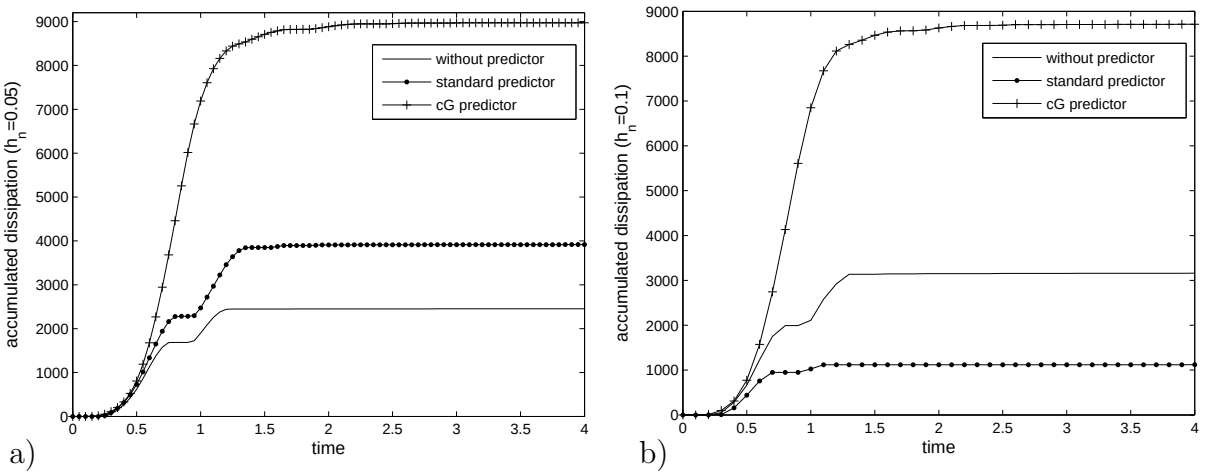

Figure 5.16.: accumulated dissipation D for: a) $h_n = 0.05$, b) $h_n = 0.1$

Thereby, the parameter is initialised as $\chi = 0$. After a first convergence of the Newton scheme, we set $\chi = 1$ and iterate until the iteration scheme reaches the tolerance a second time. Even if this approach is, in general, more expensive than a standard predictor step, it allows in most of the cases the incorporation of immense plastic deformations, as shown in Figure 5.15 a). The corresponding plot clearly demonstrates that the 'cG predictor strategy' allows for all considered time-step sizes a simulation with the minimal initial yield stress Y_0. Thereby, the applicable yield limit is nearly independent from the chosen time-step size, rendering perfect convergence of the involved iteration scheme. Contrariwise, the standard predictor is only for small time-step sizes competitive, and requires particularly for $h_n \geq 0.1$ fundamentally higher yield limits. Actually, a calcula-

tion of the present example using the standard predictor (5.35) is only possible for the purely elastic case, when $h_n = 0.2$ is chosen. Otherwise, the global iteration scheme stops after a certain number of time steps due to convergence problems. For large step sizes, even the 'ECMC-cG(1) method' without specific predictor step performs better. The differences concerning the resulting dissipation, that are related to the realisable yield limit, are indeed significant, as shown exemplarily for three time-step sizes in Figure 5.15 b) and Figure 5.16 respectively. For instance, the feasible accumulated dissipation is nearly three times higher for $h_n = 0.1$ when the 'cG predictor strategy' is taken into account, see Figure 5.16 b).

Remarks 5.5:

1. Please notice, that the best choice for the predictor step also depends on the considered example, influenced for instance by the initial as well as by the boundary conditions. Consequently, the applied strategy has to be attuned to the specific case. Nevertheless, the here proposed 'cG predictor strategy' represents an attractive alternative, facilitating the incorporation of huge plastic deformations for a wide range of time-step sizes.

2. The described procedure of the 'cG predictor step' can also be interpreted as a special projection technique, whereby the initially mechanically consistent solution of the standard quadrature rule (5.24) is finally projected to fulfil additionally the constraint of energy-consistency. A similar interpretation has also been proposed by French and Schaeffer [57] for their dynamical integration approach.

5.5. Aspects of Convergence

The superior performance of the time-stepping scheme based on the non-standard quadrature rule (5.25) concerning the obtained consistency properties has been impressively demonstrated in Section 5.3, rendering a notably robust time-integration. However, one important aspect that has not been addressed so far is the convergence behaviour of the considered 'ECMC-cG(1) method'. In this context, essential issues are

- the *mathematical consistency* of the underlying non-standard quadrature rule (5.25),

- the related *fundamental convergence* of the final scheme, especially in the plastic case, and moreover

- the resulting (global) *order of accuracy* of the integrator in the plastic case, bearing in mind that for the local integration exemplarily a first-order format of the well-accepted exponential update has been chosen, as discussed in Section 5.1.2.

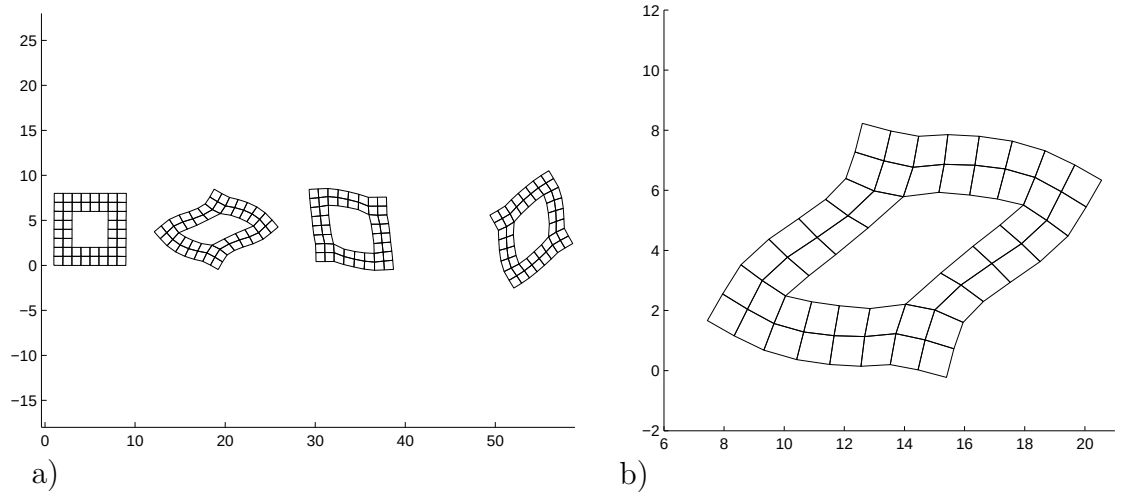

Figure 5.17.: a) sequence of the motion, b) deformed configuration $\mathcal{B}_t$ at $t = 1$

In the following, we investigate the offered convergence performance by means of various characteristic indicators, taking relative as well as integral error measures into account. As a representative numerical example, once more, the free flight of the 'Flying Frame' introduced in Section 4.5 is considered, incorporating the parameters $\rho = 3.0$, $||\bar{\boldsymbol{v}}_0|| = 85$, $f_{max} = 30$, and $T_{load} = 0.5$. Analogously to previous examples, the constitutive modelling relies on a Helmholtz energy density based on logarithmic strains combined with a 'v. Mises'-type yield function, using $\lambda = 1000$, $\mu = 500$, $Y_0 = 50$ and $H^{rd} = 100$.

5.5.1. Basic scheme

We start our investigations with the initial setup of the 'ECMC-cG(1) method' that relies on the non-standard quadrature rule (5.25) based on the elasto-plastic enhanced algorithmic stress tensor (5.26), applying the standard integration strategy which has been introduced in Equations (5.27), (5.28) [6]. The deformed configuration of the frame at $t = 1$ and some snapshots of the motion are pictured in Figure 5.17. Obviously, the plastic deformations are substantial and render a significant decrease of the total energy H, as can be seen in Figure 5.18 a). To assess the offered convergence performance of the 'basic scheme', firstly, we introduce the relative global error in the positions $\bar{\boldsymbol{q}}^h$ at time T given by

$$e_{\bar{\boldsymbol{q}}^h}(T) = \frac{||\bar{\boldsymbol{q}}^h(T) - \bar{\boldsymbol{q}}^h_{ref}(T)||}{||\bar{\boldsymbol{q}}^h_{ref}(T)||}\,. \tag{5.38}$$

[6] With regard to a compact notation, the resulting scheme will be referred to as 'basic scheme' in the subsequent discussions.

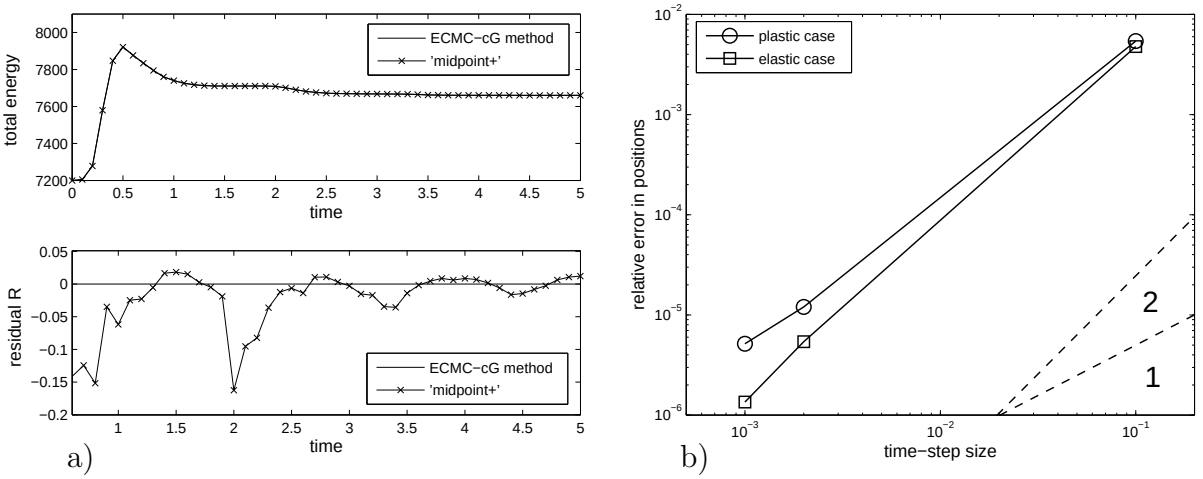

Figure 5.18.: a) total energy H & global energy-consistency based on the residual R ($h_n = 0.1$), b) relative global error $e_{\bar{\boldsymbol{q}}^h}(T)$ of the 'ECMC-cG method' at $T = 1.0$

In this context, the reference solution $\bar{\boldsymbol{q}}^h_{ref}$ has been calculated by means of the rather small time-step size $h_n = 10^{-4}$. In Figure 5.18 b), the fundamental convergence of the integrator is shown at $T = 1.0$ for the plastic as well as for the well-studied purely elastic case, defining a kind of benchmark case. In the purely elastic case, the obtained (global) order of accuracy clearly confirms the results of the literature, being second-order accurate in time when linear time shape functions are incorporated. However, as expected, the combination of linear Finite Elements in time on the global level and the basic exponential update for the local integration leads to a loss of accuracy when plastic deformations are involved. Figure 5.18 b) clearly shows that, in comparison to the elastic case, the global order of accuracy is reduced in the plastic case. Additionally, this result is confirmed in Figure 5.19 a) for further evaluation times, using $T \in \{0.1, 0.5, 1.0\}$. Nevertheless, from a practical point of view the differences are not crucial in this example, even for a non-negligible dissipation. Moreover, special emphasis is placed in this work on the claimed global energy-consistency which is guaranteed by the 'ECMC-cG(1) method' (see also Figure 5.18) unaffected by the order of accuracy of the local update, compare also Remark 3.4.1. Alternatively to the relative (global) error in the positions $e_{\bar{\boldsymbol{q}}^h}(T)$ introduced in Equation (5.38), the relative (global) error in the momenta

$$e_{\bar{\boldsymbol{p}}^h}(T) = \frac{||\bar{\boldsymbol{p}}^h(T) - \bar{\boldsymbol{p}}^h_{ref}(T)||}{||\bar{\boldsymbol{p}}^h_{ref}(T)||} \tag{5.39}$$

has been considered for the present example. Thereby, also this second error measure fortifies the foregoing results, referring to Figure 5.20 a) for a comparison to the purely elastic motion and to Figure 5.20 b), respectively, for a comparison between two different evaluation times T. So far, the convergence properties of the 'ECMC-cG(1) method' have

been investigated by means of error measures which involve only one certain evaluation time T. In addition to such discrete indicators, the mean-square norm of the error in the positions $e_{L_2}(\bar{\boldsymbol{q}}^h)$ defined by

$$e_{L_2}(\bar{\boldsymbol{q}}^h) = \left[\int_{t_a}^{t_b} \sum_{I=1}^{n_{node}} \left[\boldsymbol{q}_I^h(t) - \boldsymbol{q}_{ref,I}^h(t) \right]^2 \mathrm{d}t \right]^{\frac{1}{2}} \tag{5.40}$$

has been calculated, involving the entire evolution of the deformation during the time period $[t_a, t_b]$. The resulting convergence behaviour is pictured in Figure 5.19 b), incorporating the interval $[t_a, t_b] = [0.5, 1.0]$ which covers the major part of the plastic deformation process, compare Figure 5.18 a). Once more, the order reduction in the plastic case becomes obvious. In the foregoing investigations, the convergence of the integrator has been illustrated by means of various error measures based on fundamental variables of the global formulation, like positions or momenta. Next, special emphasis will be placed on characteristic parameters related to the global energy balance which are essentially influenced by the local update procedure. In this context, the accumulated dissipation D and the augmented Hamiltonian $\widetilde{H}$ are investigated more detailed concerning their convergence behaviour. In Figure 5.21, the accumulated dissipation as well as the augmented Hamiltonian, which is exactly conserved within the calculation accuracy independently from the applied time-step size h_n, are pictured. Analogously to the relative error in the vector-valued positions respectively momenta, we introduce the relative error in the accumulated dissipation $e_D(T)$ and the relative error in the augmented Hamiltonian $e_{\widetilde{H}}(T)$, given by

$$e_D(T) = \frac{|D(T) - D_{ref}(T)|}{|D_{ref}(T)|} \qquad \text{and} \qquad e_{\widetilde{H}}(T) = \frac{|\widetilde{H}(T) - \widetilde{H}_{ref}(T)|}{|\widetilde{H}_{ref}(T)|} \tag{5.41}$$

respectively. As shown in Figure 5.22 a) for $T \in \{1.0, 1.5\}$, the relative error in the accumulated dissipation decreases monotonically when the time-step size is reduced. The same statement holds also for the relative error in the augmented Hamiltonian, as plotted in Figure 5.22 b) for $T \in \{0.2, 1.0\}$. Moreover, it can be seen that for the here considered evaluation times the relation $T_j > T_i$ renders in both cases $e_{D/\widetilde{H}}(T_j) > e_{D/\widetilde{H}}(T_i)$, analogously to the previous results based on $e_{\bar{\boldsymbol{q}}^h}$ and $e_{\bar{\boldsymbol{p}}^h}$. Finally, the results of the 'ECMC-cG(1) method' will be compared

- with results of the modified midpoint scheme, referred to as 'midpoint+' scheme, and furthermore
- with the results of a standard Newmark scheme [7]. In this context, the charac-

[7] The Newmark integration scheme dates back to Newmark [143] and represents until today one of the most-established time-stepping schemes at all. Originally designed for linear dynamical systems, the scheme has been addressed during the last decades in many contributions, recently for instance in References [44, 87, 88]. Even if this integrator is well-documented in nearly each textbook on numerical dynamics, like e.g. References [18, 76, 177], the fundamental equations of the Newmark scheme are summarised in Appendix C for the sake of completeness.

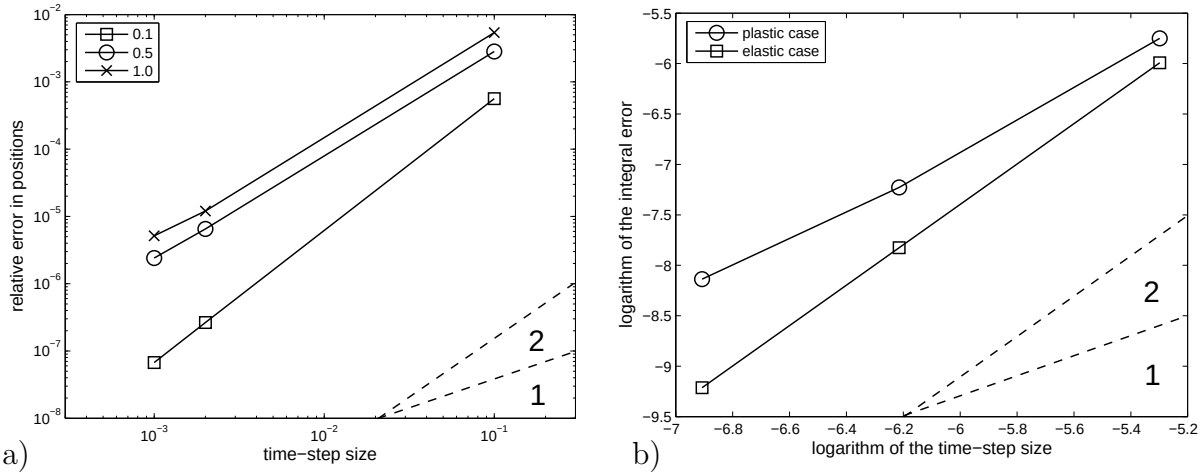

Figure 5.19.: a) relative global error $e_{\bar{\boldsymbol{q}}^h}(T)$ for $T \in \{0.1, 0.5, 1.0\}$, b) integral error $e_{L_2}(\bar{\boldsymbol{q}}^h)$ for the purely elastic/plastic case

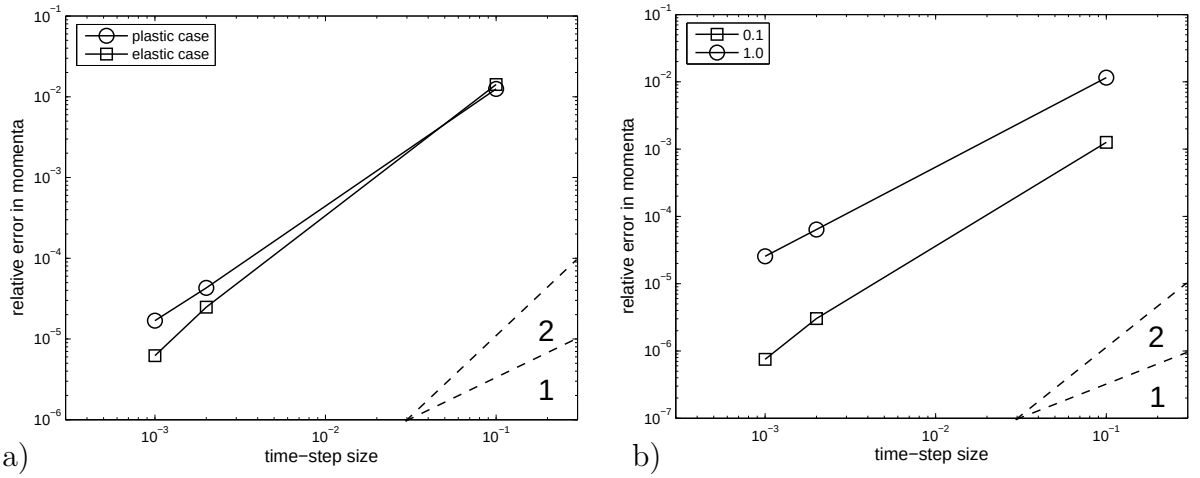

Figure 5.20.: relative global error $e_{\bar{\boldsymbol{p}}^h}(T)$: a) at $T = 0.5$ for the purely elastic/plastic case, b) for $T \in \{0.1, 1.0\}$

teristic parameters $\gamma = 0.5$ and $\beta = 0.25$ have been used, rendering the classical trapezoidal format.

In the following, the integrators will be compared based on the global accumulated dissipation D which is calculated by using three different time-step sizes, namely $h_n \in \{0.001, 0.01, 0.1\}$. The obtained dissipation plots are pictured in Figure 5.23. To investigate the convergence behaviour more detailed, the difference between the resulting accumulated dissipations of the integrators has been evaluated at $T \in \{0.4, 1.0, 1.5\}$ for the abovementioned time-step sizes, and the results are displayed in Figure 5.24. Start-

ing with a comparison between the 'ECMC-cG(1) method' based on the elasto-plastic enhanced algorithmic stress tensor (5.26) and the 'midpoint+' scheme, the results confirm one essential property of the corresponding non-standard quadrature rule: Since it holds $\boldsymbol{S}^{alg}(1/2) \to \boldsymbol{S}(\boldsymbol{C}^h(1/2), \boldsymbol{\kappa}_{1/2})$ for $h_n \to 0$, the non-standard quadrature (5.25) converges to the midpoint approximation (5.24), compare Figure 5.24 a). This fundamental property has been already pointed out for the general case of arbitrary k in Remark 3.3. A comparison between the 'ECMC-cG(1) method' and the Newmark scheme shows that in this case the differences between the accumulated dissipations are in the order of magnitude $\mathcal{O}(10^1)$ higher, due to the fundamentally distinct character of

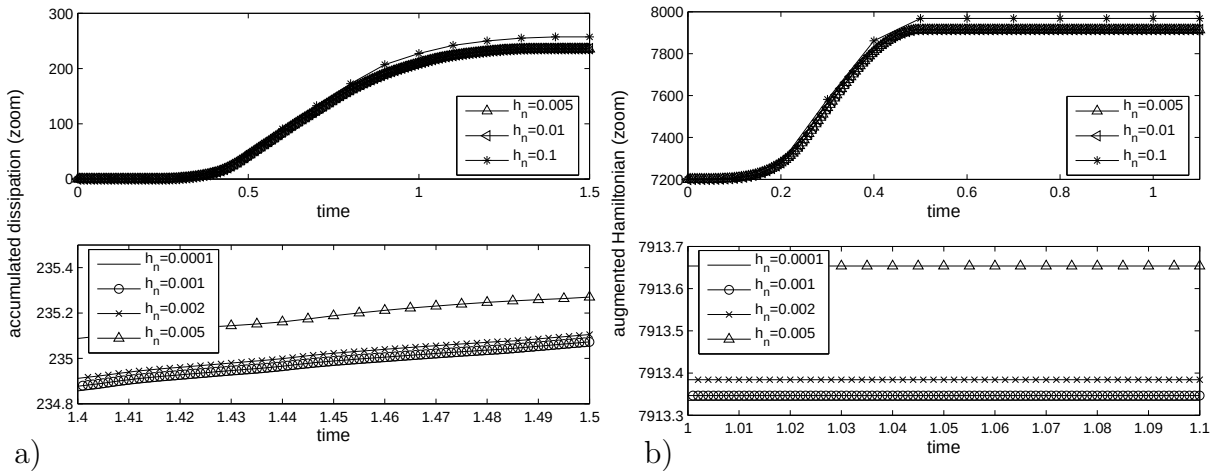

Figure 5.21.: a) accumulated dissipation D (zoom), b) augmented Hamiltonian $\widetilde{H}$ (zoom) calculated with the 'ECMC-cG(1) method'

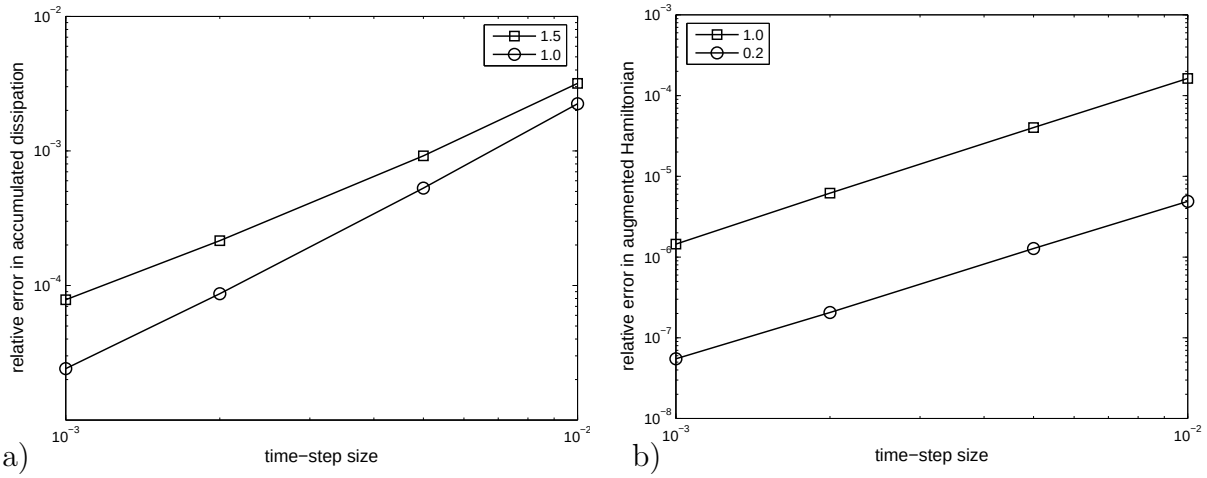

Figure 5.22.: a) relative error $e_D(T)$ for $T \in \{1.0, 1.5\}$, b) relative error $e_{\widetilde{H}}(T)$ for $T \in \{0.2, 1.0\}$

both integrators. Nevertheless, as required, the differences decrease monotonically for all of the here considered evaluation times, when the time-step size is reduced. Consequently, both integrators converge to the same solution for $h_n \rightarrow 0$, as clearly indicated by Figure 5.24 b).
In the present section, the convergence behaviour of the favoured 'ECMC-cG(1) method' has been investigated in detail. In this context, on the one hand, the fundamental convergence of this completely consistent scheme has been confirmed by using several error measures. Moreover, it has been shown based on the global accumulated dissipation that the results converge indeed to those which have been calculated by means of well-accepted standard time-stepping schemes, when the time-step size is reduced. On the other hand, it has also been demonstrated that the incorporation of the basic first-order format of the widespread exponential update leads to a reduction of the global order of accuracy, as expected. However, in our opinion, the resulting degradation is absolutely acceptable in the present example. Nevertheless, please keep in mind that the applied local update has been chosen solely as a fundamental example. In fact, the foregoing drawback could be directly circumvented by modifying the local time-integration. Such a modification is basically possible without changing the fundamental concepts on the global level, since the global framework indeed allows the application of a local return mapping procedure in a modular way. Consequently, any appropriate local update at hand could be incorporated instead.

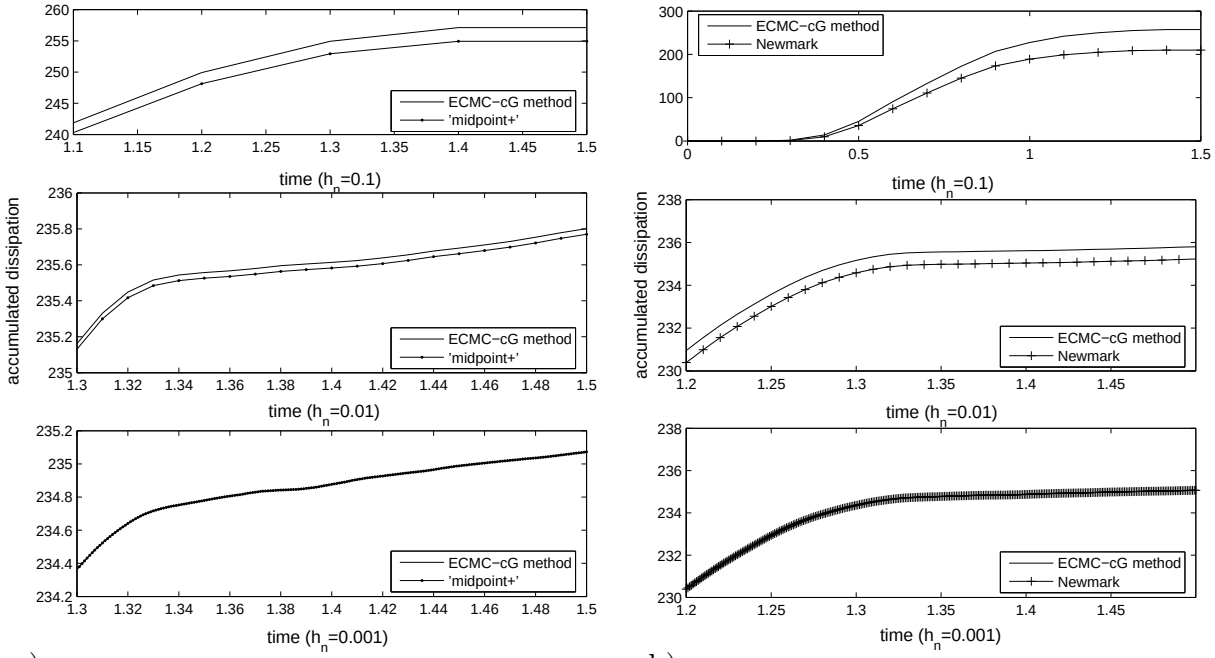

a) b)

Figure 5.23.: accumulated dissipation D using $h_n \in \{0.001, 0.01, 0.1\}$: a) 'ECMC-cG(1) method' vs. 'midpoint+' scheme, b) 'ECMC-cG(1) method' vs. Newmark scheme

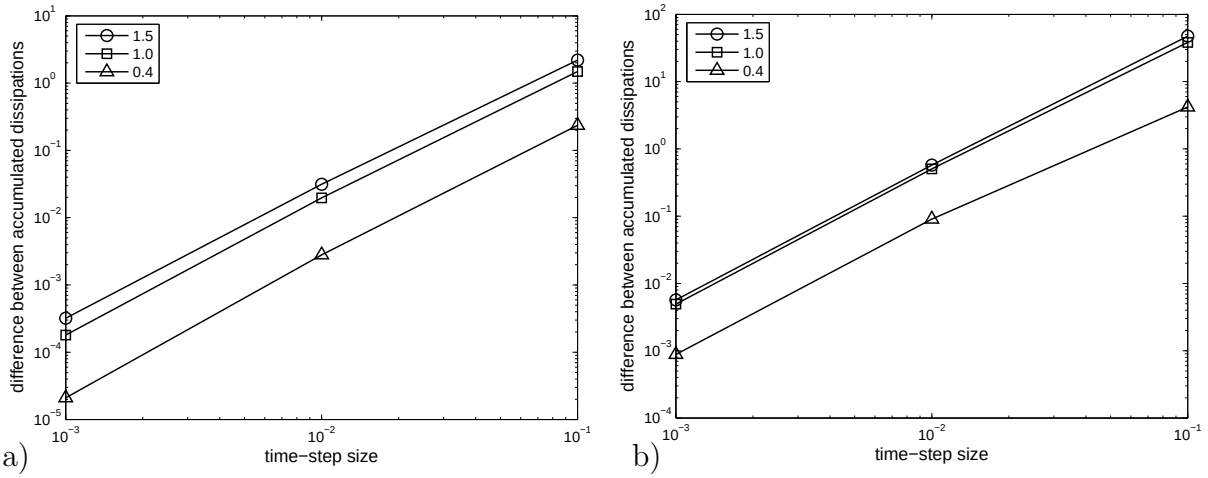

a) b)

Figure 5.24.: difference between accumulated dissipations at $T \in \{0.4, 1.0, 1.5\}$: a) 'ECMC-cG(1) method' vs. 'midpoint+' scheme, b) 'ECMC-cG(1) method' vs. Newmark scheme

5.5.2. Modified schemes

In the previous section, the fundamental convergence properties of the 'ECMC-cG(1) method' have been discussed extensively. Thereby, we have seen that the global order of accuracy is reduced when plastic deformations are involved due to the applied first-order format of the exponential update. As already mentioned, this effect can be diminished, respectively even circumvented, by modifying the local update procedure. In this context, two options are theoretically conceivable to reduce the error in the plastic case, namely:

- The application of higher-order local integration schemes, that completely circumvent any order reduction: In the present case of linear Finite Elements in time, for instance, the application of a second-order midpoint format of the exponential update, as discussed in References [118, 119, 162], certainly represents a possible alternative. However, especially in the case of arbitrary k a further increase of the local accuracy might be required. In this regard, Runge-Kutta methods have been proposed for instance by Büttner and Simeon [47] or in a nonlinear deformation context by Menzel [120], and Menzel and Steinmann [123]. Moreover, a time discretisation of the local evolution equations based on (dis)continuous Finite Elements in time could represent an attractive approach, being in accordance to the global time discretisation. In the small strain case, such a dG method has been proposed e.g. in Larsson *et al.* [100] for the integration of (visco)plastic evolution equations. Concerning the relation between classical Runge-Kutta schemes and time FE methods we refer to References [80, 81]. However, in any case the implementation effort increases and additional aspects, like for instance the enforcement of plastic incompressibility, have to be addressed when a non-standard local update procedure is chosen.

- A modification of the applied integration strategy, enabling a considerable reduction of the error in the plastic case: In the foregoing investigations the 'basic scheme', relying on the standard integration procedure given by Equations (5.27), (5.28), has been used. Since in the favoured approach the global and the local time-integration have been purposely decoupled in a sense, a change of the local time-step size is possible in the same framework without affecting the global level. Consequently, a reduction of the local time-step size, involving more intermediate stages, could also be applied potentially with regard to an error reduction.

Of course, also a combination of both options is possible to optimise the convergence performance in the plastic case. However, since in the present work the focus has been placed on the global time-integration, the local update is considered as a type of constitutive 'black box', as already mentioned. Therefore, the exemplarily chosen standard return map will be retained, and in the following the influence of the local integration strategy will be investigated. One characteristic property of the basic strategy is that

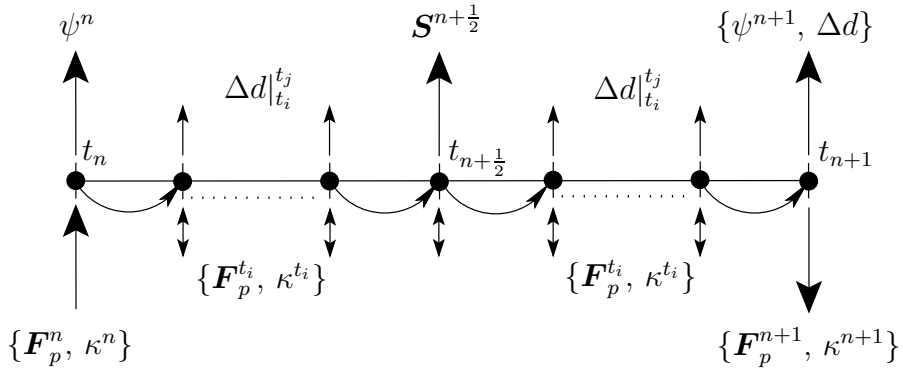

Figure 5.25.: local level: modified integration strategy (non-standard quadrature rule)

each projection step incorporates the values at $t = t_n$, compare Figure 5.2 and Figure 5.3 respectively. Contrariwise, the projection steps can also be performed sequently via the update

$$\{\boldsymbol{F}_p^{t_i}, \kappa^{t_i}\} \longrightarrow \{\boldsymbol{S}^{t_j}, \boldsymbol{F}_p^{t_j}, \kappa^{t_j}; \psi^{t_j}, \Delta d\big|_{t_i}^{t_j}\} \tag{5.42}$$

driven by $\boldsymbol{C}^h(t_j)$ with $t_j = t_i + \Delta t$ [8]. In Equation (5.42), the first step is initialised with $t_i = t_n$. Each subsequent stage is then defined by the update $t_i = t_j$. This procedure is repeated until $t_j = t_{n+1} = t_n + h_n$, compare Figure 5.25 for a sketch of the modified integration strategy. The resulting (local) dissipation increment, which is needed for the computation of the elasto-plastic enhanced algorithmic stress tensor (5.26), can be consequently calculated via the accumulation

$$\Delta d = \sum_{s=1}^{n_{st}+1} \Delta d_s \,, \tag{5.43}$$

wherein n_{st} denotes the number of intermediate stages and the partial dissipation increment for the s-th step has been defined as

$$\Delta d_s := \Delta d\big|_{t_i^s}^{t_j^s} \,. \tag{5.44}$$

Motivated by the 'basic scheme', we start our investigations with one intermediate stage at $t = t_{n+\frac{1}{2}}$, involving $n_{st} = 1$ and $\Delta t = h_n/2$. The resulting 'ECMC-cG(1) method' will be referred to as 'modified scheme 1'. The results are shown in Figure 5.26 based on the relative error in the positions $e_{\bar{\boldsymbol{q}}^h}(T)$ and the relative error in the accumulated dissipation $e_D(T)$ respectively, in both cases evaluated at $T = 1.0$. The corresponding plots clearly confirm the expected reduction of the numerical error in the plastic case, due to the application of the modified integration strategy.

[8] Please note, that also in the case of the modified integration strategy (5.42) the stresses of the continuum model indeed fulfil the yield condition at each intermediate stage since for every step a projection by means of the return map is applied, instead of a simple interpolation.

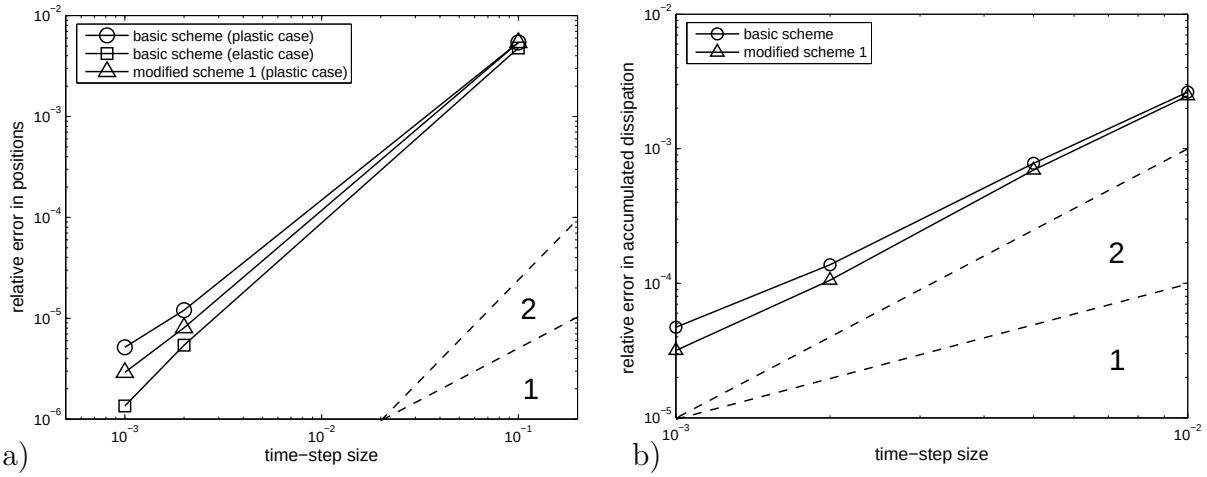

Figure 5.26.: 'modified scheme 1' vs. 'basic scheme': a) relative error $e_{\bar{\boldsymbol{q}}^h}(T)$ at $T = 1.0$, b) relative error $e_D(T)$ at $T = 1.0$

In a next step, three equidistant intermediate stages have been applied, yielding $n_{st} = 3$ and $\Delta t = h_n/4$. As pictured in Figure 5.27, the resulting 'ECMC-cG(1) method' – labelled as 'modified scheme 2' – features a further decrease of the numerical error, which has been once more investigated based on the relative measures $e_{\bar{\boldsymbol{q}}^h}(T)$ and $e_D(T)$ using the evaluation time $T = 1.0$. Due to this significant error reduction, the obtained convergence performance is indeed even competitive to the purely elastic case and the deviations are more of theoretical than of practical interest, compare Figure 5.27 a). Moreover, it is pictured in Figure 5.28 that algorithmic energy-consistency is actually guaranteed within the order of magnitude $\mathcal{O}(10^{-11})$ for each of the applied local integration procedures.

Remarks 5.6:

1. In Simo [161], the author also compares different projection strategies in the context of dynamic plasticity, dealing only with mechanically consistent time-stepping schemes. Therein, it is distinguished between a 'shifted backward-Euler scheme', a 'generalized mid-point rule', and a so-called 'product formula algorithm', whereby the last concept has been particularly recommended [9]. Please note, that our 'modified scheme 1' obviously corresponds to the product formula concept discussed also in Reference [162].

2. Furthermore, it is important to notice that based on the involved exponential update even schemes which are strictly second-order accurate might be constructed,

[9] Simo [161], page 98: 'Amongst the three return mapping strategies considered the product formula algorithm is the best performer with regard to both accuracy and robustness. The lack of significant degradation in accuracy exhibited by the product formula algorithm suggests that the choice of time step should be dictated by the convergence of the global solution scheme'.

compare Simo [162]. In this regard, the underlying integration strategy is once more quite similar to the proposed 'modified scheme 1', whereby the essential difference to the here considered approach is represented by a modified trial state for the second projection step. Hereby, the corresponding trial state incorporates not only the updated solution but also the initial trial state of the first (local) integration step. However, the author still favours the prior 'shifted backward-Euler scheme' and 'product formula algorithm' [10].

3. Although we have only addressed some basic effects in the foregoing investigations of this section, the results have clearly demonstrated that a reduction of the local time-step size also represents an appropriate concept to reduce the global error of the time-stepping scheme in the plastic case. Consequently, the proposed approach could be potentially useful concerning the design of an adaptive projection strategy, reducing the increase of the computational costs related to additional intermediate stages.

[10] Simo [162], page 416: 'On the other hand, extensive numerical experiments conducted with the two alternative strategies outlined above, some of which are reported below, support their excellent performance in spite of being only first-order accurate. Preliminary numerical experiments also suggest that the second-order accurate projected scheme described in Section 53 does not appear to exhibit a performance nearly as robust as these two, nominally less accurate, update schemes.'

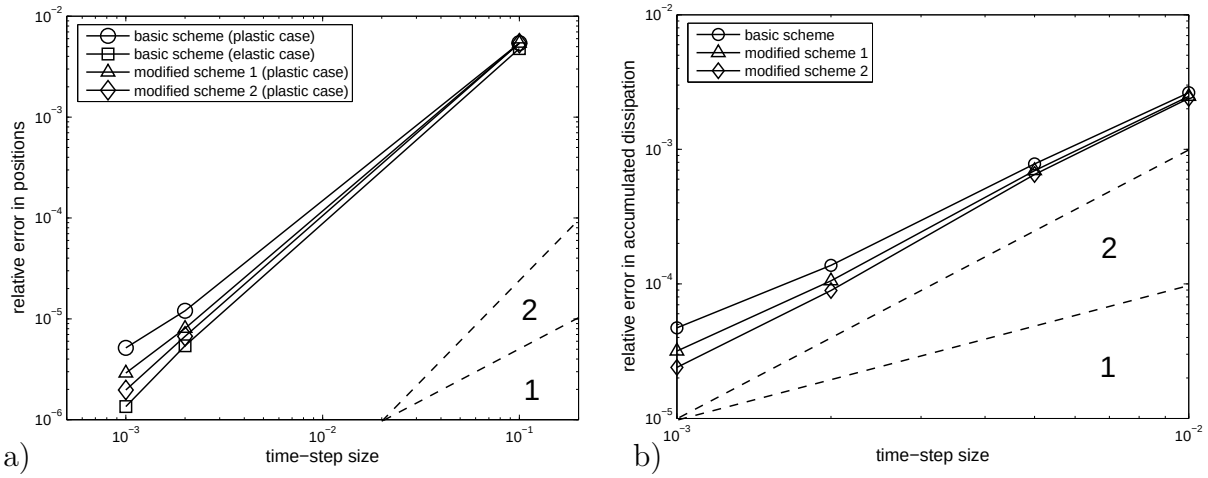

Figure 5.27.: 'modified scheme 2' vs. 'modified scheme 1' vs. 'basic scheme': a) relative error $e_{\bar{\boldsymbol{q}}^h}(T)$ at $T = 1.0$, b) relative error $e_D(T)$ at $T = 1.0$

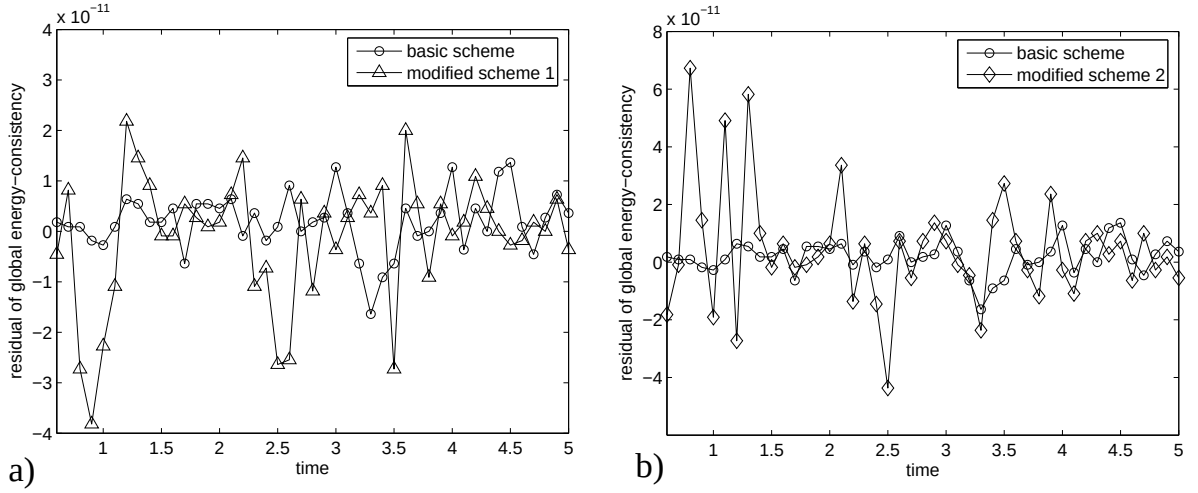

Figure 5.28.: residual R: a) 'modified scheme 1', b) 'modified scheme 2'

5.6. Assessment of Integrators

At the beginning of this chapter, the general concepts to design completely consistent Galerkin-based time-stepping schemes for dissipative systems have been specified to linear Finite Elements in time, incorporating finite elasto-plastic deformations. Moreover, fundamental properties of the resulting integrators have been already exposed based on first numerical examples. In this context, several important aspects, like the fundamental convergence behaviour or the influence of the underlying (local) integration strategy, have been addressed in previous sections. In the last section of this chapter, we present finally an extensive assessment of the advocated Galerkin-based integrators by means of a multitude of numerical examples, whereby free motion problems have been chosen to assess in detail the achievable performance of the time-stepping schemes. In this context, once more the benchmark-type return mapping procedure discussed in Section 5.1.2 has been applied exemplarily for all integrators and the local update is fitted into the global frame via the standard integration strategy of Section 5.2.2.

5.6.1. Standard vs. non-standard quadrature rule

We start with a systematic comparison between different quadrature rules that are required for the approximation of related time integrals, referring to Sections 3.3.2 and 5.2 for the general and the specific case respectively. In this context, the resulting consistency properties will be investigated more detailed based on elastic and plastic runs, classifying the resulting integrators and disclosing the frontiers of each quadrature rule. Hereby, we address in addition to the already discussed formulations, namely

- the mechanically consistent cG(1) scheme based on the approximation (5.24) [11] and
- the 'ECMC-cG(1) method' based on the elasto-plastic enhanced algorithmic stress tensor (5.26),

a further option concerning the applied quadrature rule, which is constructed as follows: In the prolog, the standard and the energy-conserving quadrature rule, that has been originally designed for the purely elastic case, have been combined intuitively to a first non-standard quadrature rule for the dissipative (elasto-plastic) case. Inspired by this 'ad hoc' formulation and motivated by the corresponding results in Chapter 2, we adopt the idea of the elastic enhancement to finite elasto-plasto-dynamics, defining a locally and temporally selective non-standard quadrature rule. Analogously to the motivating

[11] Since in the further investigations the alternative approximation (5.23) will not be considered anymore, a distinction between the classical midpoint and the so-called 'midpoint+' scheme is no longer required. Consequently, the resulting scheme will be simply denoted by 'cG method' in the following examples.

one-dimensional example, this approach involves a modification of the standard quadrature rule only if the deformation is elastic, otherwise the integration is performed based on a standard approximation of the related time integrals [12]. Consequently, this concept represents a straightforward extension of the conservative, hyperelastic case discussed in Chapter 4 to the dissipative case of elasto-plasticity considered in the present chapter. Based on the resulting conservation properties for elastic deformations combined with the positive (local) dissipation in the plastic case, the scheme will be referred to as thermodynamically consistent, motivated on the one hand by the classification discussed in Section 3.2.3 and encouraged on the other hand by the positive results of Chapter 2. Featuring still mechanical consistency, the final integrator will be abbreviated by 'TCMC-cG(1) method'. If the foregoing 'ad hoc' approach indeed affects positively the algorithmic conservation properties in the case of finite elasto-plasto-dynamics will be investigated by means of the following numerical examples.

Remarks 5.7:

1. Regarding the implementation of the non-standard quadrature rule (5.45), once more the proposed mixed strategy introduced in Section 4.4 has been applied to evaluate the elastic-enhanced algorithmic stress tensor (5.46).

2. Within a Finite Element code, the stresses have to be computed at each integration point in space required to approximate spatial integrals, compare Section 3.2. Consequently, also the decision related to the formulation (5.46) – if the standard quadrature rule has to be modified within a particular time step – is made for each spatial integration point separately, selecting those in which temporarily the deformation is elastic.

3. Please note, that the hybrid quadrature rule (5.45) basically prevents a violation

[12] Formally, the resulting non-standard quadrature rule can also be cast in a compact notation by introducing the approximation

$$\int_0^1 \boldsymbol{F}_I^{int\ h}\,\mathrm{d}\alpha \approx \sum_{J=1}^{n_{node}} \left[\int_{\mathcal{B}_0} [\nabla_{\boldsymbol{X}} N_I \otimes \nabla_{\boldsymbol{X}} N_J] : {}^{el}\boldsymbol{S}^{alg}(1/2)\,\mathrm{d}V\right] \boldsymbol{q}_J^h(1/2)\,, \tag{5.45}$$

using the so-called elastic-enhanced algorithmic stress tensor

$${}^{el}\boldsymbol{S}^{alg}(1/2) := \boldsymbol{S}_{1/2} + \chi\,\frac{2\,[\psi_{\alpha=1} - \psi_{\alpha=0}] - \boldsymbol{S}_{1/2} : [\boldsymbol{C}_2 - \boldsymbol{C}_1]}{||\boldsymbol{C}_2 - \boldsymbol{C}_1||^2}[\boldsymbol{C}_2 - \boldsymbol{C}_1]\,, \tag{5.46}$$

wherein the selection parameter χ is equal to one for elastic deformations and equal to zero for the plastic case. Nevertheless, keep in mind that, in contrast to the purely elastic case (4.27), internal variables have to be considered in Equation (5.46), yielding $\boldsymbol{S}_{1/2} := \boldsymbol{S}(\boldsymbol{C}^h(1/2), \boldsymbol{\kappa}_{1/2})$ and $\psi_\alpha(\boldsymbol{C}^h(\alpha), \boldsymbol{\kappa}_\alpha)$ respectively. Thereby, for the sake of conceptual clarity, the local integration strategy relies once more on Equations (5.27), (5.28), being in accordance with the 'basic scheme' discussed in Section 5.5.1.

of the (local) energy-consistency condition (3.49) during elastic (un)loading periods, see also Appendix A. In the plastic case, the quadrature rule remains actually unconstrained, even if a fulfilment of the dissipation inequality is of course guaranteed locally by the applied return mapping scheme. However, it will be shown that the resulting integrator features also in the plastic case an improved performance regarding the global energy balance, analogously to the introducing example of Chapter 2.

Flying Conrod

The first example in this section deals with the free motion of a 'Flying Conrod' [13], using 128 isoparametric 4-node elements for the spatial discretisation (2d, plain strain conditions) and the mass density $\rho = 3.0$. The initial configuration can be regarded in Figure 5.29 a). Starting the motion by an initial velocity in the horizontal direction with $||\bar{\boldsymbol{v}}_0|| = 258$, additionally external loads have been applied on the bushings, whereby once more a piecewise linear function with $f_{max} = 20$ and $T_{load} = 1.0$ has been incorporated. Furthermore, the time-step size has been increased from $h_n = 0.05$ to $h_n = 0.2$ at the time $t = 3.0$ and, subsequently, reduced again to $h_n = 0.1$ for $t > 6.0$. Moreover, two sets of material parameters have been applied for different regions of the conrod, namely $\lambda = 1000$, $\mu = 500$, $Y_0 = 300$, $H^{rd} = 300$ for the shaft and $\lambda = 10000$, $\mu = 5000$, $Y_0 \to \infty$ for both circlets. Consequently, only the shaft will be deformed plastically. The main purpose of the present example is to illustrate the obtained consistency properties of the 'TCMC-cG(1) method' which relies on the 'ad hoc' formulation (5.45). To investigate the algorithmic performance in detail, the plastic motion of the conrod is compared with the purely elastic case, whereby then the underlying constitutive model recaptures the hyperelastic Hencky-type model (4.11), building a bridge to Chapter 4. A sequence of the motion is pictured in Figure 5.29 b), showing the plastic motion. Furthermore, Figure 5.30 allows a direct comparison between the purely elastic and the plastic motion based on the resulting configuration at $t = 8$. As expected, the global accumulated dissipation D is equal to zero for each of the considered Galerkin-based integrators if the deformations are purely elastic, and it is (strictly) positive if plastic deformations are involved due to the application of an adequate local update algorithm for the plastic variables, as pictured in Figure 5.32. Furthermore, Figure 5.31 confirms once more that mechanical consistency, including a conservation of both momentum maps, can be guaranteed not only by time-stepping schemes which base on non-standard quadrature rules, but also by the classical 'cG(1) method', as already demonstrated in previous sections. More interesting in this context is the influence of the applied quadrature rule on the discrete energy balance. Firstly, we compare the performance of each Galerkin-based scheme based on a plot of the total

[13] In this context, the notion 'conrod' is the widespread abbreviation for connection rod which is part of a slider-crank mechanism and connects the piston with the crankshaft, for instance within a combustion engine.

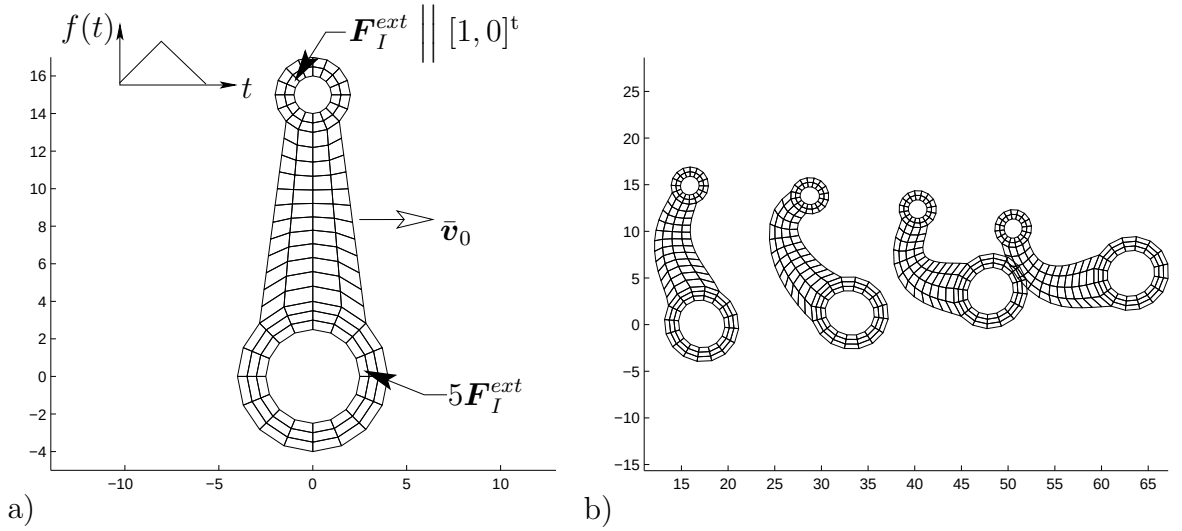

Figure 5.29.: a) initial configuration $\mathcal{B}_0$, b) sequence of the motion (plastic case)

energy H, compare Figure 5.33. In the purely elastic case, the balance of the total energy is visibly violated by the standard 'cG(1) method', referring to the results of Chapter 4. To the contrary, the integrators based on a non-standard quadrature rule guarantee by design the conservation of the total energy. Obviously, a distinction between thermodynamical and energy-consistency is not meaningful for purely elastic deformations rendering in both cases $H_{n+1} - H_n = 0$, compare also Equation (4.46). In fact, the 'TCMC-cG(1) method' and the 'ECMC-cG(1) method' are completely identical in the conservative case and result both in the approximation (4.26) based on the widespread format (4.27), that has been extensively studied in Chapter 4 based on the present constitutive format. However, in the plastic case both integrators based on non-standard quadrature rules are no longer identical and differences occur, compare Figure 5.33 b). Regarding the corresponding plots of the total energy, it can be seen that also in the present example the 'cG(1) method' features an unphysical increase of the total energy, whereas not only the plot of 'ECMC-cG(1) method' but also the plot of the 'TCMC-cG(1) method' is characterised by the claimed monotonic decrease caused by the plastic deformations, confirming the positive results of Chapter 2. Apparently, already this 'ad hoc' formulation, which basically controls the discrete energy balance for elastic deformations, leads to a substantial upgrade concerning the algorithmic energy balance, even in the plastic case. Nevertheless, the rigorous algorithmic fulfilment of a physically correct energy balance is only possible by means of an energy-consistent integrator, that controls additionally the energy decrease respectively dissipation increase in the plastic case. As already discussed in previous examples, the consequences can be studied based on the augmented Hamiltonian plotted in Figure 5.34 and, in more detail, based on the residual R pictured in Figure 5.35. Both figures illustrate unmistakably the advantage of the 'ECMC-cG(1) method' which captures exclusively a conservation of the augmented Hamiltonian, satisfying the discrete energy balance (5.33) within the order of magnitude $\mathcal{O}(10^{-10})$. Consequently, solely the 'ECMC-cG(1) method' offers a completely consistent time-integration.

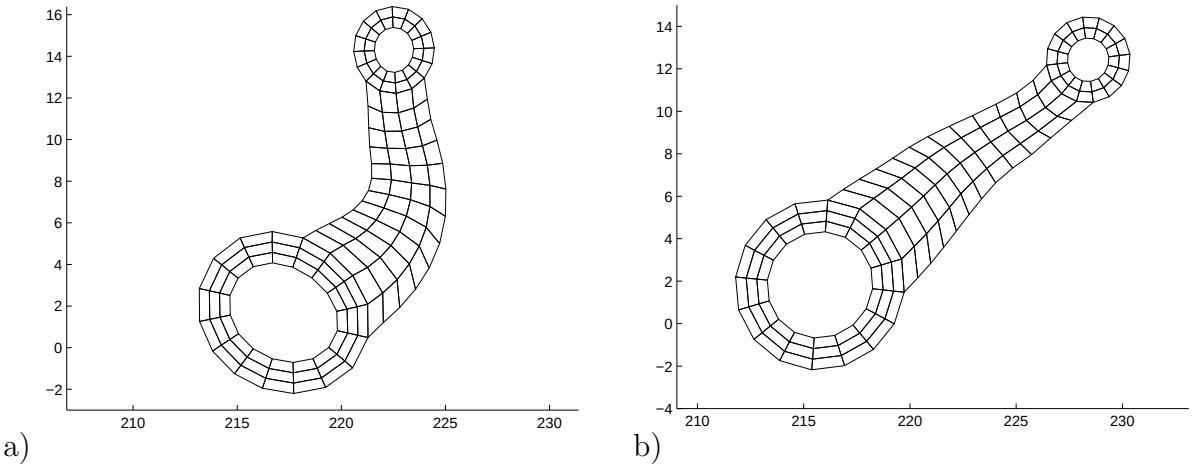

Figure 5.30.: deformed configuration at $t = 8$: a) purely elastic case, b) plastic case

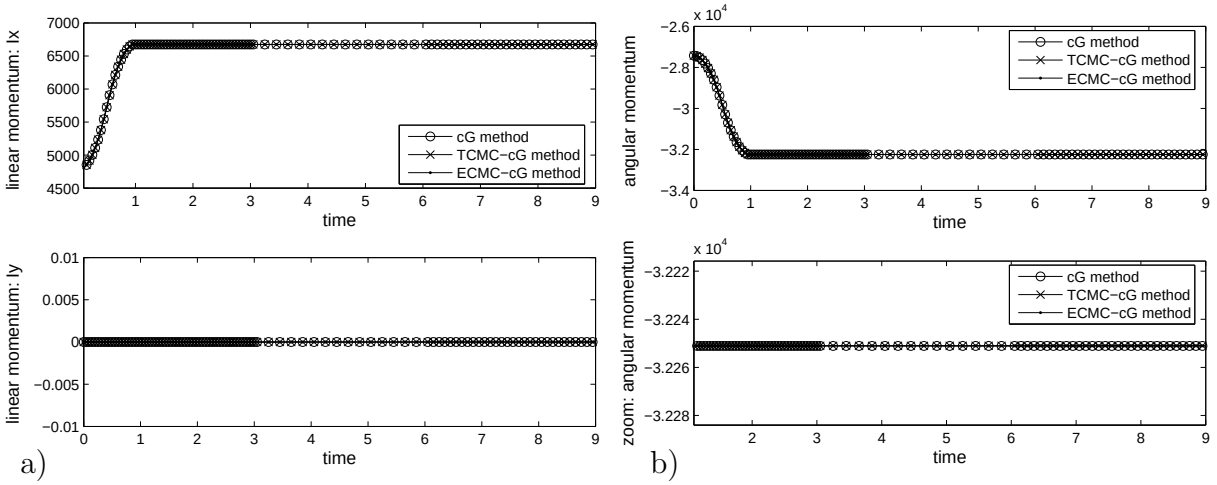

Figure 5.31.: a) linear momentum (elastic case), b) angular momentum (plastic case)

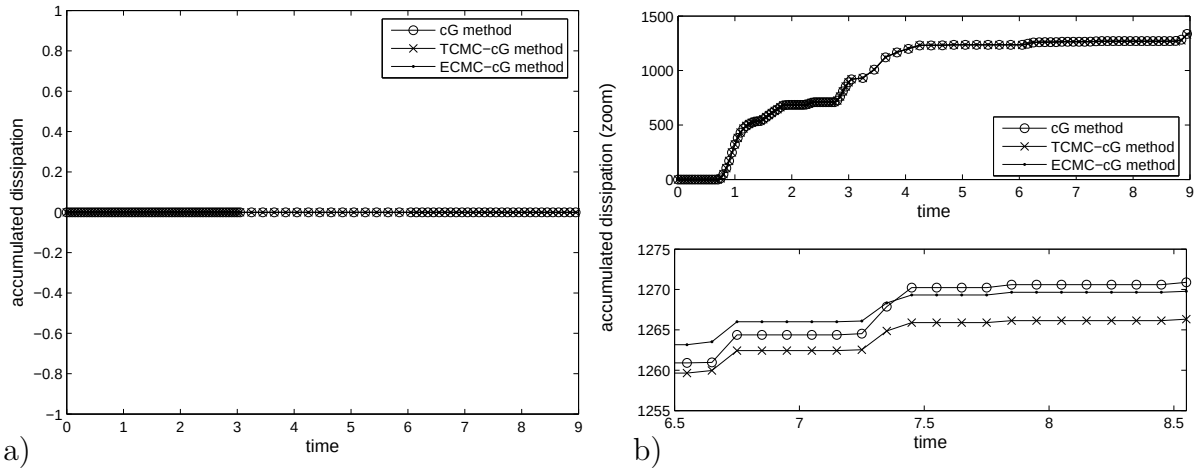

Figure 5.32.: accumulated dissipation D: a) purely elastic case, b) plastic case (zoom)

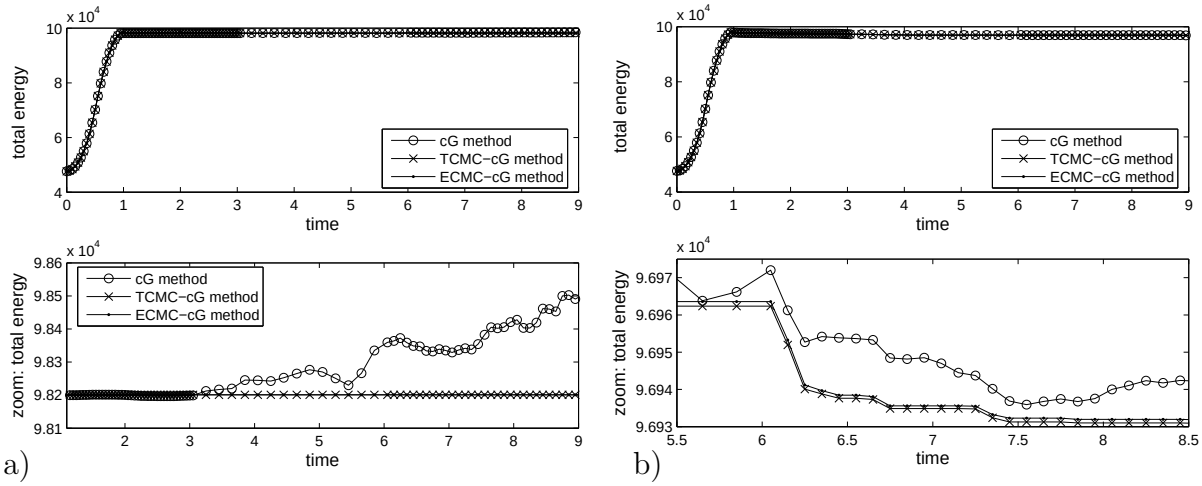

Figure 5.33.: total energy H: a) purely elastic case, b) plastic case

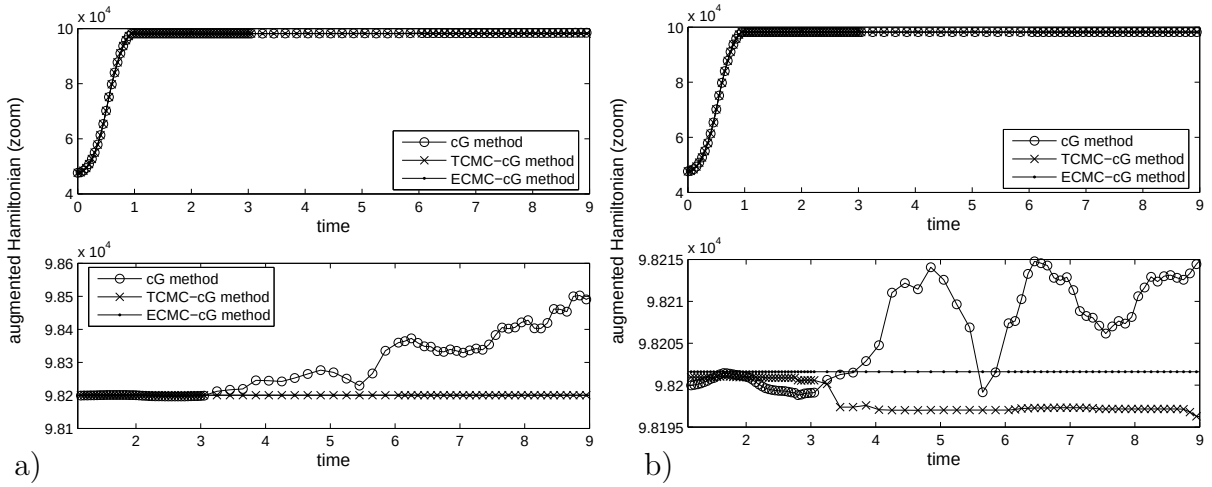

Figure 5.34.: augmented Hamiltonian $\widetilde{H}$: a) purely elastic case, b) plastic case

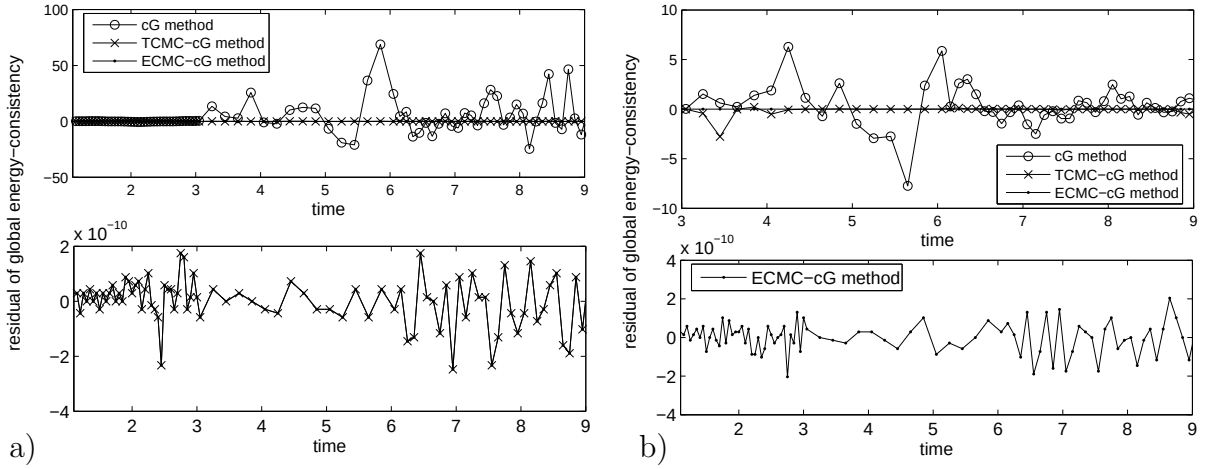

Figure 5.35.: residual R: a) purely elastic case, b) plastic case

Flying L

Finally, a three-dimensional example is considered, dealing with the spatial motion of the popular 'Flying L' [14]. Hereby, the discrete body consists of 117 isoparametric 8-node elements in space and is equipped with an initial velocity, as illustrated in Figure 5.36 a). Furthermore, external loads have been incorporated, following the same piecewise linear function as in previous examples. For the computations, the quite large time-step size $h_n = 0.1$ has been applied, incorporating the parameters $\rho = 12.0$, $||\bar{\boldsymbol{v}}_0|| = 26$, $f_{max} = 180$, $T_{load} = 1.0$, $\lambda = 9000$, $\mu = 3000$, $Y_0 = 1200$, and $H^{rd} = 300$. Analogously to the previous example, the purely elastic motion with $Y_0 \to \infty$ is compared with the plastic case, whereby once more the foregoing Galerkin-based integrators have been applied, featuring different consistency properties. An exemplary sequence of the motion is shown in Figure 5.36 b) and a direct comparison between the elastic and the plastic case is possible based on Figure 5.42 and Figure 5.43 respectively, where in both cases the deformed configurations are plotted after an identical number of time steps. Obviously, the resulting configurations clearly differ when the deformations are purely elastic, whereby a significant stretch of the 'Flying L' occurs particularly in the plastic case, compare $t = 9.0$. As pictured in Figure 5.37, each of the considered Galerkin-based integrators guarantees a mechanically consistent time-integration. Moreover, it is shown in Figure 5.38 that the results of the involved schemes concerning the accumulated dissipation are qualitatively identical, even for the here applied large time-step size. However, the plot of the total energy in Figure 5.39 exposes again the limitation of the 'cG(1) method'. Once more, the standard scheme suffers not only from oscillations of the total energy in the purely elastic case, but also from an unphysical increasing behaviour in the plastic case. Contrariwise, both integrators based on non-standard quadrature rules feature a conservation of the total energy when the deformations are elastic and a monotonic decrease when plastic deformations take place, so that the results of the foregoing example are confirmed. In a next step, the algorithmic energy balance is investigated more detailed based on a plot of the augmented Hamiltonian, compare Figure 5.40. In this context, the performance for the purely elastic case with $\widetilde{H} = H$ has been already discussed based on Figure 5.39. Therefore, special emphasis is placed on the plastic case, whereby the present results confirm once more that a conservation of the augmented Hamiltonian can only be guaranteed by means of the 'ECMC-cG(1) method'. To demonstrate also for the present example the entire potential of the 'ECMC-cG(1) method' in this regard, the residual of global energy-consistency is taken into account. Considering Figure 5.41, it can be seen that global energy-consistency is guaranteed within the order of magnitude $\mathcal{O}(10^{-11})$. To the contrary, not only the 'cG(1) method' but also the 'TCMC-cG(1) method' violates the discrete balance (5.33) in the plastic case, representing an intermediate stage between no and full energy control.

[14] Indeed, the free motion of a L-shaped block represents a widespread benchmark problem in the context of (conserving) time-stepping schemes, compare for instance Simo and Tarnow [165], Betsch and Steinmann [26], Meng and Laursen [118], Armero and Zambrana [9], and Noels *et al.* [148].

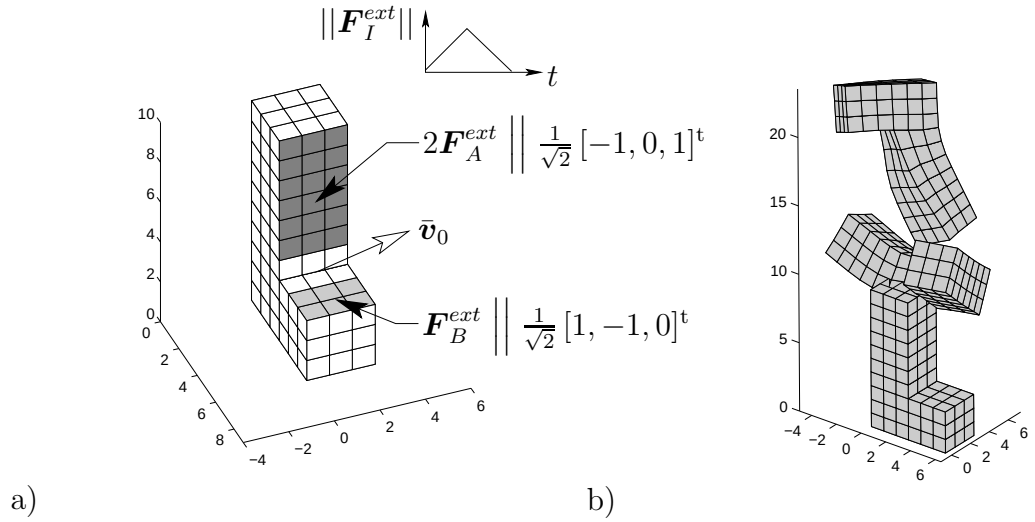

Figure 5.36.: a) initial configuration $\mathcal{B}_0$, b) sequence of the motion (plastic case)

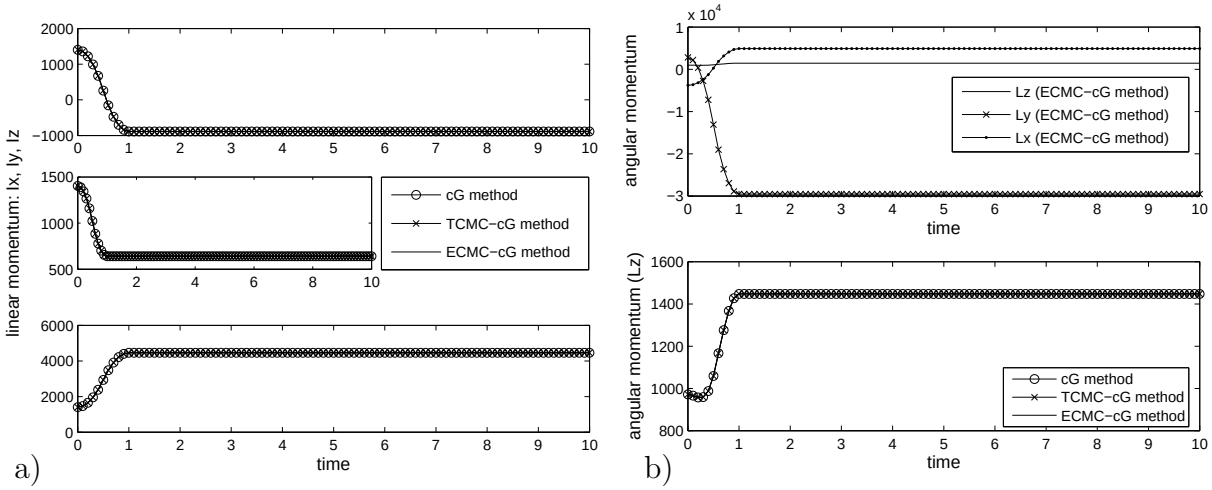

Figure 5.37.: a) linear momentum (elastic case), b) angular momentum (plastic case)

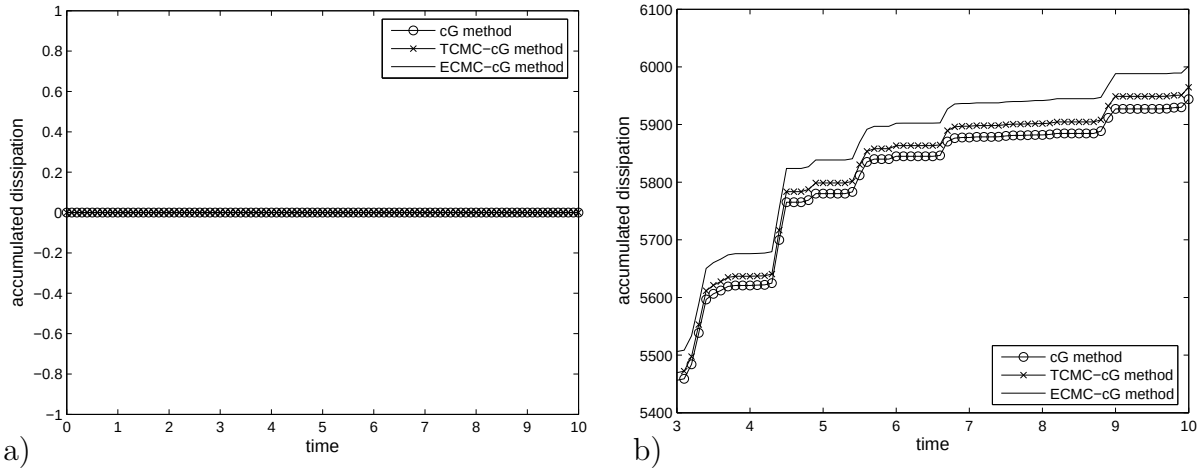

Figure 5.38.: accumulated dissipation D: a) purely elastic case, b) plastic case (zoom)

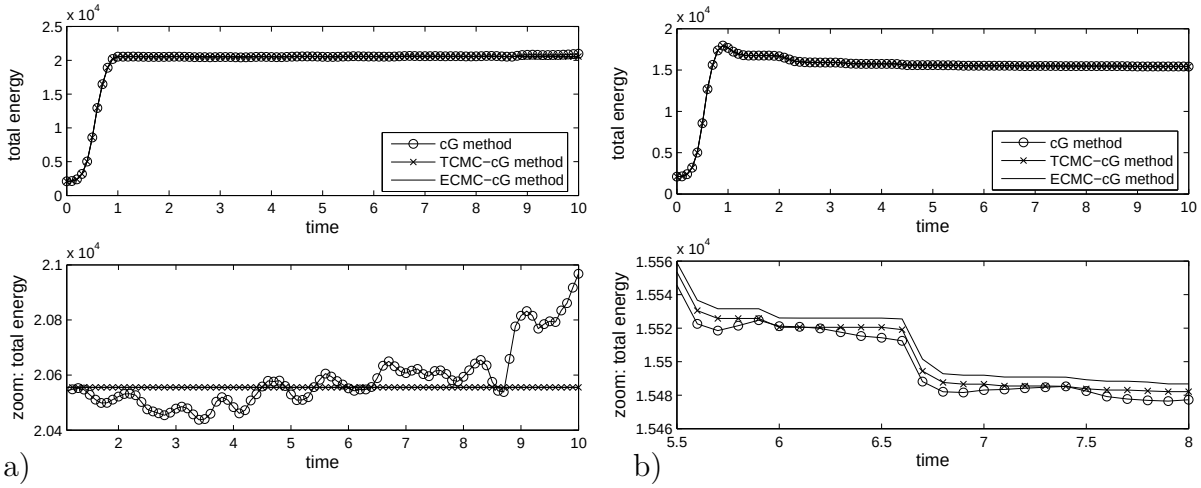

Figure 5.39.: total energy H: a) purely elastic case, b) plastic case

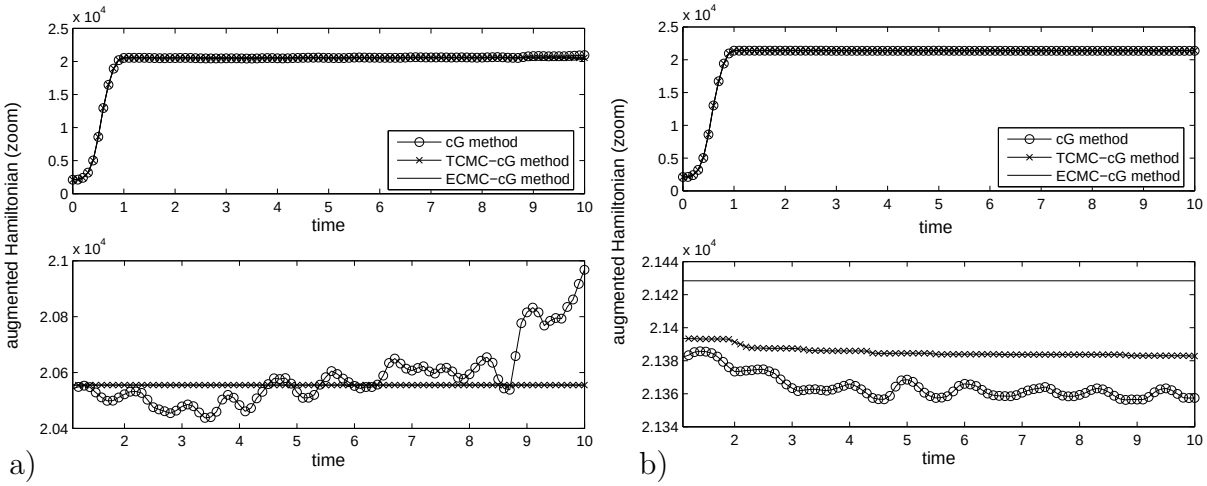

Figure 5.40.: augmented Hamiltonian $\widetilde{H}$: a) purely elastic case, b) plastic case

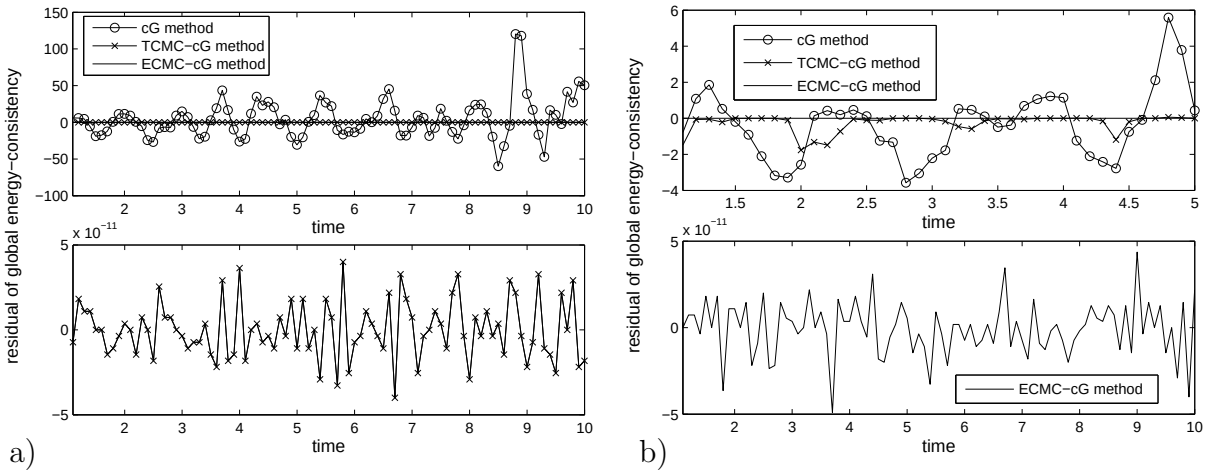

Figure 5.41.: residual R: a) purely elastic case, b) plastic case

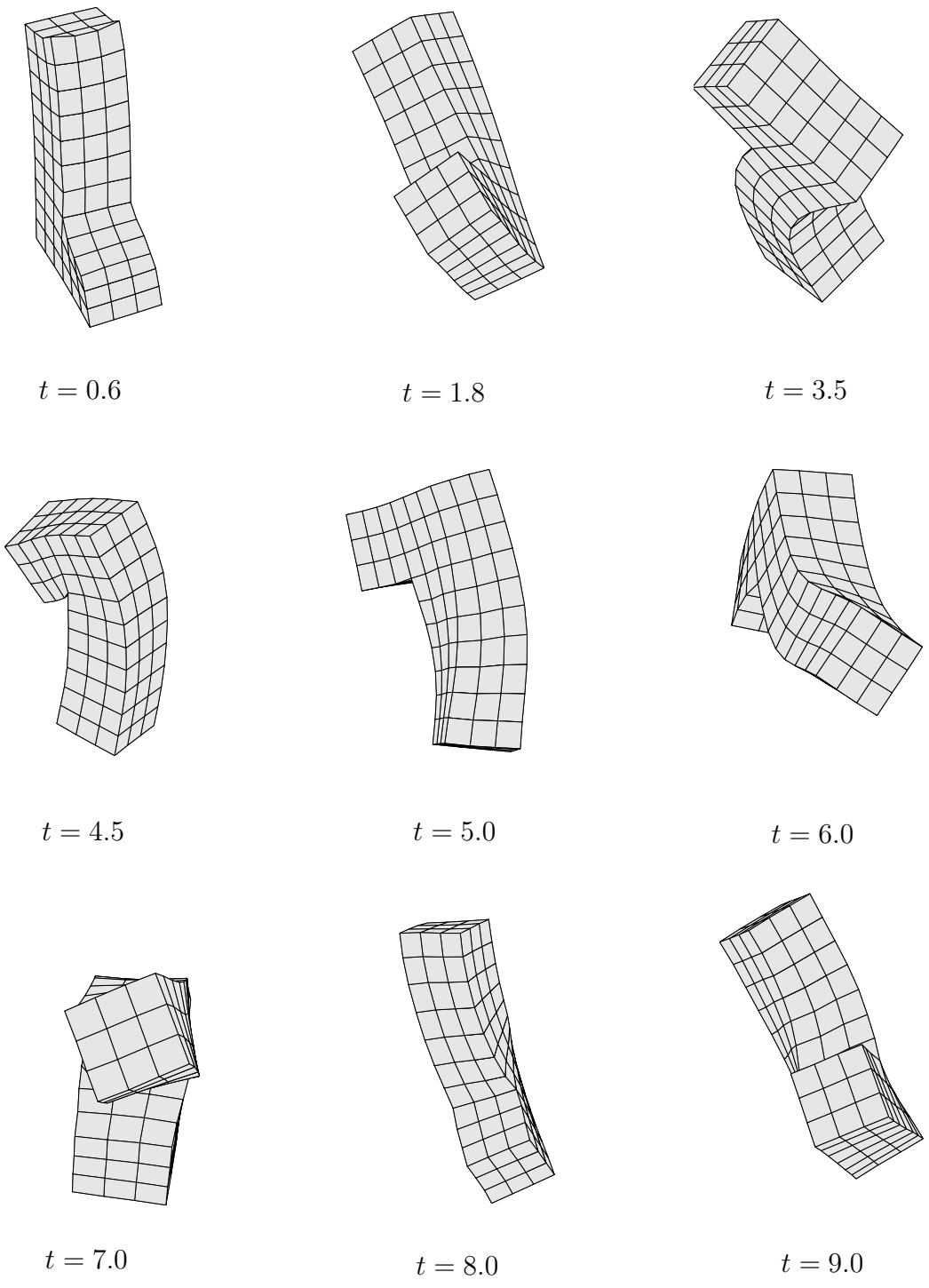

Figure 5.42.: deformed configurations $\mathcal{B}_t$ at selected times t (elastic motion)

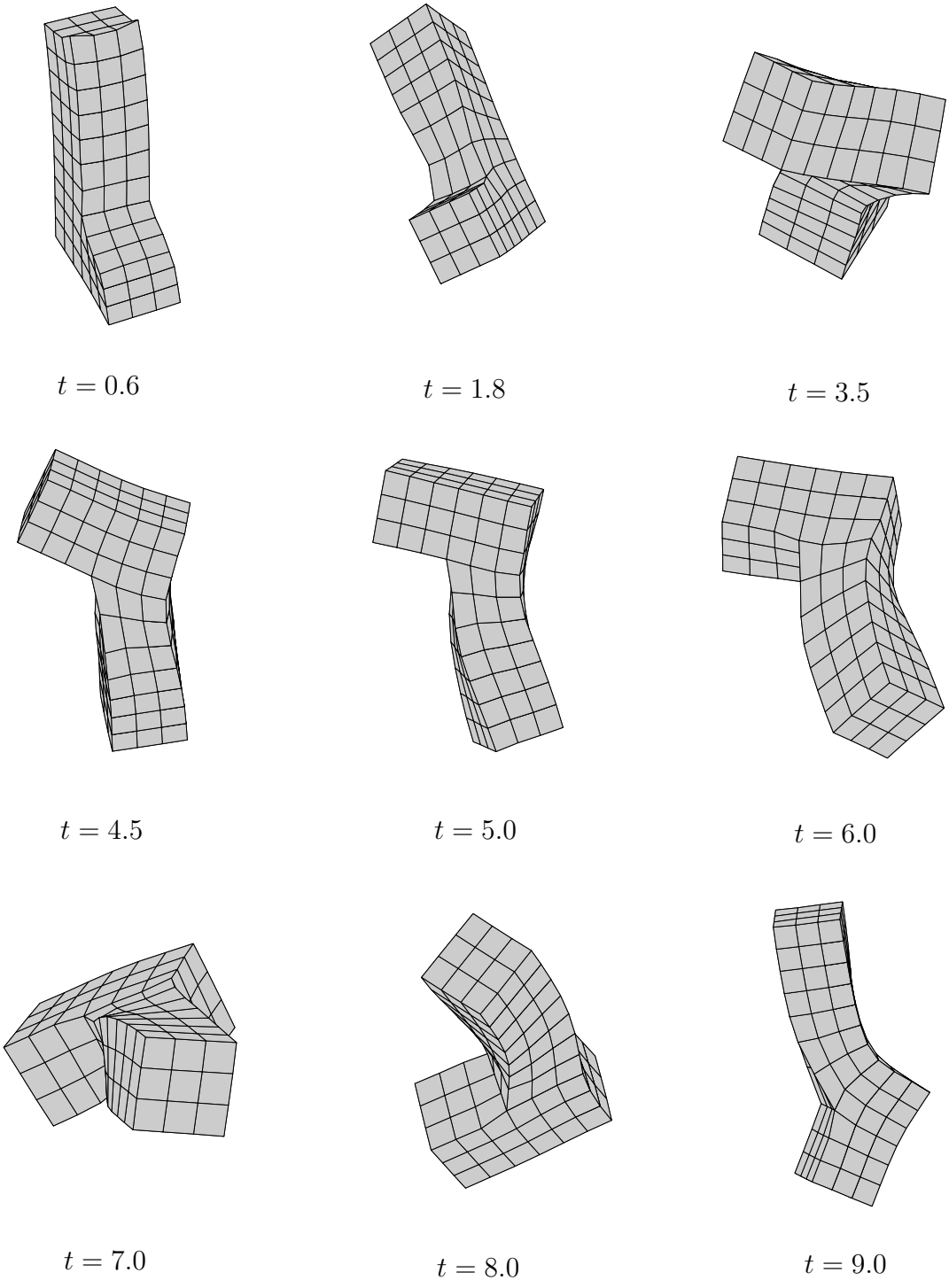

Figure 5.43.: deformed configurations $\mathcal{B}_t$ at selected times t (plastic motion)

5.6.2. Standard vs. non-standard integrator

In the previous section, the resulting performance of specific Galerkin-based time-stepping schemes, which rely on different quadrature rules, has been discussed in detail, fo-cusing on the resulting consistency properties. In this context, particularly the superior performance of the 'ECMC-cG(1) method' concerning the fulfilment of physically motivated balance laws has been clearly confirmed, enabling exclusively a completely consistent time-integration. Nevertheless, one fundamental aspect that should be definitely addressed is a final competition between the developed integrators and popular time-stepping schemes which are not only well-accepted in the computational dynamics community, but also widespread in commercial simulation software. Consequently, the performance of the proposed time FE methods, represented by the favoured 'ECMC-cG(1) method', will be compared with the performance of well-established standard integrators [15].

Flying Frame

For a first detailed comparison, we have exemplarily chosen two of the most-established integrators at all, namely

- the classical Newmark scheme using the parameters $\gamma = 0.5$, $\beta = 0.25$ and
- the Hilber-Hughes-Taylor method (abbreviated by 'HHT method') with the parameters $\gamma = 0.8$, $\beta = 0.422$, and $\alpha = -0.30$, as proposed in Reference [76].

Both standard integrators have been developed originally for linear dynamical systems. For the chosen parameters the Newmark scheme is related to the (undamped) trapezoidal rule, as already mentioned in Section 5.5.1, and the 'HHT method' has been specifically designed to provide a numerically dissipative behaviour. For the following computations, once more the 'Flying Frame' has been used, whereby the initial setup remains unchanged and is pictured in Figure 4.17 a). Concerning the involved parameters, we have incorporated $\lambda = 500$, $\mu = 250$, $Y_0 = 40$, $H^{rd} = 100$, $\rho = 3.0$, $||\bar{\boldsymbol{v}}_0|| = 85$, $f_{max} = 20$, and $T_{load} = 1.0$. To assess fairly the offered performance of the different time-stepping schemes, small as well as large time-step sizes have been applied for the simulation. Additionally, the time-step sizes have been changed during the calculation, namely from $h_n = 0.02$ to $h_n = 0.06$ respectively from $h_n = 0.1$ to $h_n = 0.3$ after $t = 2.2$, to check the robustness of the integrators. A sequence of the motion, including contour plots of the hardening variable, can be regarded in Figure 5.44 and the local evolution of the hardening parameter is pictured exemplarily for two points of the frame in Figure 5.45. However, in the following, special emphasis is placed on the resulting consistency properties. Considering Figure 5.46, the accumulated dissipation D is, once more, (strictly)

[15] Please keep in mind, that the essential equations of the considered standard integration schemes are also summarised in Appendix C.

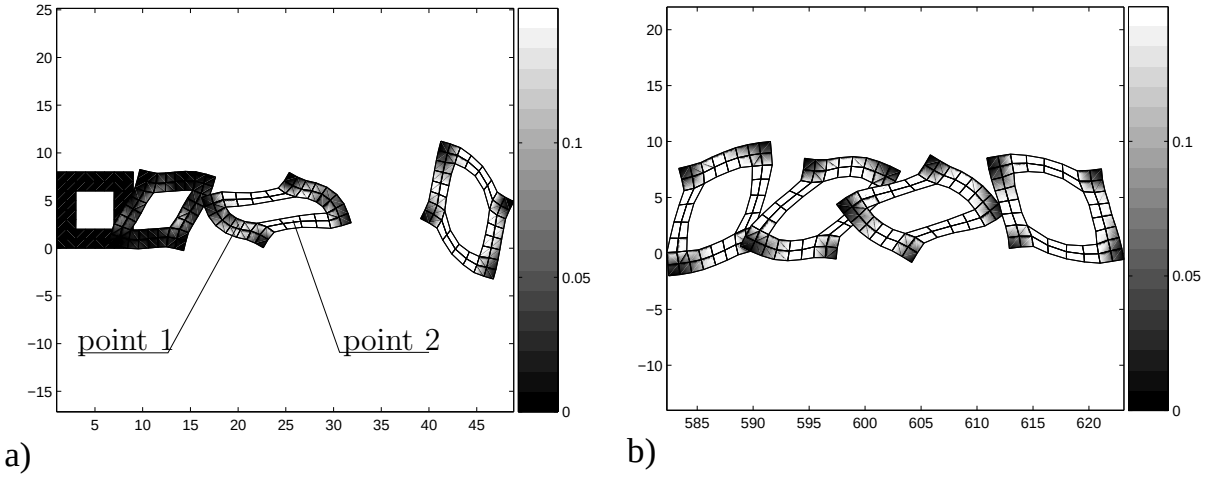

Figure 5.44.: contour plot of the hardening parameter (large time-step size): a) $t \in \{0.1, 0.8, 2, 4\}$, b) $t \in \{58.3, 59.2, 60.1, 61.3\}$

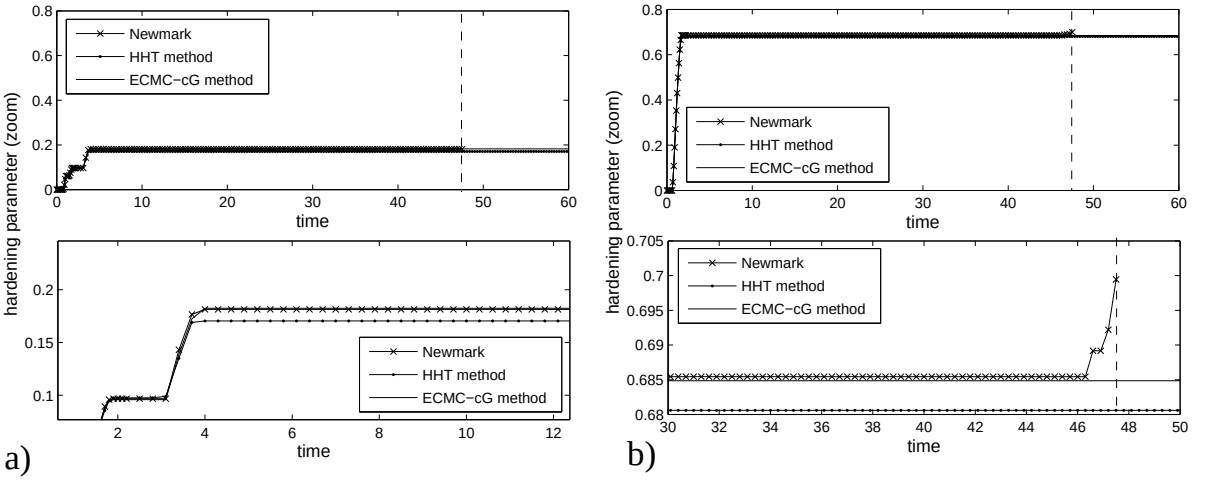

Figure 5.45.: evolution of the hardening parameter (large time-step size) in: a) point 1, b) point 2

non-negative due to the local integration and the results of the different integrators are qualitatively similar, especially for small time-step sizes. Nevertheless, the results differ quantitatively, in particular if the 'HHT method' is incorporated. Hereby, its application results in the lowest physical dissipation, which seems to be significantly underestimated when dealing with large time-step sizes. Moreover, the obtained quality of the calculated total energy H is degraded impressively, when the classical integrators are used instead of the Galerkin-based 'ECMC-cG(1) method', compare Figure 5.47. It can be clearly seen that the standard integrators are not able at all to feature a physically correct monotonic decrease of the total energy. Rather, both classical integration schemes suffer

from oscillations in the total energy which increase drastically for large time-step sizes, especially if the widespread Newmark method is applied. One might think that such aspects are only of theoretical interest, but in fact a physically correct time-integration is essential for a qualitatively correct simulation of the dynamical behaviour and, moreover, the evolution of the total energy is directly related to the robustness of the integrators, as already demonstrated in foregoing examples. This accepted fact is also confirmed by the present example, since the application of the Newmark method results in a critical energy blow-up when large time-step sizes are taken into account [16], compare Figure 5.47 b). Contrariwise, the 'HHT method' offers an unphysical decrease of the total energy caused by its numerically dissipative character. Please note furthermore, that this strong decrease of the total energy is not accompanied by a high physical dissipation D, as discussed above. To investigate the relation between the decrease of the total energy and the increase of the accumulated (physical) dissipation in detail, the augmented Hamiltonian $\widetilde{H}$ is plotted in Figure 5.48. Once more, the results of both standard integrators show an unphysical behaviour which is characterised by oscillations and an increase respectively decrease of the augmented Hamiltonian. Solely, the 'ECMC-cG(1) method' captures the conservation of the augmented Hamiltonian, as also confirmed by Figure 5.50 based on Equation (5.33). Furthermore, the standard integrators violate the conservation of angular momentum, whereas the Galerkin-based scheme features mechanical consistency, as pictured in Figure 5.49. It is important to emphasise again that the abovementioned consistency properties of the 'ECMC-cG(1) method' are obtained indeed for small as well as for large time-step sizes, unaffected by changes of the step size during the calculation. Contrariwise, the numerical performance of the here considered Newmark scheme as well as of the 'HHT method' crucially depends even qualitatively on the applied time-step size.

Remark 5.8: In Section 5.5, it has been demonstrated based on the accumulated dissipation that the differences between the 'ECMC-cG(1) method' and the Newmark scheme indeed decrease when the time-step size is reduced, converging to the same solution for $h_n \to 0$. Furthermore, the present example has shown that even for the large time-step size the Newmark scheme seems to be shadowed by the energy-consistent Galerkin-based integrator concerning the order of magnitude of the results, whereby the favoured time FE method features additionally the fulfilment of a complete set of algorithmic conservation properties, as discussed above.

[16] Analogously to previous examples, a program abort within the calculations is displayed by means of a vertical dashed line in the plots.

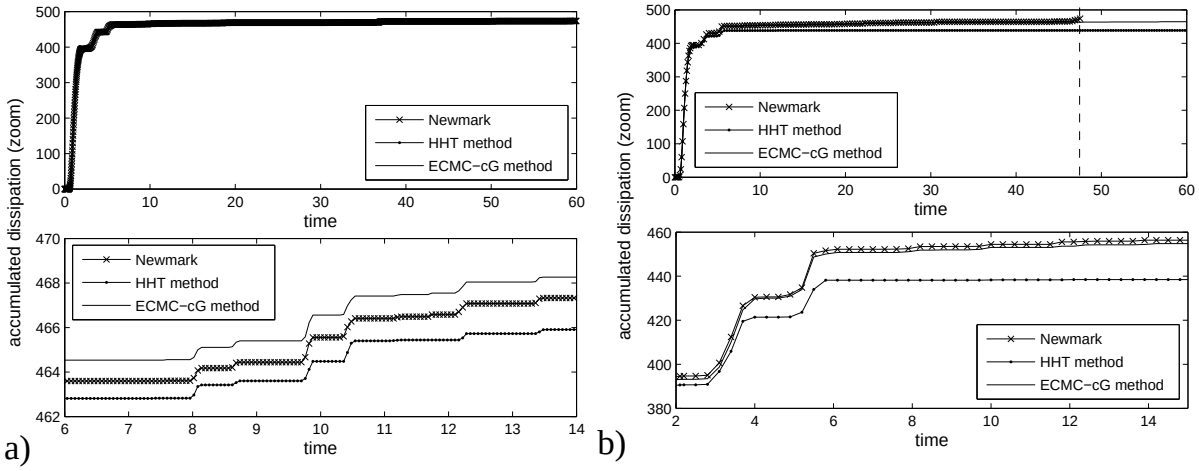

Figure 5.46.: accumulated dissipation D: a) small time-step size, b) large time-step size

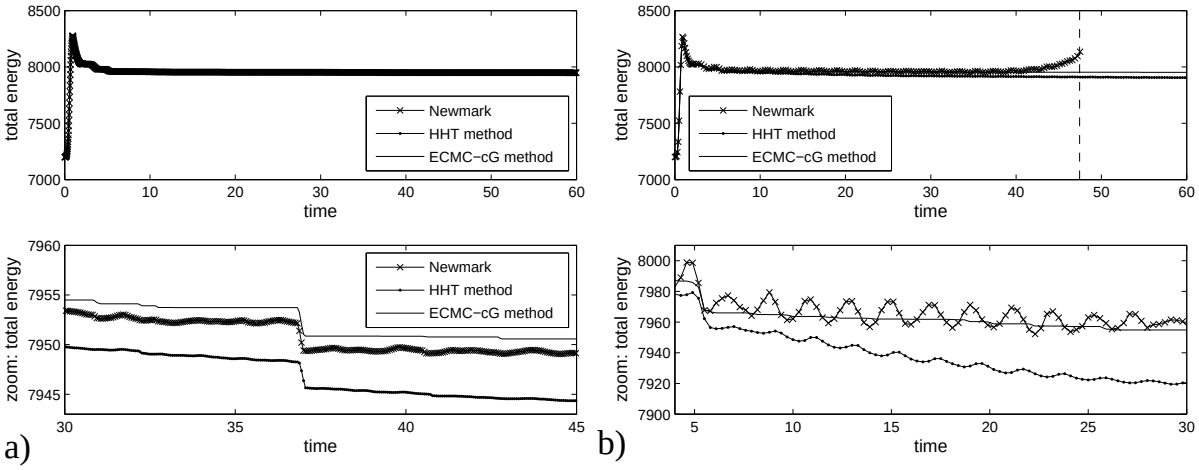

Figure 5.47.: total energy H: a) small time-step size, b) large time-step size

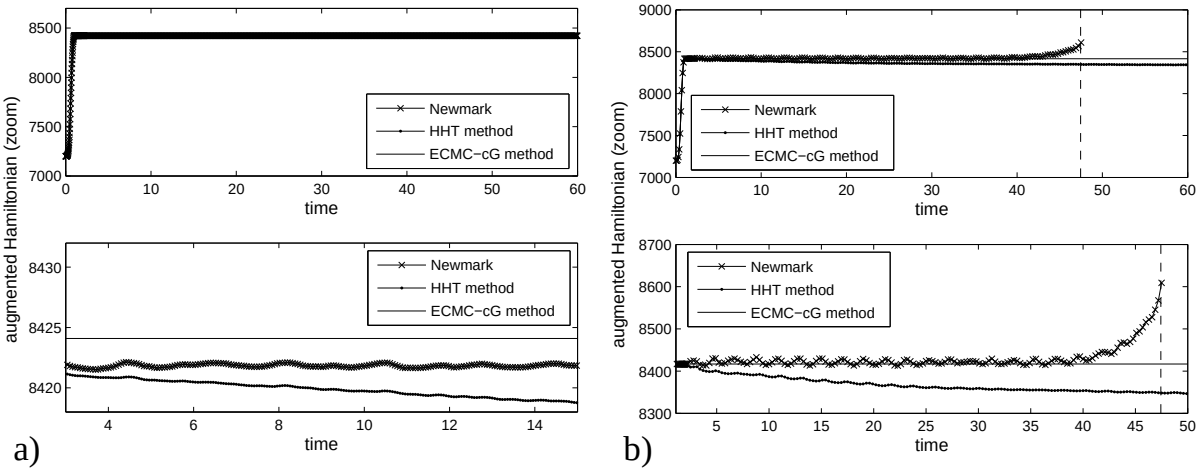

Figure 5.48.: augmented Hamiltonian $\widetilde{H}$: a) small time-step size, b) large time-step size

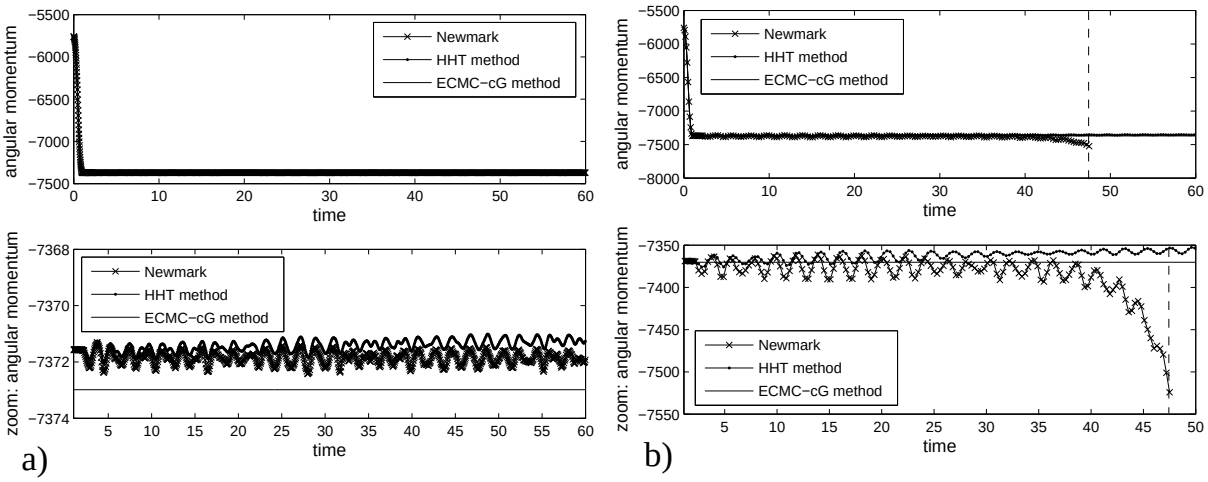

Figure 5.49.: component of the angular momentum: a) small time-step size, b) large time-step size

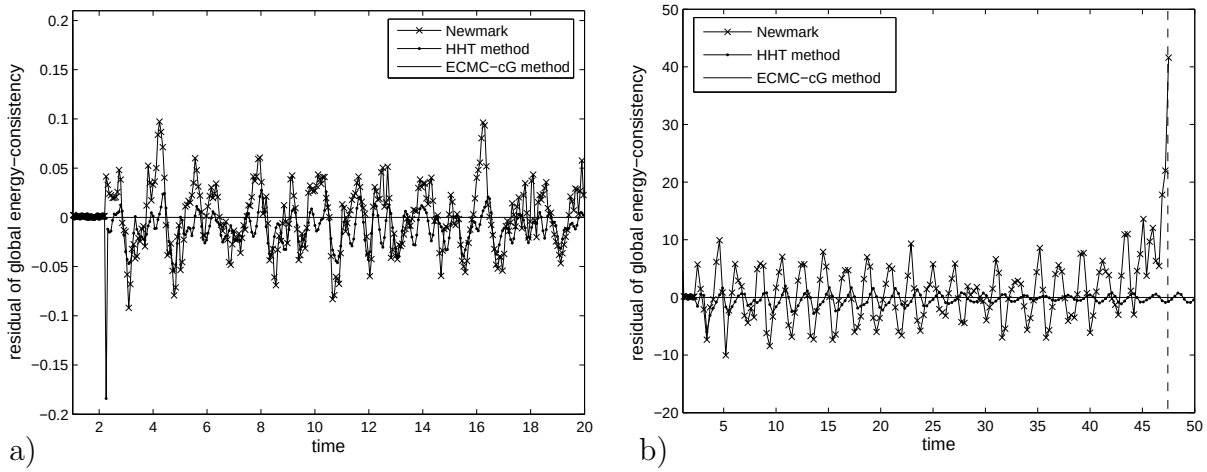

Figure 5.50.: residual R: a) small time-step size, b) large time-step size

Flying Conrod

The last example in this chapter deals with the spatial motion of a 'Flying Conrod', whereby the applied Finite Element mesh consists of 128 isoparametric 8-node elements in space, compare Figure 5.52 a). The motion of the conrod with the mass density $\rho = 9.0$ is initiated by an initial velocity, using $||\bar{\boldsymbol{v}}_0|| = 183$. Moreover, external loads act on the conrod during the loading period $T_{load} = 1.0$, whereby once more a hat function with $f_{max} = 15$ has been chosen concerning the loading history. Analogously to the 2d case investigated in Section 5.6, different material properties have been applied for both circlets and the shaft, namely $\lambda = 30\,000$, $\mu = 10\,000$, $Y_0 \to \infty$ for the circlets and $\lambda = 9000$, $\mu = 3000$, $Y_0 = 800$, $H^{rd} = 2000$ for the shaft respectively. Evaluating the resulting performance, the 'ECMC-cG(1) method' is compared in the present example with

- a general Collocation method using the parameters [17] $\gamma = 0.5$, $\beta = 0.18$, and $\theta = 1.287301$,
- the specific Wilson method with $\gamma = 0.5$, $\beta = 1/6$, $\theta = 1.4$, and once more
- the classical Newmark scheme in the trapezoidal format.

The calculations have been performed with the constant time-step size $h_n = 0.1$. To illustrate the free flight, a sequence of the motion is displayed in Figure 5.51. Moreover, some selected snapshots of the deformation are presented in Figure 5.52 b) and Figure 5.57 respectively, wherein quite large deformations of the conrod, particularly at $t = 7.0$, can be seen. As expected, a conservation of the corresponding components of the angular momentum is exclusively offered by the 'ECMC-cG(1) method', whereas the conservation of the linear momentum is even obtained when the abovementioned standard integration schemes are used, compare Figure 5.53. Moreover, Figure 5.54 demonstrates impressively that solely the 'ECMC-cG(1) method' is able to capture a thermodynamically motivated monotonic decrease of the total energy during the free motion, caused by the plastic deformations. In contrast, the standard integration schemes feature also unphysical increasing periods, whereby especially the Wilson and the Collocation method are characterised by the largest decrease of the total energy caused by a high numerical dissipation. Similar to the 'HHT method' in the previous example, the dominant numerical dissipation also yields a significant underestimation of the physical dissipation, as shown in Figure 5.55 a). In the present example, the classical Newmark scheme seems to be the most competitive standard integrator, whereby once more the calculation has stopped after a certain time period due to convergence problems of the involved iteration scheme. However, only the 'ECMC-cG(1) method' is able to guarantee a physically correct conservation of the augmented Hamiltonian, as pictured in Figure 5.55 b). Moreover, it can be seen in Figure 5.56 that the applied standard integrators

[17] In this context, all of the incorporated parameters have been taken from Reference [76].

strongly violate the discrete balance (5.33), even in the order of magnitude $\mathcal{O}(10^2)$. Contrariwise, the Galerkin-based scheme guarantees the fulfilment of the fundamental equation (3.62) also in the present example within the order of magnitude $\mathcal{O}(10^{-11})$.

Remark 5.9: Based on the foregoing numerical examples, the superior performance of the 'ECMC-cG(1) method' in comparison to widespread standard integrators has been confirmed impressively, focussing on the algorithmic conservation properties. In this context, it is important to emphasise once more that such a rigorous investigation of the fulfilment of physically motivated balance laws is initially of conceptual interest, since for smaller time-step sizes also the differences decrease. Nevertheless, the related robustness of such consistent integrators, which has been shown to be unaffected by changes of the time-step size, is also beneficial from a practical point of view, even if the computational costs are slightly higher.

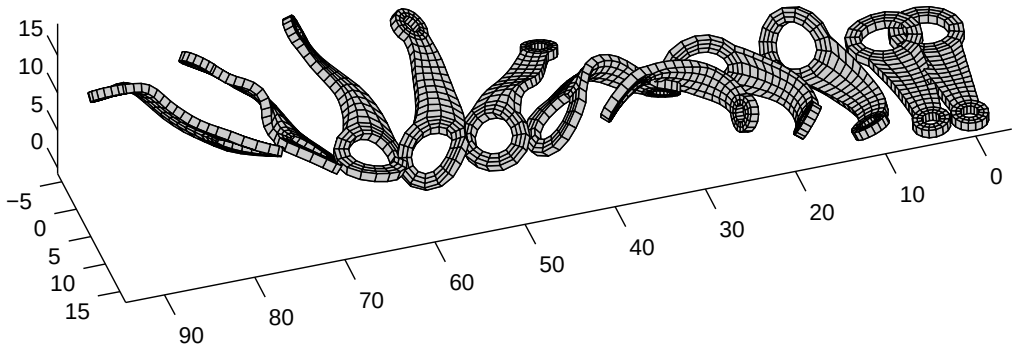

Figure 5.51.: sequence of the motion $t < 5$ (rear view)

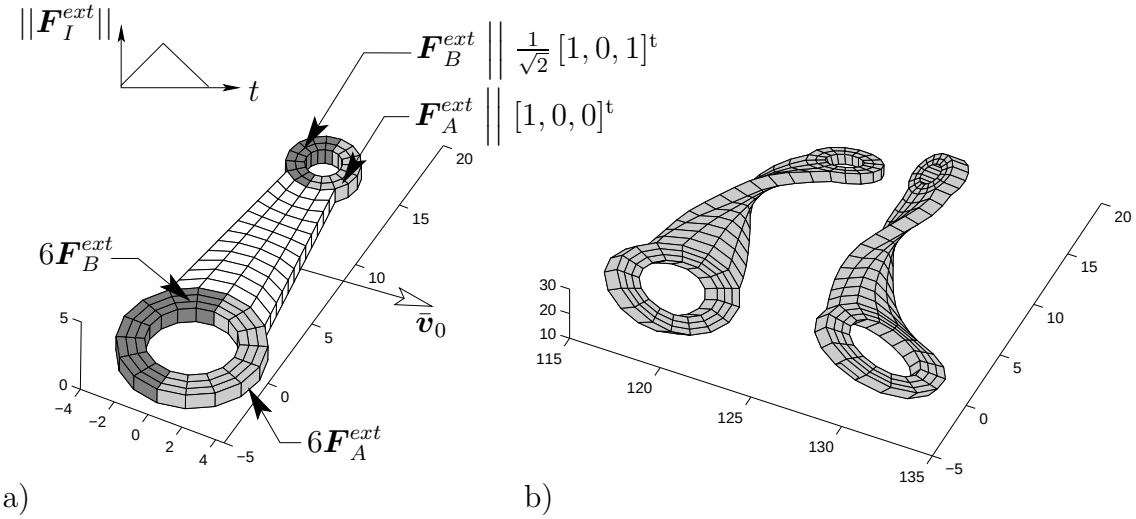

Figure 5.52.: a) initial configuration $\mathcal{B}_0$, b) deformed configurations $\mathcal{B}_t$ at $t = 7.0$ and $t = 7.5$ (front view)

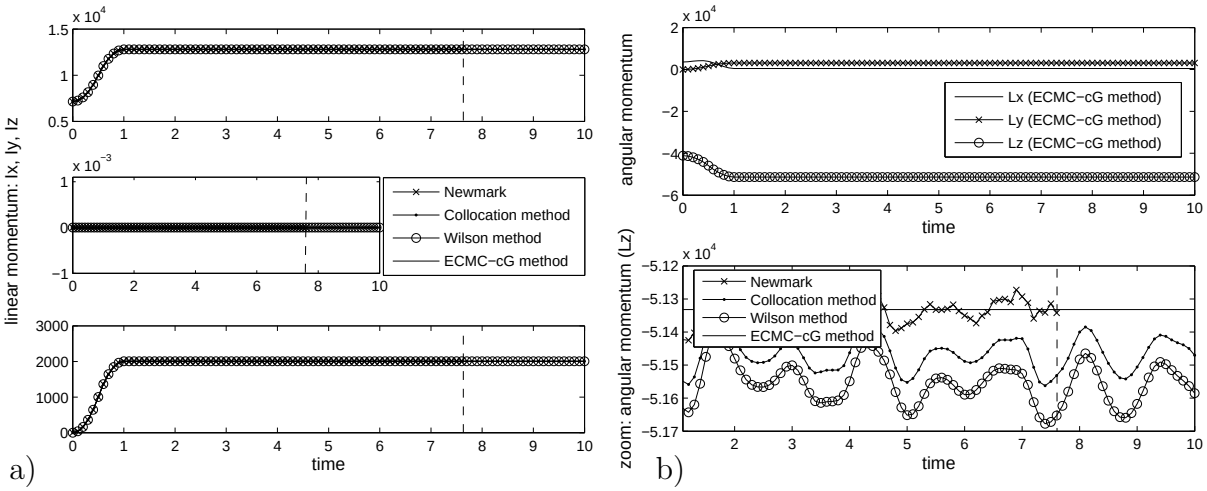

Figure 5.53.: components of: a) linear momentum, b) angular momentum

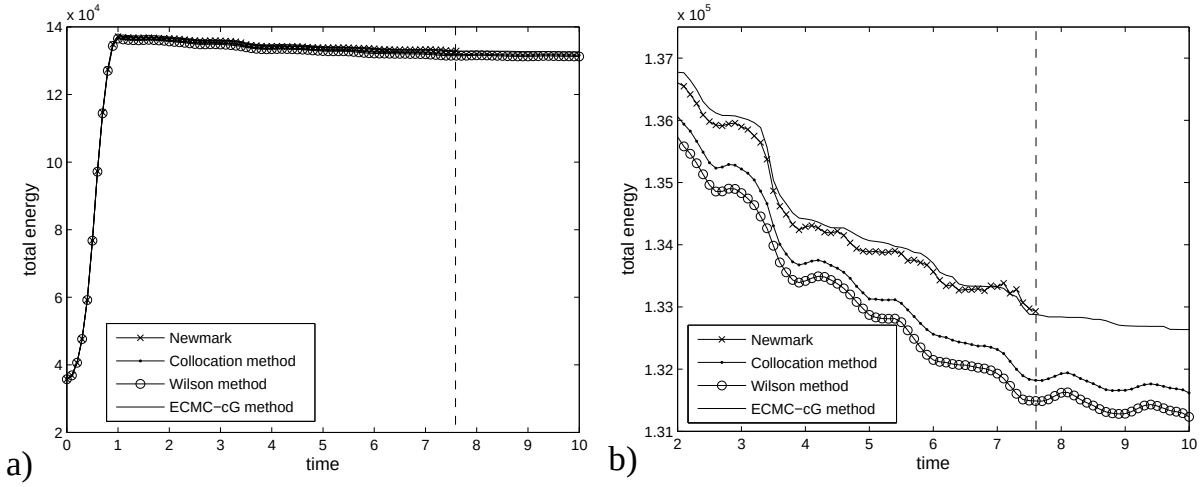

Figure 5.54.: a) total energy H, b) zoom: total energy H

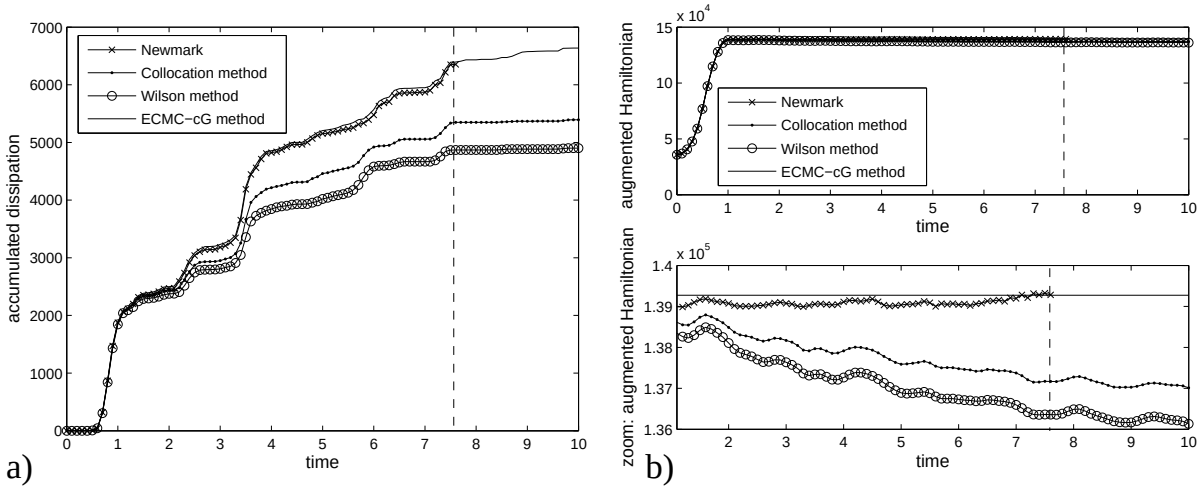

Figure 5.55.: a) accumulated dissipation D, b) augmented Hamiltonian $\widetilde{H}$

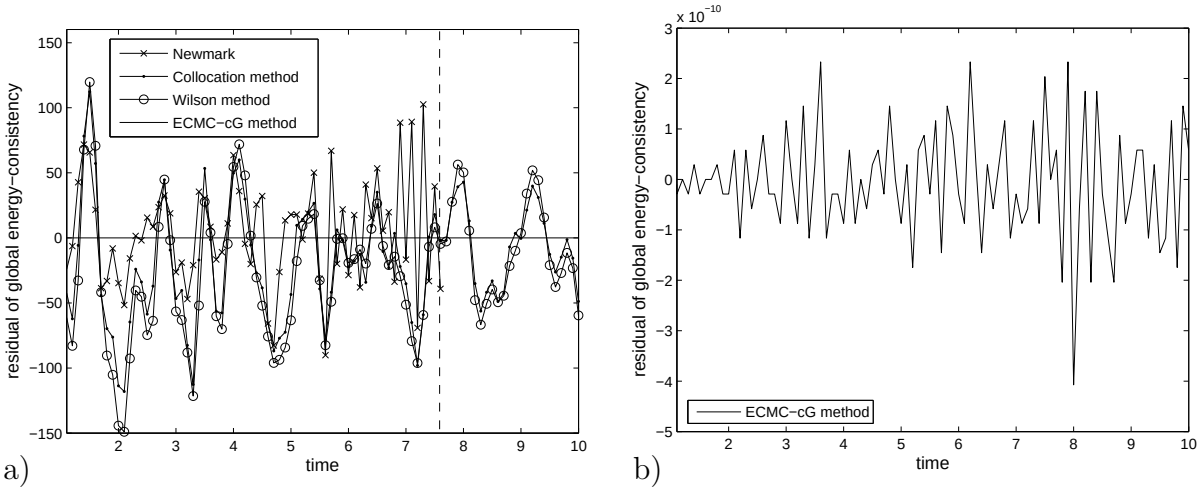

Figure 5.56.: residual R: a) comparison between integrators, b) 'ECMC-cG(1) method'

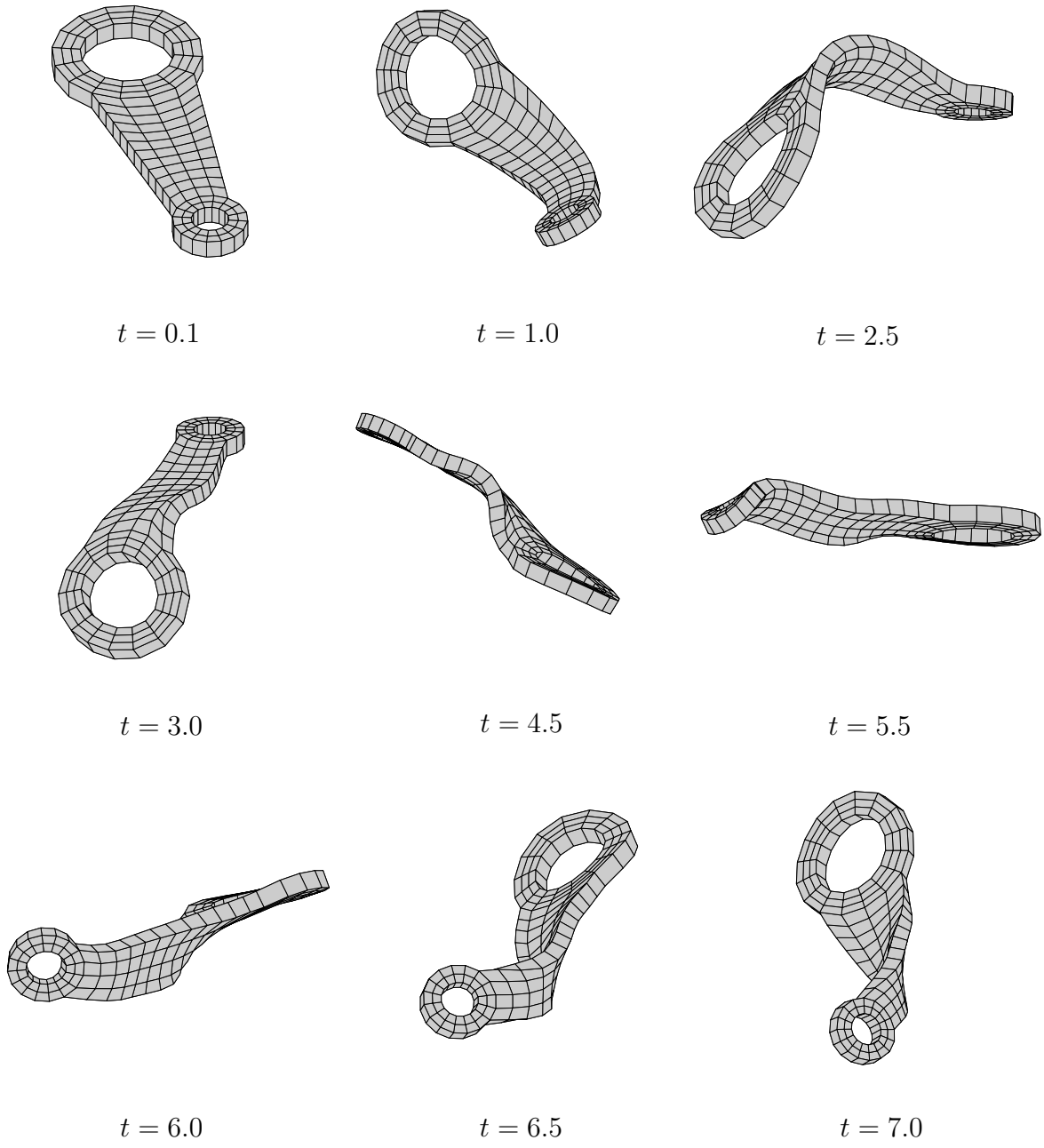

Figure 5.57.: deformed configurations $\mathcal{B}_t$ at selected times t

6. Finite Elasto-Plastic Multibody Dynamics

So far, a general framework for dissipative dynamical systems has been developed to integrate the related governing equations in a consistent manner, rendering not only a physical correct time-integration but also robust algorithms. Specifically, the fundamental concepts have been applied in the previous section to the modelling of finite elasto-plasto-dynamics, dealing with completely flexible inelastic structures based on a standard Finite Element discretisation in space. In a last step, we extend the proposed concepts to constrained dissipative dynamics, since from a practical point of view most of the technically relevant dynamical systems are subject to fulfil additional constraints during their motion.

6.1. Constrained Dissipative Dynamics

For the following investigations, we consider a finite-dimensional dynamical system characterised by the phase-space variables $\bar{\boldsymbol{z}}(t) = [\bar{\boldsymbol{q}}(t), \bar{\boldsymbol{p}}(t)]^{\mathrm{t}}$ which is constrained by the general function

$$\bar{\boldsymbol{g}}(\bar{\boldsymbol{z}}(t)) \stackrel{!}{=} \boldsymbol{0}\,. \tag{6.1}$$

The specification of the (global) vector $\bar{\boldsymbol{z}} \in \mathbb{R}^{2n}$ as well as the particular format of the involved constraints $\bar{\boldsymbol{g}} : \mathbb{R}^{2n} \to \mathbb{R}^m$ will be discussed in the next sections. Analogously to the unconstrained case discussed in Chapter 3, we cast technically the formulation of the global dynamics in a Hamiltonian-type setting, enabling a particularly compact representation and a straightforward incorporation of the additional constraints. Therefore, we introduce an extended function

$$\mathsf{H}(\bar{\boldsymbol{z}}, \bar{\boldsymbol{\mu}}; \boldsymbol{\kappa}) = H(\bar{\boldsymbol{z}}; \boldsymbol{\kappa}) + \bar{\boldsymbol{\mu}} \cdot \bar{\boldsymbol{g}}(\bar{\boldsymbol{z}})\,, \tag{6.2}$$

wherein the vector of Lagrange multipliers $\bar{\boldsymbol{\mu}} \in \mathbb{R}^m$ has been incorporated. Consequently, the resulting (semidiscrete) system of equations of motion results in

$$\begin{aligned} \dot{\bar{\boldsymbol{z}}}(t) &= \mathbb{J} \cdot \nabla_{\bar{\boldsymbol{z}}}\, \mathsf{H}(\bar{\boldsymbol{z}}(t), \bar{\boldsymbol{\mu}}(t); \boldsymbol{\kappa}(t)) \\ \boldsymbol{0} &= \bar{\boldsymbol{g}}(\bar{\boldsymbol{z}}(t))\,, \end{aligned} \tag{6.3}$$

using once more the skew-symmetric matrix $\mathbb{J}$ given by Equation (3.21). Hereby, the system (6.3) represents a set of differential algebraic equations – or short a set of 'DAEs' – which will be directly integrated in time instead of applying a reformulation. Concerning the time discretisation, the cG(k) method of the unconstrained case will be extended to the constrained formulation, following the approach by Betsch and Steinmann [28]. In this context, we apply once more the decomposition of the considered time interval (3.37) and a map of the physical sub-interval $\mathcal{T}$ to the reference interval $\mathcal{I}$ by means of the mapping (3.38). In addition to the unchanged approximations for the global phase-space variables $\bar{\boldsymbol{z}}^h \in \mathcal{P}^k$ and the corresponding test functions $\delta\bar{\boldsymbol{z}}^h \in \mathcal{P}^{k-1}$, compare Equation (3.39), the approximations

$$\bar{\boldsymbol{\mu}}^h = \sum_{i=1}^{k} \widetilde{M}_i(\alpha)\, \bar{\boldsymbol{\mu}}_i \qquad \text{and} \qquad \delta\bar{\boldsymbol{\mu}}^h = \sum_{i=1}^{k} \widetilde{M}_i(\alpha)\, \delta\bar{\boldsymbol{\mu}}_i \tag{6.4}$$

are introduced. Please note, that the resulting approximations of the (unknown) trial functions of the Lagrange multipliers $\bar{\boldsymbol{\mu}}^h \in \mathcal{P}^{k-1}$ as well as the approximated test functions $\delta\bar{\boldsymbol{\mu}}^h \in \mathcal{P}^{k-1}$ belong to the same function space. In general, the corresponding weak forms in time of the global governing equations (6.3) read

$$\begin{aligned} \int_0^1 \left[\mathbb{J}\cdot\delta\bar{\boldsymbol{z}}^h\right]\cdot\left[\mathrm{D}_\alpha\bar{\boldsymbol{z}}^h - h_n\,\mathbb{J}\cdot\nabla_{\bar{\boldsymbol{z}}}\,\mathsf{H}(\bar{\boldsymbol{z}}^h,\bar{\boldsymbol{\mu}}^h;\boldsymbol{\kappa})\right]\mathrm{d}\alpha &= 0 \\ \int_0^1 \delta\bar{\boldsymbol{\mu}}^h\cdot\mathbb{G}(\bar{\boldsymbol{z}}^h)\cdot\mathrm{D}_\alpha\bar{\boldsymbol{z}}^h\,\mathrm{d}\alpha &= 0\,, \end{aligned} \tag{6.5}$$

wherein the constraint Jacobian

$$\mathbb{G}(\bar{\boldsymbol{z}}^h) := \nabla_{\bar{\boldsymbol{z}}}\,\bar{\boldsymbol{g}}(\bar{\boldsymbol{z}}^h) \tag{6.6}$$

has been introduced. The resulting scheme can be classified as a mixed Galerkin method, abbreviated by 'mG(k) method'. By inserting the time approximations (3.39), (6.4) in Equations (6.5), we obtain for arbitrary polynomial degree k the system of equations

$$\begin{aligned} \sum_{j=1}^{k+1}\int_0^1 \widetilde{M}_i M_j^{'}\,\mathrm{d}\alpha\,\bar{\boldsymbol{z}}_j - h_n\,\mathbb{J}\cdot\int_0^1 \widetilde{M}_i\left[\nabla_{\bar{\boldsymbol{z}}}\,H(\bar{\boldsymbol{z}}^h;\boldsymbol{\kappa}) + \bar{\boldsymbol{\mu}}^h\cdot\mathbb{G}(\bar{\boldsymbol{z}}^h)\right]\mathrm{d}\alpha &= \mathbf{0} \\ \sum_{j=1}^{k+1}\int_0^1 \widetilde{M}_i M_j^{'}\,\mathbb{G}(\bar{\boldsymbol{z}}^h)\,\mathrm{d}\alpha\cdot\bar{\boldsymbol{z}}_j &= \mathbf{0} \end{aligned} \tag{6.7}$$

for $i = 1, ..., k$. Analogously to the unconstrained case, the remaining task is to evaluate the related time-integrals, whereby the applied option directly influences the resulting conservation properties of the integrator, depending crucially on the specific format of the underlying function H and the involved constraints $\bar{\boldsymbol{g}}$ respectively. For fundamental aspects concerning the obtained conservation properties of the general family of

time-stepping schemes (6.7), we refer to Betsch [20], Betsch and Steinmann [28], and references cited therein since, once again, the global structure of the equations of motion is formally identical to the well-studied conservative case.

Remarks 6.1:

1. With regard to *mechanical consistency*, the equivalence of the mG(k) method and a k-stage Gauss Runge-Kutta method, being related to k Gaussian integration points for the approximation of the second (global) time-integral in Equation $(6.7)_1$, has turned out to be helpful, as discussed in detail in References [20, 28].

2. Concerning *energy-consistency*, we can follow the same argumentation as for the unconstrained case that has been extensively described in Appendix A. Based on Equation $(6.7)_1$, however, we obtain additionally

$$\sum_{i,j=1}^{k} \bar{\boldsymbol{\mu}}_j \cdot \int_0^1 \widetilde{M}_i \widetilde{M}_j \, \mathbb{G}(\bar{\boldsymbol{z}}^h) \, \mathrm{d}\alpha \cdot \widetilde{\bar{\boldsymbol{z}}}_i = \sum_{i=1}^{k} \bar{\boldsymbol{\mu}}_i \cdot \sum_{j=1}^{k+1} \int_0^1 \widetilde{M}_i M_j' \, \mathbb{G}(\bar{\boldsymbol{z}}^h) \, \mathrm{d}\alpha \cdot \bar{\boldsymbol{z}}_j = 0 \,, \quad (6.8)$$

   compare Betsch and Steinmann [28]. Obviously, Equation (6.8) corresponds to Equation $(6.7)_2$ and, hence, it can be related to the second weak form in time $(6.5)_2$ via the approximations (3.39), (6.4). Interestingly, the left-hand side of Equation (6.8) might be also interpreted as a time-integrated and time-approximated generalisation of the classical d'Alembert statement that constraint forces are workless. Regarding the mentioned relation to the weak formulation of the constraints $(6.5)_2$, basically the following two properties of the applied time discretisation procedure are essential:

   - Firstly, the fact that the time-derivatives $\mathrm{D}_\alpha \bar{\boldsymbol{z}}^h$ and the test functions $\delta \bar{\boldsymbol{z}}^h$ belong to the same function space $\mathcal{P}^{k-1}$ has been involved, as already discussed in Remark 3.4.2 for the unconstrained case.
   - Secondly, the application of approximated Lagrange multipliers $\bar{\boldsymbol{\mu}}^h$ which are included in the same function space $\mathcal{P}^{k-1}$ as the corresponding test functions $\delta \bar{\boldsymbol{\mu}}^h$ is obviously a further significant aspect in this context, compare Equation $(6.5)_2$ with the right-hand side of Equation (6.8).

   Consequently, the chosen mG(k) method could even be regarded as the proper method of choice to transfer a (generalised) workless condition from the time-continuous to the time-discrete case.

3. Since we deal in the present chapter with constrained dynamical systems, a further requirement for the resulting integrators is the fulfilment of the underlying constraints, referred to as *kinematic consistency*. Starting with the fundamental

theorem of calculus and using the partition of unity property of the reduced shape functions in time, namely $\sum_{i=1}^{k} \widetilde{M}_i = 1$, renders

$$\bar{\boldsymbol{g}}_{\alpha=1} - \bar{\boldsymbol{g}}_{\alpha=0} = \int_0^1 \mathrm{D}_\alpha\, \bar{\boldsymbol{g}}(\bar{\boldsymbol{z}}^h)\, \mathrm{d}\alpha = \sum_{j=1}^{k+1} \int_0^1 \left[\sum_{i=1}^{k} \widetilde{M}_i \right] M_j' \, \mathbb{G}(\bar{\boldsymbol{z}}^h)\, \mathrm{d}\alpha \cdot \bar{\boldsymbol{z}}_j \,. \tag{6.9}$$

Obviously, the right-hand side of Equation (6.9) can be reformulated by changing integration and summation, so that Equation $(6.7)_2$ directly implies

$$\sum_{i=1}^{k} \sum_{j=1}^{k+1} \int_0^1 \widetilde{M}_i M_j' \, \mathbb{G}(\bar{\boldsymbol{z}}^h)\, \mathrm{d}\alpha \cdot \bar{\boldsymbol{z}}_j = \boldsymbol{0} \,. \tag{6.10}$$

Hence, considering Equations (6.9), (6.10), Equation $(6.7)_2$ yields as well the fulfilment of the discrete balance

$$\bar{\boldsymbol{g}}_{\alpha=1} - \bar{\boldsymbol{g}}_{\alpha=0} = \boldsymbol{0} \,, \tag{6.11}$$

when the involved time-integrals are calculated exactly. Assuming consistent initial values for the constraints at $t = 0$, Equation (6.11) leads straightforwardly to the fulfilment of the constraints at $t = t_{n+1}$, being related to $\alpha = 1$ via Equation (3.38).

The foregoing discussion has clearly shown that in fact the applied mG(k) method represents the adequate generalisation of the cG(k) method in the here considered context, providing a universal framework to design consistent time-stepping schemes for general constrained dynamical systems. Dealing in particular with inelastic multibody dynamics, the general format of the constraint vector (6.1) has to be specified next, whereby we basically distinguish between

- *internal constraints* that are caused by underlying assumptions of the chosen rigid body description,
- *external constraints* which are related to kinematic restrictions of the involved bearings and joints, and finally
- *coupling constraints* that correspond to the coupling of rigid and (inelastic) flexible parts.

6.1.1. Internal constraints – Rigid body dynamics

In contrast to standard approaches in the multibody community, which usually rely on the classical Euler equations or on local coordinates for the special orthogonal group SO(3) respectively, in this work a rotationless formulation is preferred to describe the rigid body kinematics, as advocated for instance in References [27, 29, 31]. The main advantages of such a description are:

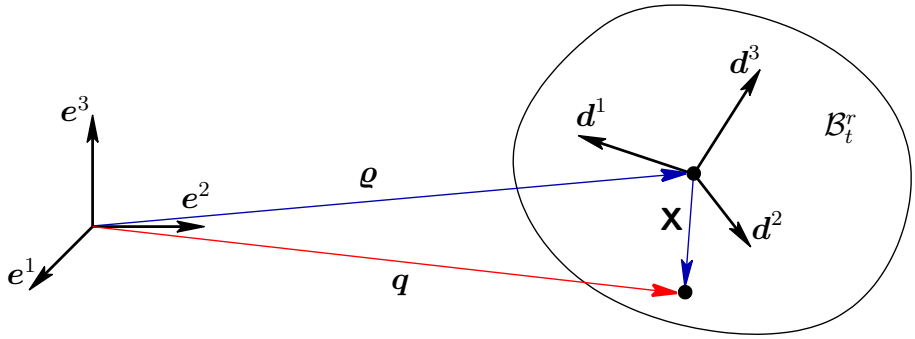

Figure 6.1.: rigid body kinematics

- First of all, the chosen formulation exhibits, independently if planar or spatial motions are considered, a quite simple structure of the resulting equations of motion, avoiding any numerical difficulties associated with the incorporation of rotational parameters.
- Moreover, it directly results in a set of DAEs with holonomic constraints which perfectly fits into the foregoing Galerkin-based time-integration framework. Hence, the favoured approach to describe the motion of rigid bodies is particularly well-suited regarding the claimed consistent time-integration.

For the following investigations, a representative rigid body $\mathcal{B}^r \subset \mathbb{R}^3$ with the mass density ρ^r is considered. Moreover, let $\boldsymbol{X} = \sum_{\tau=1}^{3} X^\tau \, \boldsymbol{e}^\tau \in \mathbb{R}^3$ denote the placement of a material point of the body in the corresponding reference configuration $\mathcal{B}_0^r$, whereby we assume for the sake of simplicity that the centre of mass of $\mathcal{B}_0^r$ coincides with the origin of the space-fixed orthonormal frame $\{\boldsymbol{e}^\tau\}$. Consequently, the current placement in the spatial configuration $\mathcal{B}_t^r$ can be formulated by means of the mapping

$$\boldsymbol{q}(\boldsymbol{X}, t) = \boldsymbol{\varrho}(t) + \sum_{\tau=1}^{3} X^\tau \, \boldsymbol{d}^\tau(t) \,, \tag{6.12}$$

as sketched in Figure 6.1. Herein, the vector $\boldsymbol{\varrho}(t) : \mathbb{R}^+ \to \mathbb{R}^3$ refers to the position of the centre of mass and $\mathbf{X}(t) := \boldsymbol{R}(t) \cdot \boldsymbol{X} = \sum_{\tau=1}^{3} X^\tau \, \boldsymbol{d}^\tau(t)$ with the rotation matrix $\boldsymbol{R} \in \mathrm{SO}(3)$ denotes the (relative) placement with respect to the director triad $\{\boldsymbol{d}^\tau(t)\}$. Hereby, the directors constitute a right-handed body-fixed frame which is assumed to be aligned with the principal axes of the rigid body. Hence, the current configuration $\mathcal{B}_t^r$ might be specified by the vector

$$\boldsymbol{q}^r(t) := [\boldsymbol{\varrho}(t), \; \boldsymbol{d}^1(t), \; \boldsymbol{d}^2(t), \; \boldsymbol{d}^3(t)]^{\mathrm{t}} \in \mathbb{R}^{12} \,, \tag{6.13}$$

including a set of redundant coordinates. Additionally, six orthonormality conditions $\boldsymbol{d}^\tau \cdot \boldsymbol{d}^\beta = \delta_{\tau\beta}$, which reflect the requirement of rigidity, have to be taken into account,

rendering the vector of internal constraints

$$\boldsymbol{g}^{int}(\boldsymbol{q}^r) = \begin{bmatrix} \frac{1}{2}\left[\boldsymbol{d}^1 \cdot \boldsymbol{d}^1 - 1\right] \\ \frac{1}{2}\left[\boldsymbol{d}^2 \cdot \boldsymbol{d}^2 - 1\right] \\ \frac{1}{2}\left[\boldsymbol{d}^3 \cdot \boldsymbol{d}^3 - 1\right] \\ \boldsymbol{d}^1 \cdot \boldsymbol{d}^2 \\ \boldsymbol{d}^1 \cdot \boldsymbol{d}^3 \\ \boldsymbol{d}^2 \cdot \boldsymbol{d}^3 \end{bmatrix} . \tag{6.14}$$

According to Equation (6.6), we obtain furthermore the corresponding constraint Jacobian of the internal constraints $\mathbb{G}^{int} := \nabla_{\boldsymbol{q}^r} \boldsymbol{g}^{int} \in \mathbb{R}^6 \times \mathbb{R}^{12}$, resulting in

$$\mathbb{G}^{int} = \begin{bmatrix} \mathbf{0}^{\mathrm{t}} & \boldsymbol{d}^{1\mathrm{t}} & \mathbf{0}^{\mathrm{t}} & \mathbf{0}^{\mathrm{t}} \\ \mathbf{0}^{\mathrm{t}} & \mathbf{0}^{\mathrm{t}} & \boldsymbol{d}^{2\mathrm{t}} & \mathbf{0}^{\mathrm{t}} \\ \mathbf{0}^{\mathrm{t}} & \mathbf{0}^{\mathrm{t}} & \mathbf{0}^{\mathrm{t}} & \boldsymbol{d}^{3\mathrm{t}} \\ \mathbf{0}^{\mathrm{t}} & \boldsymbol{d}^{2\mathrm{t}} & \boldsymbol{d}^{1\mathrm{t}} & \mathbf{0}^{\mathrm{t}} \\ \mathbf{0}^{\mathrm{t}} & \boldsymbol{d}^{3\mathrm{t}} & \mathbf{0}^{\mathrm{t}} & \boldsymbol{d}^{1\mathrm{t}} \\ \mathbf{0}^{\mathrm{t}} & \mathbf{0}^{\mathrm{t}} & \boldsymbol{d}^{3\mathrm{t}} & \boldsymbol{d}^{2\mathrm{t}} \end{bmatrix} \tag{6.15}$$

with the zero vector $\mathbf{0} \in \mathbb{R}^3$. Next, the constant mass matrix of the rigid body $\mathbb{M}^r \in \mathbb{R}^{12} \times \mathbb{R}^{12}$ is introduced as

$$\mathbb{M}^r = \begin{bmatrix} M\boldsymbol{I} & \mathbf{0} & \mathbf{0} & \mathbf{0} \\ \mathbf{0} & E_1\,\boldsymbol{I} & \mathbf{0} & \mathbf{0} \\ \mathbf{0} & \mathbf{0} & E_2\,\boldsymbol{I} & \mathbf{0} \\ \mathbf{0} & \mathbf{0} & \mathbf{0} & E_3\,\boldsymbol{I} \end{bmatrix} , \tag{6.16}$$

wherein we have incorporated the identity and zero matrices $\boldsymbol{I}, \mathbf{0} \in \mathbb{R}^3 \times \mathbb{R}^3$, the total mass M, as well as the principal values of the convected Euler tensor E_τ which are given by

$$M = \int_{\mathcal{B}_0^r} \rho^r(\boldsymbol{X})\,\mathrm{d}V \qquad \text{and} \qquad E_\tau = \int_{\mathcal{B}_0^r} [X^\tau]^2\,\rho^r(\boldsymbol{X})\,\mathrm{d}V \tag{6.17}$$

respectively. Moreover, time-differentiation of Equation (6.13) yields

$$\dot{\boldsymbol{q}}^r(t) = [\dot{\boldsymbol{\varrho}}(t),\ \dot{\boldsymbol{d}}^1(t),\ \dot{\boldsymbol{d}}^2(t),\ \dot{\boldsymbol{d}}^3(t)]^{\mathrm{t}} =: \boldsymbol{v}^r(t)\,, \tag{6.18}$$

so that the corresponding vector of momenta of the rigid body $\boldsymbol{p}^r(t) := \mathbb{M}^r \cdot \boldsymbol{v}^r(t) \in \mathbb{R}^{12}$ can be defined. Therewith, the classical Hamiltonian for one rigid body might be written as

$$H^r(\boldsymbol{q}^r, \boldsymbol{p}^r) := \frac{1}{2}\,\boldsymbol{p}^r \cdot \mathbb{M}^{r\,-1} \cdot \boldsymbol{p}^r + V^{ext}(\boldsymbol{q}^r)\,. \tag{6.19}$$

Consequently, the general format of a mixed Galerkin time-integration of constrained (dissipative) systems, given by Equations (6.7), can be specified straightforwardly to rigid body dynamics with $\bar{\boldsymbol{z}} = [\boldsymbol{q}^r, \boldsymbol{p}^r]^{\mathrm{t}} \in \mathbb{R}^{24}$ by setting $H = H^r$ and $\mathbb{G} = [\mathbb{G}^{int}\ \ \mathbf{0}] \in \mathbb{R}^6 \times \mathbb{R}^{24}$, using the zero matrix $\mathbf{0} \in \mathbb{R}^6 \times \mathbb{R}^{12}$.

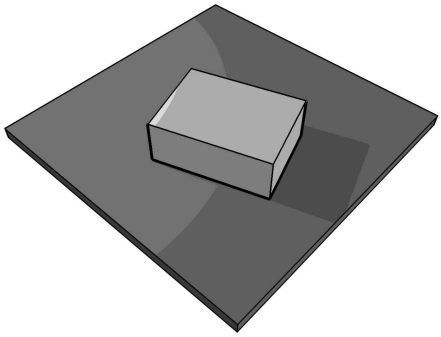

planar ($m^{ext} = 3$)

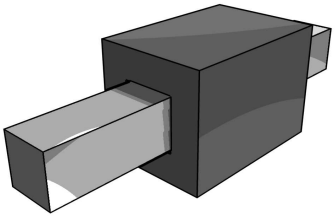

prismatic ($m^{ext} = 5$)

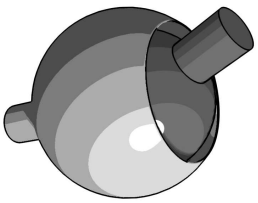

spherical ($m^{ext} = 3$)

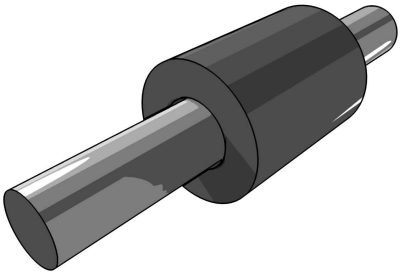

cylindrical ($m^{ext} = 4$)

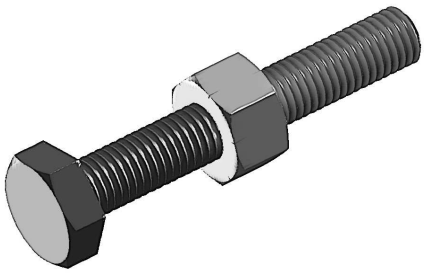

screw ($m^{ext} = 5$)

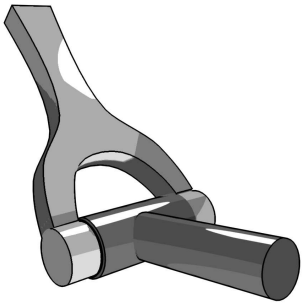

revolute ($m^{ext} = 5$)

Figure 6.2.: lower kinematic pairs

6.1.2. External constraints – Kinematic pairs

In the previous section, a rotationless formulation to model rigid body dynamics has been presented, focussing initially on the description of one rigid part. In a next step, a dynamical system which consists of two rigid bodies $\mathcal{B}^r_{1,2}$ is considered, whereby each body is characterised by the vector of internal constraints $\boldsymbol{g}^{int}_\tau$ and the mass matrix $\mathbb{M}^r_\tau$ for $\tau = 1, 2$, given by Equation (6.14) and Equation (6.16) respectively. By introducing the mass matrix of the system

$$\mathbb{M}^r_{12} = \begin{bmatrix} \mathbb{M}^r_1 & \mathbf{0} \\ \mathbf{0} & \mathbb{M}^r_2 \end{bmatrix}, \tag{6.20}$$

with $\mathbf{0} \in \mathbb{R}^{12} \times \mathbb{R}^{12}$, the classical Hamiltonian reads

$$H^r_{12}(\bar{\boldsymbol{q}}, \bar{\boldsymbol{p}}) := \frac{1}{2}\, \bar{\boldsymbol{p}} \cdot {\mathbb{M}^r_{12}}^{-1} \cdot \bar{\boldsymbol{p}} + V^{ext}(\bar{\boldsymbol{q}})\,, \tag{6.21}$$

wherein the system vectors $\bar{\boldsymbol{q}} := [\boldsymbol{q}^r_1, \boldsymbol{q}^r_2]^{\mathrm{t}} \in \mathbb{R}^{24}$ and $\bar{\boldsymbol{p}} := [\boldsymbol{p}^r_1, \boldsymbol{p}^r_2]^{\mathrm{t}} \in \mathbb{R}^{24}$ have been introduced based on

$$\boldsymbol{q}^r_\tau = [\boldsymbol{\varrho}_\tau,\ \boldsymbol{d}^1_\tau,\ \boldsymbol{d}^2_\tau,\ \boldsymbol{d}^3_\tau]^{\mathrm{t}} \qquad \text{and} \qquad \boldsymbol{p}^r_\tau = [\boldsymbol{p}_\tau,\ \boldsymbol{p}^1_\tau,\ \boldsymbol{p}^2_\tau,\ \boldsymbol{p}^3_\tau]^{\mathrm{t}}\,. \tag{6.22}$$

Furthermore, the vector of internal constraints

$$\boldsymbol{g}^{int}_{12}(\bar{\boldsymbol{q}}) := [\boldsymbol{g}^{int}_1(\boldsymbol{q}^r_1),\ \boldsymbol{g}^{int}_2(\boldsymbol{q}^r_2)]^{\mathrm{t}} \tag{6.23}$$

with $\boldsymbol{g}^{int}_\tau(\boldsymbol{q}^r_\tau) \in \mathbb{R}^6$ has to be taken into account for the two body system under consideration. Consequently, the constraint Jacobian $\mathbb{G}^{int}_{12} := \nabla_{\bar{\boldsymbol{q}}}\, \boldsymbol{g}^{int}_{12} \in \mathbb{R}^{12} \times \mathbb{R}^{24}$ results in

$$\mathbb{G}^{int}_{12} = \begin{bmatrix} \mathbb{G}^{int}_1 & \mathbf{0} \\ \mathbf{0} & \mathbb{G}^{int}_2 \end{bmatrix}, \tag{6.24}$$

using $\mathbb{G}^{int}_\tau$ given by Equation (6.15) and $\mathbf{0} \in \mathbb{R}^6 \times \mathbb{R}^{12}$. Dealing with multibody systems, in particular the interconnection of the involved rigid bodies via kinematic pairs is essential. For fundamental aspects and detailed background informations concerning this topic, we refer for instance to the textbooks [3, 58, 159] and references cited therein. Basically, it is accepted to distinguish between six so-called lower kinematic pairs. As sketched in Figure 6.2, we differ between

- planar
- spherical
- screw
- prismatic
- cylindrical
- revolute

pairs. Obviously, each of these pairs only allows a specific relative motion between the connected bodies, or with other words each joint blocks a certain number of (relative) degrees of freedom, referred to as m^{ext}. Taking these additional kinematic restrictions

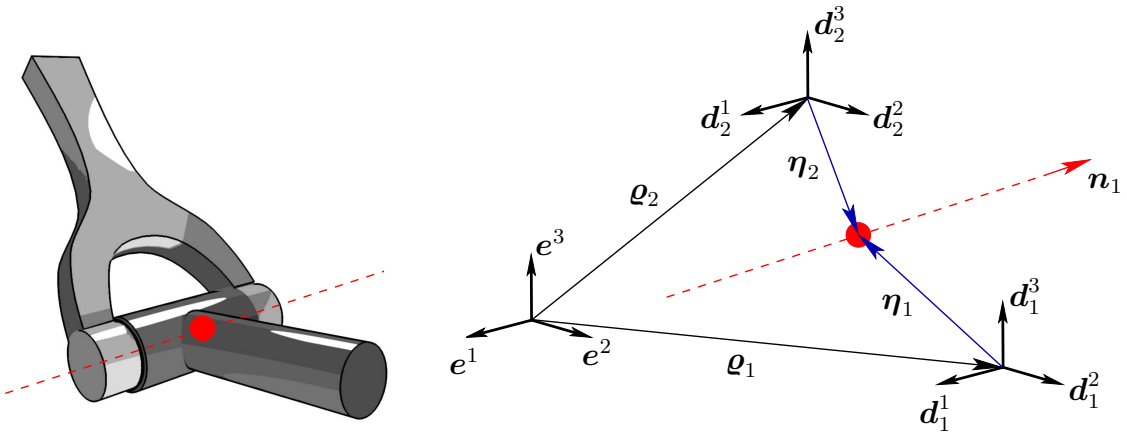

Figure 6.3.: revolute pair

into account, a vector of external constraints and the corresponding constraint Jacobian, given by

$$\boldsymbol{g}_{12}^{ext}(\boldsymbol{q}_1^r, \boldsymbol{q}_2^r) \in \mathbb{R}^{m^{ext}} \qquad \text{and} \qquad \mathbb{G}_{12}^{ext} := \nabla_{\bar{\boldsymbol{q}}}\, \boldsymbol{g}_{12}^{ext} \in \mathbb{R}^{m^{ext}} \times \mathbb{R}^{24}\,, \tag{6.25}$$

adds to the foregoing internal constraints [1]. Regarding the specific format of the external constraints in case of different kinematic pairs, we refer to the detailed investigations in Betsch and Leyendecker [23] and Leyendecker [108] [2]. In general, we finally obtain the

[1] Please note, that the chosen formulation to model joints between rigid bodies completely avoids the introduction of relative degrees of freedom and, in fact, it fits perfectly into the favoured DAE framework.

[2] Here, solely the formulation of a revolute pair with $m^{ext} = 5$ is demonstrated exemplarily, since this joint will play a central role in one of the following numerical examples, compare Section 6.3.4. Considering Figure 6.3, the corresponding vector of external constraints can be written as

$$\boldsymbol{g}_{12}^{rev} = \begin{bmatrix} \boldsymbol{\varrho}_2 + \boldsymbol{\eta}_2 - \boldsymbol{\varrho}_1 - \boldsymbol{\eta}_1 \\ \boldsymbol{n}_1 \cdot \boldsymbol{d}_2^1 - \theta_1 \\ \boldsymbol{n}_1 \cdot \boldsymbol{d}_2^2 - \theta_2 \end{bmatrix}, \tag{6.26}$$

wherein the normalised axis of rotation $\boldsymbol{n}_1 = \sum_{\tau=1}^{3} n_1^\tau \boldsymbol{d}_1^\tau$, the projection of the director $\boldsymbol{d}_2^\tau$ on this axis θ_τ, as well as the vectors $\boldsymbol{\eta}_\omega = \sum_{\tau=1}^{3} \eta_\omega^\tau \boldsymbol{d}_\omega^\tau$ have been introduced. Consequently, the constraint Jacobian reads

$$\mathbb{G}_{12}^{rev} = \begin{bmatrix} -\boldsymbol{I} & -\eta_1^1 \boldsymbol{I} & -\eta_1^2 \boldsymbol{I} & -\eta_1^3 \boldsymbol{I} & \boldsymbol{I} & \eta_2^1 \boldsymbol{I} & \eta_2^2 \boldsymbol{I} & \eta_2^3 \boldsymbol{I} \\ \boldsymbol{0}^{\mathrm{t}} & n_1^1 \boldsymbol{d}_2^{1\,\mathrm{t}} & n_1^2 \boldsymbol{d}_2^{1\,\mathrm{t}} & n_1^3 \boldsymbol{d}_2^{1\,\mathrm{t}} & \boldsymbol{0}^{\mathrm{t}} & \boldsymbol{n}_1^{\mathrm{t}} & \boldsymbol{0}^{\mathrm{t}} & \boldsymbol{0}^{\mathrm{t}} \\ \boldsymbol{0}^{\mathrm{t}} & n_1^1 \boldsymbol{d}_2^{2\,\mathrm{t}} & n_1^2 \boldsymbol{d}_2^{2\,\mathrm{t}} & n_1^3 \boldsymbol{d}_2^{2\,\mathrm{t}} & \boldsymbol{0}^{\mathrm{t}} & \boldsymbol{0}^{\mathrm{t}} & \boldsymbol{n}_1^{\mathrm{t}} & \boldsymbol{0}^{\mathrm{t}} \end{bmatrix}, \tag{6.27}$$

using $\boldsymbol{0} \in \mathbb{R}^3$ and $\boldsymbol{I} \in \mathbb{R}^3 \times \mathbb{R}^3$.

resulting constraints and constraint Jacobian of the system given by

$$\bar{\boldsymbol{g}}(\bar{\boldsymbol{q}}) = [\boldsymbol{g}_{12}^{int},\ \boldsymbol{g}_{12}^{ext}]^{\mathrm{t}} \in \mathbb{R}^{12+m^{ext}} \qquad \text{and} \qquad \mathbb{G} = \begin{bmatrix} \mathbb{G}_{12}^{int} & \mathbf{0}_1 \\ \mathbb{G}_{12}^{ext} & \mathbf{0}_2 \end{bmatrix} \in \mathbb{R}^{12+m^{ext}} \times \mathbb{R}^{48} \tag{6.28}$$

with the zero matrices $\mathbf{0}_1 \in \mathbb{R}^{12} \times \mathbb{R}^{24}$ and $\mathbf{0}_2 \in \mathbb{R}^{m^{ext}} \times \mathbb{R}^{24}$, so that by means of $H = H_{12}^r$ and $\bar{\boldsymbol{z}} = [\boldsymbol{q}_1^r, \boldsymbol{q}_2^r, \boldsymbol{p}_1^r, \boldsymbol{p}_2^r]^{\mathrm{t}} \in \mathbb{R}^{48}$ the time-integration scheme (6.7) is determined for the two body system at hand.

6.1.3. Coupling constraints – Flexible parts

To model inelastic multibody systems, the final but essential step is the investigation of the coupling between flexible parts, which have been discussed exhaustively in Chapter 3, and rigid bodies, that have been addressed in the previous sections. In the following, we consider a partitioned solid body

$$\mathcal{B} = \mathcal{B}^r \cup \mathcal{B}^f\,, \tag{6.29}$$

consisting of two rigid parts $\mathcal{B}^r = \bigcup_{\omega=1}^{2} \mathcal{B}_\omega^r$ which are connected with a semidiscrete flexible structure $\mathcal{B}^f = \bigcup_{el=1}^{n_{el}} \mathcal{B}^{el}$. In entire analogy to Chapter 3, the dynamics of the flexible part (n_{node} spatial nodes, n_{dof} degrees of freedom) is formulated by means of a vector of nodal coordinates and a vector of nodal momenta which are denoted in this context by $\boldsymbol{q}^f := [\boldsymbol{q}_1(t), ..., \boldsymbol{q}_{n_{node}}]^{\mathrm{t}} \in \mathbb{R}^{n_{dof}}$ and $\boldsymbol{p}^f := [\boldsymbol{p}_1(t), ..., \boldsymbol{p}_{n_{node}}]^{\mathrm{t}} \in \mathbb{R}^{n_{dof}}$ respectively. Using furthermore the zero matrices $\mathbf{0}_1 \in \mathbb{R}^{12} \times \mathbb{R}^{12}$ and $\mathbf{0}_2 \in \mathbb{R}^{12} \times \mathbb{R}^{n_{dof}}$, the mass matrix of the system

$$\mathbb{M}_{12}^{rf} = \begin{bmatrix} \mathbb{M}_1^r & \mathbf{0}_1 & \mathbf{0}_2 \\ \mathbf{0}_1 & \mathbb{M}_2^r & \mathbf{0}_2 \\ \mathbf{0}_2^{\mathrm{t}} & \mathbf{0}_2^{\mathrm{t}} & \mathbb{M}^f \end{bmatrix} \in \mathbb{R}^{24+n_{dof}} \times \mathbb{R}^{24+n_{dof}} \tag{6.30}$$

can be assembled, wherein $\mathbb{M}^f$ denotes the already known mass matrix of the flexible part according to Equation (3.18). Moreover, we introduce the system vectors $\bar{\boldsymbol{q}} := [\boldsymbol{q}_1^r, \boldsymbol{q}_2^r, \boldsymbol{q}^f]^{\mathrm{t}} \in \mathbb{R}^{24+n_{dof}}$ and $\bar{\boldsymbol{p}} := [\boldsymbol{p}_1^r, \boldsymbol{p}_2^r, \boldsymbol{p}^f]^{\mathrm{t}} \in \mathbb{R}^{24+n_{dof}}$ based on Equation (6.22), so that the function

$$H_{12}^{rf}(\bar{\boldsymbol{q}}, \bar{\boldsymbol{p}}; \boldsymbol{\kappa}) := \frac{1}{2}\, \bar{\boldsymbol{p}} \cdot \mathbb{M}_{12}^{rf\,-1} \cdot \bar{\boldsymbol{p}} + \Psi(\boldsymbol{q}^f; \boldsymbol{\kappa}) + V^{ext}(\bar{\boldsymbol{q}}) \tag{6.31}$$

can be defined, combining Equation (3.20) with Equation (6.21). As sketched in Figure 6.4, the actual coupling between the rigid body $\mathcal{B}_\omega^r$ and a spatial node I of the deformable part can be formulated by incorporating the so-called (nodal) coupling constraints

$$\boldsymbol{g}_I^{cou}(\bar{\boldsymbol{q}}) = \boldsymbol{\varrho}_\omega(t) + \sum_{\tau=1}^{3} X_I^\tau\, \boldsymbol{d}_\omega^\tau(t) - \boldsymbol{q}_I(t) \tag{6.32}$$

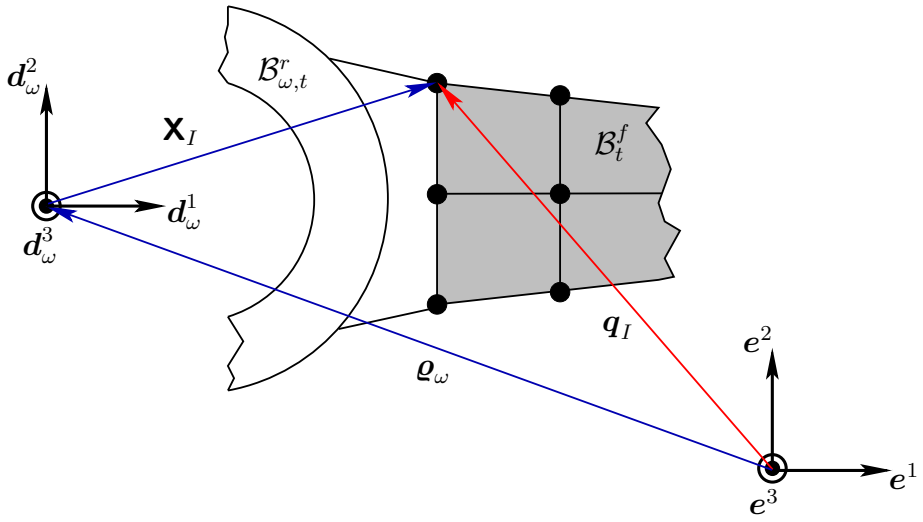

Figure 6.4.: coupling between rigid and flexible parts

with $\omega = 1, 2$ chosen adequately, depending on the fact if the considered node I is coupled to rigid body 1 or rigid body 2. Consequently, the corresponding constraint Jacobian $\mathbb{G}^{cou}_I := \nabla_{\bar{\boldsymbol{q}}}\, \boldsymbol{g}^{cou}_I \in \mathbb{R}^3 \times \mathbb{R}^{24+n_{dof}}$ reads

$$\mathbb{G}^{cou}_I = [\boldsymbol{I} \quad X^1_I\, \boldsymbol{I} \quad X^2_I\, \boldsymbol{I} \quad X^3_I\, \boldsymbol{I} \quad \mathbf{0}_1 \quad \mathbf{0}_2 \quad \mathbf{0}_2 \ \ldots\ -\boldsymbol{I} \ \ldots\ \mathbf{0}_2] \tag{6.33}$$

for the case $\omega = 1$ and

$$\mathbb{G}^{cou}_I = [\mathbf{0}_1 \quad \boldsymbol{I} \quad X^1_I\, \boldsymbol{I} \quad X^2_I\, \boldsymbol{I} \quad X^3_I\, \boldsymbol{I} \quad \mathbf{0}_2 \quad \mathbf{0}_2 \ \ldots\ -\boldsymbol{I} \ \ldots\ \mathbf{0}_2] \tag{6.34}$$

for $\omega = 2$ respectively, involving the matrices $\mathbf{0}_1 \in \mathbb{R}^3 \times \mathbb{R}^{12}$ and $\mathbf{0}_2, \boldsymbol{I} \in \mathbb{R}^3 \times \mathbb{R}^3$. Hence, for a system with n_c coupled FE-nodes the (global) vector of coupling constraints and the resulting constraint Jacobian are given by

$$\boldsymbol{g}^{cou}_{12} := [\boldsymbol{g}^{cou}_1, ..., \boldsymbol{g}^{cou}_{n_c}]^{\mathrm{t}} \in \mathbb{R}^{3\,n_c} \quad \text{and} \quad \mathbb{G}^{cou}_{12} := [\mathbb{G}^{cou}_1, ..., \mathbb{G}^{cou}_{n_c}]^{\mathrm{t}} \in \mathbb{R}^{3\,n_c} \times \mathbb{R}^{24+n_{dof}}\,. \tag{6.35}$$

Finally, the Galerkin-based time-stepping scheme (6.7) can be specified for the system under investigation with $\bar{\boldsymbol{z}} = [\boldsymbol{q}^r_1, \boldsymbol{q}^r_2, \boldsymbol{q}^f, \boldsymbol{p}^r_1, \boldsymbol{p}^r_2, \boldsymbol{p}^f]^{\mathrm{t}} \in \mathbb{R}^{48+2\,n_{dof}}$ and $H = H^{rf}_{12}$ by setting

$$\bar{\boldsymbol{g}}(\bar{\boldsymbol{q}}) = [\boldsymbol{g}^{int}_{12},\ \boldsymbol{g}^{cou}_{12}]^{\mathrm{t}} \in \mathbb{R}^{12+3\,n_c} \quad \text{and} \quad \mathbb{G} = \begin{bmatrix} \mathbb{G}^{int}_{12} & \mathbf{0}_1 \\ \mathbb{G}^{cou}_{12} & \mathbf{0}_2 \end{bmatrix} \in \mathbb{R}^{12+3\,n_c} \times \mathbb{R}^{48+2\,n_{dof}} \tag{6.36}$$

based on Equation (6.24), applying this time the zero matrices $\mathbf{0}_1 \in \mathbb{R}^{12} \times \mathbb{R}^{24+2\,n_{dof}}$ and $\mathbf{0}_2 \in \mathbb{R}^{3\,n_c} \times \mathbb{R}^{24+n_{dof}}$.

6.2. Consistent Time-Stepping Scheme

In the previous sections, all essential components to model inelastic multibody systems have been investigated step-by-step, considering the fundamental case that two rigid bodies are connected via joints or flexible structures. In the following, we consider an arbitrary multibody system with

$$\mathcal{B} = \mathcal{B}^r \cup \mathcal{B}^f \,, \tag{6.37}$$

consisting of n_r rigid parts $\mathcal{B}^r = \bigcup_{\tau=1}^{n_r} \mathcal{B}^r_\tau$ and n_f flexible structures $\mathcal{B}^f = \bigcup_{\omega=1}^{n_f} \mathcal{B}^f_\omega$. Moreover, each flexible structure $\mathcal{B}^f_\omega$ is discretised in space with n^ω_{el} elements and n^ω_{node} nodes, rendering $\mathcal{B}^f_\omega = \bigcup_{el=1}^{n^\omega_{el}} \mathcal{B}^{el}_\omega$. Consequently, the phase-space vector of the system

$$\bar{\boldsymbol{z}} = [\bar{\boldsymbol{q}}, \bar{\boldsymbol{p}}]^{\mathrm{t}} \in \mathbb{R}^{2\,[12\,n_r + 3\,n_{node}]} \tag{6.38}$$

with $n_{node} = \sum_{\omega=1}^{n_f} n^\omega_{node}$ can be introduced based on the vectors

$$\bar{\boldsymbol{q}} := [\boldsymbol{q}^r_1, \ldots, \boldsymbol{q}^r_{n_r}, \boldsymbol{q}^f_1, \ldots, \boldsymbol{q}^f_{n_f}]^{\mathrm{t}} \qquad \text{and} \qquad \bar{\boldsymbol{p}} := [\boldsymbol{p}^r_1, \ldots, \boldsymbol{p}^r_{n_r}, \boldsymbol{p}^f_1, \ldots, \boldsymbol{p}^f_{n_f}]^{\mathrm{t}} \,, \tag{6.39}$$

referring to Section 6.1.2 and 6.1.3 for the definition of the components $\boldsymbol{q}^r$, $\boldsymbol{p}^r$ and $\boldsymbol{q}^f$, $\boldsymbol{p}^f$ respectively. Furthermore, the mass matrix $\mathbb{M}^{rf} \in \mathbb{R}^{12\,n_r + 3\,n_{node}} \times \mathbb{R}^{12\,n_r + 3\,n_{node}}$ can be written for the general system at hand as

$$\mathbb{M}^{rf} = \begin{bmatrix} \mathbb{M}^r_1 & \mathbf{0}_r & \ldots & \mathbf{0}_r & \mathbf{0}_{rf,1} & \mathbf{0}_{rf,2} & \ldots & \mathbf{0}_{rf,n_f} \\ \mathbf{0}_r & \mathbb{M}^r_2 & \ldots & \mathbf{0}_r & \mathbf{0}_{rf,1} & \mathbf{0}_{rf,2} & \ldots & \mathbf{0}_{rf,n_f} \\ \vdots & \vdots & \ddots & \vdots & \vdots & \vdots & \ddots & \vdots \\ \mathbf{0}_r & \mathbf{0}_r & \ldots & \mathbb{M}^r_{n_r} & \mathbf{0}_{rf,1} & \mathbf{0}_{rf,2} & \ldots & \mathbf{0}_{rf,n_f} \\ \mathbf{0}^{\mathrm{t}}_{rf,1} & \mathbf{0}^{\mathrm{t}}_{rf,1} & \ldots & \mathbf{0}^{\mathrm{t}}_{rf,1} & \mathbb{M}^f_1 & \mathbf{0}_{f,12} & \ldots & \mathbf{0}_{f,1n_f} \\ \mathbf{0}^{\mathrm{t}}_{rf,2} & \mathbf{0}^{\mathrm{t}}_{rf,2} & \ldots & \mathbf{0}^{\mathrm{t}}_{rf,2} & \mathbf{0}^{t}_{f,21} & \mathbb{M}^f_2 & \ldots & \mathbf{0}_{f,2n_f} \\ \vdots & \vdots & \ddots & \vdots & \vdots & \vdots & \ddots & \vdots \\ \mathbf{0}^{\mathrm{t}}_{rf,n_f} & \mathbf{0}^{\mathrm{t}}_{rf,n_f} & \ldots & \mathbf{0}^{\mathrm{t}}_{rf,n_f} & \mathbf{0}^{t}_{f,1n_f} & \mathbf{0}^{t}_{f,2n_f} & \ldots & \mathbb{M}^f_{n_f} \end{bmatrix} , \tag{6.40}$$

wherein several different zero matrices with adequate dimensions have been applied, namely: $\mathbf{0}_r \in \mathbb{R}^{12} \times \mathbb{R}^{12}$, $\mathbf{0}_{rf,\tau} \in \mathbb{R}^{12} \times \mathbb{R}^{3\,n^\tau_{node}}$, and $\mathbf{0}_{f,\tau\omega} \in \mathbb{R}^{3\,n^\tau_{node}} \times \mathbb{R}^{3\,n^\omega_{node}}$. Based on Equation (6.40), hence, we obtain the function

$$H^{rf}(\bar{\boldsymbol{q}}, \bar{\boldsymbol{p}}; \boldsymbol{\kappa}) := \frac{1}{2}\,\bar{\boldsymbol{p}} \cdot \mathbb{M}^{rf\,-1} \cdot \bar{\boldsymbol{p}} + \sum_{\omega=1}^{n_f} \Psi_\omega(\boldsymbol{q}^f_\omega; \boldsymbol{\kappa}) + V^{ext}(\bar{\boldsymbol{q}}) \,, \tag{6.41}$$

incorporating optionally a separate free energy function Ψ_ω for each flexible part $\mathcal{B}^f_\omega$. Due to the applied rotationless formulation of the rigid body dynamics, once more, the related internal constraints have to be taken into account, introducing for each rigid

body $\mathcal{B}_\tau^r$ the constraint vector $\boldsymbol{g}_\tau^{int}(\boldsymbol{q}_\tau^r) \in \mathbb{R}^6$ given by Equation (6.14). Consequently, the here considered case of n_r rigid bodies involves

$$\boldsymbol{g}^{int} := [\boldsymbol{g}_1^{int}, \dots, \boldsymbol{g}_{n_r}^{int}]^t \in \mathbb{R}^{6\,n_r} \quad \text{and} \quad \mathbb{G}^{int} := \nabla_{\bar{\boldsymbol{q}}}\, \boldsymbol{g}^{int} \in \mathbb{R}^{6\,n_r} \times \mathbb{R}^{12\,n_r+3\,n_{node}}\,. \quad (6.42)$$

Hereby, the constraint Jacobian $\mathbb{G}^{int}$ can be assembled for general systems based on Equation (6.15), resulting in

$$\mathbb{G}^{int} = \begin{bmatrix} \mathbb{G}_1^{int} & \mathbf{0}_1 & \dots & \mathbf{0}_1 & \mathbf{0}_2 \\ \mathbf{0}_1 & \mathbb{G}_2^{int} & \dots & \mathbf{0}_1 & \mathbf{0}_2 \\ \vdots & \vdots & \ddots & \vdots & \mathbf{0}_2 \\ \mathbf{0}_1 & \mathbf{0}_1 & \dots & \mathbb{G}_{n_r}^{int} & \mathbf{0}_2 \end{bmatrix} \quad (6.43)$$

with $\mathbf{0}_1 \in \mathbb{R}^6 \times \mathbb{R}^{12}$ and $\mathbf{0}_2 \in \mathbb{R}^6 \times \mathbb{R}^{3\,n_{node}}$. In addition to the foregoing internal constraints, also n_{ext} external constraints are assumed to be involved in the multibody system of interest, as discussed in Section 6.1.2. In this context, external constraints of type $\boldsymbol{g}_\tau^{ext} := \boldsymbol{g}_{\varkappa\omega}^{ext}(\boldsymbol{q}_\varkappa^r, \boldsymbol{q}_\omega^r) \in \mathbb{R}^{m_\tau^{ext}}$ – acting between the rigid bodies $\mathcal{B}_\varkappa^r$ and $\mathcal{B}_\omega^r$ (see Equation (6.25)) – are collected in one vector, rendering

$$\boldsymbol{g}^{ext} := [\boldsymbol{g}_1^{ext}, \dots, \boldsymbol{g}_{n_{ext}}^{ext}]^t \in \mathbb{R}^{m^{ext}} \quad \text{and} \quad \mathbb{G}^{ext} := \nabla_{\bar{\boldsymbol{q}}}\, \boldsymbol{g}^{ext} \in \mathbb{R}^{m^{ext}} \times \mathbb{R}^{12\,n_r+3\,n_{node}} \quad (6.44)$$

with $m^{ext} = \sum_{\tau=1}^{n_{ext}} m_\tau^{ext}$. Dealing with n_f flexible parts, we have to consider additionally the corresponding coupling constraints, see Section 6.1.3 for further details. Basically, the connection of the rigid part $\mathcal{B}_\tau^r$ respectively $\mathcal{B}_\omega^r$ with the flexible structure $\mathcal{B}_\varkappa^f$ results in the coupling constraints $\boldsymbol{g}_\varkappa^{cou} := \boldsymbol{g}_{\tau\omega}^{cou}(\boldsymbol{q}_\tau^r, \boldsymbol{q}_\omega^r, \boldsymbol{q}_\varkappa^f) \in \mathbb{R}^{3\,n_c^\varkappa}$ (compare Equation (6.35)), so that for the entire system follows

$$\boldsymbol{g}^{cou} := [\boldsymbol{g}_1^{cou}, \dots, \boldsymbol{g}_{n_f}^{cou}]^t \in \mathbb{R}^{3\,n_c} \quad \text{and} \quad \mathbb{G}^{cou} := \nabla_{\bar{\boldsymbol{q}}}\, \boldsymbol{g}^{cou} \in \mathbb{R}^{3\,n_c} \times \mathbb{R}^{12\,n_r+3\,n_{node}}\,, \quad (6.45)$$

using the total number of coupled FE nodes $n_c = \sum_{\varkappa=1}^{n_f} n_c^\varkappa$. Based on Equations (6.42)-(6.45), the constraint vector of the general multibody system as well as the final constraint Jacobian can be composed. By introducing the abbreviation $m = 6\,n_r + m^{ext} + 3\,n_c$, it follows straightforwardly

$$\bar{\boldsymbol{g}}(\bar{\boldsymbol{q}}) = [\boldsymbol{g}^{int},\, \boldsymbol{g}^{ext}, \boldsymbol{g}^{cou}]^{\mathrm{t}} \in \mathbb{R}^m \quad \text{and} \quad \mathbb{G} = \begin{bmatrix} \mathbb{G}^{int} \\ \mathbb{G}^{ext} \\ \mathbb{G}^{cou} \end{bmatrix} \in \mathbb{R}^m \times \mathbb{R}^{12\,n_r+3\,n_{node}}\,, \quad (6.46)$$

wherein the general case (6.6) has been specified to $\mathbb{G} := \nabla_{\bar{\boldsymbol{q}}}\, \boldsymbol{g}$ since the constraints $(6.46)_1$ are only a function of the configuration vector of the system, compare also Remark 6.2.2. Analogously to Section 4.2 and Section 5.2, we consider next a specific representative of the general family of time-stepping schemes (6.7) and apply once again linear Finite Elements in time, using the corresponding shape functions for $k = 1$ given by Equations (4.22). When we set $H = H^{rf}$ and bear in mind that $\bar{\boldsymbol{g}}$ is only a function

of $\bar{\boldsymbol{q}}$, as already mentioned above, the resulting scheme can be written in the case of absent external loads as

$$\begin{aligned} \bar{\boldsymbol{q}}_2 - \bar{\boldsymbol{q}}_1 - \frac{h_n}{2}\,\mathbb{M}^{rf\,-1}\cdot[\bar{\boldsymbol{p}}_1 + \bar{\boldsymbol{p}}_2] &= \boldsymbol{0} \\ \bar{\boldsymbol{p}}_2 - \bar{\boldsymbol{p}}_1 + h_n \int_0^1 \bar{\boldsymbol{F}}^{sys\,h}(\alpha)\,\mathrm{d}\alpha + h_n \int_0^1 \bar{\boldsymbol{\mu}}\cdot\mathbb{G}(\alpha)\,\mathrm{d}\alpha &= \boldsymbol{0} \\ \int_0^1 \mathbb{G}(\alpha)\cdot[\bar{\boldsymbol{q}}_2 - \bar{\boldsymbol{q}}_1]\,\mathrm{d}\alpha &= \boldsymbol{0}\,, \end{aligned} \tag{6.47}$$

wherein the time-approximated system load vector $\bar{\boldsymbol{F}}^{sys\,h}$ has been introduced and the vector $\bar{\boldsymbol{\mu}} \in \mathbb{R}^m$ includes the piecewise constant Lagrange multipliers. Supposing that no additional potential – for instance related to supplemental springs – acts between the involved rigid bodies, we obtain

$$\bar{\boldsymbol{F}}^{sys\,h}(\alpha) = \big[\boldsymbol{0}_1, \ldots, \boldsymbol{0}_{n_r}, \boldsymbol{F}_1^{f\,h}(\boldsymbol{S}(\alpha)), \ldots, \boldsymbol{F}_{n_f}^{f\,h}(\boldsymbol{S}(\alpha))\big]^{\mathrm{t}} \in \mathbb{R}^{12\,n_r + 3\,n_{node}}\,, \tag{6.48}$$

using the zero vectors $\boldsymbol{0}_\omega \in \mathbb{R}^{12}$ and for each flexible part $\mathcal{B}^f_\varkappa$ the vectorial collection $\boldsymbol{F}^{f\,h}_\varkappa := [\boldsymbol{F}^{int\,h}_1, ..., \boldsymbol{F}^{int\,h}_{n^\varkappa_{node}}]^{\mathrm{t}} \in \mathbb{R}^{3\,n^\varkappa_{node}}$. In this context, the components $\boldsymbol{F}^{int\,h}_I$ refer once more to the time-approximated internal load vectors at the spatial nodes I given by Equation (3.42). In entire analogy to the previous cases, the crucial step regarding the offered consistency properties is to find adequate approximations for the remaining time-integrals in Equations (6.47). Since in the here considered cases the constraints $\bar{\boldsymbol{g}}(\bar{\boldsymbol{q}})$ are at most quadratic in the configuration vector, the time-integrals which include the corresponding constraint Jacobian $\mathbb{G}$ can already be calculated exactly with one Gaussian integration point in time, involving

$$\mathbb{G}(1/2) := \mathbb{G}\left(\frac{\bar{\boldsymbol{q}}_1 + \bar{\boldsymbol{q}}_2}{2}\right). \tag{6.49}$$

In contrast, the integration of the system load vector results in general in a highly nonlinear time-integral, as discussed in detail in the foregoing chapters. However, the application of the proposed non-standard quadrature rule (5.25) renders

$$\int_0^1 \bar{\boldsymbol{F}}^{sys\,h}(\alpha)\,\mathrm{d}\alpha \approx \bar{\boldsymbol{F}}(1/2) \tag{6.50}$$

with

$$\bar{\boldsymbol{F}}(1/2) = \big[\boldsymbol{0}_1, \ldots, \boldsymbol{0}_{n_r}, \boldsymbol{F}_1^{f\,h}(\boldsymbol{S}^{alg}(1/2)), \ldots, \boldsymbol{F}_{n_f}^{f\,h}(\boldsymbol{S}^{alg}(1/2))\big]^{\mathrm{t}} \tag{6.51}$$

based on the algorithmic stress tensor (5.26). Consequently, the final time-stepping scheme reads

$$\begin{aligned} \bar{\boldsymbol{q}}_2 - \bar{\boldsymbol{q}}_1 - \frac{h_n}{2}\,\mathbb{M}^{rf\,-1}\cdot[\bar{\boldsymbol{p}}_1 + \bar{\boldsymbol{p}}_2] &= \boldsymbol{0} \\ \bar{\boldsymbol{p}}_2 - \bar{\boldsymbol{p}}_1 + h_n\,\bar{\boldsymbol{F}}(1/2) + h_n\,\mathbb{G}^{\mathrm{t}}(1/2)\cdot\bar{\boldsymbol{\mu}} &= \boldsymbol{0} \\ \bar{\boldsymbol{g}}(\bar{\boldsymbol{q}}_2) &= \boldsymbol{0}\,, \end{aligned} \tag{6.52}$$

whereby additionally the results of Remark 6.1.3 based on Equation (6.9) have been utilised in combination with the consistent initial values $\bar{\boldsymbol{g}}(t=0)=\mathbf{0}$, compare Equation $(6.47)_3$ with Equation $(6.52)_3$. Following the argumentation in Remark 6.1, the integrator (6.52) allows a completely consistent time-integration of constrained dissipative dynamics, dealing in particular with elasto-plastic multibody systems.

Remarks 6.2:

1. Please note, that the governing equations for the rigid and the flexible parts can be separated due to the specific structure of the involved matrices in Equations (6.52). In fact, both sets of equations are only coupled via the corresponding submatrix of the constraint Jacobian $\mathbb{G}$ which is related to the coupling constraints $\boldsymbol{g}^{cou}$.

2. In the foregoing cases, all considered constraints have been of specific type: They have been holonomic and only a function of the configuration vector of the system, being at most quadratic in $\bar{\boldsymbol{q}}$. However, also other types of constraints could be handled in a quite similar way. In this context, we refer to

   - Betsch [22] regarding the incorporation of *non-holonomic constraints*, which are relevant for instance to model rolling motions, to
   - Betsch and Uhlar [31] concerning an example for *highly nonlinear constraints*, applying for the corresponding constraint Jacobian a so-called '$G-$equivariant' version of the discrete derivative by Gonzalez [62, 63], and to
   - Betsch and Steinmann [28] for the case that the constraint vector depends also on the momenta respectively the velocities of the system, enforcing the so-called '*secondary*' or '*hidden constraints*'. However, a violation of these constraints, which address additionally the requirement $\dot{\bar{\boldsymbol{g}}}(\bar{\boldsymbol{q}})=\mathbf{0}$, has been judged to be uncrucial in most of the cases, see e.g. References [28, 63, 108]. Hence, the focus is placed in this work on the enforcement of the constraints on the configuration level.

3. The proposed formulation basically suffers from two disadvantages: Firstly, the condition number of the global iteration matrix is of the order $\mathcal{O}(h_n^{-3})$, see Leyendecker *et al.* [108, 109] and references cited therein. However, this drawback could be resolved by means of adequate pre-conditioning techniques, as proposed for instance by Bottasso *et al.* [37]. Secondly, the present formulation is characterised by a comparatively large number of unknowns, namely $2\,n+m$ with $n=12\,n_r+3\,n_{node}$ instead of $n-m$ independent configurational degrees of freedom. In a first step the unknown momenta in Equation $(6.52)_2$ can be eliminated once more by means of Equation $(6.52)_1$, so that we obtain $n+m$ unknowns. Next, a further reduction of the system size can be achieved by applying the concept of a (discrete) 'null space

matrix', whose columns span the null space of the involved constraint Jacobian. By pre-multiplying Equation $(6.52)_2$ with this matrix, hence, the Lagrange multipliers are removed, resulting in a system with only n unknowns. Finally, an appropriate reparametrisation accomplishes the reduction, and we indeed end up with $n - m$ unknowns, representing the actual number of degrees of freedom. Moreover, this approach leads to an iteration matrix which is independent from the time-step size. Thus, the abovementioned conditioning problems vanish automatically by using such a reformulation based on the integration scheme (6.52). A detailed introduction as well as further numerical aspects of the 'null space method' can be found in References [21, 23, 111].

6.3. Numerical Examples

In the previous section, a general framework to extend the concepts of Chapter 3 to constrained dissipative dynamics as well as a specific time-stepping scheme based on linear Finite Elements in time has been been presented, dealing with inelastic multibody systems. In this section, we demonstrate the achievable performance of the integrator (6.52) in the context of finite elasto-plastic multibody dynamics, whereby the constitutive model relies once more on a Helmholtz energy of Hencky-type in combination with a 'v. Mises'-type yield function including linear isotropic hardening effects. Regarding the local integration of the plastic evolution equations, the exponential update combined with the standard integration strategy has been applied again. For further details, we refer to Section 5.1.2 and Section 5.2.2 respectively.

6.3.1. Flying Frame

Once again, the first example in this context picks up the motion of the 'Flying Frame' (2d, plane strain conditions), representing a kind of benchmark example also in the previous chapters. This time, however, the frame is decomposed into two rigid parts $\mathcal{B}^r_{1,2}$ – the upper and lower joist – which are connected via two flexible structures $\mathcal{B}^f_{1,2}$, see Figure 6.5 a) for an illustration. For the following computations with $h_n = 0.05$, we have used $\rho = 8.0$, $\lambda = 10000$, $\mu = 5000$, $Y_0 = 500$, $H^{rd} = 500$ for the flexible parts and the inertial parameters which are summarised in Table 6.1 for the rigid bodies. To start

Table 6.1.: inertial parameters of the involved rigid bodies

Rigid body		M	E_1	E_2
Lower joist	RB 1	30	160	10
Upper joist	RB 2	30	160	10

the motion, an initial velocity with the norm $||\bar{\boldsymbol{v}}_0|| = 6$ is applied, compare $\bar{\boldsymbol{v}} = \mathbb{M}^{rf\,-1} \cdot \bar{\boldsymbol{p}}$ based on Equations (6.39), (6.40). Moreover, external forces act on the centre of mass of each rigid body, whereby we have applied $\boldsymbol{F}_1^{ext\,r} = f(t)\,[1,0]^{\mathrm{t}} = 5\,\boldsymbol{F}_2^{ext\,r}$. Analogously to several previous examples, the function $f(t)$ is prescribed in time by a hat function with $f_{max} = 3500$ and $T_{load} = 1.0$, as sketched in Figure 6.5 a). A sequence of the motion is pictured in Figure 6.5 b) and the resulting trajectories of the centres of mass are shown in Figure 6.12 a). Regarding mechanical consistency, we refer to Figure 6.6, wherein the conservation of the linear as well as of the angular momentum can be regarded. Furthermore, the accumulated dissipation is pictured in Figure 6.7 a) and the claimed monotonic decrease of the total energy can be seen in Figure 6.7 b). Thereby, the decrease of the total energy is strictly related to the increase of the plastic dissipation, resulting in a conservation of the augmented Hamiltonian plotted in Figure 6.8 a). In analogy to Equation (5.33), we introduce also for coupled systems a residual R to assess more rigorously the fulfilment of the discrete balance of the augmented Hamiltonian. As expected, Figure 6.8 b) clearly confirms that even for the constrained case energy-consistency is guaranteed in a numerically exact manner. So far, the integrator (6.52) offers the same consistency properties which have already been discussed extensively in Chapter 5. Next, we demonstrate in detail that also the included constraints are fulfilled exactly. In the present example, only internal and coupling constraints are involved. More precisely, we have to deal in the here considered 2d case with 6 internal constraints and 12 coupled FE-nodes, resulting in the constraint vector $\bar{\boldsymbol{g}} \in \mathbb{R}^{30}$. The fulfilment of the coupling constraints is guaranteed at least within the order of magnitude $\mathcal{O}(10^{-14})$, as displayed in Figure 6.9 and Figure 6.10 for the coupling of the flexible parts to rigid body 1 (RB 1) and rigid body 2 (RB 2) respectively. Moreover, it can be seen in Figure 6.11 that also the internal constraints, which are related to the favoured rotationless formulation of the rigid body kinematics, are fulfilled within the calculation accuracy, so that kinematic consistency is indeed offered additionally by applying the discussed concepts. Finally, we compare the plastic motion with the purely elastic case, using identical material parameters but $Y_0 \to \infty$. The influence on the deformation of the frame can be studied in Figure 6.13 b) based on the configuration $\mathcal{B}_t$ at $t = 1.0$. Obviously, the plastic deformations basically take place within two spatial elements and result in a permanent stretch of the distance between both rigid bodies, as pictured in Figure 6.13 a). Furthermore, the exemplarily considered trajectory of the centre of mass of rigid body 1 is characterised in the plastic case by reduced maximum values of the y-coordinates and a visible phase shift, compare Figure 6.12 b).

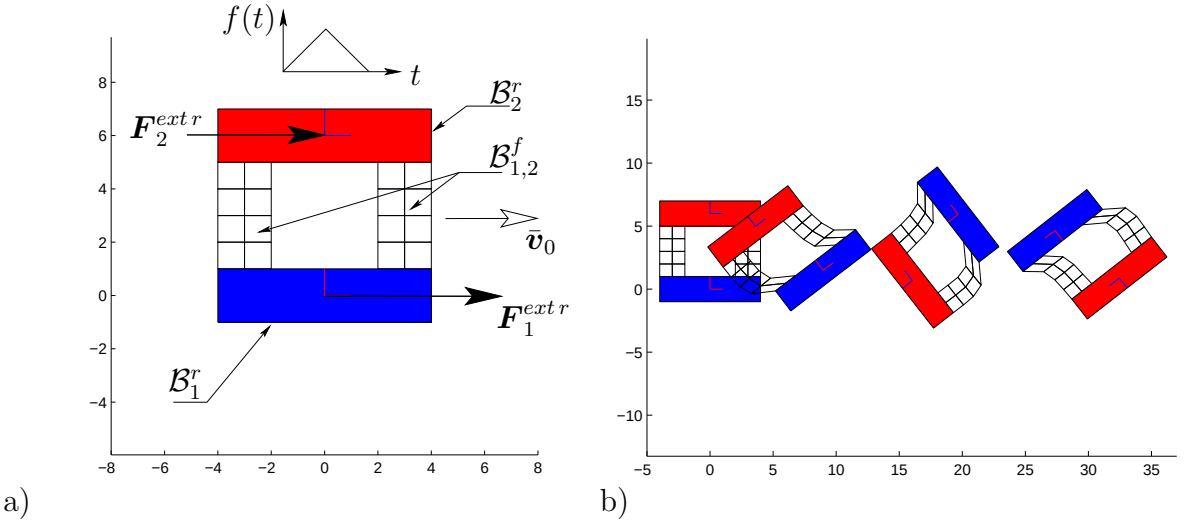

Figure 6.5.: a) initial configuration $\mathcal{B}_0$, b) sequence of the motion (plastic case)

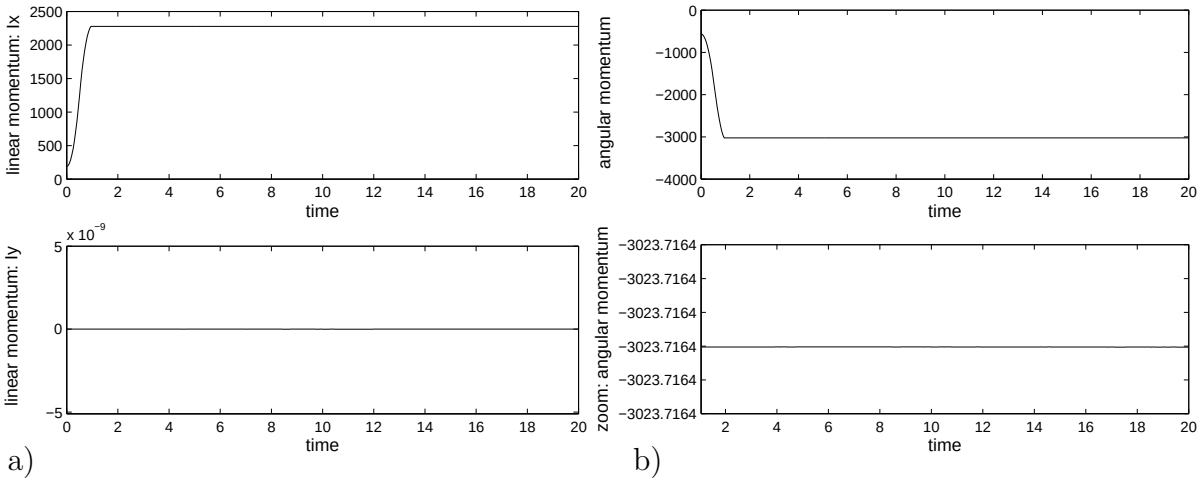

Figure 6.6.: a) linear momentum, b) angular momentum

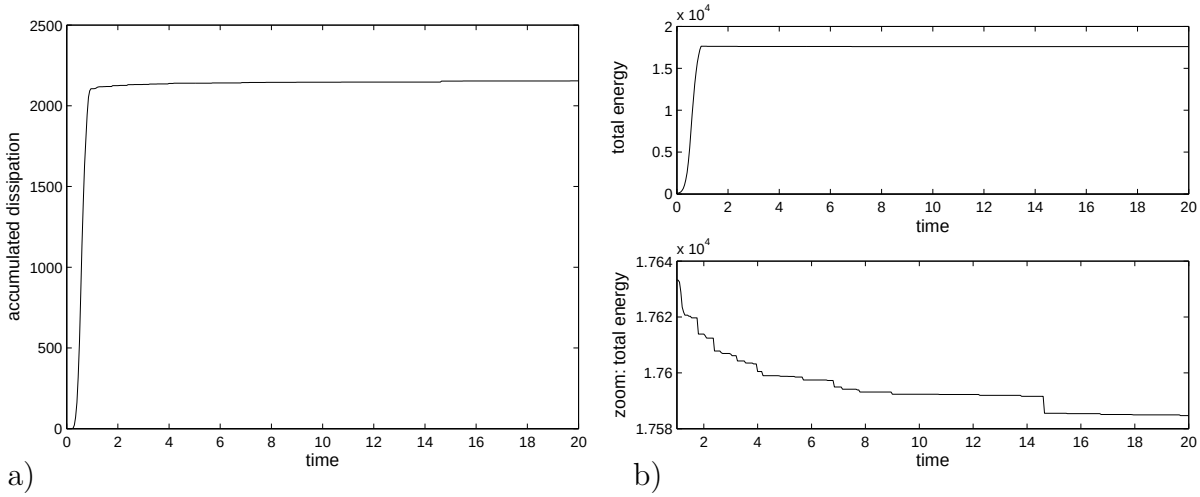

Figure 6.7.: a) accumulated dissipation D, b) total energy H

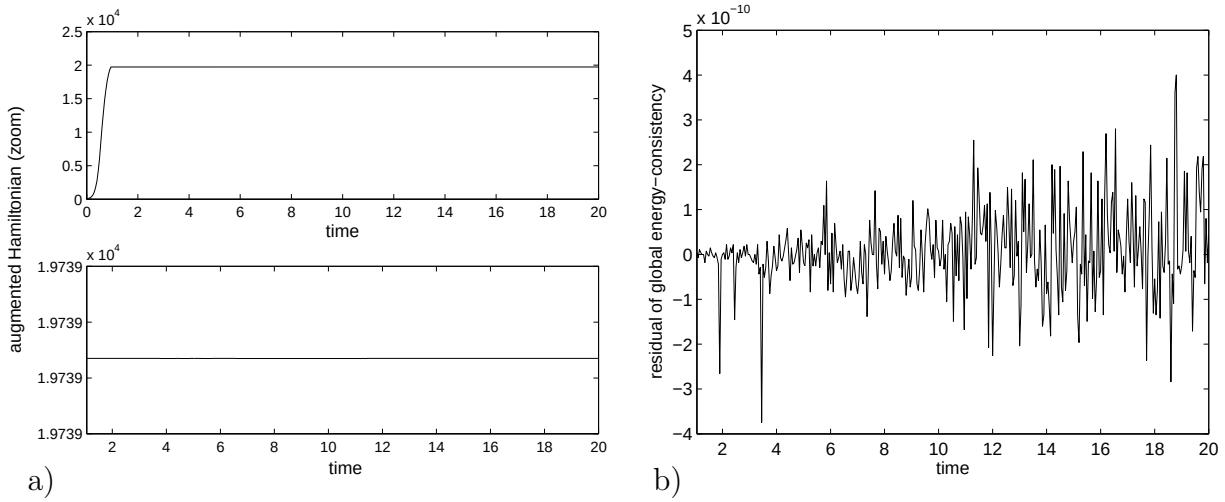

Figure 6.8.: a) augmented Hamiltonian $\widetilde{H}$, b) residual R

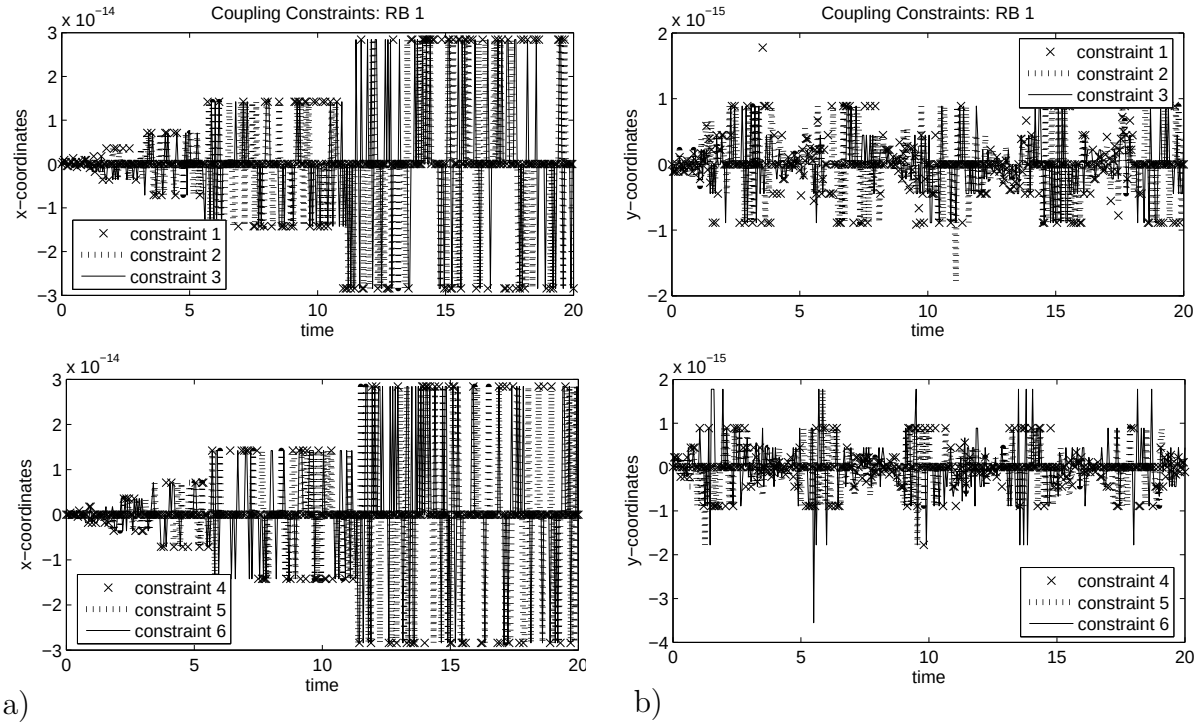

Figure 6.9.: coupling constraints between the rigid body $\mathcal{B}_1^r$ (RB 1) and the flexible parts $\mathcal{B}_{1,2}^f$: a) x-coordinates, b) y-coordinates

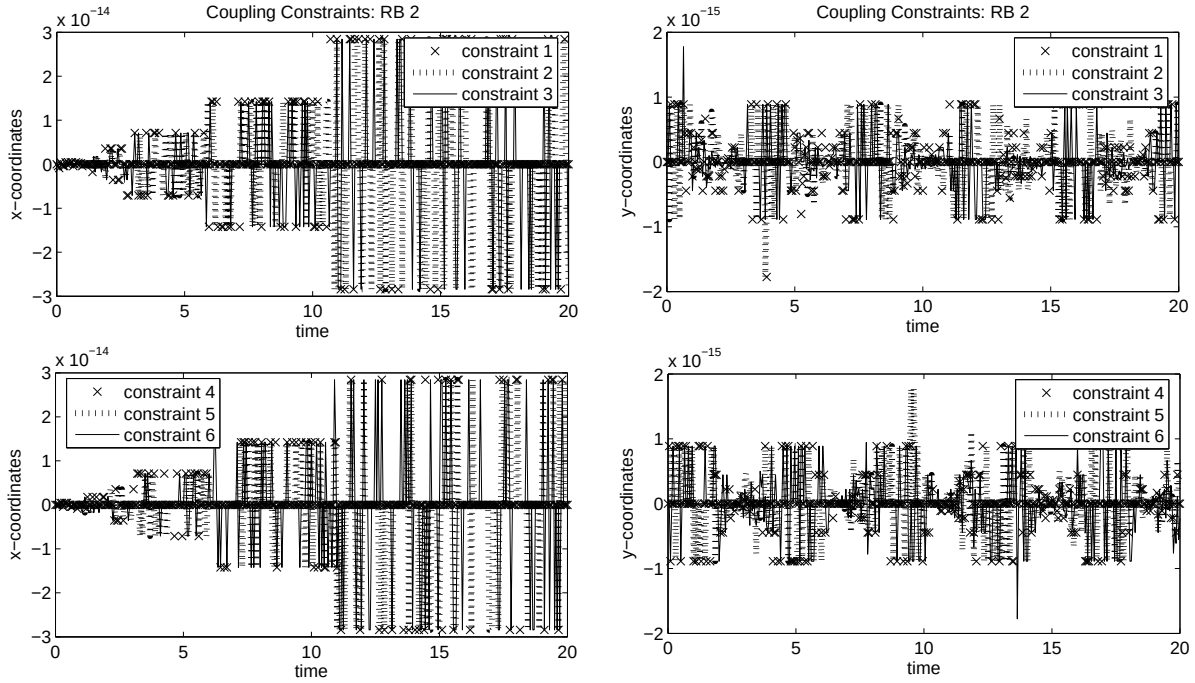

Figure 6.10.: coupling constraints between the rigid body $\mathcal{B}_2^r$ (RB 2) and the flexible parts $\mathcal{B}_{1,2}^f$: a) x-coordinates, b) y-coordinates

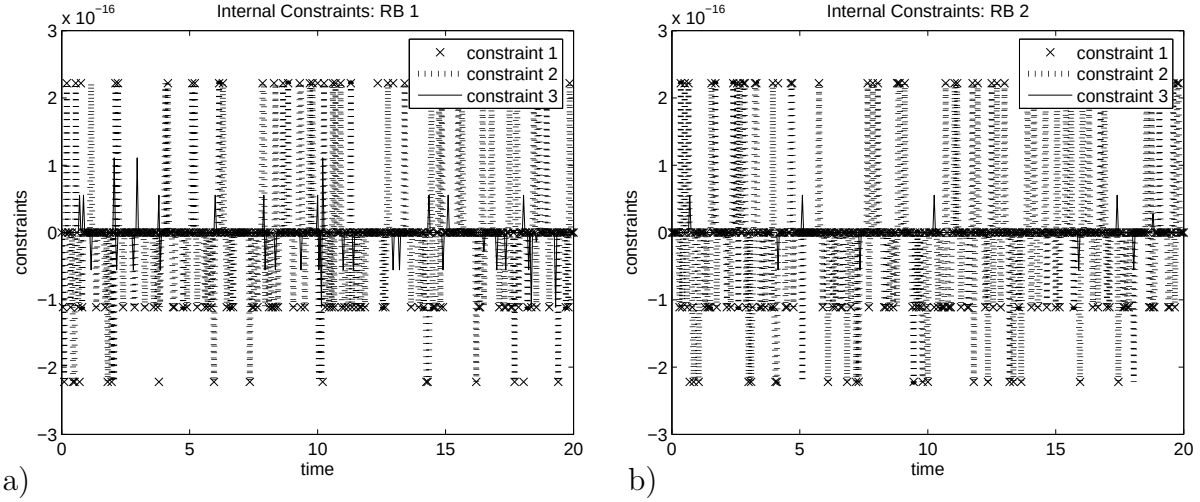

Figure 6.11.: internal constraints: a) RB 1, b) RB 2

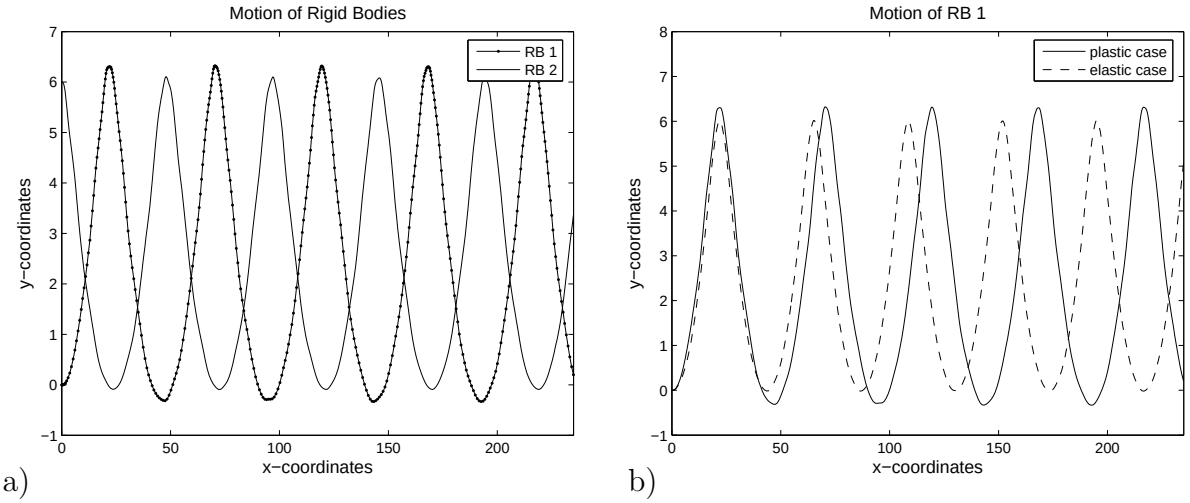

a) b)

Figure 6.12.: trajectory of the centre of mass: a) RB 1 vs. RB 2, b) elastic vs. plastic motion (RB 1)

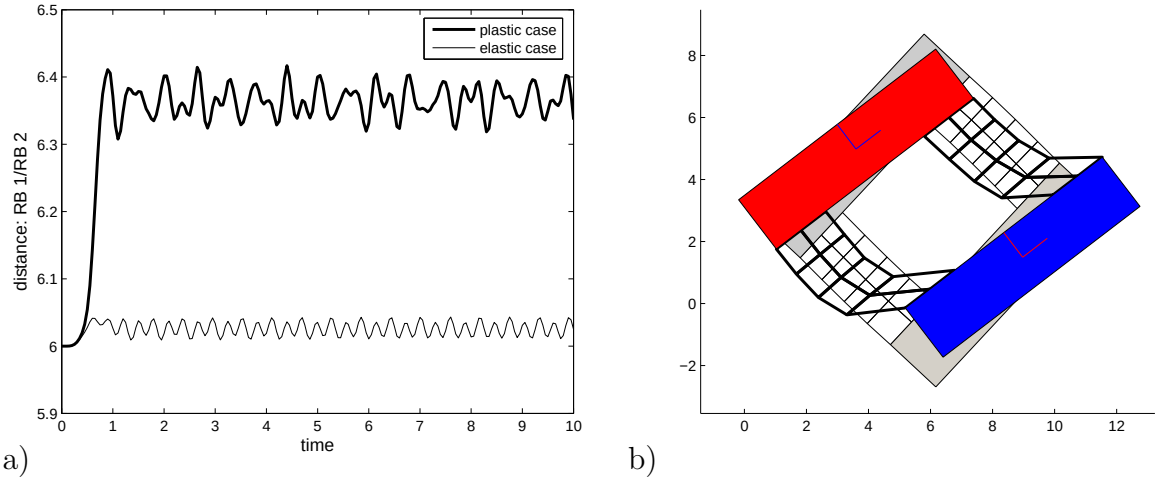

a) b)

Figure 6.13.: elastic vs. plastic motion: a) distance between the centre of mass of RB 1 and the centre of mass of RB 2, b) deformed configuration $\mathcal{B}_t$ at $t = 1.0$

6.3.2. Flying Conrod

Also the second example of this chapter refers to a specific solid body which has already been investigated previously in a fully flexible version, dealing once more with the spatial motion of a 'Flying Conrod'. However, in contrast to Section 5.6.2 the here considered conrod consists of rigid circlets $\mathcal{B}^r_{1,2}$ which are connected via a flexible shaft $\mathcal{B}^f$, using for the inelastic structure the parameters $\rho = 3.0$, $\lambda = 3000$, $\mu = 1000$, $Y_0 = 300$, $H^{rd} = 300$ and for the rigid bodies the inertial parameters listed in Table 6.2. Thereby, the shaft is coupled to each circlet via 10 FE-nodes, see Figure 6.14 a) for a sketch of the initial configuration. Thus, the constraint vector of the 3d system is given by $\bar{\boldsymbol{g}} \in \mathbb{R}^{72}$, including internal as well as coupling constraints. Again, the well-known hat function $f(t)$ with $f_{max} = 4000$ and $T_{load} = 1.0$ has been chosen to scale the external loads $\boldsymbol{F}_1^{ext\,r} = f(t)\,[1,0,0]^{\mathrm{t}} = 5\,\boldsymbol{F}_2^{ext\,r}$, acting on rigid body 1 and rigid body 2 respectively.

Table 6.2.: inertial parameters of the involved rigid bodies

Rigid body		M	E_1	E_2	E_3
Large circlet	RB 1	65.9734	412.3340	412.3340	5.4978
Small circlet	RB 2	28.2743	35.3429	35.3429	2.3562

The free flight of the conrod and in particular the deformations of the flexible part can be regarded in Figure 6.21 based on some snapshots of the motion [3], using the constant time-step size $h_n = 0.02$. Since the applied time-stepping scheme (6.52) offers a mechanically consistent time-integration, the linear and the angular momentum are both conserved in the present example, as shown in Figure 6.16. Similarly to the foregoing example, the plastic deformations lead to a notable stretch of the shaft, as can be seen in Figure 6.14 b) based on a plot of the distance between both circlets. Hereby, the resulting accumulated dissipation as well as the monotonically decreasing total energy reflect fundamental principles of thermodynamics, compare Figure 6.15. Moreover, it is displayed in Figure 6.17 that the applied non-standard quadrature rule (5.25) indeed enables a conservation of the augmented Hamiltonian, even within the order of magnitude $\mathcal{O}(10^{-10})$. Dealing with constrained dynamical systems, the focus is placed next on the algorithmic fulfilment of the involved constraints. Starting with the internal constraints of the rigid body description, the fulfilment and also the corresponding Lagrange multipliers can be considered in Figure 6.18, whereby a pseudo time-continuous plot of the multipliers has been preferred for the purpose of visual clarity. Nevertheless, please recall that from the time-FE point of view the Lagrange multipliers are actually constant within each time interval when linear shape functions in time are used, resulting in discontinuities

[3] To provide a more sophisticated presentation of the results, the body has been remodelled and rendered with the open-source tool 'POV-Ray', enabling a nearly photo-realistic visualisation of the motion.

over the interval boundaries. Analogously, the Lagrange multipliers for the coupling constraints are pictured in Figure 6.19, wherein the coupling to rigid body 1 and rigid body 2 is investigated separately. To handle efficiently the large number of coupling constraints, we introduce next for a given constraint vector $\boldsymbol{g}(t) = [g_1(t), \ldots, g_m(t)]^{\mathrm{t}} \in \mathbb{R}^m$ the maximum absolute value of its components

$$^{max}g(t_i) := \mathrm{MAX}\Big\{ \mid g_1(t_i) \mid, \ldots, \mid g_m(t_i) \mid \Big\}, \tag{6.53}$$

filtering for the considered constraints at each discrete time $t = t_i$ the maximum deviation from zero. Consequently, we obtain based on Equation (6.53) a representative upper bound for the numerical violation of the constraints under investigation. Firstly, the coupling constraints are partitioned for the following investigations concerning the coupled rigid body and the corresponding coordinates respectively. Then, the maximum value is selected for each subset by means of Equation (6.53). In Figure 6.20, it can be clearly seen that in the worst case the coupling constraints are violated in the size of 10^{-14}, so that kinematic consistency of the integrator has also been confirmed for the present example.

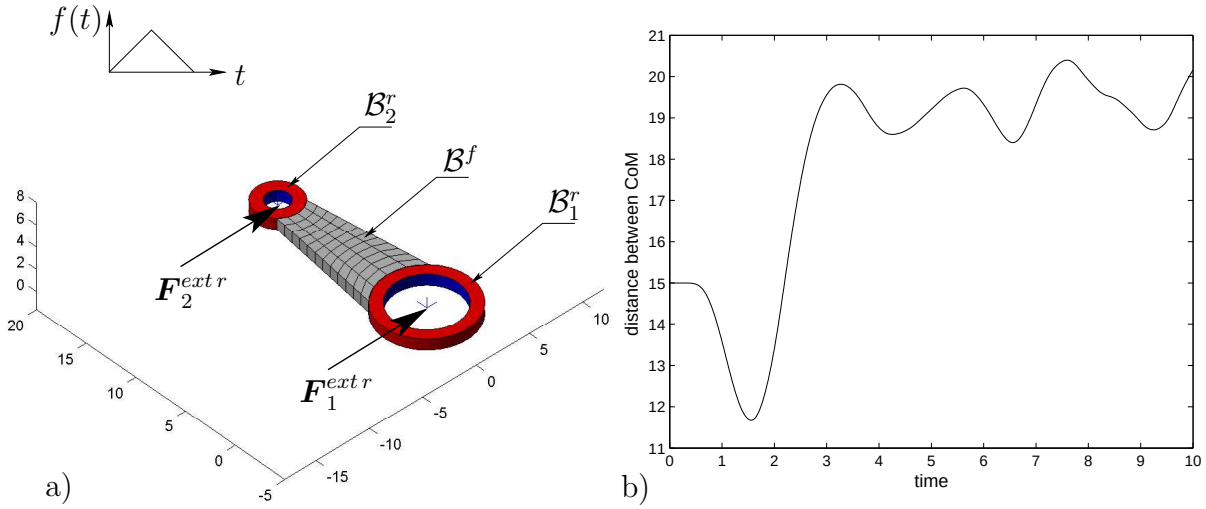

Figure 6.14.: a) initial configuration $\mathcal{B}_0$, b) distance between the centre of mass of RB 1 and the centre of mass of RB 2

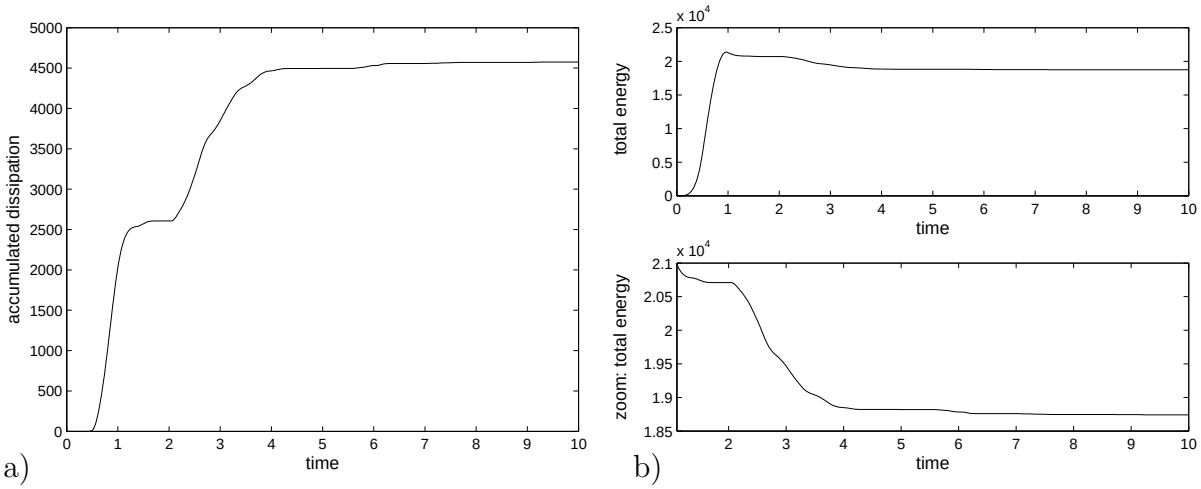

Figure 6.15.: a) accumulated dissipation D, b) total energy H

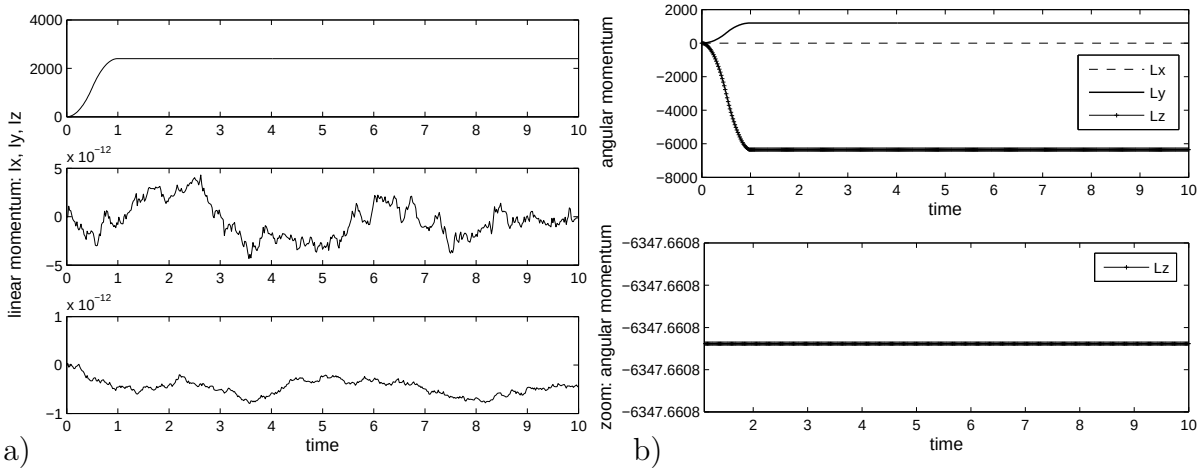

Figure 6.16.: components of: a) linear momentum, b) angular momentum

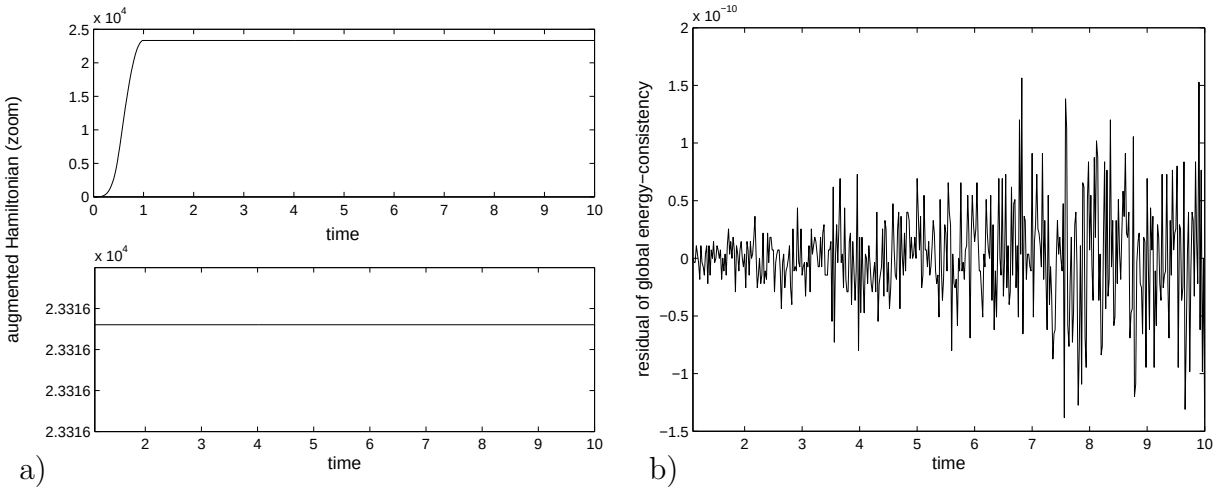

Figure 6.17.: a) augmented Hamiltonian $\widetilde{H}$, b) residual R

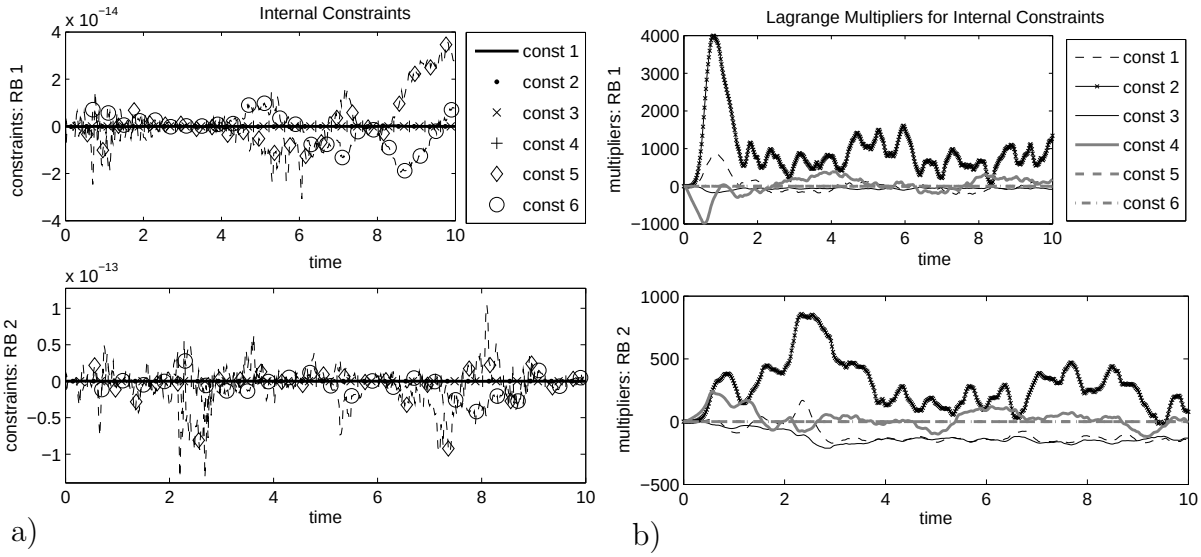

Figure 6.18.: a) internal constraints (RB 1 & RB 2), b) Lagrange multipliers for the internal constraints (RB 1 & RB 2)

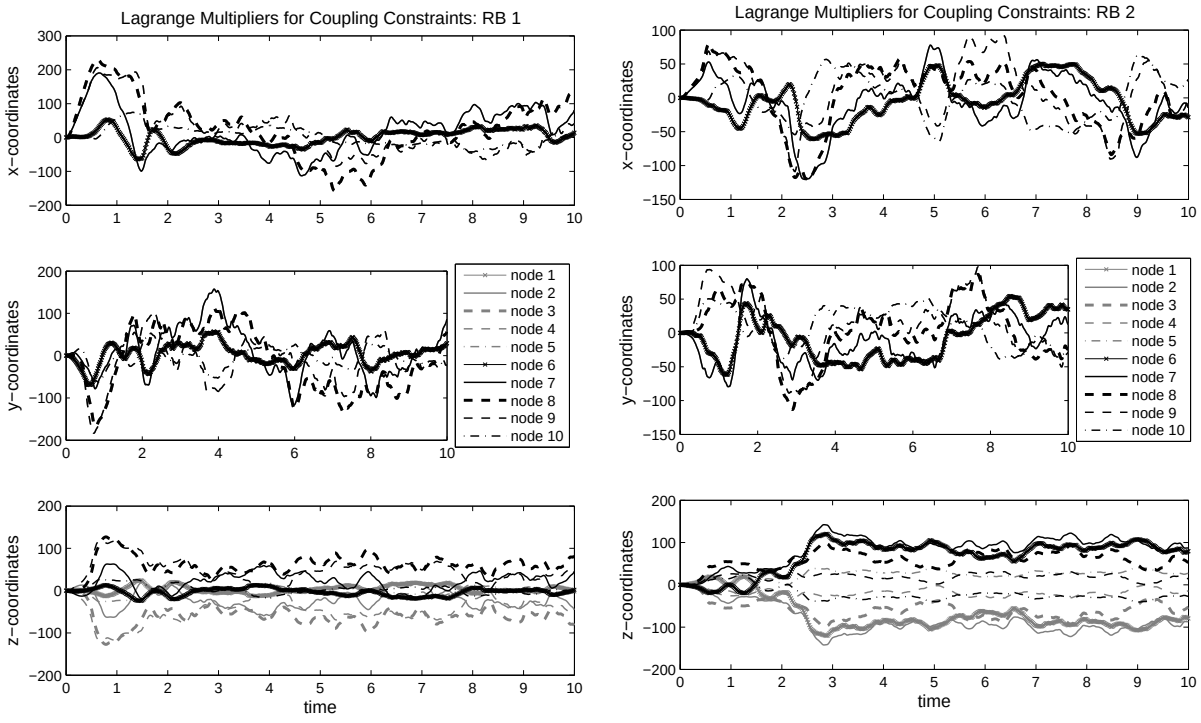

a) b)

Figure 6.19.: Lagrange multipliers for the coupling between the flexible part $\mathcal{B}^f$ and: a) the rigid body $\mathcal{B}_1^r$, b) the rigid body $\mathcal{B}_2^r$

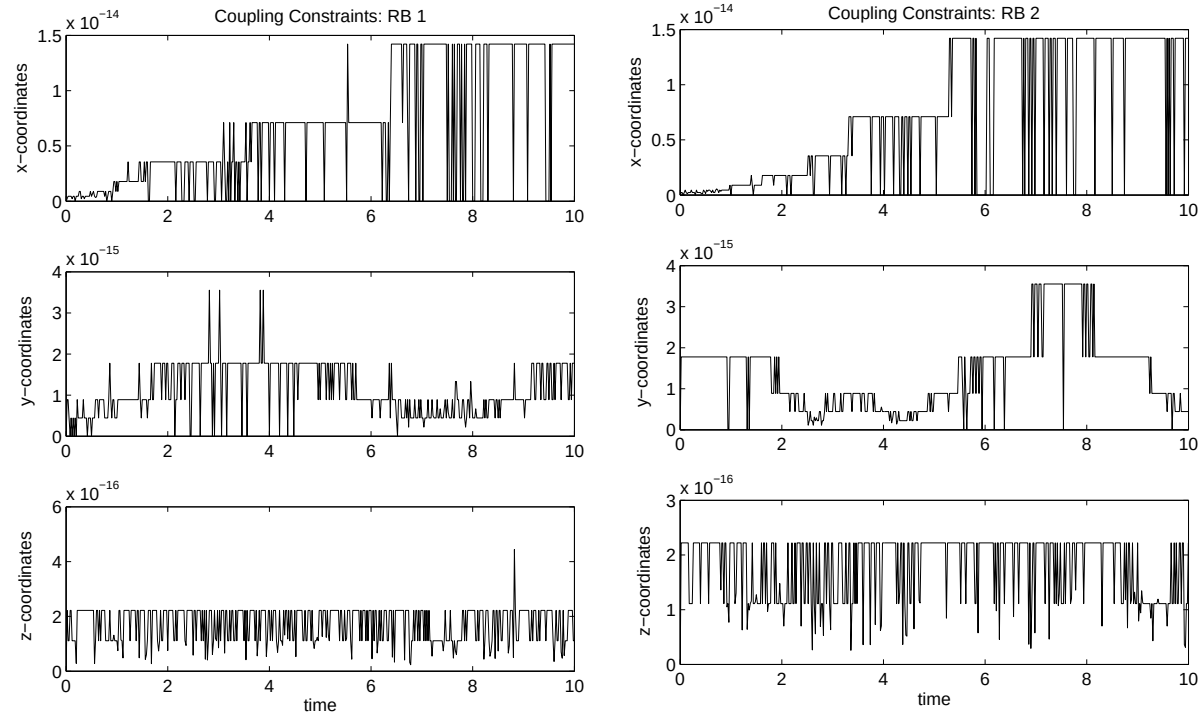

a) b)

Figure 6.20.: maximum absolute values (coupling constraints): a) RB 1, b) RB 2

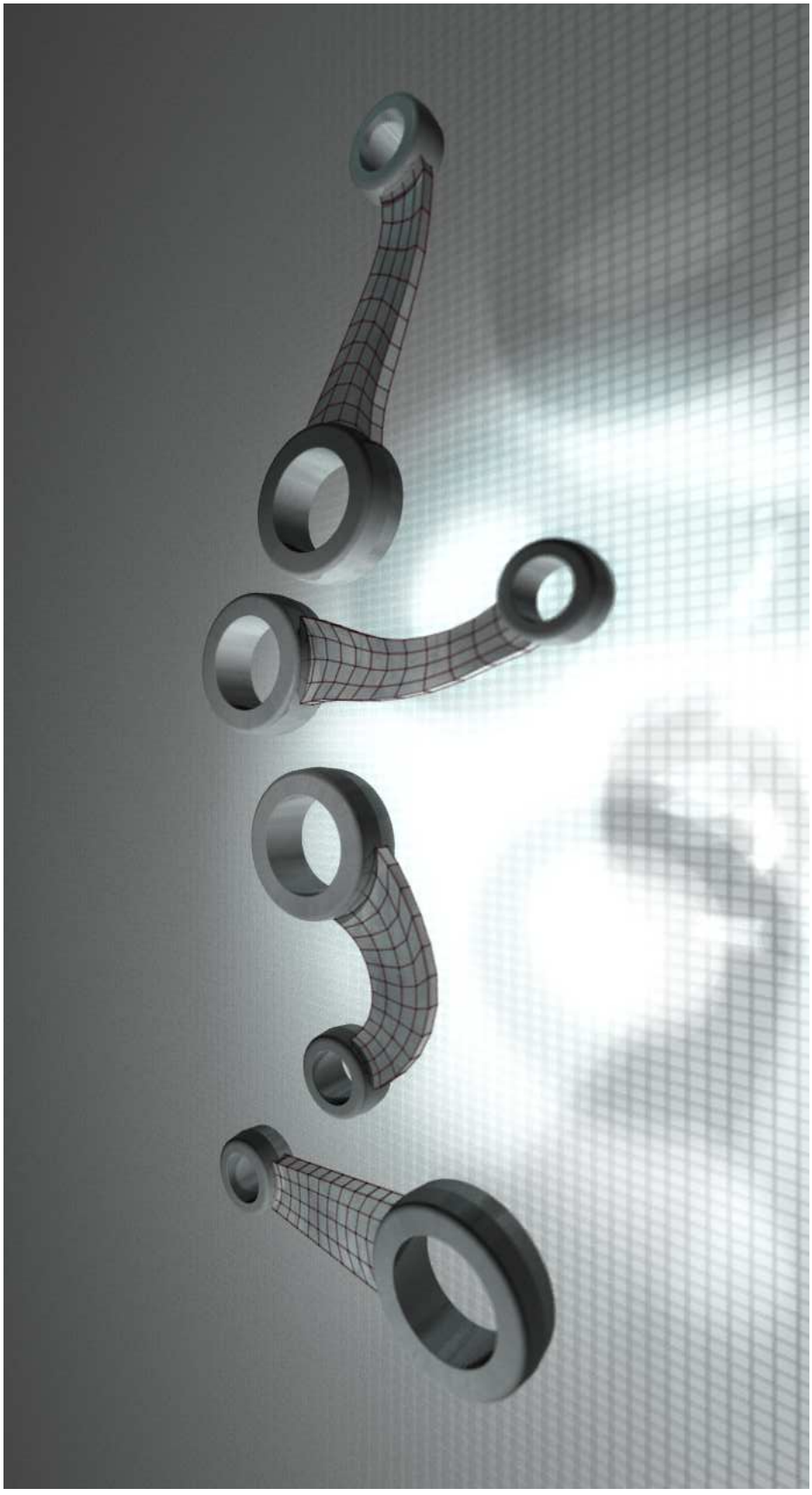

Figure 6.21.: sequence of the motion

6.3.3. Shaking Frame

In both foregoing examples, the free flight of a solid body which consists of rigid as well as flexible parts has been considered, demonstrating in particular the conservation properties of the integrator. Now, we investigate a 3d frame which can be decomposed into 3 rigid floors $\mathcal{B}^r_{1,2,3}$ and 8 flexible columns $\mathcal{B}^f_{1,\dots,8}$, whereby each flexible structure $\mathcal{B}^f_i$ is coupled to the corresponding rigid parts by means of 8 FE-nodes. Moreover, the ground floor is fixed in space and only 2 translational degrees of freedom remain, representing a two-directional sliding bearing which involves additionally 4 external constraints. Finally, the constraint vector of the system results in $\bar{\boldsymbol{g}} \in \mathbb{R}^{214}$. A sketch of the system can be regarded in Figure 6.22 a) and the applied intertial parameters of the involved rigid parts can be found in Table 6.3.

Table 6.3.: inertial parameters of the involved rigid bodies

Rigid body		M	E_1	E_2	E_3
Ground floor	RB 1	20	666.6667	666.6667	0.4167
First floor	RB 2	1500	12500	12500	31.2500
Second floor	RB 3	1500	12500	12500	31.2500

The computations have been performed with the constant time-step size $h_n = 0.1$, using for $\mathcal{B}^f_{1,\dots,4}$ the parameters $\rho_1 = 12.0$, $\lambda_1 = 300\,000$, $\mu_1 = 100\,000$, $Y_{0,1} \to \infty$, and for $\mathcal{B}^f_{5,\dots,8}$ the parameters $\rho_2 = 12.0$, $\lambda_2 = 30000$, $\mu_2 = 10000$, $Y_{0,2} = 300$, $H^{rd}_2 = 3000$. Motivated by the load case of an earthquake, the external forces $\boldsymbol{F}^{extr}_{1,j} = 5\, f_j(t)\, [1,0,0]^{\mathrm{t}}$ with $j = 1,2,3$ act on the centre of mass of rigid body 1, wherein the scaling factors $f_j(t)$ correspond to the sinusoidal 'load signals 1-3' plotted in Figure 6.22 b). In the following discussion, special emphasis will be placed on a comparison between the plastic and the purely elastic case, involving additionally $Y_{0,2} \to \infty$. To get an idea of the deformation of the system, we refer to Figure 6.32, Figure 6.33, and Figure 6.34, showing deformed configurations of the frame for the elastic as well as for the plastic motion. Therein, it can be clearly seen that the purely elastic case is characterised by notable relative motions between RB 2 and RB 3 during the entire time period. In contrast, the occurrence of plastic deformations in $\mathcal{B}^f_{5,\dots,8}$ leads to significantly reduced deflections accompanied by an increasing plastic dissipation, which is pictured in Figure 6.25 a). This result also becomes obvious when the trajectory of the centre of mass of RB 3 or the corresponding phase-space portrait is considered, as shown in Figure 6.23. In fact, the dissipation effects enable conspicuously lower levels of total, free, and especially of kinetic energy, whereby the reduced kinetic energy is also directly related to a decrease of the corresponding components of the momenta, see Figure 6.24 and Figure 6.26. Moreover, it is displayed in Figure 6.31 b) that in particular the reaction forces on RB 3 in z-direction, which are related to the coupling constraints between $\mathcal{B}^f_{5,\dots,8}$ and $\mathcal{B}^r_3$, are visibly reduced in the plastic case. Analogously, this effect can be observed in Figure 6.30 b) based

on a plot of the bearing reaction force, which acts on the centre of mass of RB 1 in z-direction. Contrariwise, the reaction forces on RB 1 in x-direction, being related to the coupling between $\mathcal{B}^f_{1,\dots,4}$ and $\mathcal{B}^r_1$, are not influenced substantially when plastic deformations are involved, compare Figure 6.31 a). Next, the consistency properties of the integrator will be demonstrated once more. In this context, the conservation of the augmented Hamiltonian can be regarded in Figure 6.25 b) for $t \in [2, 4]$, representing the only time interval without external loading. More precisely, it is shown in Figure 6.27 that energy-consistency is guaranteed within the order of magnitude $\mathcal{O}(10^{-10})$ for the elastic as well as for the plastic motion. To investigate the fulfilment of the coupling and the internal constraints, the maximum deviation approach based on Equation (6.53) has been applied once more, enabling a particularly compact representation. As confirmed by the results in Figure 6.28 and Figure 6.29 a), both types of constraints are fulfilled within the calculation accuracy, whereby the maximum violation lies in the range of 10^{-12}. Finally, each of the 4 additional external constraints is plotted in Figure 6.29 b) and Figure 6.30 a) respectively, wherein an exact fulfilment can be seen.

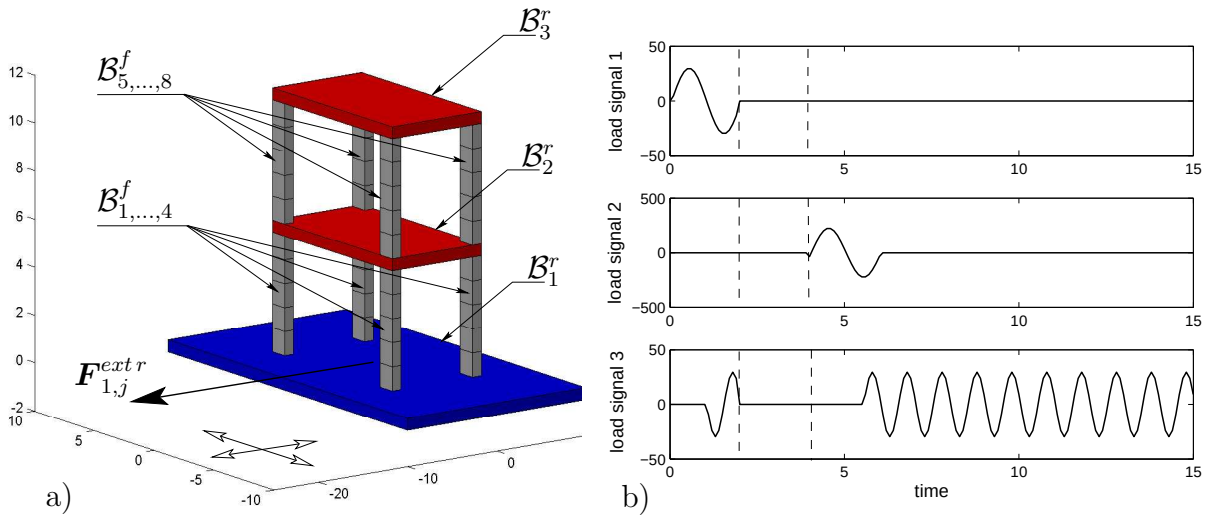

Figure 6.22.: a) initial configuration $\mathcal{B}_0$, b) loading history

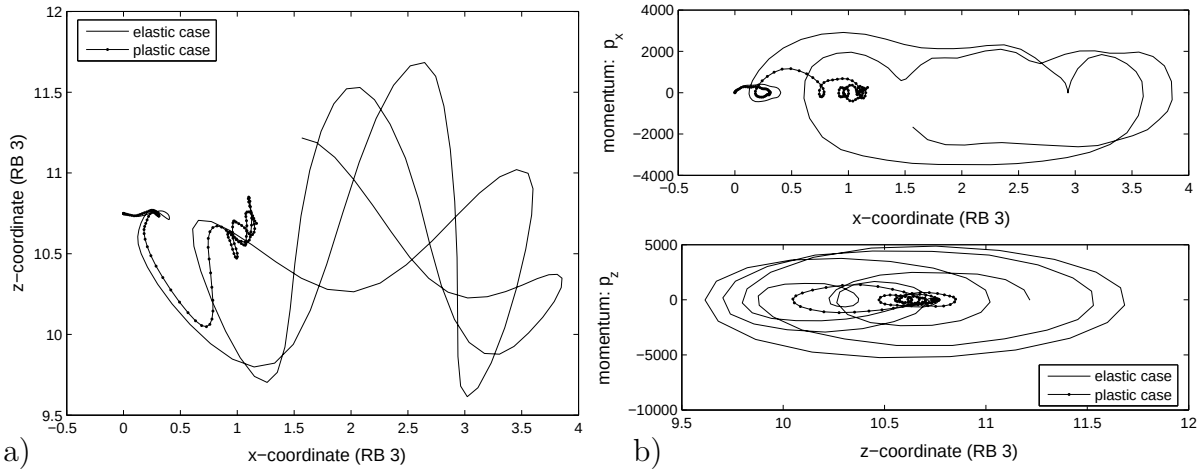

Figure 6.23.: RB 3: a) trajectory of the centre of mass, b) phase-space portraits

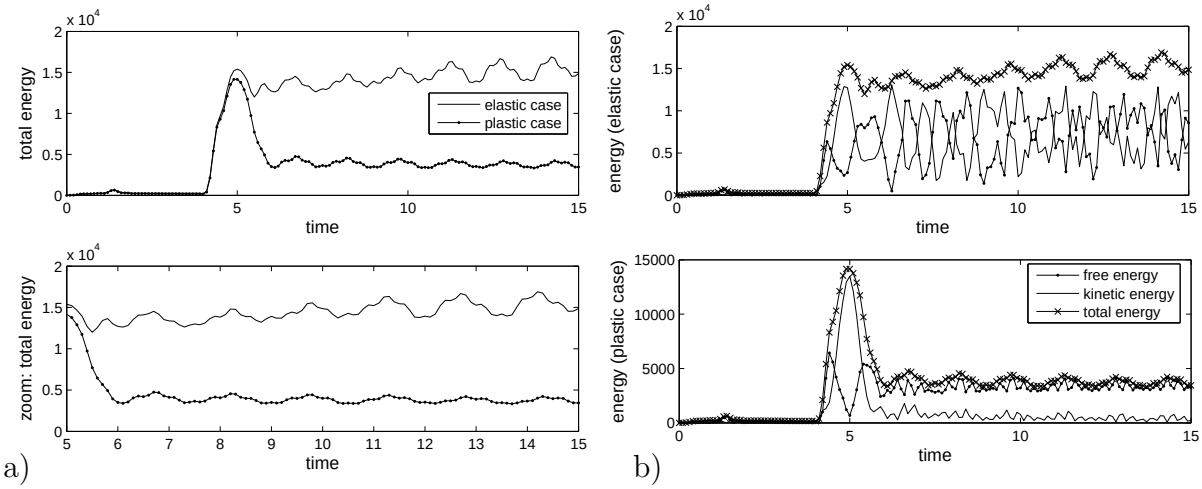

Figure 6.24.: a) total energy H, b) total energy H & energy components K, Ψ

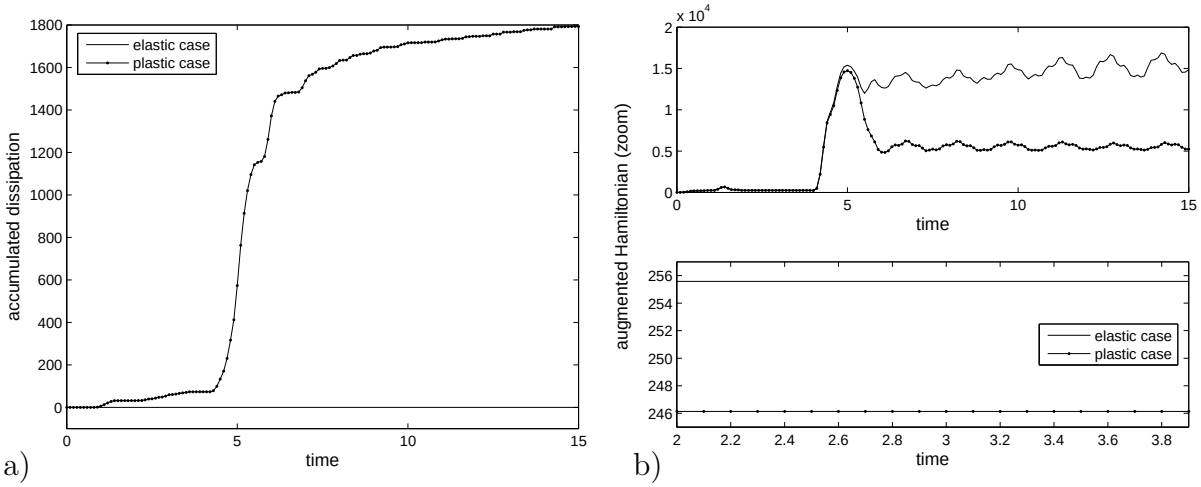

Figure 6.25.: a) accumulated dissipation D, b) augmented Hamiltonian $\widetilde{H}$

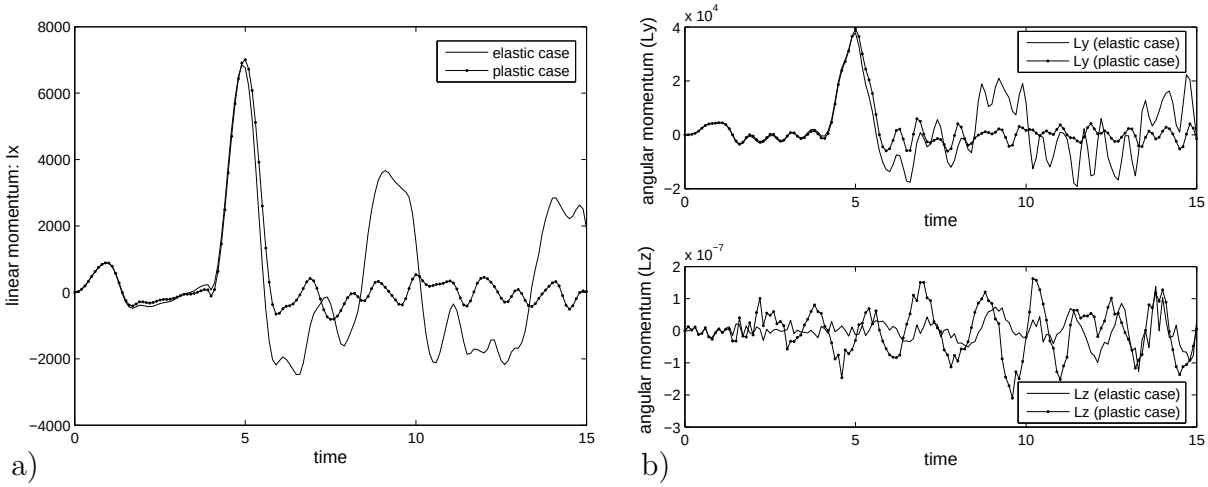

Figure 6.26.: component(s) of: a) linear momentum, b) angular momentum

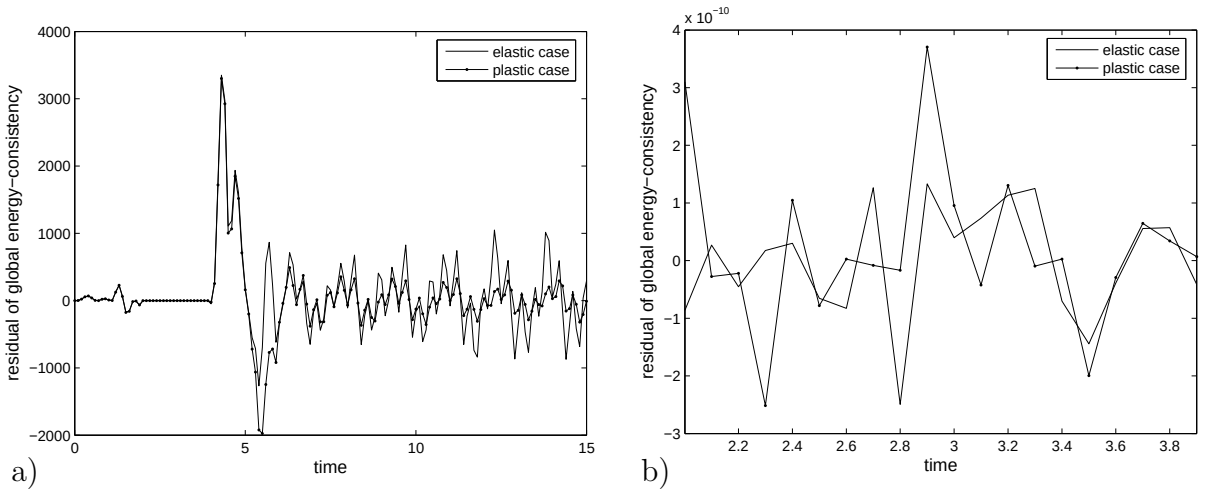

Figure 6.27.: a) residual of global energy-consistency R, b) zoom: residual R

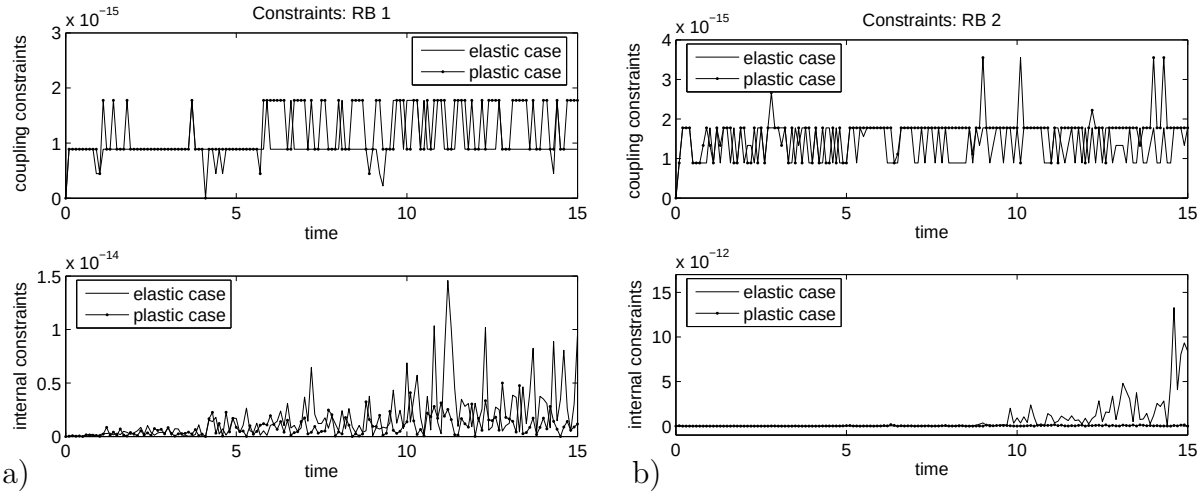

Figure 6.28.: maximum absolute values (coupling & internal constraints): a) RB 1, b) RB 2

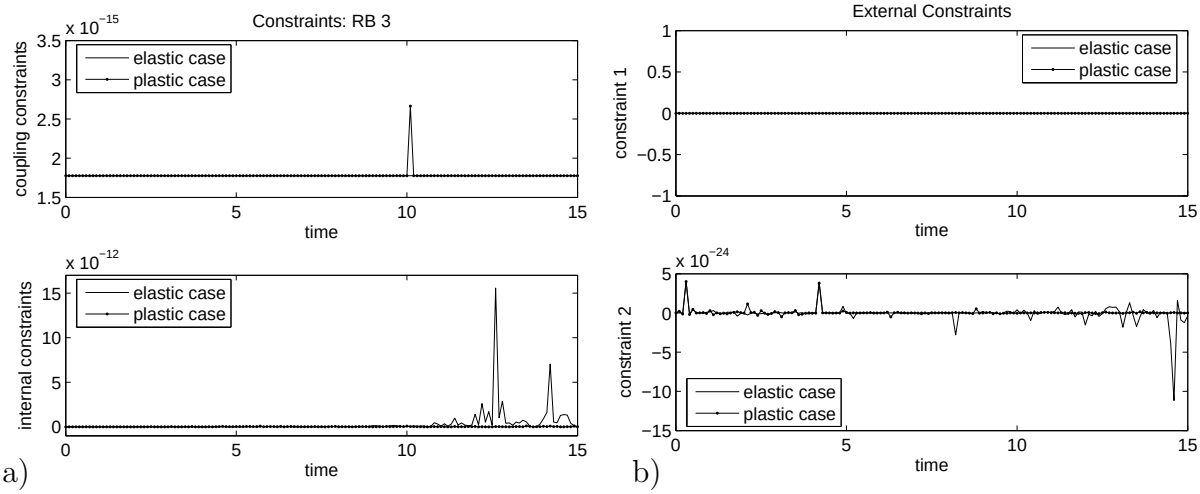

Figure 6.29.: a) maximum absolute values (coupling & internal constraints): RB 3, b) external constraint 1 & external constraint 2 (RB 1)

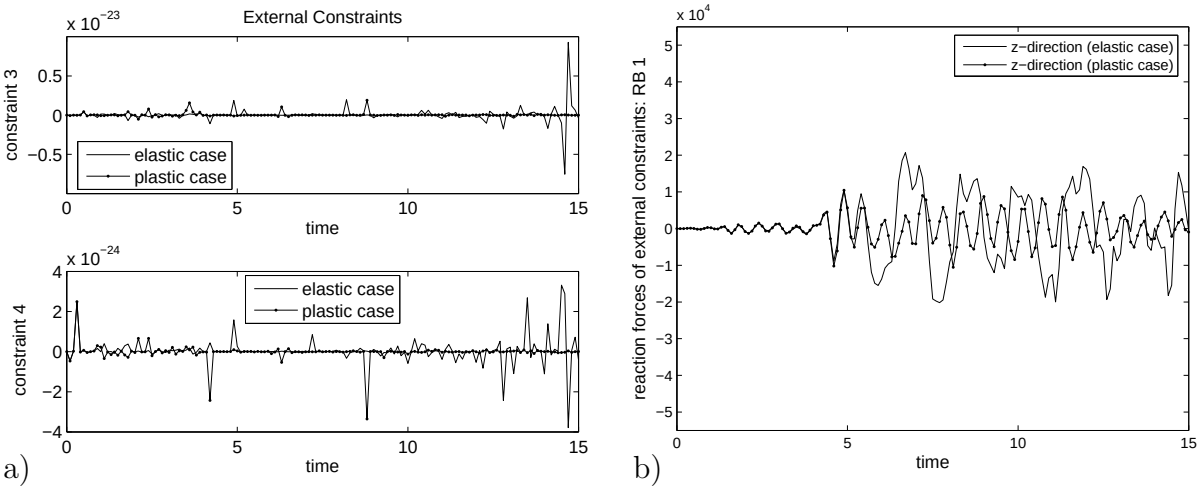

Figure 6.30.: a) external constraint 3 & external constraint 4 (RB 1), b) reaction forces related to the external constraints acting on RB 1 (z-direction)

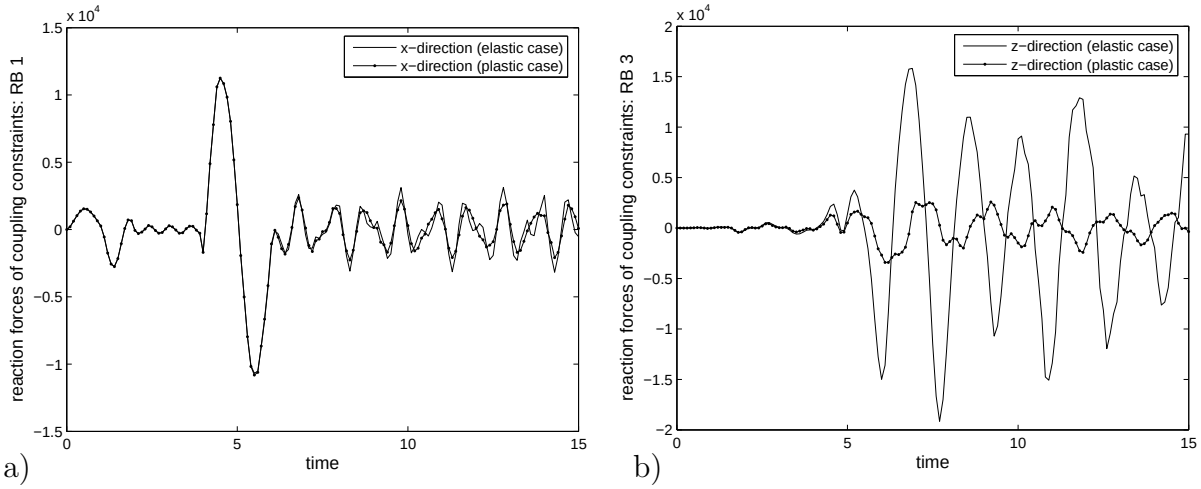

Figure 6.31.: reaction forces related to the coupling constraints acting on: a) RB 1 (x-direction), b) RB 3 (z-direction)

$t = 1.0$

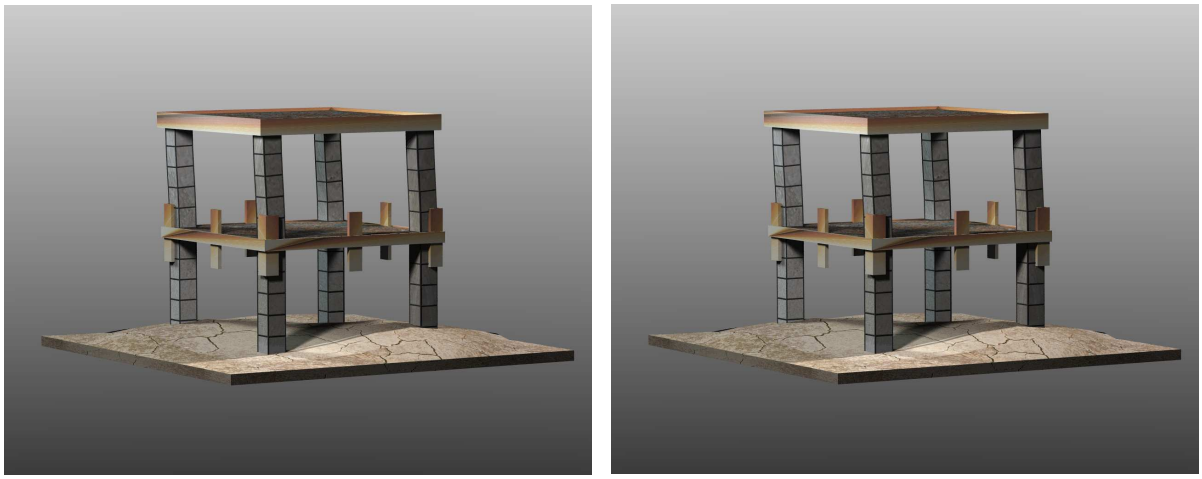

$t = 3.0$

$t = 5.0$

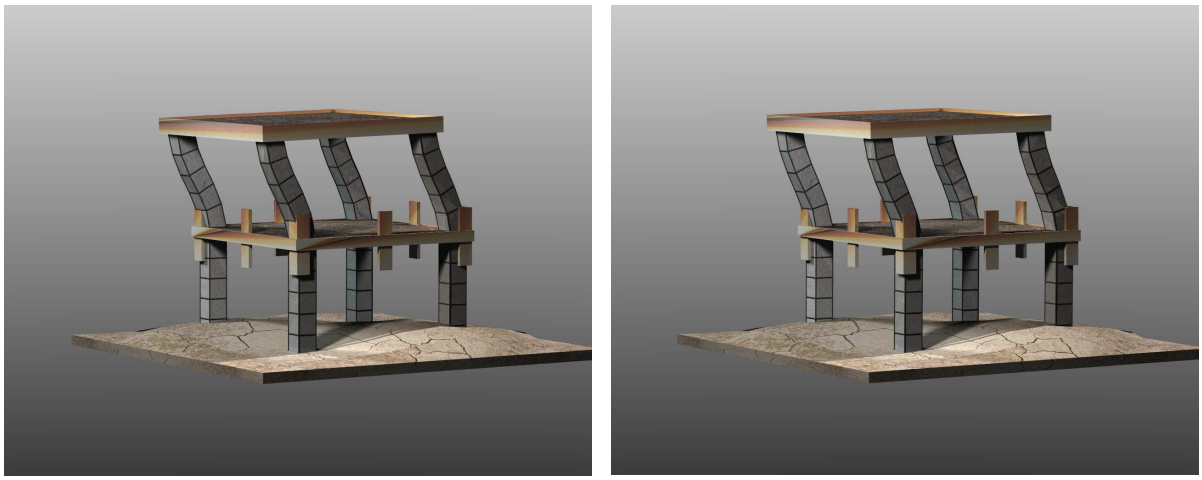

a) b)

Figure 6.32.: deformed configurations $\mathcal{B}_t$ at $t \in \{1.0, 3.0, 5.0\}$: a) elastic motion, b) plastic motion

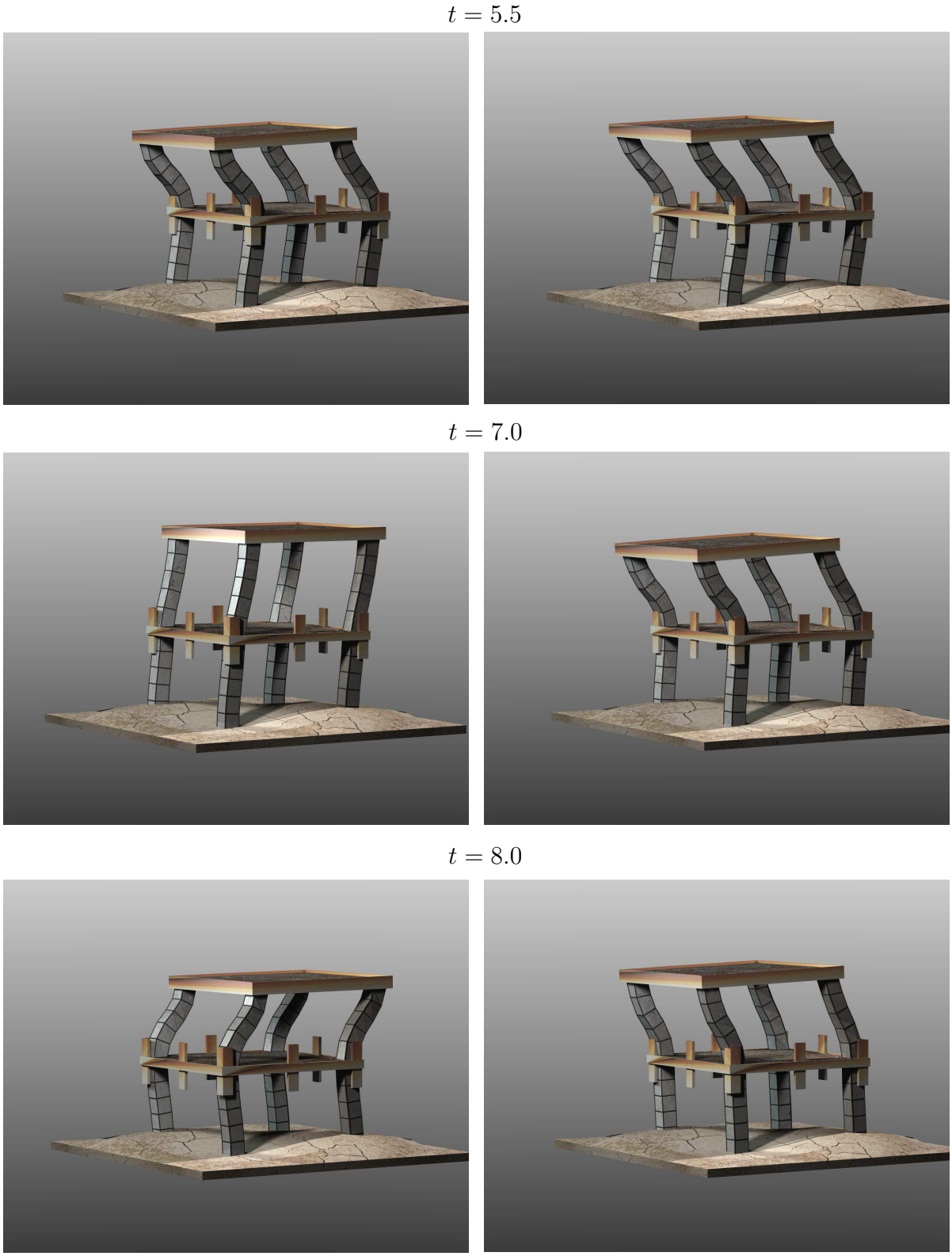

Figure 6.33.: deformed configurations $\mathcal{B}_t$ at $t \in \{5.5, 7.0, 8.0\}$: a) elastic motion, b) plastic motion

$t = 8.5$

$t = 12.0$

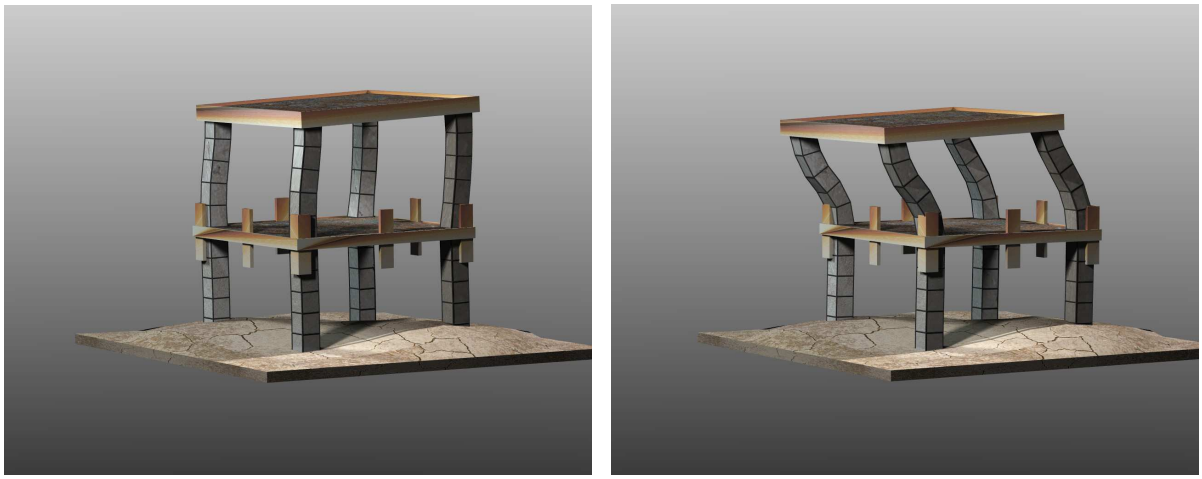

$t = 15.0$

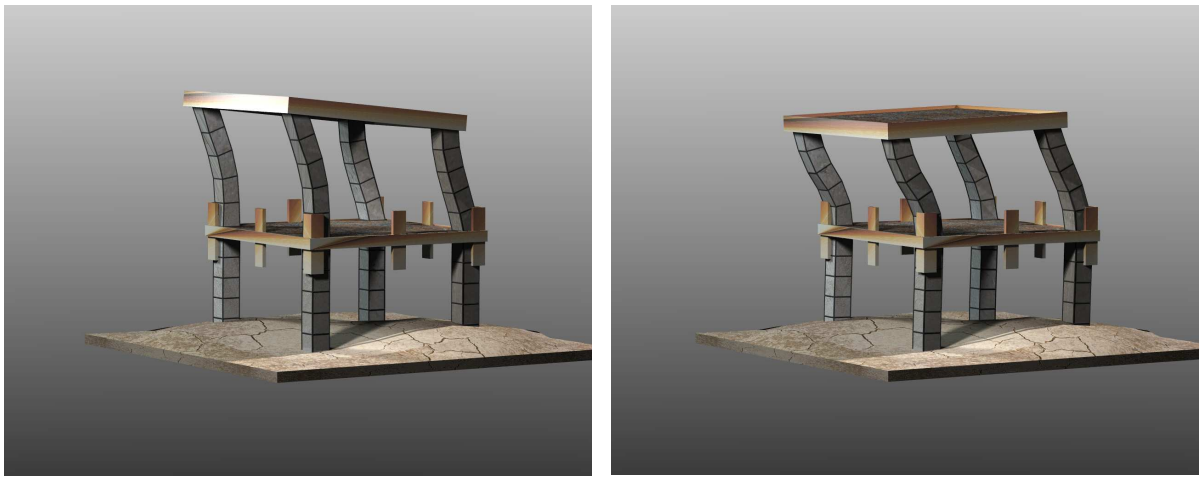

a) b)

Figure 6.34.: deformed configurations $\mathcal{B}_t$ at $t \in \{8.5, 12.0, 15.0\}$: a) elastic motion, b) plastic motion

6.3.4. Slider-Crank Mechanism

So far, we have basically investigated the case that the rigid parts are coupled with each other via flexible structures. However, in most of the technically relevant multibody systems additional joints between pairs of rigid bodies have to be taken into account. For this purpose, we consider finally a 3d 'Slider-Crank Mechanism' which transforms a translational into a rotational motion, see Figure 6.35 for an illustration. Obviously, the piston, the conrod, the rim of the wheel, as well as the nave have been modelled as rigid parts $\mathcal{B}^r_{1,\dots,4}$ with the inertial parameters summarised in Table 6.4, whereas the spokes of the wheel $\mathcal{B}^f_{1,\dots,4}$ are flexible, using $\rho = 10.0$, $\lambda = 100\,000$, $\mu = 50\,000$, $Y_0 = 1000$, $H^{rd} = 5000$. In this context, the each flexible part is coupled to the rim and the nave via 12 FE-nodes. Furthermore, the nave of the wheel is fixed in space with a bearing of revolute-type, the rim of the wheel is connected with the conrod via a revolute pair, analogously to the coupling between the conrod and the piston, and the piston by itself is fixed in space by means of a cylindrical bearing, referred to as 'External Constraint A-D'. Hence, the system vector of the foregoing constraints reads $\bar{\boldsymbol{g}} \in \mathbb{R}^{187}$, incorporating additionally the internal constraints related to the rigid body description.

Table 6.4.: inertial parameters of the involved rigid bodies

Rigid body		M	E_1	E_2	E_3
Nave	RB 1	565.4867	2827.4334	2827.4334	106.0288
Wheel rim	RB 2	1130.9734	46369.9076	46369.9076	94.2478
Conrod	RB 3	56.0000	18.6667	3658.6667	0.0467
Piston	RB 4	1280.0000	6826.6667	27306.6667	106.6667

To start the motion, we have used once more a hat function $f(t)$ for the loading history with $f_{max} = 300$ and $T_{load} = 1.0$, whereby this time the external force $\boldsymbol{F}_4^{ext\,r} = f(t)\,[0,1,0]^{\mathrm{t}}$ acts on RB 4 and additionally the external nodal loads $\boldsymbol{F}_A^{ext} = f(t)\,[0,1,0]^{\mathrm{t}}$, $\boldsymbol{F}_B^{ext} = f(t)\,[1,0,0]^{\mathrm{t}}$ act on the flexible spokes. The following results have been calculated by means of the constant time-step size $h_n = 0.05$. Four snapshots of the motion are pictured in Figure 6.46 and Figure 6.47, wherein especially the large plastic deformations of the spokes are mentionable. In addition to the deformation of the spokes, the motion of the conrod (RB 3) might be of particular interesting: Hereby, the trajectory as well as the phase-space portrait are both characterised by a circle-like pattern related to its periodic motion, see Figure 6.44 a) and Figure 6.36 a) respectively. Furthermore, we refer in this context to the typical shape of the so-called herpolhode in Figure 6.36 b), representing the trajectory of the instantaneous centre of rotation. To get a better idea of the obtained reaction forces acting on the corresponding rigid bodies, Figure 6.39 shows exemplarily some components of the reactions caused by the revolute pair ('External Constraint B') and by the coupling with the flexible spokes. Herein, the

observable high-frequency oscillations are directly affected by the vibration modes of the flexible parts, whereas the long-time periodicity is related to the rotational motion of the 'Slider-Crank Mechanism'. Once more, the accumulated dissipation plotted in Figure 6.37 b) leads to the claimed monotonic decrease of the total energy displayed in Figure 6.37 a), whereby Figure 6.38 shows additionally the conservation of the augmented Hamiltonian as well as the rigorous fulfilment of energy-consistency in the size of 10^{-10}. Dealing with constrained dynamics, the fulfilment of the involved constraints will be demonstrated in detail also for this last example. For this purpose, maximum absolute values are selected at the end of each time step based on Equation (6.53). The results for the coupling and the internal constraints can be regarded in Figure 6.40 and Figure 6.41 respectively, showing that the maximum violation of the constraints lies in the range of 10^{-15}. Furthermore, external constraints, which are denoted by 'External Constraint A-D', are used in this model, as already mentioned above. The corresponding components are plotted in Figure 6.42 and Figure 6.43, wherein it can be clearly seen that also these constraints are fulfilled in a numerically exact manner. Hence, the results have confirmed once again that kinematic consistency is indeed offered by the applied time-integration scheme (6.52). Finally, the plastic motion is compared with the purely elastic case based on $Y_0 \to \infty$. As can be seen in Figure 6.48, there are nearly no visible deformations of the spokes in the purely elastic case due to the applied stiff material parameters. In contrast, the plastic case is characterised by a notable twist between the nave and the rim, compare Figure 6.45 a). Furthermore, this twist leads – similarly to Example 6.3.1 – to a phase shift in the y-coordinate of the piston as well as in the x-coordinate of an exemplarily considered FE-node, as pictured in Figure 6.44 b) and Figure 6.45 b) respectively.

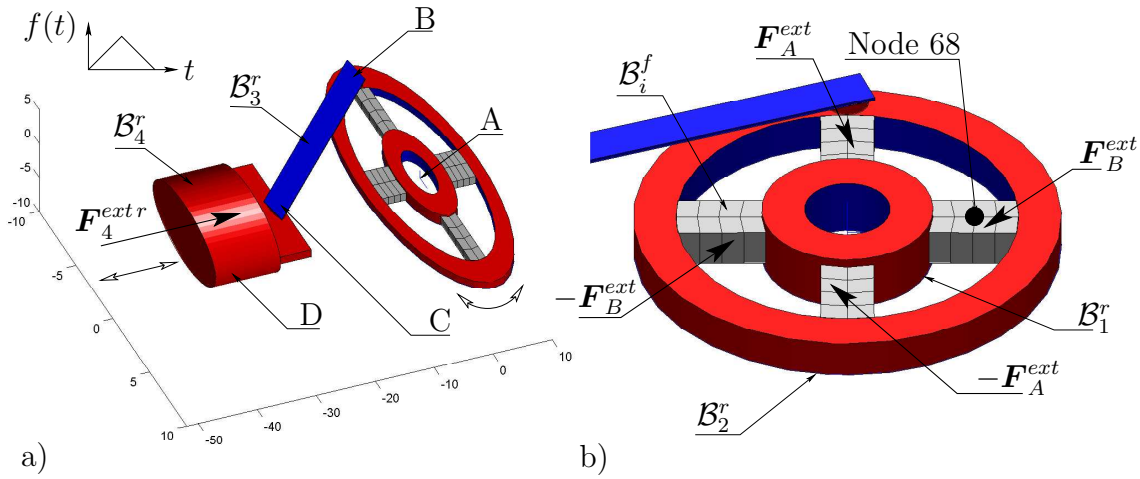

Figure 6.35.: initial configuration $\mathcal{B}_0$ of the spatial 'Slider-Crank Mechanism'

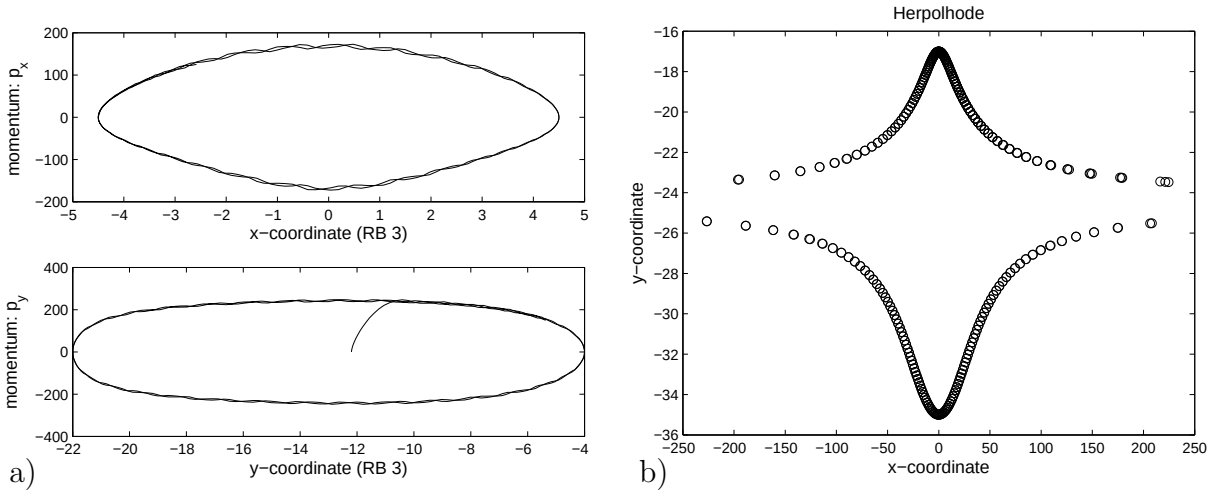

Figure 6.36.: RB 3: a) phase-space portrait, b) herpolhode

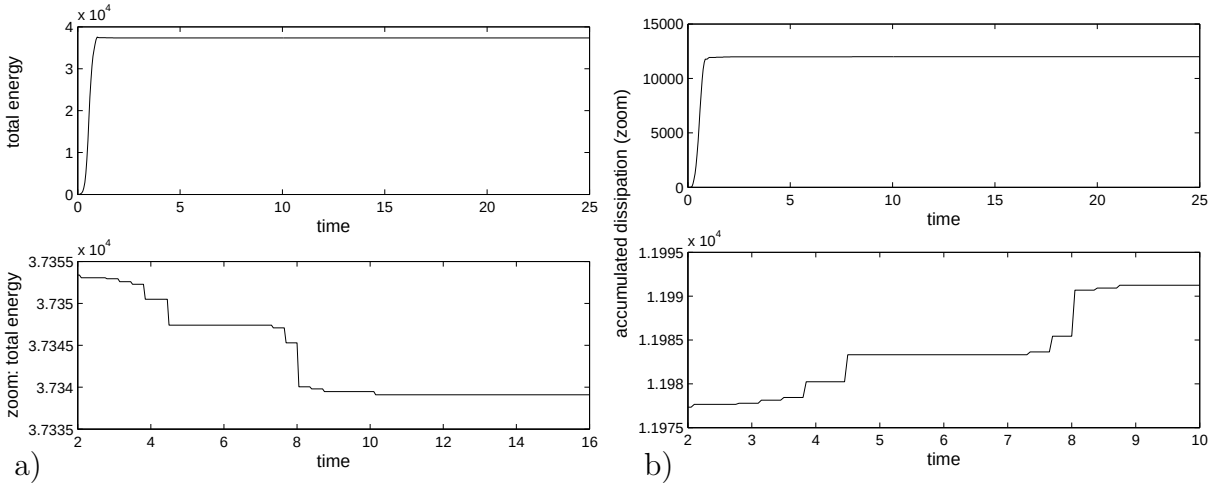

Figure 6.37.: a) total energy H, b) accumulated dissipation D

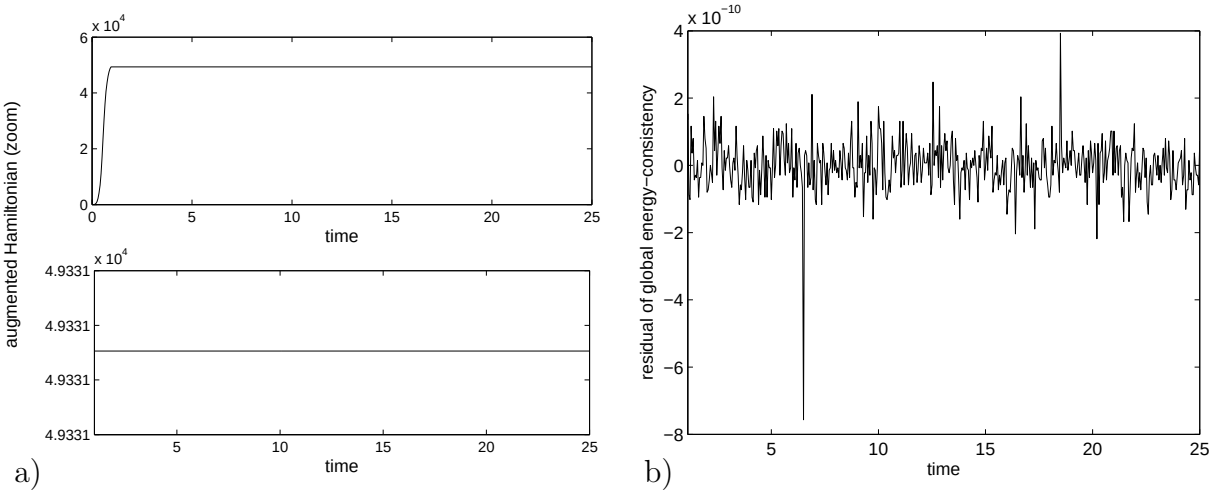

Figure 6.38.: a) augmented Hamiltonian $\widetilde{H}$, b) residual R

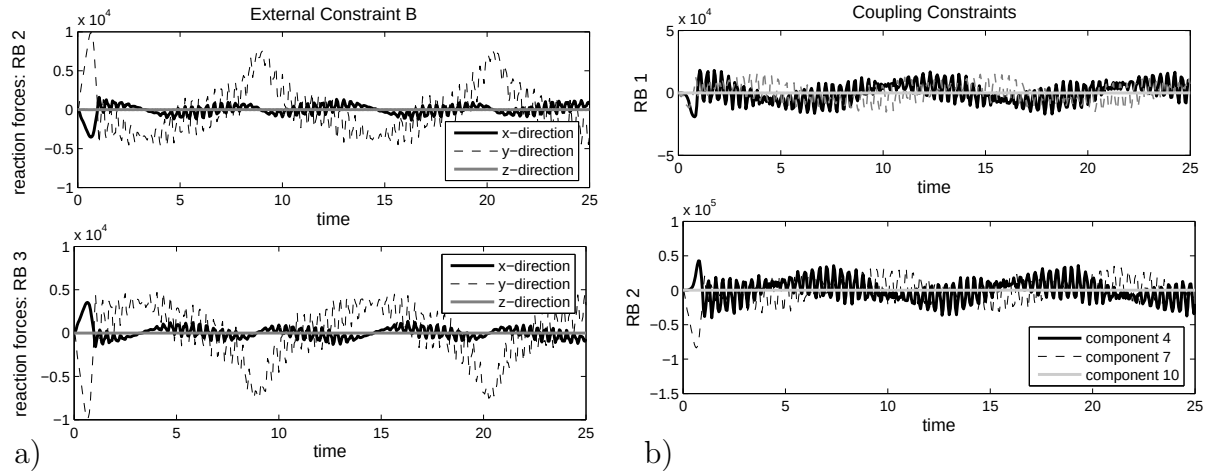

Figure 6.39.: a) reaction forces related to revolute pair (RB 2/RB 3), b) reactions related to coupling constraints (RB 1/RB 2)

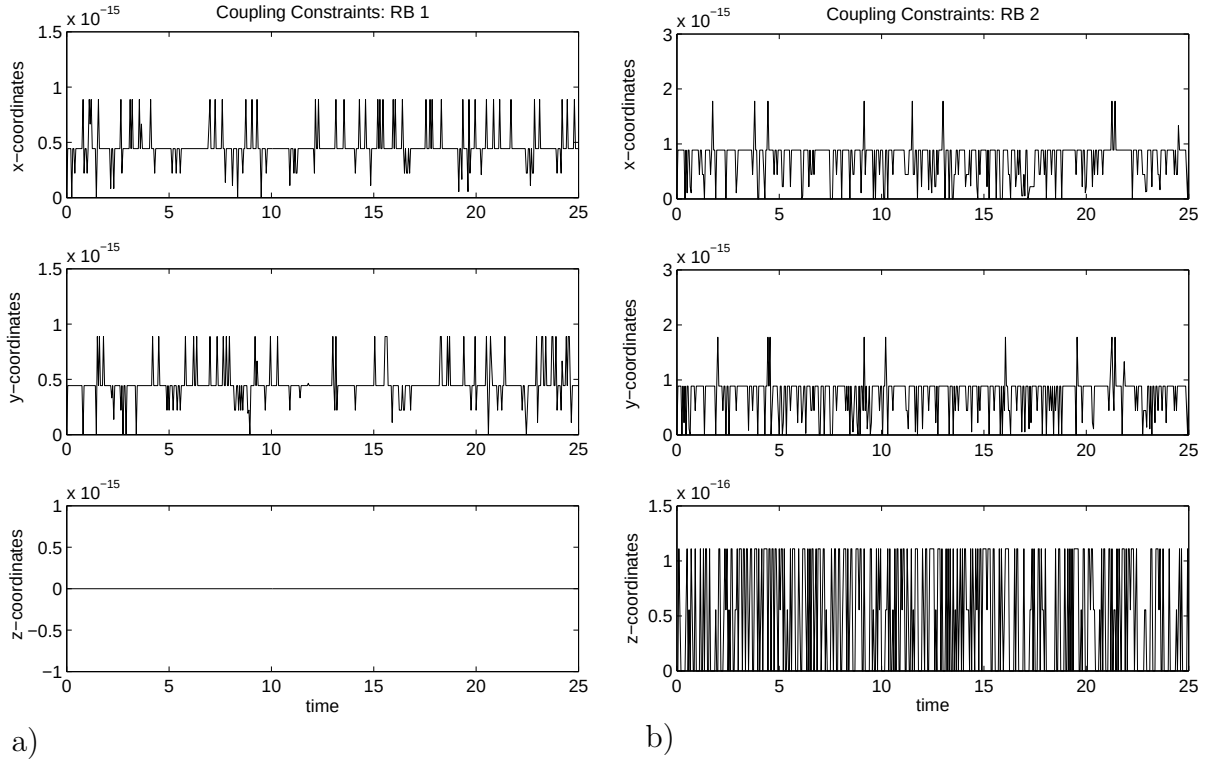

Figure 6.40.: maximum absolute values (coupling constraints): a) RB 1, b) RB 2

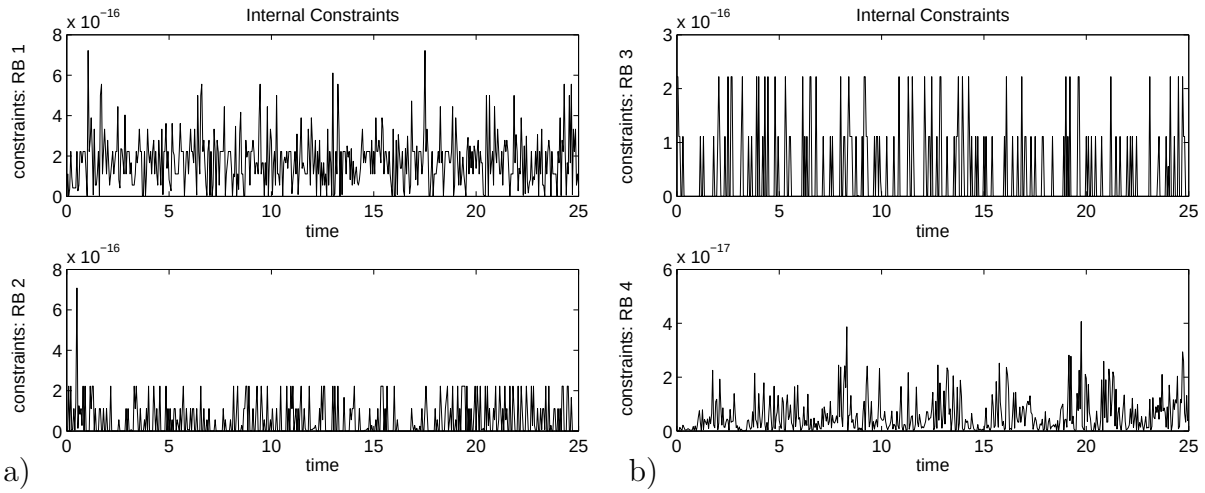

Figure 6.41.: maximum absolute values (internal constraints): a) RB1 & RB 2, b) RB 3 & RB 4

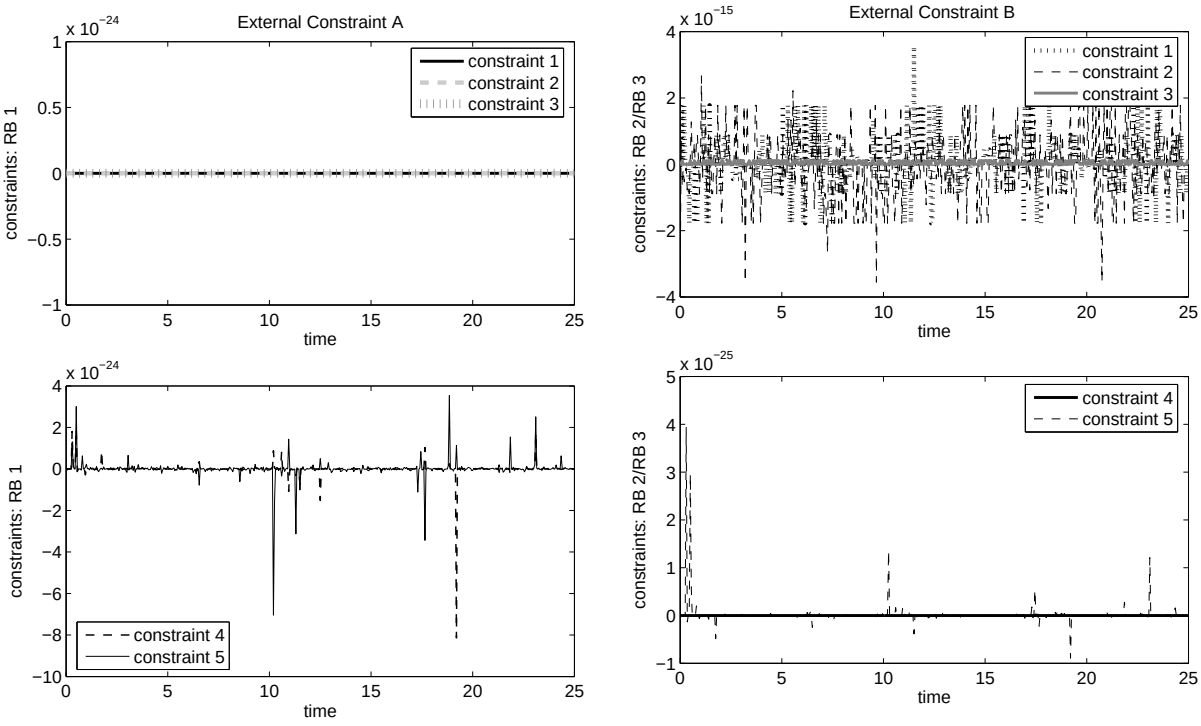

a) b)

Figure 6.42.: external constraints applied: a) to RB 1 (revolute-type), b) between RB 2/RB 3 (revolute pair)

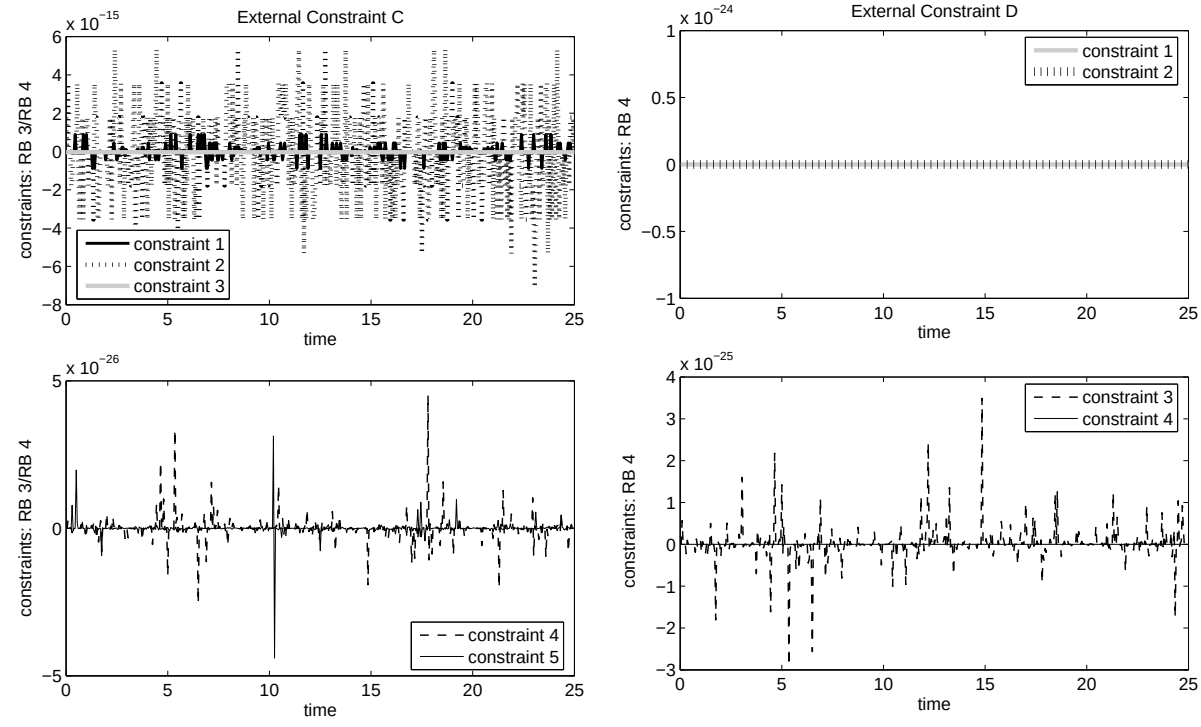

a) b)

Figure 6.43.: external constraints applied: a) between RB 3/RB 4 (revolute pair), b) to RB 4 (cylindrical-type)

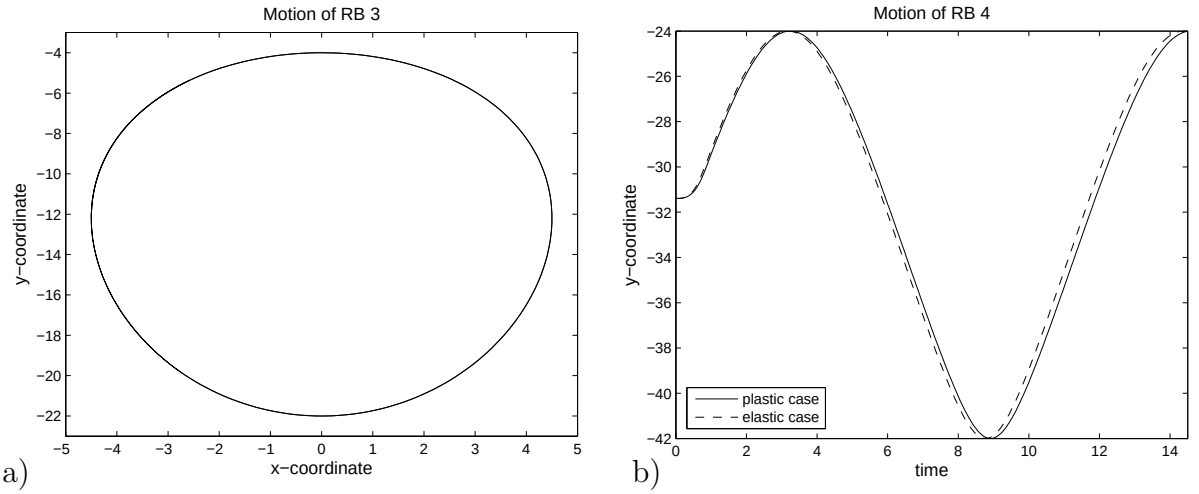

a) b)

Figure 6.44.: a) trajectory of the centre of mass (RB 3), b) elastic vs. plastic motion: y-coordinate of the centre of mass (RB 4)

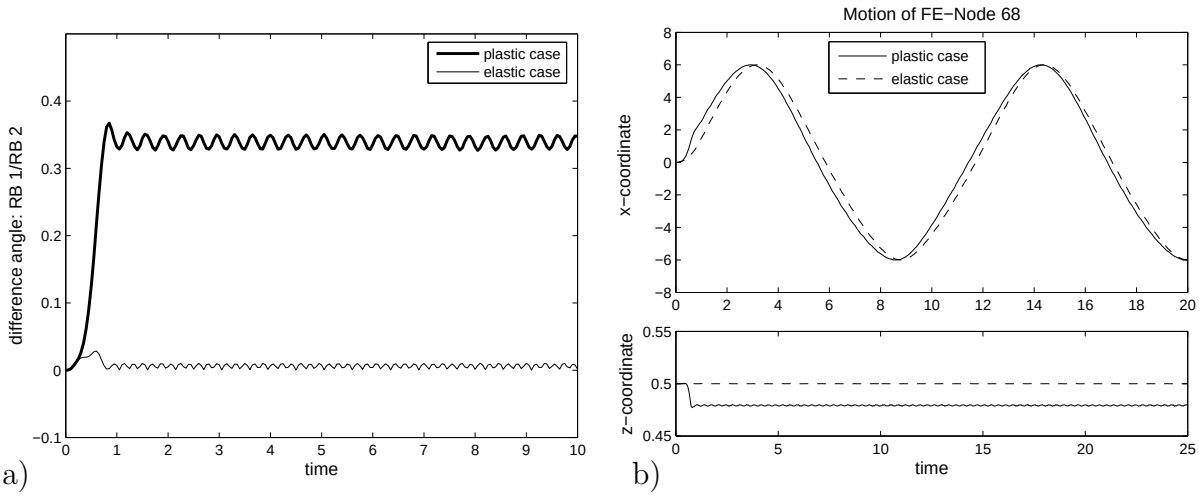

a) b)

Figure 6.45.: elastic vs. plastic motion: a) difference angle (RB 1/RB 2), b) coordinates of a FE-node

$t = 0.05$

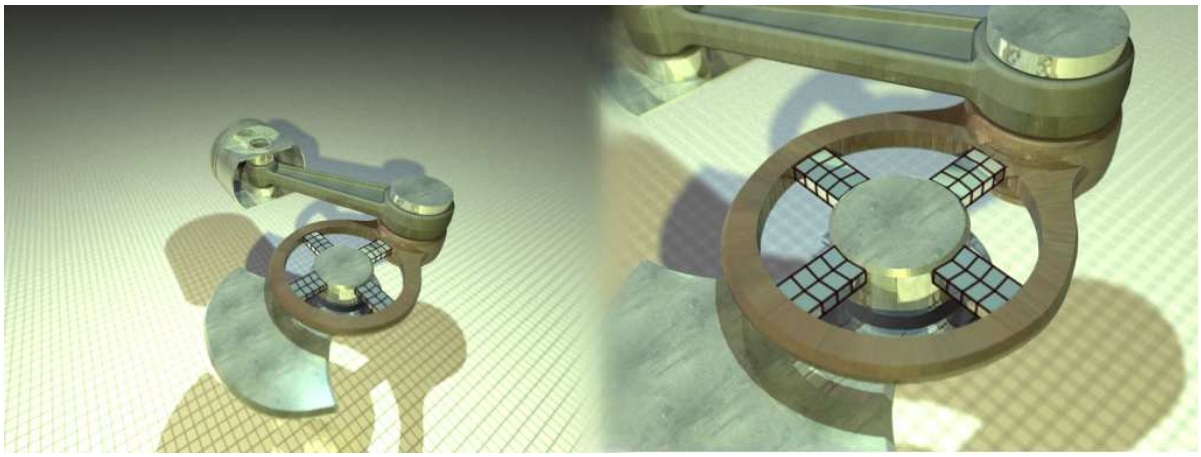

$t = 6.0$

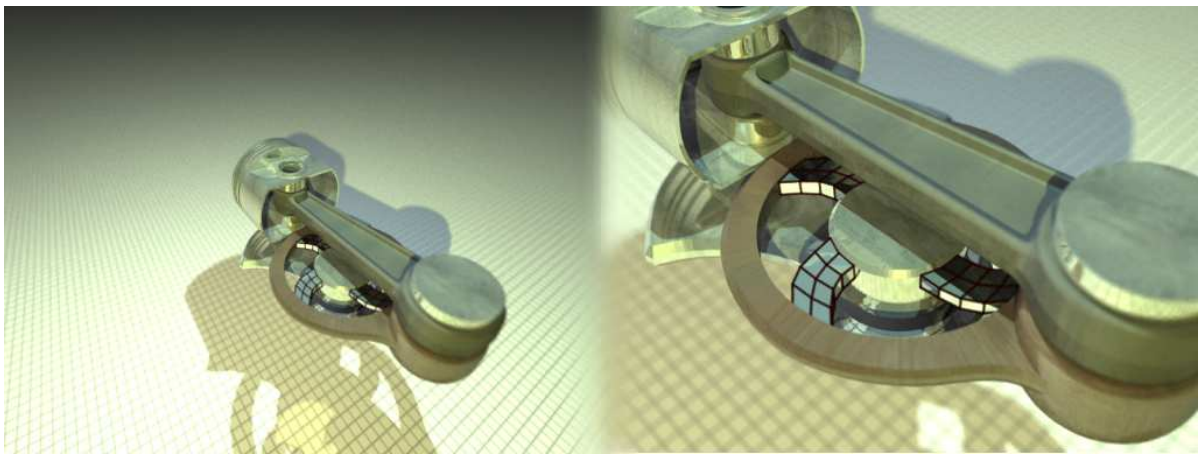

$t = 14.0$

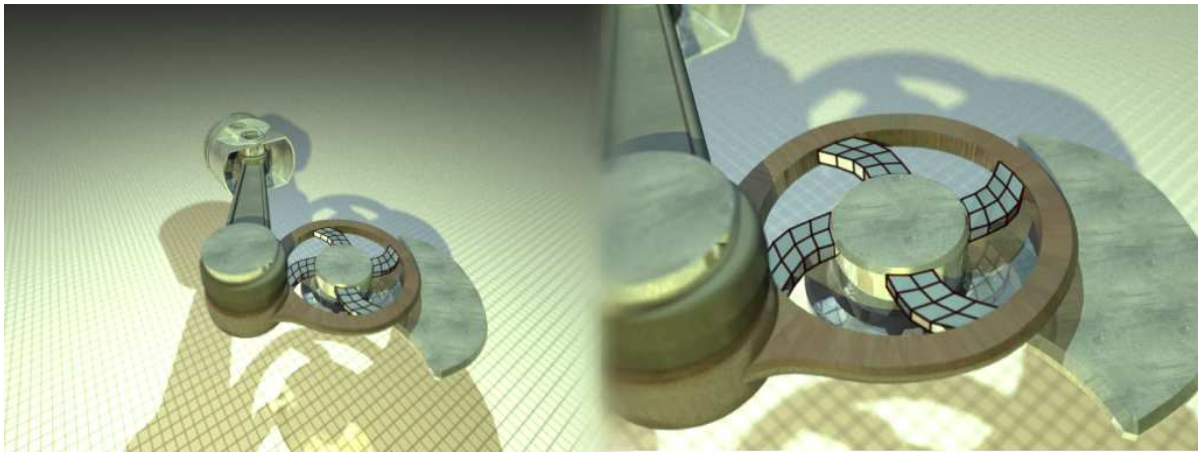

a) b)

Figure 6.46.: deformed configurations $\mathcal{B}_t$ at $t \in \{0.05, 6.0, 14.0\}$: a) overall view, b) zoom: spokes

$t = 19.5$

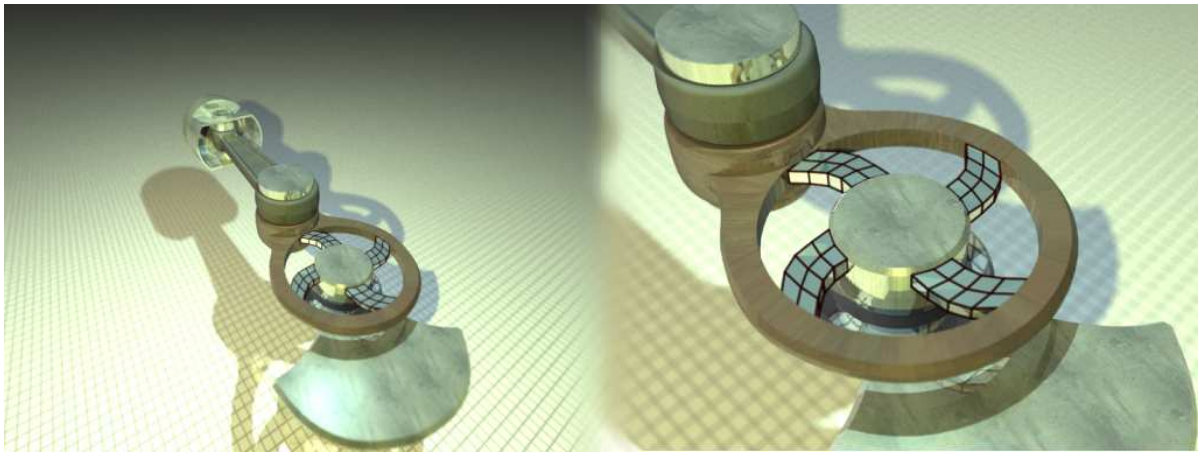

a) b)

Figure 6.47.: deformed configuration $\mathcal{B}_t$ at $t = 19.5$: a) overall view, b) zoom: spokes

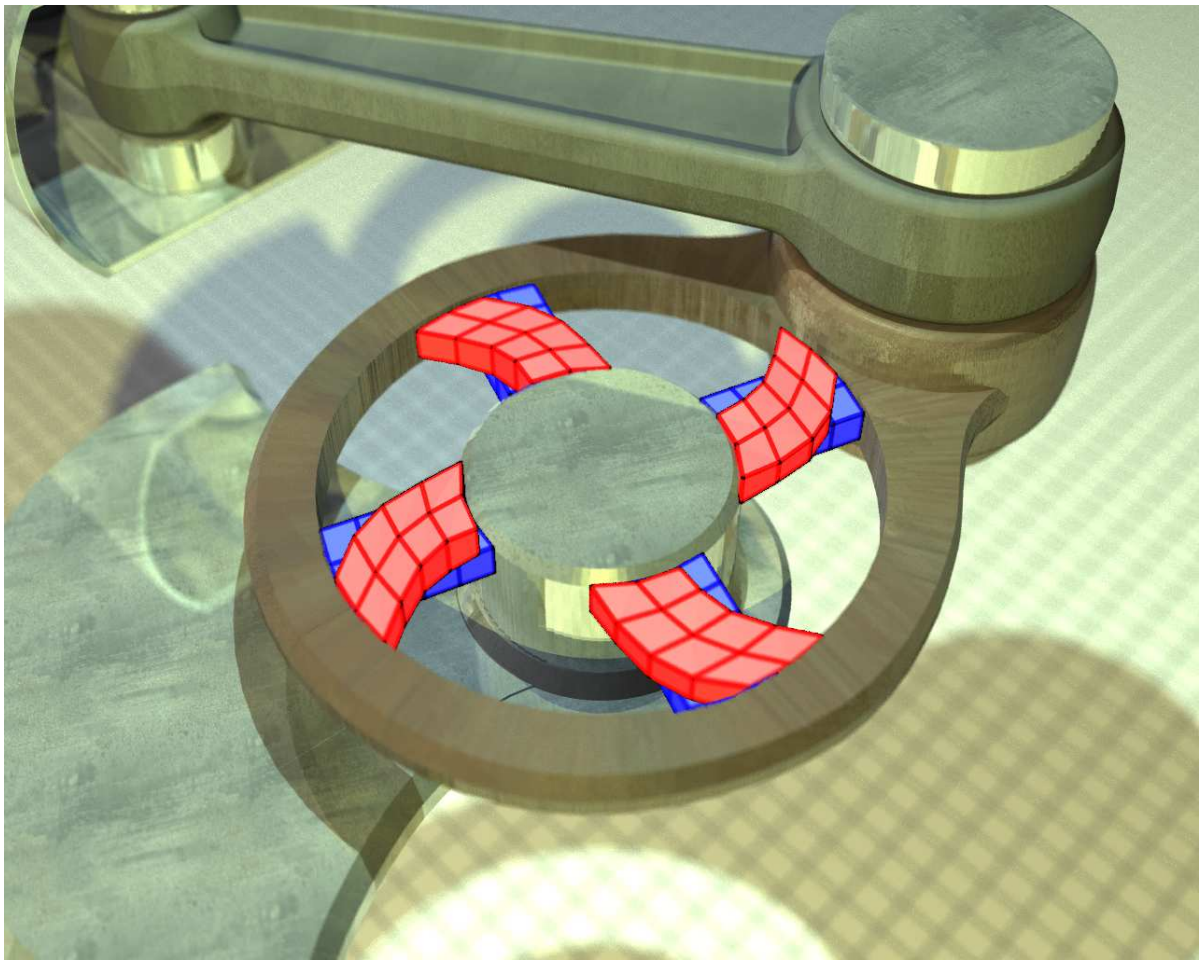

Figure 6.48.: deformed spokes $\mathcal{B}_t^f$ at $t = 1.2$: elastic (blue) vs. plastic (red) case

7. Epilog – Discussion

In this chapter, on the one hand, the main results of the present work will be summarised and discussed and, on the other hand, a brief outlook will be presented, showing potential issues that could be addressed in future investigations.

Essential Results

In the present work, the *completely consistent* time-integration of nonlinear dissipative dynamics, focussing on elasto-plastic deformations, has been investigated extensively. In this context, time FE methods represent a particularly well-suited framework to develop time-stepping schemes which offer pre-defined conservation properties, analogously to the underlying physical model. More precisely, the favoured integrators are able to capture

- the numerically exact fulfilment of involved constraints related to bearings and joints labelled as *kinematic consistency*,
- the algorithmic conservation of the linear as well as of the angular momentum referred to as *mechanical consistency*,
- a conservation of the total energy for elastic deformations respectively a strictly positive dissipation – corresponding to the second law of thermodynamics – in combination with a monotonic decrease of the total energy in the plastic case related to *thermodynamical consistency*,
- and finally a conservation of the sum consisting of the total energy and the (strictly positive) dissipation motivated by the first law of thermodynamics and classified as *energy-consistency*.

Please note, that hereby all essential consistency properties are guaranteed not only at first glance, but even within the calculation accuracy. In fact, it has been demonstrated by means of several representative numerical examples, dealing with structural as well as flexible multibody dynamics, that the favoured concepts render a superior performance compared to standard integration schemes with regard to the physical quality of the

results and also concerning the robustness of the algorithms. In particular, the referred properties qualify the proposed completely consistent integration schemes for long-time simulations. In the following, the essential results of different chapters will be discussed separately.

Friction-element oscillator: Presenting numerical aspects of nonlinear dynamics in a nutshell, the notable influence of (material) nonlinearities on the algorithmic performance of time-stepping schemes has been demonstrated based on a friction-element oscillator. Hereby, the importance of an adequate approximation of involved time-integrals has been pointed out and the performance of different quadrature rules has been discussed.

Fundamental concepts: In the third chapter, a general framework for the consistent time-integration of inelastic continuum dynamics has been presented, using a fully nonlinear theory and an internal variable formulation to model the constitutive behaviour. The discretisation in space as well as in time rely both on a Finite Element approach, whereby concerning the time-integration a continuous Galerkin method has been applied. Analogously to Chapter 2, standard and non-standard quadrature rules have been discussed in detail with regard to the achievable conservation properties. To guarantee mechanical as well as energy-consistency, a specifically designed non-standard quadrature has been introduced based on an 'enhanced algorithmic stress tensor' which can be derived from a constrained optimisation problem. Thereby, it is important to keep in mind that all presented concepts are actually general enough to include also higher-order schemes and to cover various types of inelastic effects.

Elastodynamics: In this chapter, the general concepts of Chapter 3 have been specified to hyperelasticity formulated in principal stretches, using linear Finite Elements in time. Concerning the evaluation of the eigenvalue-based constitutive laws, a well-established and efficient perturbation technique has been applied. Regarding the implementation, several pitfalls occur which have been shown to be directly related to numerical artefacts of the 'stress enhancement', including the oscillating numerical limit transition in general and the coupling of the numerical behaviour and the applied perturbation size in particular. Furthermore, it has been demonstrated that these effects can significantly influence the numerical as well as the mechanical performance of the resulting time integrator, especially, when dealing with small time-step sizes and mechanically stiff problems. Moreover, we have presented the 'mixed strategy' for the evaluation of the 'enhanced algorithmic stresses' as an appropriate remedy for the numerical problems, whereby the effectiveness of the proposed approach has been verified on the local as well as on the global level. Finally, the suggested concept has been tested by means of two representative numerical examples. In this context, it has been shown that the developed strategy allows the claimed efficient and robust time-integration for a wide range of problems, rendering mechanical consistency as well as an algorithmic conservation of

the total energy within the calculation accuracy.

Elasto-plasto-dynamics: Next, the Galerkin-based time-integration of finite elasto-plasto-dynamics has been considered, whereby a multiplicative formulation of large strain plasticity and an eigenvalue-based elastic response have been incorporated. Based on linear time approximations and different quadrature rules, the resulting time-stepping schemes have been combined, as a fundamental example, with a well-established first-order accurate exponential update for finite plasticity, which has been formulated with respect to the intermediate configuration. However, also other local update schemes could be embedded instead without affecting the basic ideas, since we conceptually favour a separate treatment of global and local time-integration. In this context, we have investigated furthermore different integration strategies how to fit the local update into the global framework and the resulting convergence performance of each option has been discussed as well. To demonstrate the excellent performance of the proposed algorithms, several numerical examples have been presented, including a comparison to selected customary integrators that have been originally designed for linear structural dynamics. Thereby, it has been clearly confirmed that especially the completely consistent scheme based on the so-called elasto-plastic enhanced algorithmic stress tensor – referred to as 'ECMC-cG method' – is particularly well-suited to simulate stiff and non-stiff problems, dealing even with huge plastic deformations. In fact, global energy-consistency is guaranteed by the proposed method in a 'numerically exact manner' which implies a fulfilment of the discrete balance of the augmented Hamiltonian in the range of the calculation accuracy. In total, the advocated scheme is able to manage systems with different mechanical stiffnesses, it is robust concerning changes of the time-step size, and it respects fundamental principles of the underlying physical model.

Elasto-plastic multibody dynamics: In a last step, the scope has been extended to constrained dissipative dynamics in general and elasto-plastic multibody systems in particular. In contrast to classical approaches in the multibody dynamics community, the modelling of the inelastic flexible parts relies hereby on a fully nonlinear continuum theory and a subsequent Finite Element discretisation in space, as discussed in Chapter 3. Moreover, the actual constitutive modelling of the elasto-plastic material behaviour is identical to the concepts of Chapter 5, so that the present approach is indeed able to cover finite deformations as well as large strains. Even if the formulation of the flexible parts has already been discussed extensively in other chapters, the incorporation of constraints leads to various additional issues, resulting in a set of differential algebraic equations. To integrate this system consistently in time, the previously discussed continuous Galerkin method of the unconstrained case has been adequately extended to the mixed Galerkin method for constrained systems, using a formulation based on Lagrange multipliers. To model multibody systems, rigid bodies have been taken into account, whereby we have favoured a rotationless formulation which is beneficial with regard to the claimed consistent integration but additionally involves internal constraints due to

requirements of rigidity. In addition to these internal constraints, the coupling of rigid and flexible parts as well as the modelling of bearings and joints has given rise to further constraints, referred to as coupling and external constraints respectively. Once more, the general concepts have been specified finally to one particular time-stepping for finite elasto-plastic multibody dynamics, using on the global level linear shape functions in time combined with properly chosen quadrature rules. For the local integration, we have applied again the exponential update as a kind of benchmark example. Finally, the performance of the algorithm has been investigated by means of four numerical examples, considering free flight as well as bounded motions. In all cases, it has been shown that the resulting integrator indeed guarantees a completely consistent time-integration which includes: the numerically exact fulfilment of all involved constraints, the conservation of both momentum maps, a strictly positive dissipation as well as the corresponding monotonic decrease of the total energy, and also the conservation of the augmented Hamiltonian.

Future Perspectives

In the following, we briefly address some issues that might be of interest for future investigations. In this context, the open aspects have been classified in three categories which represent essential steps during a typical simulation process, namely: modelling, discretisation, and evaluation.

Modelling: In the present contribution, a widespread isotropic plasticity model has been applied, focussing on the time-integration of the obtained equations of motion. However, the conceptual uncoupling between global and local level also allows to incorporate *other types of plasticity*, considering for instance non-associated or anisotropic plasticity models. Even *other dissipation effects* that rely on an internal variable concept – like e.g. visco-elasticity, visco-plasticity, or fatigue effects – could be treated similarly due to the generality of the proposed formulation.

Discretisation: Without question, one of the most important tasks for future work is the consideration of *higher-order local update algorithms* to circumvent any order reduction of the global scheme in the plastic case. In fact, the entire potential of the here presented framework for a consistent time-integration can only be exploited, when also local schemes of theoretically arbitrary order are available. Possibly, one interesting approach could be for instance the design of Galerkin-based local updates, dealing however with inequality constraints. A further important issue could be the option to include additionally a controllable type of *numerical dissipation*, which might be useful for certain applications. Please note, that a completely consistent algorithm also represents for this case an optimal point of departure. Moreover, the numerical treatment of *plastic incompressibility* should be addressed in following projects to avoid locking effects, whereby

the applied formulation should be chosen carefully and potential consequences for the consistency of the time-integration scheme have to be taken into account. Finally, the investigation of adequate concepts to *adapt the time-step size* – on the global or possibly on the local level corresponding to the discussed 'modified integration strategy' – seems to be an interesting aspect, especially with regard to computational efficiency.

Evaluation: In each chapter of the present contribution, special emphasis has been placed on the validation of the proposed algorithms by means of several numerical examples which have clearly confirmed the excellent performance of the advocated integration schemes. Nevertheless, there are still important aspects that should be investigated in more detail. At first, the *computational costs*, which are slightly higher for the consistent scheme in comparison to standard integrators, should be fairly evaluated based on some benchmark computations. Secondly, it would be certainly interesting to investigate in a next step the benefit of the proposed concepts based on *real-world applications*, where also experimental data are available.

A. Energy-Consistency

In the following, a detailed investigation of the algorithmic energy-consistency properties of the proposed Galerkin-based integrators for nonlinear dynamics will be presented, covering a huge family of dissipative models that essentially rely on a formulation based on internal variables. In this context, the fundamental equations of Section 3.3.3 will be derived step by step, including various additional aspects. The present chapter is hereby structured as follows:

- Firstly, a global condition for energy-consistency is derived in Section A.1, referring directly to results of the semidiscrete case. Thereby, the resulting global condition (3.60) basically represents a restriction for the approximation of the time-integrated internal load vector, motivating the design of adequate non-standard quadrature rules.
- Subsequently, this global condition is transferred in Section A.2 to the equivalent local statement (3.61) which has to be satisfied by the involved (time-integrated) stresses, encouraging the introduction of the specific non-standard quadrature rule (3.47) based on an appropriate algorithmic modification of the stress tensor.
- Finally, it is demonstrated in Section A.3 that the abovementioned local condition for energy-consistency is indeed satisfied by means of the particularly designed enhanced algorithmic stress tensor (3.51).

Consequently, the present chapter confirms in detail the qualification of the proposed non-standard quadrature rule (3.47) based on the enhanced algorithmic stress tensor (3.51) concerning the guarantee of algorithmic energy-consistency related to Equation (3.62).

A.1. Global Condition

For the purpose of a completely consistent time-integration, the developed time FE methods have to fulfil a global energy-consistency condition related to the conservation of the augmented Hamiltonian $\widetilde{H}$, according to the semidiscrete case (3.34). As mentioned above, we start with the development of this global condition, representing

a criterion for the approximation of a corresponding time-integral. According to the procedure proposed in Betsch and Steinmann [26] for elastic material behaviour, the point of departure is constituted by the general form of discrete equations of motion as given in Equation (3.41). Additionally, the vectors $\widetilde{\bar{\boldsymbol{z}}}_i$ for $i = 1, ..., k$ are introduced, consisting of linear combinations of the known vectors $\bar{\boldsymbol{z}}_j = [\bar{\boldsymbol{q}}_j, \bar{\boldsymbol{p}}_j]^{\mathrm{t}}$ at the time nodes $j = 1, ..., k+1$. After scalar-multiplication with $\mathbb{J} \cdot \widetilde{\bar{\boldsymbol{z}}}_i$ and subsequent summation over $i = 1, ..., k$, we obtain

$$\sum_{i=1}^{k} \sum_{j=1}^{k+1} \int_0^1 \widetilde{M}_i M_j^{'} \, \mathrm{d}\alpha \; \bar{\boldsymbol{z}}_j \cdot \left[\mathbb{J} \cdot \widetilde{\bar{\boldsymbol{z}}}_i \right] - h_n \int_0^1 \widetilde{M}_i \, \nabla_{\bar{\boldsymbol{z}}} \, H(\bar{\boldsymbol{z}}^h; \boldsymbol{\kappa}) \, \mathrm{d}\alpha \cdot \left[\mathbb{J}^{\mathrm{t}} \cdot \mathbb{J} \right] \cdot \widetilde{\bar{\boldsymbol{z}}}_i = 0 \,. \quad \text{(A.1)}$$

Taking additionally the equivalence relation $\sum_{i=1}^{k} \widetilde{M}_i \widetilde{\bar{\boldsymbol{z}}}_i = \sum_{i=1}^{k+1} M_i^{'} \bar{\boldsymbol{z}}_i$ into account, Equation (A.1) can be reformulated as

$$\sum_{i,j=1}^{k+1} \int_0^1 M_i^{'} M_j^{'} \, \mathrm{d}\alpha \; \bar{\boldsymbol{z}}_j \cdot \left[\mathbb{J} \cdot \bar{\boldsymbol{z}}_i \right] - h_n \int_0^1 M_i^{'} \, \nabla_{\bar{\boldsymbol{z}}} \, H(\bar{\boldsymbol{z}}^h; \boldsymbol{\kappa}) \, \mathrm{d}\alpha \cdot \left[\mathbb{J}^{\mathrm{t}} \cdot \mathbb{J} \right] \cdot \bar{\boldsymbol{z}}_i = 0 \,. \quad \text{(A.2)}$$

Next, by making use of the skew-symmetry of $\mathbb{J}$ defined in Equation (3.21) and the time-approximations of $\bar{\boldsymbol{z}}^h$ corresponding to Equation (3.39), the first part of Equation (A.2) results in

$$\sum_{i,j=1}^{k+1} \int_0^1 M_i^{'} M_j^{'} \, \mathrm{d}\alpha \; \bar{\boldsymbol{z}}_j \cdot \left[\mathbb{J} \cdot \bar{\boldsymbol{z}}_i \right] = \int_0^1 \mathrm{D}_\alpha \bar{\boldsymbol{z}}^h \cdot \mathbb{J} \cdot \mathrm{D}_\alpha \bar{\boldsymbol{z}}^h \, \mathrm{d}\alpha = 0 \,. \quad \text{(A.3)}$$

Moreover, orthogonality of the (symplectic) matrix $\mathbb{J}^{\mathrm{t}} = \mathbb{J}^{-1}$ yields for the second part of Equation (A.2)

$$\sum_{i=1}^{k+1} \int_0^1 M_i^{'} \, \nabla_{\bar{\boldsymbol{z}}} \, H(\bar{\boldsymbol{z}}^h; \boldsymbol{\kappa}) \, \mathrm{d}\alpha \cdot \bar{\boldsymbol{z}}_i = 0 \,. \quad \text{(A.4)}$$

It is important to emphasise that Equation (A.4) is naturally given by the applied time discretisation procedure of the semidiscrete system of equations by means of a cG(k)-method. According to Equations (3.41), Equation (A.4) can be specified via

$$\sum_{i=1}^{k+1} \int_0^1 M_i^{'} \, \bar{\boldsymbol{F}}^{int \, h} \, \mathrm{d}\alpha \cdot \bar{\boldsymbol{q}}_i + \int_0^1 M_i^{'} \, \mathbb{M}^{-1} \cdot \bar{\boldsymbol{p}}^h \, \mathrm{d}\alpha \cdot \bar{\boldsymbol{p}}_i = 0 \,, \quad \text{(A.5)}$$

representing the time-integrated and time-approximated version of the semidiscrete Equation (3.32). So far, the investigations are technically identical to the purely elastic case due to the unchanged global structure of the underlying equations of motion, which have been used as starting point for the foregoing derivation. Nevertheless, dissipation

effects come inherently into play when Equation (A.5) is next linked to the corresponding (total) energy balance based on the semidiscrete Equation (3.31). Once more, a time-integration of Equation (3.31) and the incorporation of the approximations (3.39) renders straightforwardly the related time-approximated statement

$$H_{\alpha=1} - H_{\alpha=0} + \Delta D \stackrel{!}{=} \sum_{i=1}^{k+1} \int_0^1 M_i' \, \bar{\boldsymbol{F}}^{int\,h} \, \mathrm{d}\alpha \cdot \bar{\boldsymbol{q}}_i + \int_0^1 M_i' \, \mathbb{M}^{-1} \cdot \bar{\boldsymbol{p}}^h \, \mathrm{d}\alpha \cdot \bar{\boldsymbol{p}}_i \,, \qquad \text{(A.6)}$$

wherein the calculation of the involved time-integrals still has to be specified. However, please keep in mind that the discrete energy balance (A.6) solely holds if each integral is calculated exactly. By using the fundamental theorem of calculus and taking the (inverse) chain rule into account, we obtain

$$\sum_{i=1}^{k+1} \int_0^1 M_i' \, \mathbb{M}^{-1} \cdot \bar{\boldsymbol{p}}^h \, \mathrm{d}\alpha \cdot \bar{\boldsymbol{p}}_i = \int_0^1 \mathrm{D}_\alpha K \, \mathrm{d}\alpha = K_{\alpha=1} - K_{\alpha=0} \qquad \text{(A.7)}$$

based on the derivative $\mathrm{D}_\alpha \bar{\boldsymbol{p}}^h = \sum_{i=1}^{k+1} M_i' \, \bar{\boldsymbol{p}}_i$. Thus, the last part in Equation (A.6) captures indeed the correct increment of the kinetic energy K. Nevertheless, the time integral which includes the internal load vector has to be approximated by an appropriate quadrature rule, as already discussed in Section 3.3.2. By inserting Equation (A.7) into Equation (A.6), we obtain directly the (reduced) global condition

$$\sum_{i=1}^{k+1} \int_0^1 M_i' \, \bar{\boldsymbol{F}}^{int\,h} \, \mathrm{d}\alpha \cdot \bar{\boldsymbol{q}}_i \stackrel{!}{=} \Psi_{\alpha=1} - \Psi_{\alpha=0} + \Delta D \,, \qquad \text{(A.8)}$$

which has to be fulfilled by the applied quadrature rule concerning the guarantee of energy-consistency in the completely discrete setting. Since in general the condition (A.8) will not be satisfied by a standard quadrature rule, however, it defines a proper criterion for the design of adequate non-standard quadrature rules.

A.2. Global vs. Local Condition

In this section, the global condition (A.8) will be reduced to a local statement which has to be fulfilled by means of the involved (time-integrated) stresses, involving some derivation-steps from the overall requirement to a demand for each spatial integration point. In this context, it will be shown that the resulting local condition actually represents a discrete version of the constraint (3.49) that has been used to design the energy-consistent-enhanced algorithmic stress tensor (3.51). Based on the definition of the global vectors $\bar{\boldsymbol{F}}^{int\,h} := [\boldsymbol{F}_1^{int\,h}, ..., \boldsymbol{F}_{n_{node}}^{int\,h}]^{\mathrm{t}}$ and $\bar{\boldsymbol{q}}_i := [\boldsymbol{q}_1^i, ..., \boldsymbol{q}_{n_{node}}^i]^{\mathrm{t}}$ respectively,

Equation (A.8) can, together with Equation (3.42), be represented as

$$\sum_{I,J=1}^{n_{node}} \int_0^1 \left[\int_{\mathcal{B}_0} [\nabla_{\boldsymbol{X}} N_I \otimes \nabla_{\boldsymbol{X}} N_J] : \boldsymbol{S}(\alpha)\, \mathrm{d}V\, \boldsymbol{q}_J^h(\alpha) \right] \cdot \sum_{i=1}^{k+1} M_i^{'}(\alpha)\, \boldsymbol{q}_I^i \, \mathrm{d}\alpha$$
$$\stackrel{!}{=} \Psi_{\alpha=1} - \Psi_{\alpha=0} + \Delta D\,, \tag{A.9}$$

wherein the time-derivatives of the shape functions $M_i^{'}(\alpha)$ as well as the time-approximated coordinate-vector $\boldsymbol{q}_J^h(\alpha)$ at the spatial node J are only functions of the (reference-) time α. Hence, Equation (A.9) can be rewritten by changing summation and integration, yielding

$$\int_0^1 \int_{\mathcal{B}_0} \sum_{I,J=1}^{n_{node}} [\nabla_{\boldsymbol{X}} N_I \otimes \nabla_{\boldsymbol{X}} N_J] : \boldsymbol{S}(\alpha) \left[\boldsymbol{q}_J^h(\alpha) \cdot \sum_{i=1}^{k+1} M_i^{'}(\alpha)\, \boldsymbol{q}_I^i \right] \mathrm{d}V\, \mathrm{d}\alpha$$
$$\stackrel{!}{=} \Psi_{\alpha=1} - \Psi_{\alpha=0} + \Delta D\,. \tag{A.10}$$

Using furthermore the free energy Ψ and the (global) accumulated dissipation D results in

$$\int_{\mathcal{B}_0} \int_0^1 \sum_{I,J=1}^{n_{node}} [\nabla_{\boldsymbol{X}} N_I \otimes \nabla_{\boldsymbol{X}} N_J] : \boldsymbol{S}(\alpha) \left[\boldsymbol{q}_J^h(\alpha) \cdot \sum_{i=1}^{k+1} M_i^{'}(\alpha)\, \boldsymbol{q}_I^i \right] \mathrm{d}\alpha\, \mathrm{d}V$$
$$\stackrel{!}{=} \int_{\mathcal{B}_0} \left[\psi_{\alpha=1} - \psi_{\alpha=0} + \int_0^1 \mathcal{D}\, \mathrm{d}\alpha \right] \mathrm{d}V\,. \tag{A.11}$$

Applying a quadrature rule in space and enforcing condition (A.11) at the corresponding integration points, we directly obtain the condition in a local format

$$\int_0^1 \sum_{I,J=1}^{n_{node}} [\nabla_{\boldsymbol{X}} N_I \otimes \nabla_{\boldsymbol{X}} N_J] : \boldsymbol{S}(\alpha) \left[\boldsymbol{q}_J^h(\alpha) \cdot \sum_{i=1}^{k+1} M_i^{'}(\alpha)\, \boldsymbol{q}_I^i \right] \mathrm{d}\alpha$$
$$\stackrel{!}{=} \psi_{\alpha=1} - \psi_{\alpha=0} + \int_0^1 \mathcal{D}\, \mathrm{d}\alpha\,, \tag{A.12}$$

which has to be fulfilled at each spatial Gaussian integration point. Incorporating additionally an adequate quadrature rule for each time-integral in Equation (A.12) yields, together with $\mathrm{D}_\alpha \boldsymbol{q}_I^h(\alpha) = \sum_{i=1}^{k+1} M_i^{'}(\alpha)\, \boldsymbol{q}_I^i$, the relation

$$\sum_{l=1}^{n_{gp_{t1}}} \boldsymbol{S}(\zeta_l) : \sum_{I,J=1}^{n_{node}} [\nabla_{\boldsymbol{X}} N_I \otimes \nabla_{\boldsymbol{X}} N_J] \, [\boldsymbol{q}_J^h(\zeta_l) \cdot \mathrm{D}_\alpha \boldsymbol{q}_I^h(\zeta_l)]\, w_l$$
$$\stackrel{!}{=} \psi_{\alpha=1} - \psi_{\alpha=0} + \sum_{m=1}^{n_{gp_{t2}}} \mathcal{D}(\zeta_m)\, w_m \tag{A.13}$$

with an adequate number of integration points in time $n_{gp_{t1}}$ and $n_{gp_{t2}}$ respectively. If the approximation of the right Cauchy-Green tensor $\boldsymbol{C}$ given by Equation (3.44) and the (inverse) chain rule are taken into account, Equation (A.13) renders

$$\psi_{\alpha=1} - \psi_{\alpha=0} + \sum_{m=1}^{n_{gp_{t2}}} \mathcal{D}(\zeta_m)\, w_m \stackrel{!}{=} \sum_{l=1}^{n_{gp_{t1}}} \boldsymbol{S}(\zeta_l) : \frac{1}{2}\mathrm{D}_\alpha \boldsymbol{C}(\zeta_l)\, w_l \,, \tag{A.14}$$

that can be interpreted as a local condition for energy-consistency which must be fulfilled at each spatial integration point. Hereby, Equation (A.14) represents obviously a fully discrete version of the constraint (3.49) that has been used in Section 3.3.2 to obtain the enhanced algorithmic stress tensor (3.51). Consequently, the local condition (A.14) is indeed fulfilled by design when the algorithmic stresses $\boldsymbol{S}^{alg}$ are incorporated, as demonstrated more detailed in Section A.3. Consequently, the global condition for energy-consistency (A.8) holds as well, when the internal load vector is calculated based on $\boldsymbol{S}^{alg}$, defining exactly the non-standard quadrature rule (3.47). Including additionally Equation (A.7), it hence follows based on Equation (A.5) the relation

$$K_{\alpha=1} - K_{\alpha=0} + \Psi_{\alpha=1} - \Psi_{\alpha=0} + \Delta D = 0 \,, \tag{A.15}$$

according to the above derivation. Based on the definition of the augmented Hamiltonian $\widetilde{H}$, one finally gets the (global) energy-consistency for the completely discrete system

$$\widetilde{H}_{\alpha=1} - \widetilde{H}_{\alpha=0} = 0 \tag{A.16}$$

in analogy to the semidiscrete case (3.34).

Remark A.1: For the foregoing derivation, the number of integration points in time $n_{gp_{ti}}$ has initially not been restricted. Nevertheless, please recall that the respective number of time integration points is directly influenced by the demanded collocation property of the cG(k)-method, involving $n_{gp_{t1}} = k$. Basically, the approximation of the dissipation integral is independent from the global level due to the local character of the underlying internal variable formulation, being linked to the equations of motion only implicitly via the stresses. Consequently, the corresponding number of integration points $n_{gp_{t2}}$ is allowed to differ from $n_{gp_{t1}}$, even if order-consistency requires $n_{gp_{t1}} = k = n_{gp_{t2}}$, compare also Remark 3.4.

A.3. Local Condition

In Equation (3.51), the so-called energy-consistent-enhanced algorithmic stress tensor $\boldsymbol{S}^{alg}$ has been introduced, being in accordance with the constraint (3.49). Moreover, it has been discussed in Section A.2 that the fulfilment of the local condition (A.14), related to a discrete format of the constraint (3.49), renders indeed the desired global energy-consistency of the Galerkin-based time-stepping schemes. Finally, we demonstrate more

detailed in the following that the proposed enhanced algorithmic stress tensor $\boldsymbol{S}^{alg}$ fulfils indeed this prior constraint, independently of the applied polynomial degree.

General case

First, the general case based on a cG(k)-method with an arbitrary polynomial degree k for the involved time-approximations is considered. Starting with the discrete constraint (3.49), equivalent to the local condition (A.14), it should hold

$$\psi_{\alpha=1} - \psi_{\alpha=0} + \sum_{m=1}^{n_{gp_{t2}}} \mathcal{D}(\zeta_m)\, w_m - \sum_{l=1}^{n_{gp_{t1}}} \boldsymbol{S}^{alg}(\zeta_l) : \frac{1}{2}\mathrm{D}_\alpha \boldsymbol{C}(\zeta_l)\, w_l \stackrel{!}{=} 0 \tag{A.17}$$

based on the particularly designed algorithmic stress tensor, wherein once more the integration points for the underlying one-dimensional time-domain are denoted by ζ_l, ζ_m and w_l, w_m represent the corresponding weights of the quadrature rule. It is important to highlight the difference between the assumed strain approximation in time $\boldsymbol{C}^h(\alpha)$ introduced in Equation (3.45) and a cG-approximation of the right Cauchy-Green tensor $\boldsymbol{C}(\alpha)$ based on Equation (3.44), involving time approximations of the nodal coordinates $\bar{\boldsymbol{q}}^h := [\boldsymbol{q}_1^h, ..., \boldsymbol{q}_{n_{node}}^h]^{\mathrm{t}}$. Consequently, it has to be distinguished as well between a time-derivative of the assumed strain approximation $\mathrm{D}_\alpha \boldsymbol{C}^h$, rendering

$$\boldsymbol{C}^h(\alpha) = \sum_{i=1}^{k+1} M_i(\alpha)\, \boldsymbol{C}_i \Rightarrow \mathrm{D}_\alpha \boldsymbol{C}^h = \mathrm{D}_\alpha \boldsymbol{C}^h(M_i'(\alpha), \boldsymbol{C}_i) \tag{A.18}$$

and a time-derivative of the cG-approximation $\mathrm{D}_\alpha \boldsymbol{C}$, involving

$$\begin{aligned} \boldsymbol{C}(\alpha) &= \sum_{I,J=1}^{n_{node}} \boldsymbol{q}_I^h(\alpha) \cdot \boldsymbol{q}_J^h(\alpha)\, \nabla_{\boldsymbol{X}} N_I \otimes \nabla_{\boldsymbol{X}} N_J \\ \Rightarrow \mathrm{D}_\alpha \boldsymbol{C} &= \mathrm{D}_\alpha \boldsymbol{C}(\boldsymbol{q}_{I,J}^h(\alpha), \mathrm{D}_\alpha \boldsymbol{q}_{I,J}^h(\alpha))\,. \end{aligned} \tag{A.19}$$

For subsequent elaborations, it is absolutely necessary to apply the appropriate approximation in time of the right Cauchy-Green tensor. As already mentioned in Section 3.3.2, an assumed strain approximation $\boldsymbol{C}^h(\alpha)$ should be used with respect to objectivity requirements for stress evaluations as well as for the directional part of $\boldsymbol{S}^{alg}$. Regarding other approximations, use of the cG-approximation $\boldsymbol{C}(\alpha)$ has to be made regarding the essential step from the global to a local condition for energy-consistency, represented by Equation (A.13) and Equation (A.14) respectively. Consequently, this approximation strategy involves also a mixed term in the denominator of the scalar-valued scaling factor of $\boldsymbol{S}^{alg}$. Inserting the algorithmic stress tensor (3.51) – including a quadrature rule for the involved time-integrals – in Equation (A.17), it follows together with Equations

(A.18), (A.19)

$$\begin{aligned}
&\psi_{\alpha=1} - \psi_{\alpha=0} + \sum_{m=1}^{n_{gp_{t2}}} \mathcal{D}(\zeta_m)\, w_m - \sum_{l=1}^{n_{gp_{t1}}} \left[\boldsymbol{S}(\boldsymbol{C}^h(\zeta_l), \boldsymbol{\kappa}_l) : \frac{1}{2} \mathrm{D}_\alpha \boldsymbol{C}(\zeta_l) \right] w_l \\
- &\sum_{l=1}^{n_{gp_{t1}}} \left[2 \frac{\psi_{\alpha=1} - \psi_{\alpha=0} + \sum_{n=1}^{n_{gp_{t2}}} \mathcal{D}(\zeta_n)\, w_n}{\sum_{p=1}^{n_{gp_{t1}}} [\sum_{c=1}^{k+1} M_c'(\zeta_p) \boldsymbol{C}_c] : \mathrm{D}_\alpha \boldsymbol{C}(\zeta_p)\, w_p} \sum_{e=1}^{k+1} M_e'(\zeta_l) \boldsymbol{C}_e : \frac{1}{2} \mathrm{D}_\alpha \boldsymbol{C}(\zeta_l) \right] w_l \\
+ &\sum_{l=1}^{n_{gp_{t1}}} \left[2 \frac{\sum_{o=1}^{n_{gp_{t1}}} [\boldsymbol{S}(\boldsymbol{C}^h(\zeta_o), \boldsymbol{\kappa}_o) : \frac{1}{2} \mathrm{D}_\alpha \boldsymbol{C}(\zeta_o)]\, w_o}{\sum_{p=1}^{n_{gp_{t1}}} [\sum_{c=1}^{k+1} M_c'(\zeta_p) \boldsymbol{C}_c] : \mathrm{D}_\alpha \boldsymbol{C}(\zeta_p)\, w_p} \sum_{e=1}^{k+1} M_e'(\zeta_l) \boldsymbol{C}_e : \frac{1}{2} \mathrm{D}_\alpha \boldsymbol{C}(\zeta_l) \right] w_l \stackrel{!}{=} 0\,.
\end{aligned} \tag{A.20}$$

Obviously, Equation (A.20) can be reduced to

$$\begin{aligned}
&\psi_{\alpha=1} - \psi_{\alpha=0} + \sum_{m=1}^{n_{gp_{t2}}} \mathcal{D}(\zeta_m)\, w_m - \sum_{l=1}^{n_{gp_{t1}}} \left[\boldsymbol{S}(\boldsymbol{C}^h(\zeta_l), \boldsymbol{\kappa}_l) : \frac{1}{2} \mathrm{D}_\alpha \boldsymbol{C}(\zeta_l) \right] w_l \\
- &\psi_{\alpha=1} + \psi_{\alpha=0} - \sum_{n=1}^{n_{gp_{t2}}} \mathcal{D}(\zeta_n)\, w_n + \sum_{o=1}^{n_{gp_{t1}}} \left[\boldsymbol{S}(\boldsymbol{C}^h(\zeta_o), \boldsymbol{\kappa}_o) : \frac{1}{2} \mathrm{D}_\alpha \boldsymbol{C}(\zeta_o) \right] w_o = 0\,.
\end{aligned} \tag{A.21}$$

As demonstrated above, the constraint (3.49), related to the local energy-consistency condition (A.14), is fulfilled in general by making use of the energy-consistent-enhanced algorithmic stress tensor $\boldsymbol{S}^{alg}$, demanding a consistent approximation in time of $\boldsymbol{C}$ and adequate quadrature rules.

Linear case

Since especially linear time approximations are of particular significance, the foregoing general equations will be specified in this section to linear Finite Elements in time corresponding to $k = 1$, involving one Gaussian integration point in time with $\zeta = 1/2$ and $w = 1$. Consequently, the general condition (A.17) can be written as

$$\psi_{\alpha=1} - \psi_{\alpha=0} + \Delta d - \frac{1}{2} \boldsymbol{S}^{alg}(1/2) : [\boldsymbol{C}_2 - \boldsymbol{C}_1] \stackrel{!}{=} 0\,, \tag{A.22}$$

wherein this time the local dissipation increment has been abbreviated by Δd, corresponding also to Equation (5.30). Once more, the distinction between the assumed strain approximation in time

$$\boldsymbol{C}^h(\alpha) = [\boldsymbol{C}_2 - \boldsymbol{C}_1]\alpha + \boldsymbol{C}_1 \tag{A.23}$$

and the cG(1)-approximation of the right Cauchy-Green tensor

$$\boldsymbol{C}(\alpha) = \sum_{I,J=1}^{n_{node}} \left[[\boldsymbol{q}_I^2 - \boldsymbol{q}_I^1]\alpha + \boldsymbol{q}_I^1 \right] \cdot \left[[\boldsymbol{q}_J^2 - \boldsymbol{q}_J^1]\alpha + \boldsymbol{q}_J^1 \right] \nabla_{\boldsymbol{X}} N_I \otimes \nabla_{\boldsymbol{X}} N_J \tag{A.24}$$

is taken into account. Introducing the difference $\Delta \boldsymbol{q}_I := \boldsymbol{q}_I^2 - \boldsymbol{q}_I^1$ between the position of a spatial node I at the time nodes 1 ($\alpha = 0$) and 2 ($\alpha = 1$), the time-derivatives of the approximations (A.23), (A.24) yield

$$\begin{aligned} \mathrm{D}_\alpha \boldsymbol{C}^h &= \boldsymbol{C}_2 - \boldsymbol{C}_1 && \text{(A.25)} \\ \mathrm{D}_\alpha \boldsymbol{C} &= 2\,\mathbb{I}^{sym} : \sum_{I,J=1}^{n_{node}} \nabla_{\boldsymbol{X}} N_I \otimes \nabla_{\boldsymbol{X}} N_J \, [\boldsymbol{q}_J^h \cdot \Delta \boldsymbol{q}_I] \,. && \text{(A.26)} \end{aligned}$$

When additionally evaluating Equation (A.26) at the midpoint in time $\alpha = 1/2$, corresponding to one Gaussian integration point, it follows directly

$$\mathrm{D}_\alpha \boldsymbol{C}^h(1/2) = \boldsymbol{C}_2 - \boldsymbol{C}_1 = \mathrm{D}_\alpha \boldsymbol{C}(1/2) \,. \tag{A.27}$$

Consequently, there is no difference between both time-derivatives $\mathrm{D}_\alpha \boldsymbol{C}^h$ and $\mathrm{D}_\alpha \boldsymbol{C}$, respectively, if linear Finite Elements in time are applied and $\mathrm{D}_\alpha \boldsymbol{C}(\alpha)$ is evaluated at the midpoint. Reducing the general relation (A.20) to the linear case renders

$$\begin{aligned} & \psi_{\alpha=1} - \psi_{\alpha=0} + \Delta d - \boldsymbol{S}(\boldsymbol{C}^h(1/2), \boldsymbol{\kappa}_{1/2}) : \frac{1}{2}[\boldsymbol{C}_2 - \boldsymbol{C}_1] \\ - \; & \frac{\psi_{\alpha=1} - \psi_{\alpha=0} + \Delta d}{[\boldsymbol{C}_2 - \boldsymbol{C}_1] : [\boldsymbol{C}_2 - \boldsymbol{C}_1]} \, [\boldsymbol{C}_2 - \boldsymbol{C}_1] : [\boldsymbol{C}_2 - \boldsymbol{C}_1] \\ + \; & \frac{\boldsymbol{S}(\boldsymbol{C}^h(1/2), \boldsymbol{\kappa}_{1/2}) : \frac{1}{2}[\boldsymbol{C}_2 - \boldsymbol{C}_1]}{[\boldsymbol{C}_2 - \boldsymbol{C}_1] : [\boldsymbol{C}_2 - \boldsymbol{C}_1]} \, [\boldsymbol{C}_2 - \boldsymbol{C}_1] : [\boldsymbol{C}_2 - \boldsymbol{C}_1] \stackrel{!}{=} 0 \,. \end{aligned} \tag{A.28}$$

Obviously, Equation (A.28) also follows directly from the local energy-consistency condition (A.22) by inserting $\boldsymbol{S}^{alg}$ of the linear case, compare also Equation (5.26). By straightforward calculation, we finally obtain

$$\begin{aligned} & \psi_{\alpha=1} - \psi_{\alpha=0} + \Delta d - \boldsymbol{S}(\boldsymbol{C}^h(1/2), \boldsymbol{\kappa}_{1/2}) : \frac{1}{2}[\boldsymbol{C}_2 - \boldsymbol{C}_1] \\ - \; & \psi_{\alpha=1} + \psi_{\alpha=0} - \Delta d + \boldsymbol{S}(\boldsymbol{C}^h(1/2), \boldsymbol{\kappa}_{1/2}) : \frac{1}{2}[\boldsymbol{C}_2 - \boldsymbol{C}_1] = 0 \end{aligned} \tag{A.29}$$

and, hence, it has been shown also for the special case $k = 1$ that the fulfilment of the local energy-consistency condition is indeed guaranteed by means of the energy-consistent-enhanced algorithmic stress tensor $\boldsymbol{S}^{alg}$.

B. Challenges in Visualisation

In the foregoing chapters, all essential ingredients for a completely consistent time-integration have been presented in detail and investigated extensively. Next, we demonstrate that the applied numerical concepts involve furthermore interesting visualisation tasks, enabling possibly a better understanding of the specific algorithms [1].

B.1. Motivation

To obtain a completely consistent time-integration, the essential step has been the introduction of adequate non-standard quadrature rules which basically enable the algorithmic fulfilment of the physically motivated energy balance. In this context, the crucial difference between the standard Gauss and the more sophisticated non-standard quadrature rule is directly related to the tensor-valued difference between the standard stresses of the continuum model and the algorithmic stresses used in the discrete setting. Hereby, a very interesting aspect is the spatial distribution of the corresponding difference tensor field. Indeed, such a comparison between both tensor fields could probably provide a deeper insight into the numerical behaviour of the related time-stepping schemes. In this regard, important issues are for instance: the correlation between the corrections and the underlying deformation, the influence of the time-step size and the material properties, the evolution of the corrections in time, or the existence of characteristic patterns within the difference tensor field. Dealing with two different tensor fields and possibly a large number of time steps, a satisfying visualisation is in general a non-trivial task. Moreover, an additional difficulty for the specific problem at hand is constituted by the fact that a direct physical interpretation of the stress enhancement and the algorithmic stress tensor, respectively, is not valid, compare also Remark 5.4.1. Focussing on the purely elastic case discussed in Chapter 4 and applying linear Finite Elements in time, we aim in the following at a visualisation of the differences between the algorithmic stress tensor $\boldsymbol{S}^{alg}(1/2)$ given by Equation (4.27) and the continuum stress field $\boldsymbol{S}(1/2)$ to investigate the nature of the corrections, as also discussed in Mohr *et al.* [134].

[1] The presented results are part of an interdisciplinary collaboration with the 'Computer Graphics Group' of the University of Kaiserslautern within the International Research Training Group 1131 'Visualisation of Large and Unstructured Data Sets. Applications in Geospatial Planning, Modeling, and Engineering' founded by the German Research Foundation DFG, see Mohr *et al.* [133].

B.2. Comparative Tensor Visualisation

To generate a benchmark data set, the motion of a 'Flying L' based on 36 4-node Finite Elements in space (2d, plane strain conditions) is considered, compare Betsch and Steinmann [26]. The specific constitutive behaviour relies on a Hencky law given by Equation (4.11), using the parameters $\rho = 1.0$, $\lambda = 10000$, and $\mu = 5000$. Once more, an initial velocity with $||\bar{\boldsymbol{v}}_0|| = 50$ has been incorporated and the applied external loads are prescribed in time by a piecewise linear hat function with $f_{max} = 50.0$, $T_{load} = 3.0$. The initial configuration $\mathcal{B}_0$ as well as a sequence of the motion, which has been calculated with the time-step size $h_n = 0.4$, can be regarded in Figure B.1. Our goal is to provide multiple different visualisation tools to support the understanding of both the spatial distribution of the algorithmic enhancement terms as well as their effect on the stress field, entering the equations of motion. Therefore, we examine the data in a spatial context from different points of view and combine basic visualisation techniques such as colour coding, transparency effects, and scaling in order to provide the most helpful tools, distinguishing between:

- **Component-based approach:** We start with an investigation based on the stress components S_{ij} and S_{ij}^{alg}. Taking the symmetry properties of both tensor fields into account, the three independent components are collected in 3d vectors

$$\boldsymbol{s} := [S_{11}, S_{22}, S_{12}]^{\mathrm{t}} \qquad \text{and} \qquad \boldsymbol{s}^{alg} := [S_{11}^{alg}, S_{22}^{alg}, S_{12}^{alg}]^{\mathrm{t}} \tag{B.1}$$

  respectively, being motivated by the classical Voigt notation. Next, the difference of both vectors $\Delta\boldsymbol{s} := \boldsymbol{s}^{alg} - \boldsymbol{s}$ is calculated and the resulting vectors are plotted in the corresponding Gauss points of the reference configuration $\mathcal{B}_0$. By connecting these vectors, quad-patches can be created for each element in space. Even if the resulting patches are indeed 3d, the visualisation has been simplified by considering only their 2d projection. Based on this visualisation, the loss of one dimension has been compensated by adding circles at each Gauss point whose radii correspond to the Euclidean norm of the difference vectors. The results can be regarded in Figure B.2 a), using linear scaling to avoid overlapping [2]. Therein, it is clearly demonstrated that the proposed approach is well-suited to highlight regions of the body in which large corrections occur. However, the results are hard to interpret, since this approach obviously lacks in physical meaning.

- **Invariant-based technique:** Another approach consists of visualising the difference in the tensor invariants as ellipsoids which are given by the components' basis

$$(x, y, z) = \left(\Delta J_1, \Delta J_2, \frac{\Delta J_1 + \Delta J_2}{2}\right), \tag{B.2}$$

[2] In this context, the applied transfer functions as well as the resulting redistributions are plotted in the top-right corners of the corresponding figures.

where ΔJ_i denote the differences between the principal invariants represented by the trace and the determinant of both tensor fields, compare Equations (4.2) for the 3d case. To investigate a potential correlation between the deformation and the corrections, the norm of the assumed strain approximation in time of the right Cauchy-Green tensor $||\boldsymbol{C}^h(1/2)||$ has been additionally incorporated. Hereby, the following colour-coding has been used: from blue to red for an increasing norm of the deformation measure. Please note, that a logarithmic scaling has been applied in the present case, since the occurring differences are much greater than in the foregoing approach. In comparison to the previous visualisation based on the stress components, the corresponding plot provides a slightly better view on the spatial distribution of the corrections, since the regions with extremely large corrections are not so dominant due to the mentioned logarithmic scaling, see Figure B.2 b). However, an interpretation of the pictured glyphs is still difficult.

- **Spectral-based concepts:** Next, we turn our attention to changes in measures which rely on a spectral decomposition of the tensors under investigation. Following the approach discussed in Section 4.1, the decomposed continuum and algorithmic stresses result in

$$\boldsymbol{S}^{alg} = \sum_{i=1}^{2} {}^{\boldsymbol{S}}\lambda_i^{alg} \; {}^{\boldsymbol{S}}\boldsymbol{N}_i^{alg} \otimes {}^{\boldsymbol{S}}\boldsymbol{N}_i^{alg} \qquad \text{and} \qquad \boldsymbol{S} = \sum_{i=1}^{2} {}^{\boldsymbol{S}}\lambda_i \, {}^{\boldsymbol{S}}\boldsymbol{N}_i \otimes {}^{\boldsymbol{S}}\boldsymbol{N}_i \quad \text{(B.3)}$$

respectively. Since the actual goal is to show how the stresses are modified by the algorithmic correction term, the rotation of the principal stress directions ${}^{\boldsymbol{S}}\boldsymbol{N}_i$ and changes in the principal stresses ${}^{\boldsymbol{S}}\lambda_i$ are considered, whereby particularly the rotation seems to be an interesting issue in this context. As seen in Figure B.3 a), the difference in the angle between the eigenvectors ${}^{\boldsymbol{S}}\boldsymbol{N}_i$ (blue) and ${}^{\boldsymbol{S}}\boldsymbol{N}_i^{alg}$ (red) is too small for direct visualisation purposes.
Therefore, we propose in a first step an amplified display based on wedges that indicate the direction of the rotation with a colour sweep. The visualisation in Figure B.3 b) employs a uniform scaling of the major eigenvectors and the computed angles are equalised this time based on an appropriate nonlinear transfer function. Since the main objective is to indicate rotation, the change in the magnitude of eigenvalues has been mapped linearly to the radii of the circles, being least distracting from the main visualisation goal. In Figure B.3 b), it can be seen that in some elements large modifications of the angle are combined with small changes in the eigenvalues and vice versa. A particularly interesting aspect of this approach is the incorporation of both principal directions, enabling a quite intuitive visualisation. Nevertheless, the wedge-based concept obviously lacks in clarity due to the small size of the glyphs.
Hence, we consider in a second step a simple yet very effective visualisation of sign and magnitude of the rotation based on colour-coding, where blue indicates negative rotation in the mathematical sense and red positive. Again, an equalisation

of the value range is necessary to address nuances in the angle distribution close to zero. Analogously to the wedge-based technique, the differences in the tensor eigenvalues are included by means of scaled radii. Hereby, the applied transfer function plays once more a decisive role concerning the offered informations. As can be seen in Figure B.4 a), a linear scaling of the eigenvalues only allows to disclose regions of large corrections. In contrast, a nonlinear transfer function shows more subtle details and, hence, it allows to identify even the occurring patterns within the spatial distribution, compare Figure B.4 b).

- **Level-of-detail visualisation:** The last approach bases on a multiresolution paradigm which provides qualitative informations at a global scale, while allowing also to investigate in detail the local behaviour at an adequate zoom level. The large scale visualisation in Figure B.5 illustrates the differences in eigenvalues via the circle diameters and the angle as well as the direction of rotation via the circle colours. The detail level depicts the magnitude and angle modification as a sweep between the individual representations of $\boldsymbol{S}$ and $\boldsymbol{S}^{alg}$. Hereby, the employed glyphs are created in the following way: Each pair of principal directions $[{}^{\boldsymbol{S}}\boldsymbol{N}_i, {}^{\boldsymbol{S}}\boldsymbol{N}_i^{alg}]$ is scaled by the eigenvalues $[{}^{\boldsymbol{S}}\lambda_i, {}^{\boldsymbol{S}}\lambda_i^{alg}]$ and gives rise to a cross of two orthogonal lines. Furthermore, the eigenvalues are the radii of an ellipse aligned with the principal directions. If different colours are assigned for the continuum and the algorithmic stresses respectively, the linear sweep between both crosses and ellipses renders the complex glyph visualisation pictured in Figure B.5. This visualisation tool indeed incorporates most of the advantages of the different methods that have been discussed before. It allows, on the one hand, an excellent detection of regions in which large modifications occur. On the other hand, a detailed physical-based insight can be obtained by zooming-in, offering informations both on magnitude and rotation.

In the present section, several concepts to visualise the differences between the continuum and the algorithmic stress tensor field have been broached to understand better the influence and the functioning of the underlying non-standard quadrature rule. Eventually, we can summarise that for the present task a nested visualisation which involves different basic techniques seems to be the most promising approach, since one single method is usually not capable of giving sufficient insight into all interesting aspects. In this context, especially the application of spectral-based concepts has turned out to be a convenient tool concerning a comparison of both tensor fields, even if the presented basic investigations are not yet sufficient to come to a final decision. However, the here considered fundamental aspects represent an encouraging point of departure to investigate in future work the actual behaviour of the algorithmic stress modification. Hereby, in particular the influence of the time-step size and the stiffness, the spatial distribution as well as the evolution in time should be studied in detail based on different data sets, addressing for instance the question of time and space continuity of the stress modification.

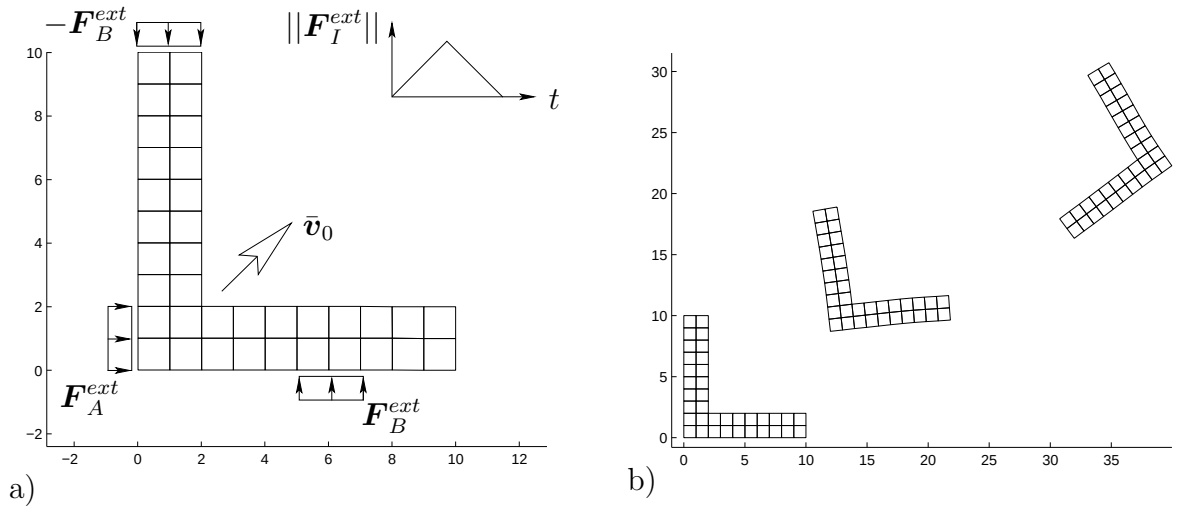

Figure B.1.: a) initial configuration $\mathcal{B}_0$, b) sequence of the elastic motion

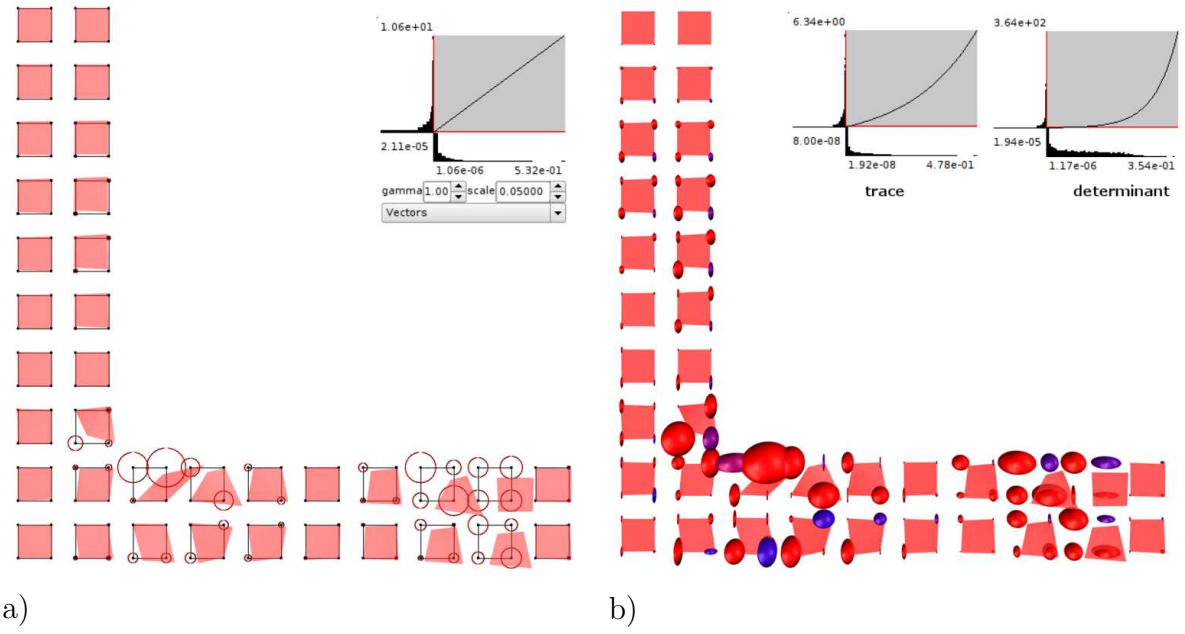

Figure B.2.: comparison of the tensor fields $\boldsymbol{S}(1/2)$ and $\boldsymbol{S}^{alg}(1/2)$ for time-step 11, using: a) a component-based approach, b) an invariant-based technique

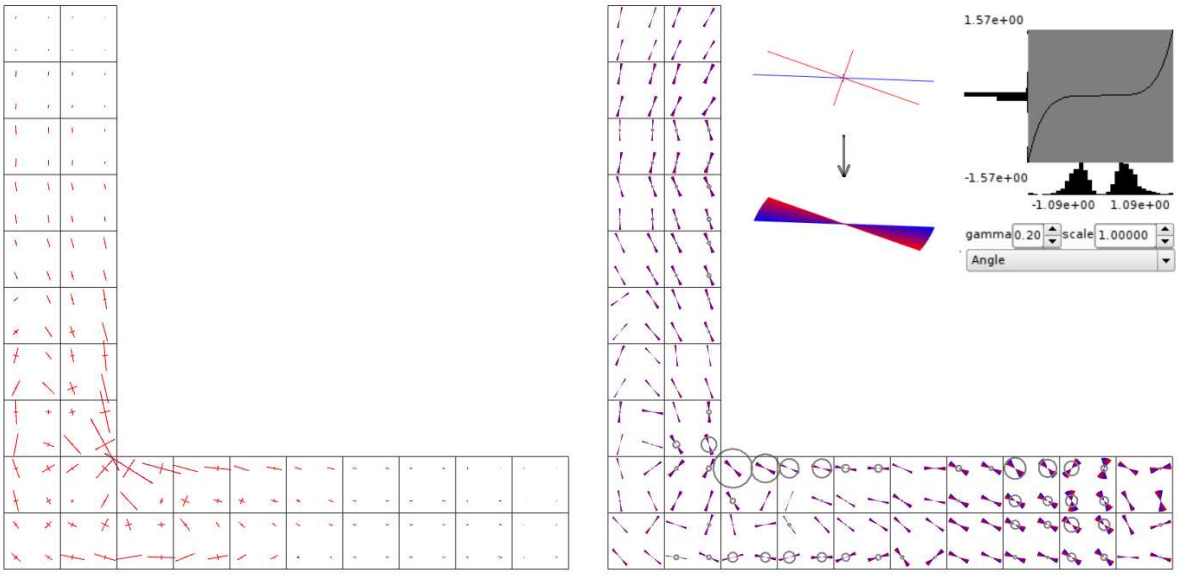

a) b)

Figure B.3.: comparison of the tensor fields $\boldsymbol{S}(1/2)$ and $\boldsymbol{S}^{alg}(1/2)$ for time-step 11, using spectral-based concepts: a) plot of the principal directions (angle unscaled), b) visualisation based on wedges (nonlinearly scaled angle)

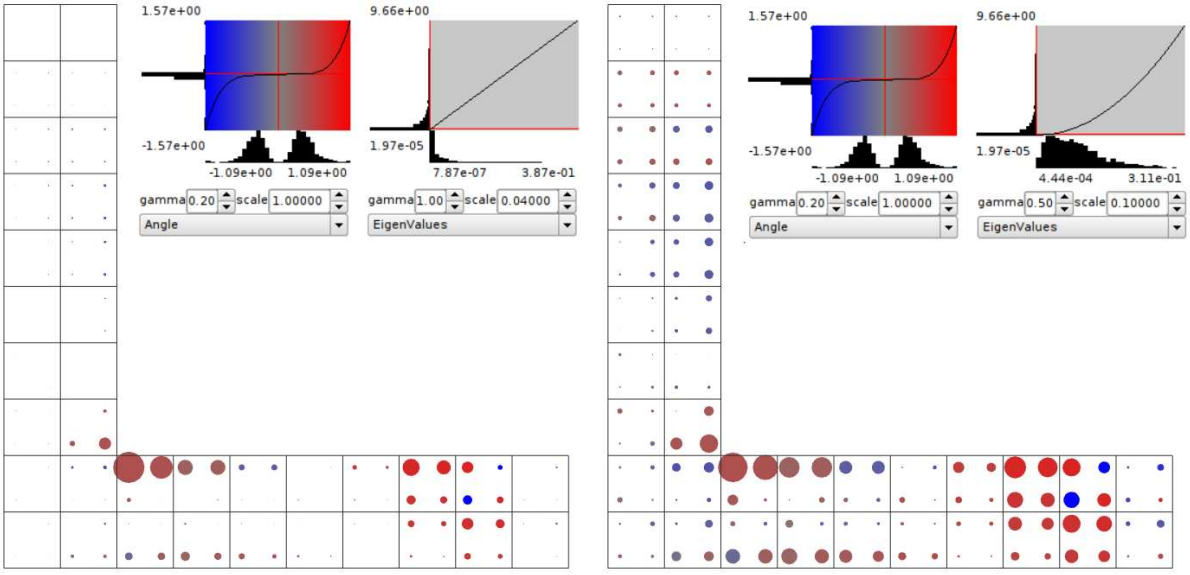

a) b)

Figure B.4.: comparison of the tensor fields $\boldsymbol{S}(1/2)$ and $\boldsymbol{S}^{alg}(1/2)$ for time-step 11, using spectral-based concepts: a) colour-coded discs (linearly scaled eigenvalues), b) colour-coded discs (nonlinearly scaled eigenvalues)

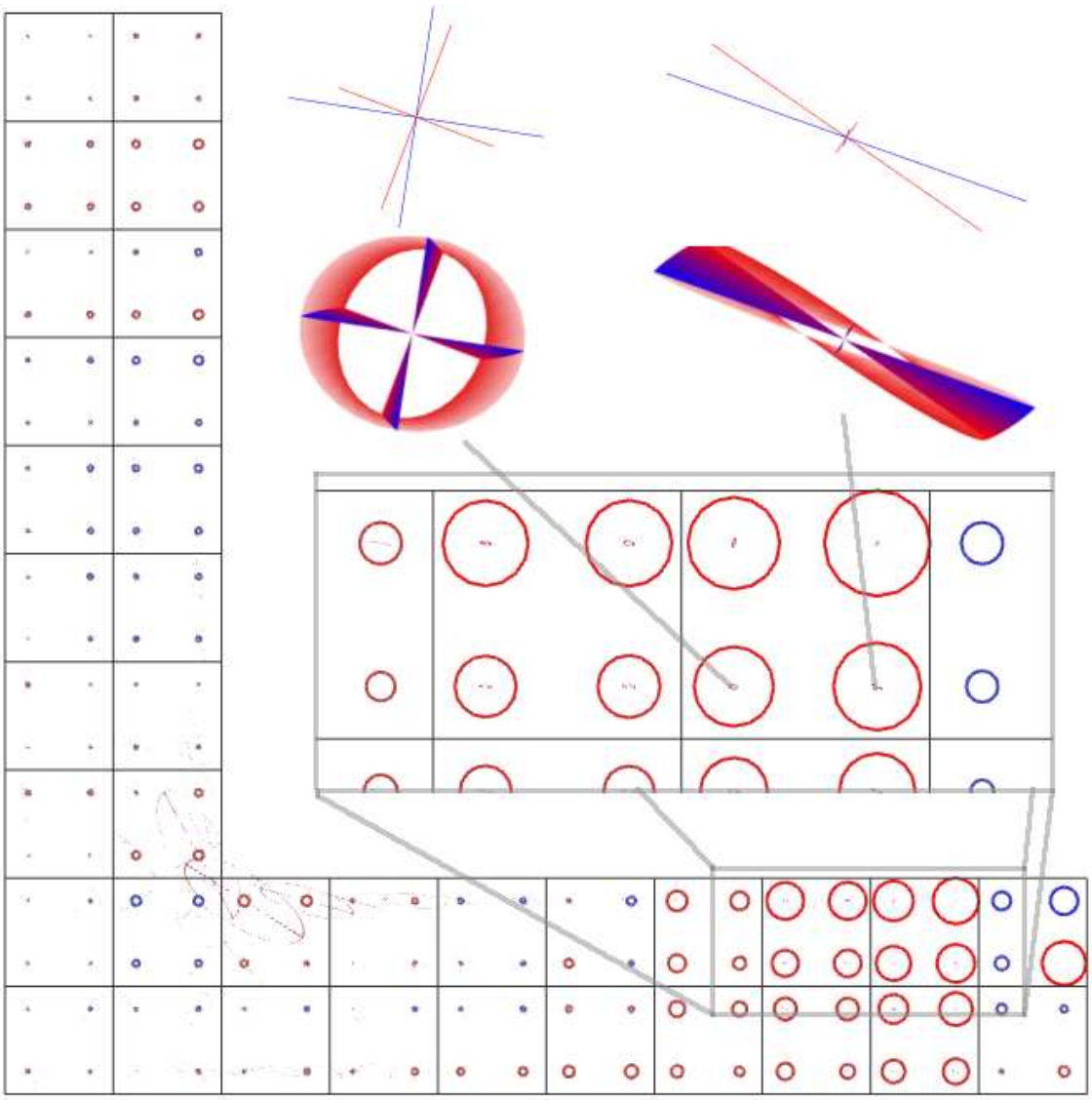

Figure B.5.: level-of-detail visualisation, showing more qualitative facts at a large scale while depicting specific details after an appropriate zoom

C. Standard Time Integrators

In this paragraph, we summarise briefly the essential equations of some standard time-stepping schemes based on Finite Differences that are involved in Section 5.5.1 and Section 5.6.2 for the purpose of a comparison to the proposed time FE methods.

C.1. Newmark Scheme

Probably, the Newmark scheme represents the most commonly used time-stepping scheme in computational dynamics at all, compare for instance References [18, 19, 76, 143, 162, 177]. Firstly, we introduce the standard format of approximations

$$\begin{aligned} \bar{\boldsymbol{u}}_{n+1} &= \bar{\boldsymbol{u}}_n + h_n\,\bar{\boldsymbol{v}}_n + \frac{h_n^2}{2}\left[[1-2\,\beta]\,\bar{\boldsymbol{a}}_n + 2\,\beta\,\bar{\boldsymbol{a}}_{n+1}\right] \\ \bar{\boldsymbol{v}}_{n+1} &= \bar{\boldsymbol{v}}_n + h_n\left[[1-\gamma]\,\bar{\boldsymbol{a}}_n + \gamma\,\bar{\boldsymbol{a}}_{n+1}\right], \end{aligned} \tag{C.1}$$

involving the two parameters β [1] and γ. Furthermore, the semidiscrete vector of nodal accelerations $\bar{\boldsymbol{a}}(t) = [\boldsymbol{a}_1(t), ..., \boldsymbol{a}_{n_{node}}(t)]^{\mathrm{t}} := \dot{\bar{\boldsymbol{v}}}(t)$ and nodal displacements $\bar{\boldsymbol{u}}(t) = [\boldsymbol{u}_1(t), ..., \boldsymbol{u}_{n_{node}}(t)]^{\mathrm{t}} := \bar{\boldsymbol{q}}(t) - \bar{\boldsymbol{X}}$, respectively, have been incorporated in Equation (C.1), whereby $\bar{\boldsymbol{X}} = [\boldsymbol{X}_1, ..., \boldsymbol{X}_{n_{node}}]^{\mathrm{t}}$ denotes the global vector of nodal placements in the reference configuration. A reformulation of Equations (C.1) renders straightforwardly the alternative representations in displacement form

$$\begin{aligned} \bar{\boldsymbol{a}}_{n+1} &= \alpha_1\,[\bar{\boldsymbol{u}}_{n+1} - \bar{\boldsymbol{u}}_n] - \alpha_2\,\bar{\boldsymbol{v}}_n - \alpha_3\,\bar{\boldsymbol{a}}_n \\ \bar{\boldsymbol{v}}_{n+1} &= \alpha_4\,[\bar{\boldsymbol{u}}_{n+1} - \bar{\boldsymbol{u}}_n] + \alpha_5\,\bar{\boldsymbol{v}}_n + \alpha_6\,\bar{\boldsymbol{a}}_n \end{aligned} \tag{C.2}$$

with the unknown vector $\bar{\boldsymbol{u}}_{n+1}$. Therein, the coefficients α_i can be computed by

$$\begin{aligned} \alpha_1 &= \frac{1}{\beta\,h_n^2}, \quad \alpha_2 = \frac{1}{\beta\,h_n}, \quad \alpha_3 = \frac{1}{2\,\beta} - 1\,, \\ \alpha_4 &= \frac{\gamma}{\beta\,h_n}, \quad \alpha_5 = 1 - \frac{\gamma}{\beta}, \quad \alpha_6 = h_n - \frac{\gamma}{2\,\beta}\,h_n\,. \end{aligned} \tag{C.3}$$

[1] Please do not confuse the classical notation of the parameter β with the (scalar-valued) conjugated thermodynamical force of the plasticity formulation, introduced in Equation $(5.9)_2$.

Enforcing the semidiscrete balance of momentum at time t_{n+1} yields

$$\mathbb{M} \cdot \bar{\boldsymbol{a}}_{n+1} + \bar{\boldsymbol{F}}^{int}(\bar{\boldsymbol{u}}_{n+1}) = \bar{\boldsymbol{F}}^{ext}_{n+1} \,, \tag{C.4}$$

analogously to Equation (3.23) [2]. Inserting furthermore the approximations (C.2) in Equation (C.4) leads to a set of nonlinear equations formulated in the displacement vector. Finally, both parameters β and γ have to be chosen to obtain a specific representative of the Newmark time-stepping family. In this context, a popular choice for the parameters is $\beta = 0.25$ and $\gamma = 0.5$, resulting in the so-called trapezoidal rule which is known to be energy-conserving for linear dynamical systems. However, in the context of nonlinear dynamics the foregoing scheme is neither energy-conserving/consistent nor mechanically consistent. Further details can also be found in the textbooks [18, 76, 177] and references cited therein.

C.2. HHT Methods

In the literature, several concepts, which often base on the Newmark scheme, have been proposed to incorporate numerical dissipation without losing accuracy, unlike the classical Newmark algorithm with $\gamma > 0.5$. A widespread formulation has been suggested for instance by Hilber, Hughes, and Taylor [74] for linear dynamical systems, the so-called 'HHT methods' or 'α-methods'. In a linear context, the resulting scheme has also been discussed extensively in Hughes [76], whereby the extension to nonlinear dynamics renders

$$\mathbb{M} \cdot \bar{\boldsymbol{a}}_{n+1} + \bar{\boldsymbol{F}}^{int}(\bar{\boldsymbol{u}}_{n+1+\alpha}) = \bar{\boldsymbol{F}}^{ext}(t_{n+1+\alpha}) \,. \tag{C.5}$$

Herein, the evaluation time $t_{n+1+\alpha} := [1+\alpha]\, t_{n+1} - \alpha\, t_n$ and the modified displacement vector

$$\bar{\boldsymbol{u}}_{n+1+\alpha} := [1+\alpha]\, \bar{\boldsymbol{u}}_{n+1} - \alpha\, \bar{\boldsymbol{u}}_n \tag{C.6}$$

have been incorporated in addition to the fundamental formulas of the Newmark scheme given by Equations (C.1), that are still valid. Obviously, for $\alpha = 0$ the classical Newmark family is recaptured and, consequently, Equation (C.5) coincides with Equation (C.4). Furthermore, a reduction of the parameter α leads to an increasing numerical dissipation. Motivated by stability properties in the linear case, a typical choice is given by $\alpha \in [-1/3, 0]$ in combination with $\beta = [1-\alpha]^2/4$ and $\gamma = [1-2\alpha]/2$, as advocated also in Reference [76].

[2] Although there is no damping matrix involved in Equation (C.4), damping effects can also be included implicitly by means of a corresponding constitutive model, like for instance visco-elasticity.

C.3. Collocation Methods

A further generalisation of the Newmark scheme is represented by the family of Collocation methods, offering numerical dissipation for high-frequency modes as well. In contrast to the foregoing 'HHT methods', where the acceleration vector at t_{n+1} enters into the balance of momentum, the Collocation methods base on a unified evaluation time for the accelerations, the displacements, and the external loads, yielding in the nonlinear case

$$\mathbb{M} \cdot \bar{\boldsymbol{a}}_{n+\theta} + \bar{\boldsymbol{F}}^{int}(\bar{\boldsymbol{u}}_{n+\theta}) = \bar{\boldsymbol{F}}^{ext}_{n+\theta} \,. \tag{C.7}$$

Herein, on the one hand, the vectors

$$\begin{aligned} \bar{\boldsymbol{a}}_{n+\theta} &= [1-\theta]\, \bar{\boldsymbol{a}}_n + \theta\, \bar{\boldsymbol{a}}_{n+1} \\ \bar{\boldsymbol{F}}^{ext}_{n+\theta} &= [1-\theta]\, \bar{\boldsymbol{F}}^{ext}_n + \theta\, \bar{\boldsymbol{F}}^{ext}_{n+1} \end{aligned} \tag{C.8}$$

have been incorporated and, on the other hand, the formulas of the classical Newmark scheme (C.1) have been altered, involving

$$\begin{aligned} \bar{\boldsymbol{u}}_{n+\theta} &= \bar{\boldsymbol{u}}_n + \theta\, h_n\, \bar{\boldsymbol{v}}_n + \frac{[\theta\, h_n]^2}{2} \left[[1-2\,\beta]\, \bar{\boldsymbol{a}}_n + 2\,\beta\, \bar{\boldsymbol{a}}_{n+\theta} \right] \\ \bar{\boldsymbol{v}}_{n+\theta} &= \bar{\boldsymbol{v}}_n + \theta\, h_n \left[[1-\gamma]\, \bar{\boldsymbol{a}}_n + \gamma\, \bar{\boldsymbol{a}}_{n+\theta} \right] \end{aligned} \tag{C.9}$$

related to $t_{n+\theta} = t_n + \theta\, h_n$. Once more, the classical Newmark scheme is included within the general family of Collocation methods and can be recovered by incorporating $\theta = 1$. Concerning further details and fundamental investigations in the context of linear structural dynamics, we refer again to the textbooks [18, 76].

Remark C.1: Please notice, that even the Wilson-θ-methods (or short: Wilson methods), which have been used as well in Section 5.6.2 for a comparison to the favoured time FE scheme, are contained in the class of Collocation methods discussed above. In fact, they can be easily regained by setting $\beta = 1/6$ and $\gamma = 0.5$.

Bibliography

[1] J. A. C. Ambrosio and P. E. Nikravesh. Elasto-plastic deformations in multibody dynamics. *Nonlin. Dynamics*, 3:85–104, 1992.

[2] J. A. C. Ambrosio, M. F. O. S. Pereira, and J. P. Dias. Distributed and discrete nonlinear deformations on multibody dynamics. *Nonlin. Dynamics*, 10:359–379, 1996.

[3] J. Angeles. *Fundamentals of Robotic Mechanical Systems*. Springer, 1997.

[4] J. Argyris and D. Scharpf. Finite elements in time and space. *Journal of the Royal Aeronautical Society*, 73:1041–1044, 1969.

[5] F. Armero. Energy-dissipative momentum-conserving time-stepping algorithms for finite strain multiplicative plasticity. *Comput. Methods Appl. Mech. Engrg.*, 195:4862–4889, 2006.

[6] F. Armero. Assumed strain finite element methods for conserving temporal integrations in non-linear solid dynamics. *Int. J. Numer. Meth. Engng*, DOI: 10.1002/nme.2233, 2007.

[7] F. Armero and I. Romero. On the formulation of high-frequency dissipative time-stepping algorithms for nonlinear dynamics. Part I: low-order methods for model problems and nonlinear elastodynamics. *Comput. Methods Appl. Mech. Engrg.*, 190:2603–2649, 2001.

[8] F. Armero and I. Romero. On the formulation of high-frequency dissipative time-stepping algorithms for nonlinear dynamics. Part II: second-order methods. *Comput. Methods Appl. Mech. Engrg.*, 190:6783–6824, 2001.

[9] F. Armero and C. Zambrana-Rojas. Volume-preserving energy-momentum schemes for isochoric multiplicative plasticity. *Comput. Methods Appl. Mech. Engrg.*, 196:4130–4159, 2007.

[10] E. Artioli, F. Auricchio, and L. Beirao da Veiga. Integration schemes for von-Mises plasticity models based on exponential maps: numerical investigations and theoretical considerations. *Int. J. Numer. Meth. Engng*, 64:1133–1165, 2005.

[11] E. Artioli, F. Auricchio, and L. Beirao da Veiga. A novel 'optimal' exponential-based integration algorithm for von-Mises plasticity with linear hardening: Theoretical analysis on yield consistency, accuracy, convergence and numerical investigations. *Int. J. Numer. Meth. Engng*, 67:449–498, 2006.

[12] E. Artioli, F. Auricchio, and L. Beirao da Veiga. Generalized midpoint integration algorithms for J_2 plasticity with linear hardening. *Int. J. Numer. Meth. Engng*, 72:422–463, 2007.

[13] E. Artioli, F. Auricchio, and L. Beirao da Veiga. Second-order accurate integration algorithms for von-Mises plasticity with a nonlinear kinematic hardening mechanism. *Comput. Methods Appl. Mech. Engrg.*, 196:1827–1846, 2007.

[14] O. A. Bauchau. Computational schemes for flexible nonlinear multi-body systems. *Multibody System Dynamics*, 2:169–225, 1998.

[15] O. A. Bauchau and C. L. Bottasso. On the design of energy preserving and decaying schemes for flexible, non-linear multi-body systems. *Comput. Methods Appl. Mech. Engrg.*, 169:61–79, 1999.

[16] O. A. Bauchau, C. L. Bottasso, and L. Trainelli. Robust integration schemes for flexible multibody systems. *Comput. Methods Appl. Mech. Engrg.*, 192:395–420, 2003.

[17] O. A. Bauchau and T. Joo. Computational schemes for non-linear elasto-dynamics. *Int. J. Numer. Meth. Engng*, 45:693–719, 1999.

[18] T. Belytschko and T. J. R. Hughes. *Computational Methods for Transient Analysis*. Mechanics and Mathematical Methods – Computational Methods in Mechanics. North–Holland, 1983.

[19] T. Belytschko, W. Liu, and B. Moran. *Nonlinear Finite Elements for Continua and Structures*. Wiley, 2000.

[20] P. Betsch. *Computational Methods for Flexible Multibody Dynamics*. Habilitation thesis, University of Kaiserslautern, 2002.

[21] P. Betsch. The discrete null space method for the energy consistent integration of constrained mechanical systems. Part I: Holonomic constraints. *Comput. Methods Appl. Mech. Engrg.*, 194:5159–5190, 2005.

[22] P. Betsch. Energy-consistent numerical integration of mechanical systems with mixed holonomic and nonholonomic constraints. *Comput. Methods Appl. Mech. Engrg.*, 195:7020–7035, 2006.

[23] P. Betsch and S. Leyendecker. The discrete null space method for the energy consistent integration of constrained mechanical systems. Part II: Multibody dynamics. *Int. J. Numer. Meth. Engng*, 67:499–552, 2006.

[24] P. Betsch and P. Steinmann. Conservation properties of a time FE method. Part I: Time-stepping schemes for N-body problems. *Int. J. Numer. Meth. Engng*, 49:599–638, 2000.

[25] P. Betsch and P. Steinmann. Inherently energy conserving time finite elements for classical mechanics. *J. Comput. Phys.*, 160:88–116, 2000.

[26] P. Betsch and P. Steinmann. Conservation properties of a time FE method. Part II: Time-stepping schemes for non-linear elastodynamics. *Int. J. Numer. Meth. Engng*, 50:1931–1955, 2001.

[27] P. Betsch and P. Steinmann. Constrained integration of rigid body dynamics. *Comput. Methods Appl. Mech. Engrg.*, 191:467–488, 2001.

[28] P. Betsch and P. Steinmann. Conservation properties of a time FE method. Part III: Mechanical systems with holonomic constraints. *Int. J. Numer. Meth. Engng*, 53:2271–2304, 2002.

[29] P. Betsch and P. Steinmann. A DAE approach to flexible multibody dynamics. *Multibody System Dynamics*, 8:367–391, 2002.

[30] P. Betsch and P. Steinmann. Constrained dynamics of geometrically exact beams. *Comput. Mech.*, 31:49–59, 2003.

[31] P. Betsch and S. Uhlar. Energy-momentum conserving integration of multibody dynamics. *Multibody System Dynamics*, 17:243–289, 2007.

[32] J. Betten. Interpolation methods for tensor functions. In X. J. R. Avula *et al.*, editor, *Mathematical Modelling in Science and Technology*. Pergamon Press, 1984.

[33] G. Biakeu and L. Jezequel. Simplified crash models using plastic hinges and the large curvature description. *Multibody System Dynamics*, 9:25–37, 2003.

[34] J. Bonet. Large strain viscoelastic constitutive models. *Int. J. Solids Struct.*, 38:2953–2968, 2001.

[35] J. Bonet and R. D. Wood. *Nonlinear Continuum Mechanics for Finite Element Analysis*. Cambridge University Press, 1997.

[36] M. Borri, C. L. Bottasso, and L. Trainelli. Integration of elastic multibody systems by invariant conserving/dissipating algorithms. I. Formulation. *Comput. Methods Appl. Mech. Engrg.*, 190:3669–3699, 2001.

[37] C. L. Bottasso, O. A. Bauchau, and A. Cardona. Time-step-size-independent conditioning and sensitivity to perturbations in the numerical solution of index three differential algebraic equations. *SIAM J. Sci. Comput.*, 29:397–414, 2007.

[38] C. L. Bottasso, O. A. Bauchau, and J. Choi. An energy decaying scheme for nonlinear dynamics of shells. *Comput. Methods Appl. Mech. Engrg.*, 191:3099–3121, 2002.

[39] C. L. Bottasso, M. Borri, and L. Trainelli. Integration of elastic multibody systems by invariant conserving/dissipating algorithms. II. Numerical schemes and applications. *Comput. Methods Appl. Mech. Engrg.*, 190:3701–3733, 2001.

[40] C. L. Bottasso and L. Trainelli. An attempt at the classification of energy decaying schemes for structural and multibody dynamics. *Multibody System Dynamics*, 12:173–185, 2004.

[41] I. N. Bronstein and S. Semendyayev. *Handbook of Mathematics*. Van Nostrand Co, 1985.

[42] O. T. Bruhns, H. Xiao, and A. Meyers. Constitutive inequalities for an isotropic elastic strain-energy function based on Hencky's logarithmic strain tensor. *Proc. Roy. Soc. A*, 457:2207–2226, 2001.

[43] Q. V. Bui. Energy conserving and dissipative time finite element schemes for n-body stiff problems. *Int. J. Numer. Meth. Engng*, 61:1359–1389, 2004.

[44] Q. V. Bui. Modified Newmark family for non-linear dynamic analysis. *Int. J. Numer. Meth. Engng*, 61:1390–1420, 2004.

[45] Q. V. Bui. On the enforcing energy conservation of time finite elements for particle systems. *Int. J. Numer. Meth. Engng*, 68:967–992, 2006.

[46] Q. V. Bui. On the enforcing energy conservation of time finite elements for discrete elasto-dynamics problems. *Int. J. Numer. Meth. Engng*, 70:127–162, 2007.

[47] J. Büttner and B. Simeon. Runge-Kutta methods in elastoplasticity. *Applied Numerical Mathematics*, 41:443–458, 2002.

[48] J. Chung and G. J. M. Hulbert. A time integration algorithm for structural dynamics with improved numerical dissipation: The generalized-α method. *J. Appl. Mech.*, 60:371–375, 1993.

[49] M. A. Crisfield and J. Shi. An energy conserving co-rotational procedure for non-linear dynamics with finite elements. *Nonlin. Dynamics*, 9:37–52, 1996.

[50] R. de Borst and O. M. Heeres. A unified approach to the implicit integration of standard, non-standard and viscous plasticity models. *Int. J. Numer. Anal. Meth. Geomech.*, 26:1059–1070, 2002.

[51] J. P. Dias and M. S. Pereira. Dynamics of flexible mechanical systems with contact-impact and plastic deformations. *Nonlin. Dynamics*, 8:491–512, 1995.

[52] E. Eich-Soellner and C. Führer. *Numerical Methods in Multibody Dynamics*. Teubner, 1998.

[53] M. Ekh and A. Menzel. Efficient iteration schemes for anisotropic hyperelasto-plasticity. *Int. J. Numer. Meth. Engng*, 66:707–721, 2006.

[54] K. Eriksson, D. Estep, P. Hansbo, and C. Johnson. *Computational Differential Equations*. Cambridge University Press, 1996.

[55] D. J. Estep and D. French. Global error control for the continuous Galerkin finite element method for ordinary differential equations. *Mathematical Modelling and Numerical Analysis*, 28:815–852, 1994.

[56] A. L. Eterovic and K. J. Bathe. A hyperelastic-based large strain elasto-plastic constitutive formulation with combined isotropic-kinematic hardening using the logarithmic stress and strain measures. *Int. J. Numer. Meth. Engng*, 30:1099–1114, 1990.

[57] A. D. French and J. W. Schaeffer. Continuous finite element methods which preserve energy properties for nonlinear problems. *Applied Mathematics and Computations*, 39:271–295, 1990.

[58] M. Geradin and A. Cardona. *Flexible Multibody Dynamics*. Wiley, 2001.

[59] J. Gerstmayr. *A Solution Strategy for Elasto-Plastic Multibody Systems and Related Problems*. Phd thesis, University of Linz, 2001.

[60] J. Gerstmayr. The absolute coordinate formulation with elasto-plastic deformations. *Multibody System Dynamics*, 12:363–383, 2004.

[61] J. Gerstmayr and H. Irschik. Vibrations of the elasto-plastic pendulum. *Int. J. Non–Linear Mechanics*, 38:111–122, 2003.

[62] O. Gonzalez. Time integration and discrete Hamiltonian systems. *J. Nonlinear Sci.*, 6:449–467, 1996.

[63] O. Gonzalez. Mechanical systems subject to holonomic constraints: Differential-algebraic formulations and conservative integration. *Physica D*, 132:165–174, 1999.

[64] O. Gonzalez. Exact energy and momentum conserving algorithms for general models in nonlinear elasticity. *Comput. Methods Appl. Mech. Engrg.*, 190:1763–1783, 2000.

[65] A. E. Green and P. M. Naghdi. A general theory of an elasto-plastic continuum. *Arch. Rational Mech. Anal.*, 18:251–281, 1965.

[66] A. E. Green and W. Zerna. *Theoretical Elasticity*. Clarendon Press, 1954.

[67] M. Gross. *Conserving Time Integrators for Nonlinear Elastodynamics*. Phd thesis, University of Kaiserslautern, 2004.

[68] M. Gross, P. Betsch, and P. Steinmann. Conservation properties of a time FE method. Part IV: Higher order energy and momentum conserving schemes. *Int. J. Numer. Meth. Engng*, 63:1849–1897, 2005.

[69] M. E. Gurtin. *An Introduction to Continuum Mechanics*. Academic Press, 1981.

[70] E. Hairer, C. Lubich, and G. Wanner. *Geometric Numerical Integration – Structure-Preserving Algorithms for Ordinary Differential Equations*. Springer, 2nd edition, 2006.

[71] W. Han and B. D. Reddy. *Plasticity – Mathematical Theory and Numerical Analysis*. Springer, 1999.

[72] P. Hansbo. A note on energy conservation for Hamiltonian systems using continuous time finite elements. *Commun. Numer. Methods Engng.*, 17:863–869, 2001.

[73] P. Haupt. *Continuum Mechanics and Theory of Materials*. Advanced Texts in Physics, Springer, 2000.

[74] H. M. Hilber, T. J. R. Hughes, and R. L. Taylor. Improved numerical dissipation for time integration algorithms in structural dynamics. *Earthquake Engng Struct. Dyn.*, 5:283–292, 1977.

[75] G. A. Holzapfel. *Nonlinear Solid Mechanics – A Continuum Approach for Engineering*. Wiley, 2000.

[76] T. J. R. Hughes. *The Finite Element Method*. Prentice-Hall, 1987.

[77] T. J. R. Hughes, T. K. Caughey, and W. K. Liu. Finite-element methods for nonlinear elastodynamics which conserve energy. *J. Appl. Mech.*, 45:366–370, 1978.

[78] T. J. R. Hughes and G. J. M. Hulbert. Space-time finite element methods for elastodynamics: Formulations and error estimates. *Comput. Methods Appl. Mech. Engrg.*, 66:339–363, 1988.

[79] G. J. M. Hulbert. Time finite element methods for structural dynamics. *Int. J. Numer. Meth. Engng*, 33:307–331, 1992.

[80] B. L. Hulme. Discrete Galerkin and related one-step methods for ordinary differential equations. *Math. Comput.*, 26:881–891, 1972.

[81] B. L. Hulme. One-step piecewise polynomial Galerkin methods for initial value problems. *Math. Comput.*, 26:415–426, 1972.

[82] A. Ibrahimbegovic. Equivalent spatial and material descriptions of finite deformation elastoplasticity in principal axes. *Int. J. Solids Struct.*, 31:3027–3040, 1994.

[83] A. Ibrahimbegovic and S. Mamouri. Energy conserving/decaying implicit time-stepping scheme for nonlinear dynamics of three-dimensional beams undergoing finite rotations. *Comput. Methods Appl. Mech. Engrg.*, 191:4241–4258, 2002.

[84] A. Ibrahimbegovic, S. Mamouri, R. Taylor, and A. Chen. Finite element method in dynamics of flexible multibody systems: modeling of holonomic constraints and energy conserving integration schemes. *Multibody System Dynamics*, 4:195–223, 2000.

[85] A. Ibrahimbegovic, R. L. Taylor, and H. Lim. Non-linear dynamics of flexible multibody systems. *Comput. Struct.*, 81:1113–1132, 2003.

[86] B. Jeremic and Z. Cheng. Significance of equal principal stretches in computational hyperelasticity. *Commun. Numer. Methods Engng.*, 21:477–486, 2005.

[87] C. Kane, J. E. Marsden, M. Ortiz, and M. West. Variational integrators and the Newmark's algorithm for conservative and dissipative mechanical systems. *Int. J. Numer. Meth. Engng*, 49:1295–1325, 2000.

[88] S. Krenk. Energy conservation in Newmark based time integration algorithms. *Comput. Methods Appl. Mech. Engrg.*, 195:6110–6124, 2006.

[89] S. Krenk. State-space time integration with energy control and 4'th order accuracy for linear dynamic systems. *Int. J. Numer. Meth. Engng*, 65:595–619, 2006.

[90] S. Krenk. The role of geometric stiffness in momentum and energy conserving time integration. *Int. J. Numer. Meth. Engng*, 71:631–651, 2007.

[91] D. Kuhl. *Stabile Zeitintegrationsalgorithmen in der nichtlinearen Elastodynamik dünnwandiger Tragwerke*. Phd thesis, Universität Stuttgart, 1996.

[92] D. Kuhl and M. A. Crisfield. Energy-conserving and decaying algorithms in non-linear structural dynamics. *Int. J. Numer. Meth. Engng*, 45:569–599, 1999.

[93] D. Kuhl and G. Meschke. Numerical analysis of dissolution processes in cementitious materials using discontinuous and continuous Galerkin time integration schemes. *Int. J. Numer. Meth. Engng*, 69:1775–1803, 2007.

[94] D. Kuhl and E. Ramm. Constraint energy momentum algorithm and its application to non-linear dynamics of shells. *Comput. Methods Appl. Mech. Engrg.*, 136:293–315, 1996.

[95] D. Kuhl and E. Ramm. Generalized energy-momentum method for non-linear adaptive shell dynamics. *Comput. Methods Appl. Mech. Engrg.*, 178:343–366, 1999.

[96] D. Kuhl and E. Ramm. Time integration in the context of energy control and locking free finite elements. *Arch. Comput. Methods Engrg. – State of the art reviews*, 7:299–332, 2000.

[97] R. A. LaBudde and D. Greenspan. Energy and momentum conserving methods of arbitrary order for the numerical integration of equations of motion. I. Motion of a single particle. *Numerische Mathematik*, 25:323–346, 1976.

[98] R. A. LaBudde and D. Greenspan. Energy and momentum conserving methods of arbitrary order for the numerical integration of equations of motion. II. Motion of a system of particles. *Numerische Mathematik*, 26:1–16, 1976.

[99] F. Larsson, P. Hansbo, and K. Runesson. Space-time finite elements and an adaptive strategy for the coupled thermoelasticity problem. *Int. J. Numer. Meth. Engng*, 56:261–293, 2003.

[100] F. Larsson, K. Runesson, and P. Hansbo. Time finite elements and error computation for (visco)plasticity with hardening or softening. *Int. J. Numer. Meth. Engng*, 56:2213–2232, 2003.

[101] T. A. Laursen and X. N. Meng. A new solution procedure for application of energy-conserving algorithms to general constitutive models in nonlinear elastodynamics. *Comput. Methods Appl. Mech. Engrg.*, 190:6309–6322, 2001.

[102] E. H. Lee. Elastic-plastic deformation at finite strains. *J. Appl. Mech.*, 36:1–6, 1969.

[103] B. Leimkuhler and S. Reich. *Simulating Hamiltonian Dynamics*. Cambridge University Press, 2004.

[104] E. Lens and A. Cardona. An energy preserving/decaying scheme for nonlinearly constrained multibody systems. *Multibody System Dynamics*, 18:435–470, 2007.

[105] E. Lens, A. Cardona, and M. Geradin. Energy preserving time integration for constrained multibody systems. *Multibody System Dynamics*, 11:41–61, 2004.

[106] A. Lew, J. E. Marsden, M. Ortiz, and M. West. Asynchronous variational integrators. *Arch. Rational Mech. Anal.*, 167:85–146, 2003.

[107] A. Lew, J. E. Marsden, M. Ortiz, and M. West. Variational time integrators. *Int. J. Numer. Meth. Engng*, 60:153–212, 2004.

[108] S. Leyendecker. *Mechanical integrators for constrained dynamical systems in flexible multibody dynamics*. Phd thesis, University of Kaiserslautern, 2006.

[109] S. Leyendecker, P. Betsch, and P. Steinmann. Energy-conserving integration of constrained Hamiltonian systems – A comparison of approaches. *Comput. Mech.*, 33:174–185, 2004.

[110] S. Leyendecker, P. Betsch, and P. Steinmann. Objective energy-momentum conserving integration for the constrained dynamics of geometrically exact beams. *Comput. Methods Appl. Mech. Engrg.*, 195:2313–2333, 2006.

[111] S. Leyendecker, P. Betsch, and P. Steinmann. The discrete null space method for the energy-consistent integration of constrained mechanical systems. Part III: Flexible multibody dynamics. *Multibody System Dynamics*, 19:45–72, 2008.

[112] E. Love and D. L. Sulsky. An energy-consistent material-point method for dynamic finite deformation plasticity. *Int. J. Numer. Meth. Engng*, 65:1608–1638, 2006.

[113] J. Lubliner. *Plasticity Theory*. MacMillan Publishing Company, 1990.

[114] L. E. Malvern. *Introduction to the Mechanics of a Continuous Medium*. Prentice-Hall, 1969.

[115] J. E. Marsden and T. J. R. Hughes. *Mathematical Foundations of Elasticity*. Prentice-Hall, 1996.

[116] J. E. Marsden, C. Kane, and M. Ortiz. Symplectic-energy-momentum preserving variational integrators. *J. Math. Phys.*, 40:3353–3371, 1999.

[117] J. E. Marsden and M. West. Discrete mechanics and variational integrators. *Acta Numer.*, 10:357–514, 2001.

[118] X. N. Meng and T. A. Laursen. Energy consistent algorithms for dynamic finite deformation plasticity. *Comput. Methods Appl. Mech. Engrg.*, 191:1639–1675, 2002.

[119] X. N. Meng and T. A. Laursen. On energy consistency of large deformation plasticity models, with application to the design of unconditionally stable time integrators. *Finite Elements in Analysis and Design*, 38:949–963, 2002.

[120] A. Menzel. *Modelling and Computation of Geometrically Nonlinear Anisotropic Inelasticity*. Phd thesis, University of Kaiserslautern, 2002.

[121] A. Menzel. Relations between material, intermediate and spatial generalised strain measures for anisotropic multiplicative inelasticity. *Acta Mech.*, 182:231–252, 2006.

[122] A. Menzel, M. Ekh, K. Runesson, and P. Steinmann. A framework for multiplicative elastoplasticity with kinematic hardening coupled to anisotropic damage. *Int. J. Plasticity*, 21:397–434, 2005.

[123] A. Menzel and P. Steinmann. A theoretical and computational setting for anisotropic continuum damage mechanics at large strains. *Int. J. Solids Struct.*, 38:9505–9523, 2001.

[124] A. Menzel and P. Steinmann. Geometrically nonlinear anisotropic inelasticity based on fictitious configurations: Application to the coupling of continuum damage and multiplicative elasto-plasticity. *Int. J. Numer. Meth. Engng*, 56:2233–2266, 2003.

[125] A. Menzel and P. Steinmann. On the spatial formulation of anisotropic multiplicative elasto-plasticity. *Comput. Methods Appl. Mech. Engrg.*, 192:3431–3470, 2003.

[126] C. Miehe. Computation of isotropic tensor functions. *Commun. Numer. Methods Engng.*, 9:889–896, 1993.

[127] C. Miehe. Aspects of the formulation and finite element implementation of large strain isotropic elasticity. *Int. J. Numer. Meth. Engng*, 37:1981–2004, 1994.

[128] C. Miehe. Exponential map algorithm for stress updates in anisotropic multiplicative elastoplasticity for single crystals. *Int. J. Numer. Meth. Engng*, 39:3367–3390, 1996.

[129] C. Miehe. Comparison of two algorithms for the computation of fourth-order isotropic tensor functions. *Comput. Struct.*, 66:37–43, 1998.

[130] C. Miehe. A constitutive frame of elastoplasticity at large strains based on the notion of a plastic metric. *Int. J. Solids Struct.*, 35:3859–3897, 1998.

[131] C. Miehe and N. Apel. Anisotropic elastic-plastic analysis of shells at large strains. A comparison of multiplicative and additive approaches to enhanced finite element design and constitutive modelling. *Int. J. Numer. Meth. Engng*, 61:2067–2113, 2004.

[132] C. Miehe and E. Stein. A canonical model of multiplicative elasto-plasticity: Formulation and aspects of the numerical implementation. *Euro. J. Mech. A/Solids*, 11:25–43, 1992.

[133] R. Mohr, T. Bobach, G. Reis, Y. Hijazi, A. Menzel, P. Steinmann, and H. Hagen. Comparative tensor visualization within the framework of consistent time-stepping schemes. In *Visualization of Large and Unstructured Data Sets*. Accepted for publication, 2008.

[134] R. Mohr, A. Menzel, and P. Steinmann. Galerkin-based time integrators for geometrically nonlinear elasto-plastodynamics – Challenges in modeling and visualization. In *Visualization of Large and Unstructured Data Sets*, volume S-4, pages 185–194. GI-Edition Lecture Notes in Informatics (LNI), 2006.

[135] R. Mohr, A. Menzel, and P. Steinmann. Assessment of Galerkin-based time integrators for finite elasto-plasto-dynamics. In C. L. Bottasso, P. Masarati, and L. Trainelli, editors, *Multibody Dynamics*. ECCOMAS Thematic Conference, Milano, 2007.

[136] R. Mohr, A. Menzel, and P. Steinmann. Conservation properties of Galerkin-based time integrators for geometrically nonlinear elasto-plasto-dynamics. In O. T. Bruhns and A. Meyers, editors, *IMPLAST – Symposium on Plasticity and Impact Mechanics*, pages 431–438. The University Press Bochum, 2007.

[137] R. Mohr, A. Menzel, and P. Steinmann. Conservation properties of Galerkin-based time-stepping schemes for finite elasto-plasto-dynamics. In E. Onate, D. R. J. Owen, and B. Suarez, editors, *COMPLAS IX – International Conference on Computational Plasticity*, pages 948–951. CIMNE, Barcelona, 2007.

[138] R. Mohr, A. Menzel, and P. Steinmann. Galerkin-based mechanical integrators for finite elastodynamics formulated in principal stretches – Pitfalls and remedies. Submitted for publication, 2007.

[139] R. Mohr, A. Menzel, and P. Steinmann. A consistent time FE-method for large strain elasto-plasto-dynamics. *Comput. Methods Appl. Mech. Engrg.*, 2008. doi: 10.1016/j.cma.2008.02.002.

[140] R. Mohr, A. Menzel, and P. Steinmann. Finite elasto-plasto-dynamics – Challenges & solutions. In *Visualization of Large and Unstructured Data Sets*. Accepted for publication, 2008.

[141] R. Mohr, S. Uhlar, A. Menzel, and P. Steinmann. Time-FE methods for the nonlinear dynamics of constrained inelastic systems. In *IUTAM – Symposium on Theoretical, Modelling and Computational Aspects of Inelastic Media*. Submitted for publication, 2008.

[142] K. N. Morman. The generalized strain measure with application to nonhomogeneous deformations in rubber-like solids. *J. Appl. Mech.*, 53:726–728, 1986.

[143] N. M. Newmark. A method of computation for structural dynamics. *ASCE Journal of the Engineering Mechanics Division*, 85:67–94, 1959.

[144] L. Noels, L. Stainier, and J. P. Ponthot. An energy-momentum conserving algorithm for non-linear hypoelastic constitutive models. *Int. J. Numer. Meth. Engng*, 59:83–114, 2004.

[145] L. Noels, L. Stainier, and J. P. Ponthot. On the use of large time steps with an energy momentum conserving algorithm for non-linear hypoelastic constitutive models. *Int. J. Solids Struct.*, 41:663–693, 2004.

[146] L. Noels, L. Stainier, and J. P. Ponthot. Energy conserving balance of explicit time steps to combine implicit and explicit algorithms in structural dynamics. *Comput. Methods Appl. Mech. Engrg.*, 195:2169–2192, 2006.

[147] L. Noels, L. Stainier, and J. P. Ponthot. An energy momentum conserving algorithm using the variational formulation of visco-plastic updates. *Int. J. Numer. Meth. Engng*, 65:904–942, 2006.

[148] L. Noels, L. Stainier, and J. P. Ponthot. A first-order energy-dissipative momentum-conserving scheme for elasto-plasticity using the variational updates formulation. *Comput. Methods Appl. Mech. Engrg.*, 197:706–726, 2008.

[149] R. W. Ogden. *Non-Linear Elastic Deformations*. Ellis Horwood, 1984.

[150] W. Preuss and G. Wenisch. *Lehr- und Übungsbuch – Numerische Mathematik*. Carl Hanser Verlag, 2001.

[151] L. Rosati and N. Valoroso. A return map algorithm for general isotropic elasto/visco-plastic materials in principal space. *Int. J. Numer. Meth. Engng*, 60:461–498, 2004.

[152] K. Runesson, F. Larsson, and P. Hansbo. Space-time finite elements and adaptive strategy for the coupled poroelasticity problem. In *IUTAM – Symposium on Theoretical and Numerical Methods in Continuum Mechanics of Porous Materials*. Springer, 2001.

[153] K. Runesson, A. Samuelsson, and L. Bernspang. Numerical technique in plasticity including solution advancement control. *Int. J. Numer. Meth. Engng*, 22:769–788, 1986.

[154] K. Runesson, S. Sture, and K. Willam. Integration in computational plasticity. *Comput. Struct.*, 30:119–130, 1988.

[155] C. Sansour. A time integration scheme with energy-momentum conservation for a shell formulation with arbitrary geometric and material non-linearities. *Comput. Struct.*, 82:2753–2763, 2004.

[156] C. Sansour, W. Wagner, P. Wriggers, and J. Sansour. An energy-momentum integration scheme and enhanced strain finite elements for the non-linear dynamics of shells. *Int. J. Non–Linear Mechanics*, 37:951–966, 2002.

[157] C. Sansour, P. Wriggers, and J. Sansour. Nonlinear dynamics of shells: Theory, Finite Element formulation, and integration schemes. *Nonlin. Dynamics*, 13:279–305, 1997.

[158] C. Sansour, P. Wriggers, and J. Sansour. On the design of energy-momentum integration schemes for arbitrary continuum formulations. Applications to classical and chaotic motion of shells. *Int. J. Numer. Meth. Engng*, 60:2419–2440, 2004.

[159] W. Schiehlen. *Technische Dynamik*. Teubner, 1986.

[160] A. A. Shabana. *Dynamics of Multibody Systems*. Wiley, 1989.

[161] J. C. Simo. Algorithms for static and dynamic multiplicative plasticity that preserve the classical return mapping schemes of the infinitesimal theory. *Comput. Methods Appl. Mech. Engrg.*, 99:61–112, 1992.

[162] J. C. Simo. Numerical analysis and simulation of plasticity. In P. G. Ciarlet and J. L. Lions, editors, *Handbook of Numerical Analysis*, volume 6, pages 183–499. North–Holland, 1998.

[163] J. C. Simo and S. Govindjee. Non-linear B-stability and symmetry preserving return mapping algorithms for plasticity and viscoplasticity. *Int. J. Numer. Meth. Engng*, 31:151–176, 1991.

[164] J. C. Simo and T. J. R. Hughes. *Computational Inelasticity*. Springer, 1997.

[165] J. C. Simo and N. Tarnow. The discrete energy-momentum method. Conserving algorithms for nonlinear elastodynamics. *Z. angew. Math. Phys.*, 43:757–792, 1992.

[166] J. C. Simo and N. Tarnow. A new energy and momentum conserving algorithm for the non-linear dynamics of shells. *Int. J. Numer. Meth. Engng*, 37:2527–2549, 1994.

[167] J. C. Simo, N. Tarnow, and M. Doblare. Non-linear dynamics of three-dimensional rods: Exact energy and momentum conserving algorithms. *Int. J. Numer. Meth. Engng*, 38:1431–1473, 1995.

[168] J. C. Simo, N. Tarnow, and K. K. Wong. Exact energy-momentum conserving algorithms and symplectic schemes for nonlinear dynamics. *Comput. Methods Appl. Mech. Engrg.*, 100:63–116, 1992.

[169] J. C. Simo and R. L. Taylor. Quasi-incompressible finite elasticity in principal stretches. Continuum basis and numerical algorithms. *Comput. Methods Appl. Mech. Engrg.*, 85:273–310, 1991.

[170] J. C. Simo and K. K. Wong. Unconditionally stable algorithms for rigid body dynamics that exactly preserve energy and momentum. *Int. J. Numer. Meth. Engng*, 31:19–52, 1991.

[171] H. Sugiyama and A. A. Shabana. Application of plasticity theory and absolute nodal coordinate formulation to flexible multibody system dynamics. *ASME J. Mech. Design*, 126:478–487, 2004.

[172] H. Sugiyama and A. A. Shabana. On the use of implicit integration methods and the absolute nodal coordinate formulation in the analysis of elasto-plastic deformation problems. *Nonlin. Dynamics*, 37:245–270, 2004.

[173] N. Tarnow and J. C. Simo. How to render second order time-stepping algorithms fourth order accurate while retaining the stability and conservation properties. *Comput. Methods Appl. Mech. Engrg.*, 115:233–252, 1994.

[174] T. C. T. Ting. Determination of $\boldsymbol{C}^{1/2}$, $\boldsymbol{C}^{-1/2}$ and more general isotropic functions of $\boldsymbol{C}$. *J. Elasticity*, 15:319–323, 1985.

[175] Y. U. Vetyukov, J. Gerstmayr, and H. Irschik. Modeling spatial motion of 3D deformable multibody systems with nonlinearities. *Multibody System Dynamics*, 15:67–84, 2006.

[176] M. West. *Variational Integrators*. Phd thesis, California Institute of Technology, Pasadena, 2004.

[177] P. Wriggers. *Nichtlineare Finite-Element-Methoden*. Springer, 2001.

[178] O. C. Zienkiewicz and R. L. Taylor. *The Finite Element Method*. McGraw-Hill, 1991.

Curriculum Vitae

Name:	Rouven Mohr
Geburtsdatum:	22. August 1979
Geburtsort:	Saarbrücken
Nationalität:	deutsch
Familienstand:	ledig

1986 – 1990	Grundschule Eschringen
1990 – 1999	Otto-Hahn-Gymnasium Saarbrücken, Abschluss: Allgemeine Hochschulreife
1999 – 2005	Wehrersatzdienst, Bundesanstalt Technisches Hilfswerk THW
10/2000 – 02/2005	Studium des Maschinenbaus, Technische Universität Kaiserslautern, Vertiefungsrichtung: Energietechnik, Abschluss: Diplom-Ingenieur
seit 03/2005	Promotionsstudent als Stipendiat im Internationalen DFG-Graduiertenkolleg 1131 "Visualization of Large and Unstructured Data Sets: Applications in Geospatial Planning, Modeling, and Engineering", Lehrstuhl für Technische Mechanik, Technische Universität Kaiserslautern

UKL/LTM-Schriftenreihe

bereits veröffentlicht wurden:

1 Menzel, A.: Modelling and Computation of Geometrically Nonlinear Anisotropic Inelasticity.
2002, ISBN 3-925178-86-4

2 Betsch, P.: Computational Methods for Flexible Multibody Dynamics.
2002, ISBN 3-925178-92-9

3 Liebe, T.: Theory and numerics of higher gradient inelastic material behavior.
2003, ISBN 3-936890-09-9

4 Groß, M.: Conserving Time Integrators for Nonlinear Elastodynamics.
2004, ISBN 3-936890-37-4

5 Kuhl, E.: Theory and Numerics of Open System Continuum Thermodynamics – Spatial and Material Settings –.
2004, ISBN 3-936890-42-0

6 Sunyk, R.: On Aspects of Mixed Continuum-Atomistic Material Modelling.
2004, ISBN 3-936890-51-X

7 Arockiarajan, A.: Computational Modeling of Domain Switching Effects in Piezoceramic Materials – A Micro-Macro Mechanical Approach.
2005, ISBN 3-936890-92-7

8 Mergheim, J.: Computational Modeling of Strong and Weak Discontinuties.
2006, ISBN 3-939432-02-4; 978-3-939432-02-4-9

9 Delibas, B.: Rate dependent nonlinear properties of perovskite tetragonal piezoelectric materials using a micromechanical model.
2006, ISBN 3-939432-05-9; 978-3-939432-05-0

10 Leyendecker, S.: Mechanical integrators for constrained dynamical systems in flexible multibody dynamics.
2006, ISBN 3-939432-09-1; 978-3-939432-09-8

11 Denzer, R.: Computational Configurational Mechanics.
2006, ISBN 3-939432-12-1; 978-3-939432-12-8

12 Krol, O.: Thermo-Mechanical Modelling of Solids and Interfaces – Theory, Numerics and Applications. 2007, ISBN 978-3-939432-45-6

13 Kleuter, B.: Generalized Parameter Identification for Finite Viscoelasticity. 2007, ISBN 978-3-939432-53-1

14 Menzel, A.: Frontiers in Inelastic Continuum Mechanics. 2007, ISBN 978-3-939432-55-5

15 Himpel, G.: Computational Modeling of Biomechanical Phenomena – Remodeling, Growth and Reorientierung. 2008, ISBN 978-3-939432-62-3

16 Bargmann, S.: Theory and numerics of non-classical thermo-hyperelasticity. 2008, ISBN 978-3-939432-77-7

17 Hirschberger, C. B.: A Treatise on Micromorphic Continua. Theory, Homogenization, Computation. 2008, ISBN 978-3-939432-80-7

18 Mohr, R.: Consistent Time-Integration of Finite Elasto-Plasto-Dynamics. 2008, ISBN 978-3-939432-81-4